UNIVERSITY OF SOUTHAMPTON

Faculty of Engineering and Physical Sciences

School of Engineering

Building a Bridge Over the Valley of Death: A Practical Development of Textile Supercapacitors

Volume 1 of 1

by

Nicholas David George Hillier

[CPhys, MPhys]

ORCiD: 0000-0002-3544-8329

A thesis for the degree of

Doctor of Philosophy

June 2023

University of Southampton

Abstract

Faculty of Engineering and Physical Sciences

School of Engineering

Doctor of Philosophy

Building a Bridge Over the Valley of Death: A Practical Development of Textile Supercapacitors

by Nicholas David George Hillier

This thesis presents a practical development of textile supercapacitors for e-textile applications. Textile supercapacitors are seen as a crucial enabling technology for future e-textiles as a power management component. A wealth of research has gone into developing these devices over the previous decade, however, this research has broadly focused on electrochemical performance alone, and has led to the development of devices which are unlikely to transition from the laboratory to the real-world. Underpinned by a design philosophy of sustainability and scalability, this work has developed the performance of an all carbon single-layer textile supercapacitor without the need for exotic electrode materials or challenging production methodologies. The device is later integrated within a first of a kind textile power module capable of powering future e-textile applications.

A simple spray deposition technique is used to produce single-layer all textile supercapacitors. Three commercial activated carbons are evaluated as potential electrode materials and the electrode ink formulation is optimised with a 9:1 ratio of active material to conductive additive. A device with a capaitance of 23.6 $mF.cm^{-2}$, energy density of 2.1 $\mu Wh.cm^{-2}$ and power density of 0.11 $mW.cm^{-2}$ is achieved, demonstrating the capability of basic materials and industry friendly production methods.

The electrolyte plays a pivotal role in the performance of the textile supercapacitor, both in terms of energy density as well as operational voltage. A series of electrolytes are evaluated, including an aqueous PVA electrolyte, edible electrolyte and organic polymer electrolyte. The aqueous electrolyte is shown to have severe degradation over a few days, making it impractical for real-world use. The edible electrolyte is shown to outperforms the aqueous electrolyte but still suffers from low voltage limits. The novel organic electrolyte is shown to be much more stable and increased the energy device of the carbon textile supercapacitor by 9x, achieving an energy density of 18.9 μWh.cm^{-2}, capable of power real-world applications.

A textile power module designed for built environment or low mobility applications is presented, produced from the developed textile supercapacitor from the previous chapters and a flexible rectenna. The prototype system presented a first of a kind design, and achieved a literature leading end-to-end efficiency of 38%. This was further developed and achieved an end-to-end efficiency of 46% and capable of power a Bluetooth Low Energy transceiver system for $>$100 s from a single charge.

Contents

List of Figures

List of Tables

Declaration of Authorship

I declare that this thesis and the work presented in it is my own and has been generated by me as the result of my own original research.

I confirm that:

1. This work was done wholly or mainly while in candidature for a research degree at this University;
2. Where any part of this thesis has previously been submitted for a degree or any other qualification at this University or any other institution, this has been clearly stated;
3. Where I have consulted the published work of others, this is always clearly attributed;
4. Where I have quoted from the work of others, the source is always given. With the exception of such quotations, this thesis is entirely my own work;
5. I have acknowledged all main sources of help;
6. Where the thesis is based on work done by myself jointly with others, I have made clear exactly what was done by others and what I have contributed myself;
7. Parts of this work have been published as:
    - N. Hillier, S. Yong, and S. Beeby, "Optimization of carbon electrodes for solid-state e-textile supercapacitors," Journal of Physics: Conference Series, vol. 1407, p. 012059, 2019.

- N. Hillier, S. Yong, and S. Beeby, "Calendar life of textile supercapacitors," in 2019 19th International Conference on Micro and Nanotechnology for Power Generation and Energy Conversion Applications (PowerMEMS), 2019, pp. 1–5.
- N. Hillier, S. Yong, and S. Beeby, "The good, the bad and the porous: A review of carbonaceous materials for flexible supercapacitor applications," Energy Reports, vol. 6, pp. 148–156, 2020.
- N. Hillier, S. Yong, and S. Beeby, "Culinary inspired electrolytes for textile supercapacitors," Energy Reports, vol. 7, pp. 81–86, 2021.
- N. Hillier, S. Yong, A. Cruden, and S. Beeby, "Acetonitrile-free organic electrolyte for textile supercapacitor applications," Journal of The Electrochemical Society, vol. 168, no. 8, p. 080520, aug 2021.
- M. Wagih, N. Hillier, S. Yong, A. S. Weddell, and S. Beeby, "Rf-powered wearable energy harvesting and storage module based on e-textile coplanar waveguide rectenna and supercapacitor," IEEE Open Journal of Antennas and Propagation, vol. 2, pp. 302–314, 2021.
- S. Yong, N. Hillier, and S. Beeby, "The influence of textile substrate on the performance of multilayer fabric supercapacitors," Journal of Industrial Textiles, vol. 50, no. 9, pp. 1397–1408, 2021.
- M. Wagih, N. Hillier, A. S. Weddell, and S. Beeby, "E-textile rf energy harvesting and storage using organic-electrolyte carbon-based supercapacitors," in 2021 IEEE MTT-S International Microwave Workshop Series on Advanced Materials and Processes for RF and THz Applications (IMWS-AMP), 2021, pp. 391–393.
- M. Wagih, N. Hillier, A. S. Weddell, and S. Beeby, "Textile-based radio frequency energy harvesting and storage using ultra-compact rectennas with high effective-to-physical area ratio," in 2021 IEEE 20th International Conference on Micro and Nanotechnology for Power Generation and Energy Conversion Applications (PowerMEMS), 2021, pp. 32–35

Signed:..... Date:.....

Acknowledgements

Thanks must go to the Engineering and Physical Sciences Research Council under the grant EP/L016818/1 and the School of Electronics and Computer Science at the University of Southampton for sponsoring this PhD. I would also like to personally thank my supervisory team, Professor Steve Beeby, Professor Andy Cruden and Dr. Sheng Yong for their guidance and support. In particular I would like to thank Sheng for his guidance and patience with the experimental work. Your input was exceedingly helpful and I would have been lost in the wilderness otherwise.

At times, a PhD can feel like an insurmountable individual endeavour but the truth is it delivered through the support of many people.

I would like to thank the people who have inspired and taught me throughout my academic career. To Mr. Charlie and Mr. Thomas who inspired me to go into the sciences. To Cordy Lewis (Mott) who believed in me when many didn't and gave me the second chance I needed. To Sanja Barkovic, Stuart Harmon and Steven Turner who made me the experimentalist I am today. To my ever patient collaborator Dr. Mahmoud Wagih. Thank you all dearly.

This would not have been possible without my close friends who have held me up, consoled me and championed me throughout. To Clarice Goff who started this journey with me. I would not have had the courage to take this opportunity without your love and strength. To the other students of the Energy Storage CDT, in particular Dr. Ewan Fraser and Dr. James Le Houx. To Ben Craig, the man who pulled me out of so many dark holes. This thesis is a testament to your friendship and kindness. To the Marshall- Pullins; Dom, Jess, Alfie-Ray, Arthur, Rupert and Betsy-Rose, for being my biggest cheerleaders. To Dr. Andrew Lamb and Connie Pallister for being such rocks and frankly glorious humans. To Rory Penman and Dr. Ben Chichester for their

unwavering support, advice and fantastic times. This would have not been possible without you both. To Emma Waddell who pulled me together at the final hurdles of this PhD. I will forever be grateful for your care, compassion and love. My profoundest thanks to all of you.

Finally to my family, the most important people to me throughout this PhD. To Samuel, you constantly inspire me with your intellect, passion and sheer kindness. You have driven me to be the example you deserve. To my parents, David and Lynne, you are the reason I am who I am today. Without your support, nothing I have achieved would have been possible. You are my rocks and my greatest support and I am eternally grateful for everything you have done for me. This thesis is dedicated to you and your love. Thank you.

Abbreviations

ACF Activated Carbon Fabric.

AFM Atomic Force Microscope.

BET Brunauer-Emmett-Teller.

BFC Microbial Biofuel Cell.

BJH Barret-Joyner-Halenda.

$\mathbf{C_{diff}}$ Diffusion Capacitance.

$\mathbf{C_{dl}}$ Double layer Capacitance.

$\mathbf{C_H}$ Helmholtz Layer Capacitance.

CNT Carbon Nanotube.

CPE Constant Phase Element.

CPW Coplanar Waveguide.

CV Cyclic Voltammetry.

CVD Chemical Vapour Deposition.

DSSC Dye-sensitised Solar Cell.

e-textile electronic textile.

EDL Electric Double Layer.

EIRP Effective Isotropic Radiated Power.

EIS Electrochemical Impedance Spectroscopy.

EPR Equivalent Parallel Resistance.

ESR Equivalent Series Resistance.

ESW Electrochemical Stability Window.

GCD Galvanostatic Charge Discharge.

IoT Internet of Things.

LSV Linear Sweep Voltammetry.

MVP Minimal Viable Product.

MWCNT Multi-walled Carbon Nanotube.

OSC Organic Solar Cell.

PCE Power Conversion Efficiency.

PHE Power Harvesting Efficiency.

PMIC Power Management Integrated Circuit.

RC Resistor-Capacitor.

RFID Radio Frequency Identification.

SEM Scanning Electron Microscope.

TENG Triboelectric Nanogenerators.

TSC Textile Supercapacitor.

VNA Vector Network Analyser.

Chemical Formulae

1 2 4-TCB 1,2,4-Trichlorobenzene.

ACN Acetonitrile.

ADN Adiponitrile.

ADP Ammonium Dihydrogenphosphate.

$BaTiO_3$ Barium Titanate.

Bi_2Te_3 Bismuth Telluride.

DMSO Dimethyl Sulfoxide.

EMITFSI 1-ethyl-3-methylimidazolium Bis(trifluoromethyl-1-sulfonyl)imide.

EVA Poly(ethylene-co-vinyl acetate).

Fe_2O_3 Iron Oxide.

FEP Fluorinated Ethylene Propylene.

GO Graphene Oxide.

H_2SO_4 Sulphuric Acid.

H_3PO_4 Phosphoric Acid.

ITO-PET Indium Tin oxide coated Polyethylene Terephthalate.

KCl Potassium Chloride.

$KNaNbO_3$ Potassium Sodium Niobate.

KOH Potassium Hydroxide.

Li_2SO_4 Lithium Sulphate.

LiCl Lithium Chloride.

$LiClO_4$ Lithium Perchlorate.

LiTFSI Lithium Bis(trifluoromethanesulphonyl)imide.

MnO_2 Manganese Dioxide.

MoO_3 Molybdenum Trioxide.

MSG Monosodium Glutamate.

Na_2SO_4 Sodium Sulphate.

NaCl Sodium Chloride.

Nb_2O_5 Niobium Pentoxide.

NdFeB Neodymium Iron Boron.

NiCo-BOH Nickel Cobalt-Bimetallic Oxyhydroxide.

$NiCo_2O_4$ Nickel Cobalt Oxide.

$NiCo_2S_4$ Nickel Cobalt Sulfide.

P3HT:ICBA Poly(3-hexylthiophene):Indene-C_{60} Bisadduct.

PAM Polyacrylamide.

PAN Polyacrylonitrile.

PANI Polyaniline.

PbTe Lead Telluride.

PC Propylene Carbonate.

PEDOT:PSS Poly(3,4-ethylenedioxythiophene) Polystyrene Sulfante.

PMMA Poly(Methyl Methacrylate).

PP Polypropylene.

PPy Polypyrrole.

PT Polyiophene.

PVA Polyvinyl Alcohol.

PVDF Poly(vinylidenefluoride).

PVDF-HFP Poly(vinylidenefluoride-hexfluoropropylene).

PZT Lead Zirconate Titanate.

rGO Reduced Graphene Oxide.

RuO_2 Ruthenium Oxide.

SN Succinonitrile.

$TEABF_4$ Tetraethylammonium Tetrafluoroborate.

TiO_2 Titanium Dioxide.

WO_3 Tungsten Trioxide.

$ZnCl_2$ Zinc Chloride.

ZnO Zinc Oxide.

To my parents, without whom this would never have been possible.

Chapter 1

Introduction

Wearable technologies are rapidly becoming commonplace in our daily lives. Since the launch of consumer goods such as the Fitbit, and later the Apple watch and Google glasses, the lives of many have become entwined with these devices. The use of wearable technology stretches from healthcare [1] and sport [2] to defence [3] and consumer [4]. The wearable technology market is widely anticipated to be in excess of US$70 billion by 2025 [5] and with their functionality and compatibility with the Internet of Things (IoT) this market size can only increase further. Amongst the plethora of wearable technology sub-categories, smart textiles or electronic textiles (e-textiles) show great promise. Simply, an e-textile is a device that introduces electronic functionality into a traditional textile, which is appealing for many applications as they are able to utilise the textile as a flexible and breathable scaffold. When one also considers the ubiquity of clothing and its inherent close proximity to the end user, it becomes evident that e-textiles will shape the lives of many.

Sensors [6–8], actuators [9,10] and displays [11] have all been incorporated within e-textiles, allowing for a wide range of functionality; however, increasingly, the bottleneck for further design is the power management and supply of the e-textile. External batteries [12] are an obvious solution, offering a simple and energy-dense solution, though for many applications, heavy and rigid batteries would be cumbersome and would dramatically affect the wearability of the garment. Extra considerations, such as how to wash the garment, would also force a change of

consumer behaviour and habits. This is unacceptable if one wishes e-textiles to be widely adopted. Further to the consumer focused concerns, specialist applications (such as the military) may find external battery units an additional risk [13]. E-textile power management must be discrete and must be incorporated within the textile to limit external connections and enable the end-user to treat the e-textile as though it were a traditional garment. Energy harvesting has been widely seen as a solution to this power management conundrum. Mechanically coupled transducers, such as triboelectric [14, 15] or piezoelectric [16, 17] devices, and energy converters, such as photovoltaics [18], have all been demonstrated within e-textiles. However, a person is not always moving, the sun is not always shining, and these devices do not offer power upon demand, only power upon production. This problem is analogous to the temporal problem with renewable energy on the electrical grids and the solution is the same: energy storage.

The integration of energy storage in e-textiles has seen a surge in research intensity over the previous decade, with textile supercapacitors being the initial (and most significant) research theme. The long cycle life, high power density, good energy density and fast charge-discharge rates make supercapacitors appealing for integration into an energy harvester-based textile power unit. The research has focused, primarily, on electrode materials and ever-increasing performance metrics, which has proved very successful in bearing increasingly higher capacitance. However, many of the best performing devices utilise exotic materials or material structures and few devices have moved beyond the laboratory environment. Increasingly, the practical considerations (washability, calendar lifetime and ageing, safety, sustainability, interconnections, etc.) are having to be considered to translate this research into a real-world technology.

1.1 Aims and Objectives

The overall aim of this thesis is to produce a practical energy storage solution for future e-textile applications. To deliver this aim, the project has been split into three themes: *Device Performance*, *Electrolyte Selection* and *Device Safety and Integration*. These

three themes were judged to be the significant areas overlooked by the literature and the main limitations to the wider adoption of e-textile energy storage.

- **Device Performance**. The device performance theme is the broadest of the three and covers material optimisation, production and integration. The incorporation of the supercapacitor into a single layer of textile is a relatively recent development and a great deal of work is still required to understand the optimisation of the production and the effect this has on the electrochemical performance. Textile selection, ink properties and manufacturing techniques must all be investigated methodically. This is achieved via:
  - Investigation of optimal deposition and curing procedure
  - Investigation of suitability of unprocessed commercial activated carbons as electrode materials
  - Investigation of correct ink formulation from an electrochemical perspectives.
- **Electrolyte Selection**.The literature is lacking justifications for the selection of certain electrolytes. This is interesting, as the electrolyte has a significant effect on the performance of the textile supercapacitors. The concentration and conductivity, ion size and operating potential window all influence the performance. In many cases of e-textiles the addition of a gelling agent to the electrolyte (for practical and safety reasons) furthers the complication. Almost universally, this is achieved through the addition of Polyvinyl Alcohol (PVA) into aqueous electrolytes, but again without justification. This theme looks to challenge the commonly held consensus on electrolytes. This is achieved via:
  - Studying the role PVA has in the performance of the textile supercapacitor
  - Investigating the performance of benign aqueous electrolytes
  - Developing and testing of a high voltage, low hazard electrolyte to increase the energy density of the simple carbon TSC design.
- **Device Safety and Integration**.This theme encompasses two distinct ideas, the idea of reliability and safety and the idea of system integration. Within the

literature the experimental assessment of the reliability and safety of TSCs is limited and often 1-dimensional. If the device is flexible, for example, then bending testing is undertaken but thermal stability is ignored. Equally, the community seems to have been blinkered to the integration of TSCs into actual power units. With the charging characteristics of the device being assessed only in ideal laboratory conditions on battery analysers or ideal discrete components and not while connected to other e-textile devices. Very few end-to-end textile power units have been demonstrated, the few produced being done relatively recently. This theme looks to evaluate the TSCs in real-world situations and as part of larger, more complex systems. This is achieved via:

- Assessment of the durability of the unpackaged TSCs, including bending, cutting and puncture testing
- Assessment of the thermal stability of the unpackaged TSC
- Development of a proof-of-principle textile power module containing an e-textile energy harvester and TSC
- Development of a Minimal Viable Product (MVP) textile power module capable of powering a real-world external product.

1.2 Novelty

- Assessment of commercially available activated carbons for the use in textile supercapacitor electrodes
- Rationalised production methodology for single layer textile supercapacitors, that can be readily scaled for mass production
- The first calendar life assessment of textile supercapacitors
- The development and assessment of benign electrolytes for textile supercapacitor applications
- Production of the highest end-to-end efficiency textile power module using textile supercapacitors and a wearable RF energy harvester

- Development of an acetonitrile-free high voltage electrolyte for textile supercapacitors
- The first use of traditional energy storage metrology for e-textile devices

Chapter 2

Literature Review

In this chapter, background literature spanning the full supercapacitor landscape is discussed. The technical work within this project spans a number of disciplines, thus some initial underpinning theory and terminology is presented in section 2.1 and section 2.2. Section 2.1 presents the energy storage mechanisms of capacitors, electrolytic capacitors, supercapacitors and pseudocapacitors, while section 2.2 presents and discusses textiles and the benefits and challenges of their use within wearable applications. Section 2.3 discusses the crucial components of a TSCs, the electrodes and the electrolyte. The plethora of material options available for electrodes is critiqued in section 2.3.1 while section 2.3.2 discusses the commonly accepted electrolytes for TSC and highlights where these could be improved upon. The state-of-the-art in TSC research is presented section 2.4, forming a benchmark for the devices produced within this work. Section 2.5 presents complimentary technologies to the TSC, which can be combined to form practical textile power units. Finally, a summary of the literature and the gaps within the literature are provided in section 2.6.

This chapter has been presented in-part, in two published works [19] and [20].

2.1 From Electrostatic to Super: the progression of capacitors

2.1.1 Electrostatic

The electrostatic capacitor consists of two conducting parallel plates of area, A, separated by a distance, d. Between these plates is a dielectric material with a relative permittivity, ϵ_r, as seen in Figure 2.1. The capacitance, C, of this device can be simply calculated using equation 2.1.

$$C = \frac{\epsilon_0 \epsilon_r A}{d} \tag{2.1}$$

where ϵ_0 is the permittivity of free space, ϵ_0 = 8.854x10^{-12} F.m^{-1}.

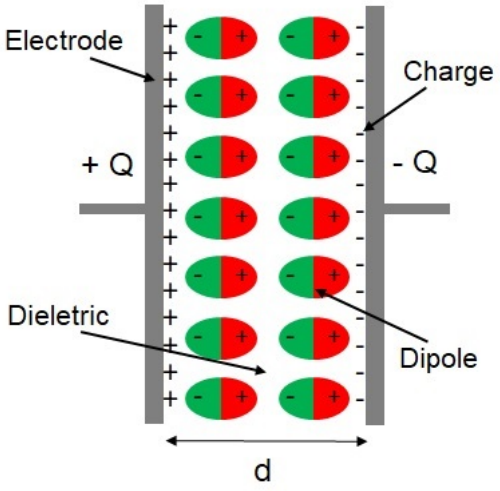

FIGURE 2.1: Schematic of a parallel plate capacitor. The charge builds on the opposing plates generating an internal electric field. This field acts as the storage mechanism.

Initially, capacitive devices were formed from jars of glass surrounded by tin foil, the famous Leyden Jars [21]. However, whether the device is a glass jar or a parallel plate capacitor the mechanism of energy storage is the same. A potential difference across the plates will induce a charge build up on the plates, resulting in an internal electric field. Once the external potential difference is removed, the charges are no longer held on the plates and the internal electric field breaks down. Being an electrostatic

mechanism and not an electrochemical mechanism (such as the storage observed in a battery), the charge/discharge rate of the capacitors is very high.

The energy stored in a capacitor, U, can be calculated from equation 2 and is dependent on the overall capacitance, C and the potential, V,

$$U = \int_0^Q V\,dq = \frac{1}{C}\int_0^Q q\,dq = \frac{1}{C}\frac{Q^2}{2} = \frac{1}{2}CV^2 \tag{2.2}$$

where Q denotes charge.

Crudely, it can be seen that the best way to increase the energy storage of a capacitor is to increase the voltage as the energy has a squared relationship with the voltage. However, the maximum voltage is limited by the break down voltage of the selected dielectric. Above this limit, the device will no longer function. Increasing the energy stored, therefore, becomes a matter of increasing the capacitance of your device. From equation 2.1 this can be achieved from increasing ϵ_r or A or by decreasing d. Increasing ϵ_r is achievable but limited, even the ceramic dielectrics have a permittivity limit of the order of 10^3 [22]. Increasing the surface area or decreasing the separation distance also meet practicable limits for real-world devices. Evidently, for high-energy applications a step change is required.

2.1.2 Electrolytic Capacitors

Electrolytic capacitors are a family of capacitors that differ from electrostatic capacitors by the use of an electrolyte that reacts with the metal foil or powder. This reaction forms a thin oxide layer that acts as the dielectric and enables small separation distances. The surface of the metal is also sintered/etched to roughen it, increasing the surface area. A further difference is the asymmetry of the electrodes found within the devices. Where the parallel plates have symmetric metallic plates, the electrolytic capacitor has a metallic anode and the electrolyte actually works at the cathode. A 'secondary' cathode of further metallic material is used to contact the working electrolyte cathode to the current collectors. Within this family of capacitors, three main subfamilies exist, namely:

- Aluminium electrolytic capacitors
- Tantalum electrolytic capacitors
- Niobium electrolytic capacitors

The aluminium subfamily use an etched aluminium foil and aluminium oxide as the dielectric layer produced during anodisation. The electrolyte used can be either solid or liquid in phase, though most commonly the non-solid electrolyte is seen. The oxide layer produced during anodisation is proportional to the voltage applied to the anode [23, 24] though fine control is not possible and is challenging to achieve thickness < 1 nm. Tantalum capacitors [25] differ from aluminium with a sintered 'slug' formed from tantalum powder being utilised instead of a foil. The dielectric oxide layer for these capacitors is tantalum pentoxide. Niobium capacitors share similar characteristics in physical make up to the tantalum capacitor but were developed to make use of the cheaper starting material [26]. In all of these devices, greater capacitance is seen compared to that of the parallel plate capacitors. However, these devices are polarised and a reversed bias can damage them, so great care is required in their use.

2.1.3 Super

The final family of electrostatic capacitor is the supercapacitor, also known as an ultracapacitor or an electrochemical capacitor. For clarity of this work, no distinction will be made and the term 'super' will be an umbrella definition for this form of capacitor. These devices offer orders-of-magnitude greater energy storage than a traditional capacitor [27] and better discharge times [28]. In the pantheon of energy storage options, supercapacitors are seen as a power dense technology and sit between the power quality and bridging power regimes, see Figure 2.2 . The characteristics of fast charge/discharge rates, good cycle life and high power density (while still exhibiting good energy density) make them appealing across a number of sectors, from protecting the battery in electric vehicles [29] and grid applications [30] to wearable technology [31–33].

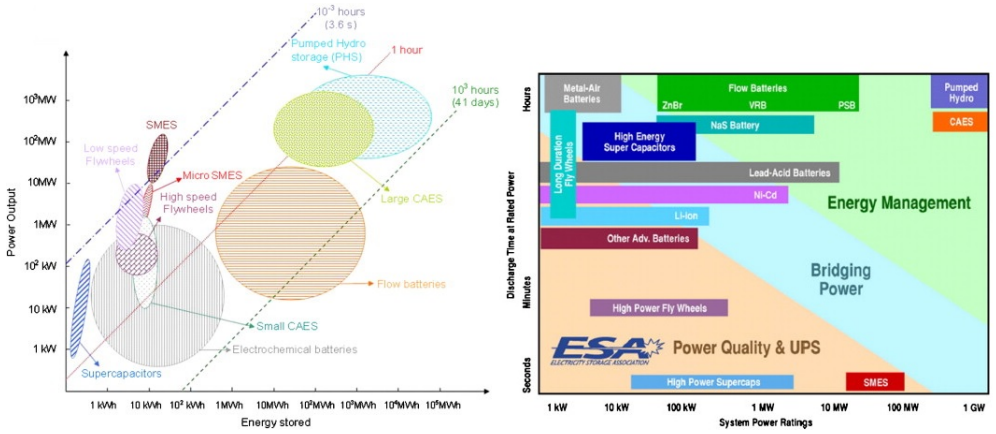

FIGURE 2.2: Two comparisons of different energy storage technologies. Left) Compares the technologies via a Ragone plot where it is apparent that the supercapacitors do not store as much energy as comparable technologies such as batteries. Right) Compares the technologies against discharge time at rated power. In this figure, supercapacitors have been further separated into high power and high energy, demonstrating the flexibility of the technology. Image modified from [28]

As with the previous families of capacitor, the storage mechanism for supercapacitors is electrostatic but, instead of forming a charge separation at the electrodes, the charge separation is at the interface of each electrode and the electrolyte (the so-called electrical double layer (EDL)). This differs considerably from a battery where the whole bulk of the electrode is utilised through faradic reactions. As the mechanism is a surface phenomenon for supercapacitors to be 'super', the electrodes must have a significant surface area to be able to store enough energy. Hence, many are produced from activated carbons whose surface area can be $> 3000\ m^2.g^{-1}$ [35]. Supercapacitors are produced with two symmetric electrodes, current collectors, an electrolyte and a charge separator that allows ion conduction but is electrically insulating. A schematic of a supercapacitor can be seen in Figure 2.3.

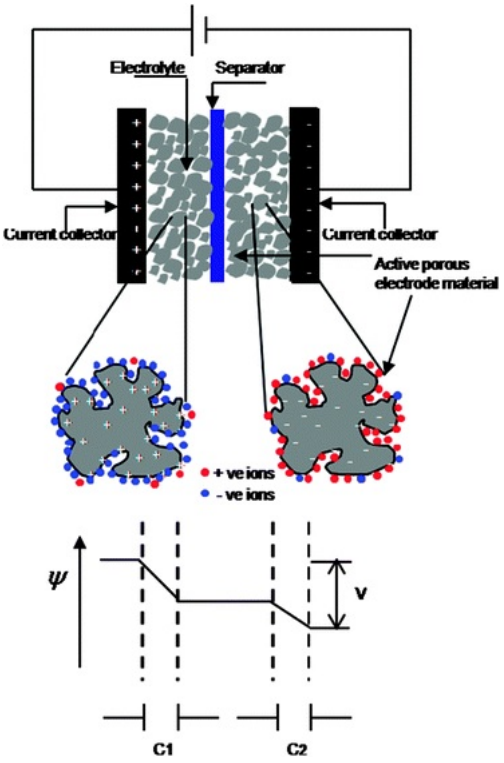

FIGURE 2.3: A schematic of a supercapacitor illustrating the constituent parts of the device. The zoomed in image of individual particles within the porous bulk of the electrode shows how the anions and cations are stored within the pores. The potential, Ψ, throughout the device is shown in the bottom image. At each double layer there is a capacitive element (c1 and c2) which is explain in more detail in section 3. Image modified from [34]

As explained above, a supercapacitor is super for a number of reasons: the Electric Double Layer (EDL) (leading to a very small separation), a very high surface area from porous carbon electrodes and multiple intrinsic capacitances. However, further discussion is required to understand the physical meaning behind these and to understand their importance.

The electrical double layer is a phenomenon arising at the interface of a charged object and a liquid, in this case the electrode and the electrolyte. With a charged boundary, a balancing counter charge will form in the liquid with a concentration near the surface. The physical mechanism of this interface has gone through refinement with three clear models appearing [37]: the Helmholtz model, the Gouy-Chapman model and the Stern model. The Helmholtz model introduces the first description of the double layer, though is now considered an oversimplification. In this description, an oppositely charged layer will be formed on the surface from the electrolyte to balance the charge

on the electrode. These layers of opposite charges will remain until the circuit between the polarised electrodes is removed. Importantly, these layers were viewed as rigid with a separation distance equal to the length between the surface and the centre of the counter ion. The Gouy-Chapman theory takes this model further by introducing thermal fluctuations that will have an effect on the ions. This work was undertaken independently of each other, however, both scientists introduced the idea of a diffuse layer of ions within the electrolyte. Instead of being held rigidly at the surface (as in Helmholtz's theory), the ions are in a diffuse region. The ion concentration within the Gouy-Chapman theory follows a Boltzmann distribution at the surface but fails at highly charged double layers [38]. The assumption of the ions as point charges (with no-limit on how closely they can approach the surface) also made this model inaccurate at a quantitative level. Finally, the theoretical understanding was furthered by Stern (but also Grahame [39] and Parsons [40]) to include multiple regions, bringing together the ideas of Helmholtz and Gouy-Chapman. In this model there are three regions, two compact regions (the inner and outer Helmholtz layers) and a diffusion layer. Unlike the model by Helmholtz, the inner rigid layer was split to account for different closest approaches of the finite sized ions. This distance is dependent upon electrolyte-solvent interactions and surface polarity. In this case the total Double layer Capacitance (C_{dl}) is a linear combination of both a Helmholtz Layer Capacitance (C_H), and a Diffusion Capacitance (C_{diff}).

$$\frac{1}{C_{dl}} = \frac{1}{C_H} + \frac{1}{C_{diff}} \tag{2.3}$$

The conceptual differences are illustrated in Figure 2.4 where Ψ and Ψ_0 denote the potential and electrode potential respectively. The progression, and in the case of Stern adoption, of different ideas of the mechanism of the double layer can be clearly seen. The inner Helmholtz layer defines the important separation distance, d, seen in Equation 2.1.

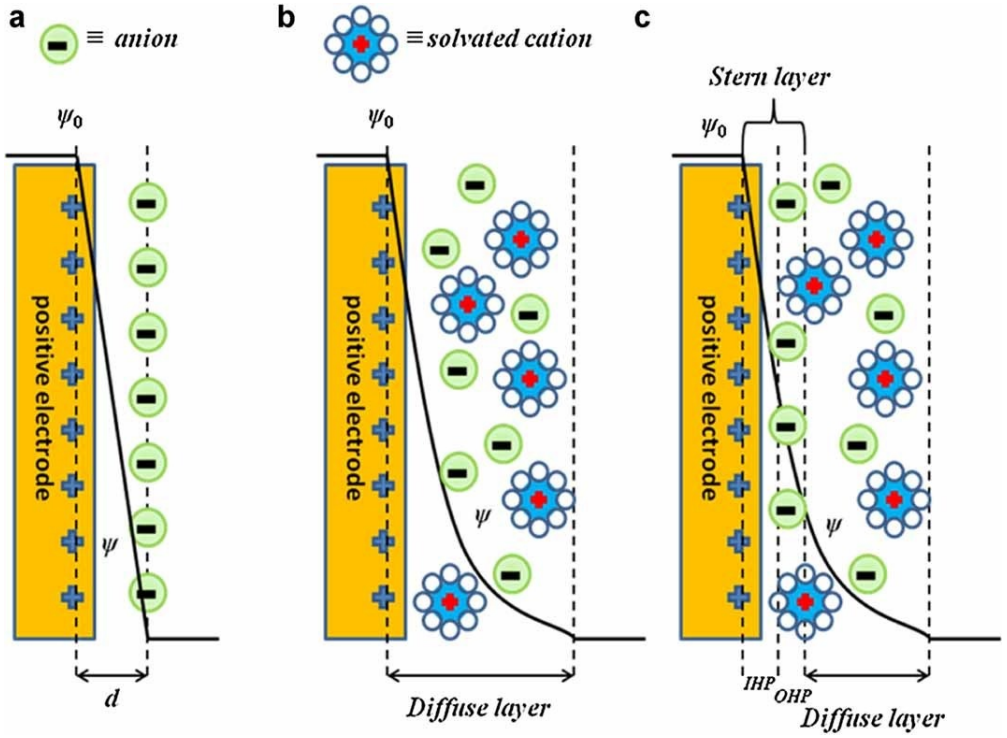

FIGURE 2.4: Illustration of the three principle theories of the electric double layer mechanism in historical order from left to right. A. is the Helmholtz model, B. is the Gouy-Chapman and C. is the Stern model. Image modified from [35].

The above theories somewhat satisfactorily explain the interaction of a changed plane with a liquid, however previously it has been mentioned that the boundary in a supercapacitor is not a perfect plane. In fact, on a porous electrode interface, these models do not account for the behaviour of the ions in the different scales of pore (nano, micro and meso). The structure of the electrode is unquestionably important to the overall storage potential of the capacitor. From Equation 2.1, it would be assumed that the important characteristic of the electrode material is the surface area, however, studies have shown that in fact pore size and distribution play a far more significant role [36–38] with no linear relationship between capacitance and surface area. The nature of meso pores (2 – 50 nm) and micro pores (1-2 nm) have been investigated and found to have effects on the energy and power densities of the capacitor [39]. It is seen that the meso pores are important for the ion transport into and out of the electrode and a greater density of these is found to improve the power density. The micro pores however are seen to have a closer relationship with the energy storage capacity and an increased number of this scale of pore will increase the energy storage of the supercapacitor. This relationship of the increased capacitance with more micro pores

can be understood as a better matching of pore size to solvated ion volume. For a maximum capacitance, one would want the minimum distance between the pore wall and the centre of the ion. This will occur when the pore volume/size is of the same order of the solvated ion and the ion adsorption into the pore is optimal. This was observed in [40] where Largeot *et al.* found the normalised capacitance drops off as the pores increase beyond the scale of the ions. One may then conclude that to best optimise a capacitor the application must be selected (power vs energy) and then a distribution of either micro or meso pores picked and produced. However, an 'anomalous' capacitance has been observed in carbon electrodes where the pore sizes are below the size of the solvated ions (nano pores $<$1 nm) [34]. This is certainly a counter intuitive result; however, Chmiola *et al.* [39] found a 100% increase in normalised capacitance as the pore size approached the crystallographic diameter of the ion. This could be due to a distortion of the solvation shell upon squeezing into the smaller pore (distortion of solvation shells has been reported elsewhere [41]) allowing a closer nearest approach, again reducing the separation distance seen in equation 2.1 and thus increasing the capacitance.

2.1.4 Beyond Electrostatics: pseudocapacitors

Pseudocapacitors [42–44] differ from electrostatic supercapacitors by the mechanism in which they store charge. Whereas supercapacitors store physical charges at the electrode-electrolyte boundary, pseudocapacitors store charge via fast, and highly reversible, faradic reactions. For those with an electrochemical background, this may seem to imply that pseudocapacitors are in fact batteries. However, this is not the case and are distinguished from batteries due to a linear (or near-linear) dependence of charge with changing potential [45]. The charges in the faradic reactions are admitted and extracted from the electrode material via charge-transfer across the interface. During this charge-transfer the oxidation state of the material is changed. The physical processes occurring at the electrode can be split into three mechanisms:

1. Fast intercalation of ions into the bulk, that does not result in a phase change [46]. An example of which is Li^+ ions intercalated into mesoporous films of Niobium Pentoxide (Nb_2O_5).

2. Ion absorption onto the electrode surface, manifesting via underpotential deposition [47] or electrosorption valency [48] as seen in charged metals [49].

3. Surface redox reactions [50], such as those exhibited in Ruthenium Oxide (RuO_2) [51].

Pseudocapacitors are appealing due to the increased energy density over supercapacitors and have been explored by the research community, however, they are hindered by poor cycle-life. The construction of hybrid devices or composite electrodes could mitigate this problem and allow the exploitation of the theoretically high capacitances of pseudocapacitor materials. However, when one remembers the tenants of this thesis (scalable and sustainable), pseudocapacitive materials are outside of the scope and this thesis will look to avoid pseudocapacitive effects within the TSCs.

2.2 Textiles: separating the warp from the weft

Textiles are ubiquitous in our everyday lives and span across industries, from upholstery to clothing. With textiles worn on our bodies, and within our home, their use in future wearable technologies is evident. Being able to bring the technology as close to the end user as possible, without having to change user behaviour, is imperative. Throughout this thesis, textiles are used as the substrate that the supercapacitors will be built within. The inherent open structure makes a good scaffold for the electrode material and the electrolyte can be readily absorbed. However, textiles are produced from various materials and with different manufacturing processes which introduces a number of variables that must be considered. A list of key textile terms can be found in Table 2.1 which will be referred to throughout the thesis.

TABLE 2.1: Key Terminology within the Textile Industry

Key Term	Definition
Crimp	The ratio of the length of a yarn to that of its length once woven.
Denier	The linear mass density of a fibre. Equivalent to the mass in grams per 9000 meters of fibre.
Ends per inch[α]	The number of warp threads per inch of a woven fabric.
Fibre	A natural or synthetic length of material exhibiting a large aspect ratio, that forms a yarn/thread when brought together.
Knit	A method of textile production where the yarn is interconnected into a mesh of loops.
Picks per inch	The number of weft threads per inch of a woven fabric.
Plain weave	A weave where the textile is formed by lifting and lowering one warp thread across one weft thread.
Twill	A weave exhibiting a diagonal pattern once produced. A weft thread is passed over one warp thread before being passed under two or more of the following warp threads.
Warp	The lengthwise thread within a weave. These are the threads held in place on a loom during weaving.
Weave	A method of textile production where threads are interlaced in a repeating pattern, orthogonal to each other.
Weft	The transverse thread which is drawn through the warp threads during weaving.
Yarn	A length of interlocked fibers used in weaving and knitting.

α The normalisation using inch in 'picks per inch' and 'ends per inch' is an industry standard.

Within this thesis a supplementary conversion to SI units will always be made.

The textiles of particular interest to the TSC community are cotton, polyester, blends of polyester and cotton, and silk. Cotton textile is, unsurprisingly, produced from the soft fibres found around the seeds of the cotton plant. These fibres are composed of long cellulose chains and can be easily spun into yarns for weaving. The nature of the yarns produces comfortable and highly breathable textiles, making it exceedingly attractive for clothing. Polyester textile is produced from the synthetic polymer yarns that contain the ester functional group, often polyethylene terephthalate. The fibres are produced via melt extrusion and drawing before being woven. The two threads

are often blended together to achieve a polyester-cotton textile that has the benefits of the breathability of the cotton but the hardiness of the polyester. Cotton and polyester fibres are the two most consumed fibres globally [52], and as such, any energy storage technology must work with these textiles to achieve the desired scalability. Inherent differences between the fibres, such as the hydrophobia, make universal production methods challenging. Where cotton may readily absorb a carbon electrode ink, polyester may not. Silk textile is a woven textile produced from a naturally occurring protein fibre. The fibre material is produced from insect larvae and the fibre itself is produced via throwing, a process in which a number of raw silk filaments are twisted together. Due to the farming processes, silk is an expensive textile, however the lightness, strength and thickness make it appealing for applications where volume is the limitation, not the cost.

In the work of Yong *et al.* [20] these common textiles were compared as substrates for multi layer TSCs. In this work, the polyester-cotton fabric was found to achieve the highest areal capacitance (118 $mF.cm^{-2}$ compared to 56.6 $mF.cm^{-2}$ for silk and 14.9 $mF.cm_{-2}$). This significant difference in areal capacitance was attributed to the increased carbon loading potential onto, and within, the polyester-cotton. The polyester could achieve a loading percentage of 14.1%wt (Carbon:Textile) compared to 2.23%wt for the cotton. However, in further work by the authors [53] when the same textiles were used for single layer devices the thinner textiles required the addition of a polymer membrane to prevent failure. The polymer membrane was a copolymer (Poly(ethylene-co-vinyl acetate) (EVA) and PMMA) that acted as an electrochemical separator that was impregnated into the textiles before the electrode deposition, and prevented full penetration of the carbon inks. This however adds complexity to the fabrication process that is undesirable for a scalable device. A single layer device has the advantage of an incredibly low profile, which greatly improves the user experience. To the authors view, this would require less user behavioural change and make the adoption of TSCs easier for the end-user. As such, a ~ 400 μm thick, plain weave, cotton has been selected as the substrate for this thesis as it requires no pre-requisite treatment and is inherently more recyclable than polyester-cotton [54]. These two advantages align precisely with the ethos of this thesis of scalable and

sustainable.

2.3 Textile Supercapacitors

The research into textile supercapacitors has seen considerable growth over the previous decade, evidenced by a simple publication search on Web of Science [55], Figure 2.5. Key-term searches such as "Wearable Supercapacitor" have seen a publication increase from single digits in 2011 to hundreds in 2021. Publications in the field of TSCs have also grown from single digits to nearly 200 publications per year. Figure 2.6 shows the 100 most common words found within the titles of the 1131 publications from 2010 to 2022 (year to date). As one would expect, the most common words are supercapacitor/supercapacitors. However, secondary words such as 'flexible', 'carbon', 'porous', 'high-performance', 'oxide' and 'graphene' demonstrate the focus of research being dominated by the production of advanced, flexible electrode materials. It is only until the third and fourth level of key words does one begin to see 'solid-state' or 'aqueous' which are related to the development or use of electrolytes within the literature. This focus on electrode material development is also seen in the journals which appear most often within the literature search with chemistry/electrochemical journals, such as ACS Applied Materials & Interfaces, Journal of Materials Chemistry A and Electrochemia Acta dominating. The field though is much broader than just the electrode materials and by 2021 this diversification of research effort is seen with 93 unique journals being covered within the 177 publications. This shows the multi-disciplinary nature of the topic and need for new approaches to overcome the technological challenges still present.

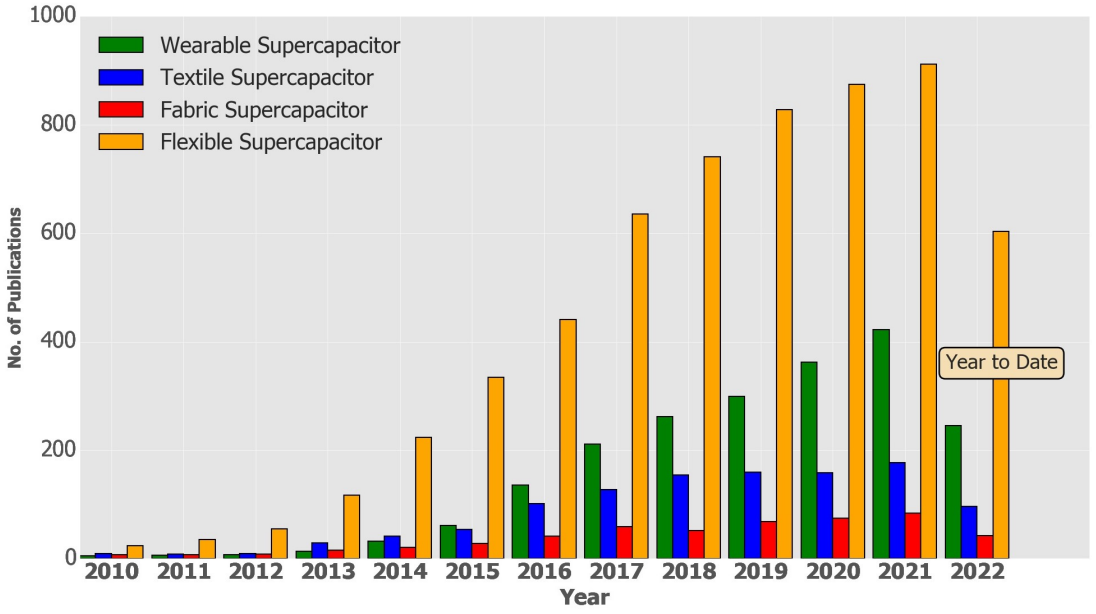

FIGURE 2.5: The number of publications per year searchable from Web of Science. Key term searches "Wearable Supercapacitor", "Textile Supercapacitor", "Fabric Supercapacitor" and "Flexible Supercapacitor" were chosen to cover the full research landscape. Data collected August 31st 2022 [55]

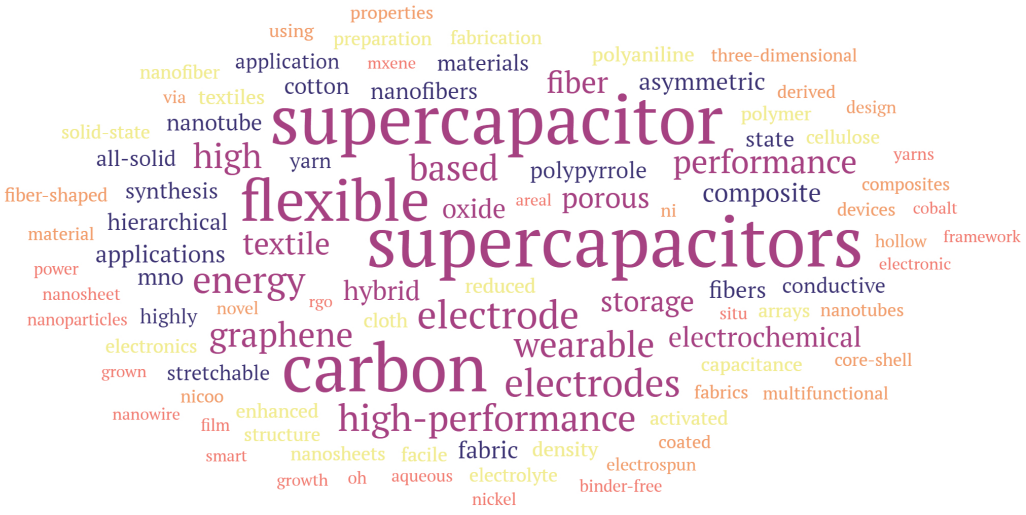

FIGURE 2.6: A word cloud generated from the 100 most common words found in the titles of 1131 publications covering the topic of textile supercapacitors from 2010 to 2022 (year to date).

Broadly, TSCs can be split into two families (Figure 2.7) that consist of further sub families. The first family is the traditional multi-layer plate design that is akin to a rigid supercapacitor. In this design, parallel layers of materials (current collectors, electrodes, and separators/electrolyte) are layered together to then be encapsulated or

left exposed. Though traditionally the active layers (electrode, electrolyte) are physically different layers, the work of Yong *et al.* [56] demonstrated how these can be incorporated into a single layer. The stacked parallel plate design is often utilised by flexible supercapacitors that use a fabric cloth as a substrate. The second family is the yarn (or fibre) where the active material is formed into a fibre. This fibre can then be constructed into a yarn in a twisted or parallel [57] or coaxial [58] structure. Conductive coatings, electrolyte introduction and encapsulation occurs during the fabrication reducing the bulk of the device considerably compared to that of the parallel stack capacitor. The fabrication of the yarn family is, however, more intricate than those of the parallel stack fabric capacitor (wet spinning, electrodeposition, biscrolling, etc) and the scalability of the production process for real-world demonstrators is questionable. Yarn devices also suffer from a fundamental problem of requiring greater lengths to increase the capacitance but therefore increasing the resistance of the device, causing greater losses. The parallel stack configuration however reduces resistance as the area is increased, making it more appropriate for upscaling.

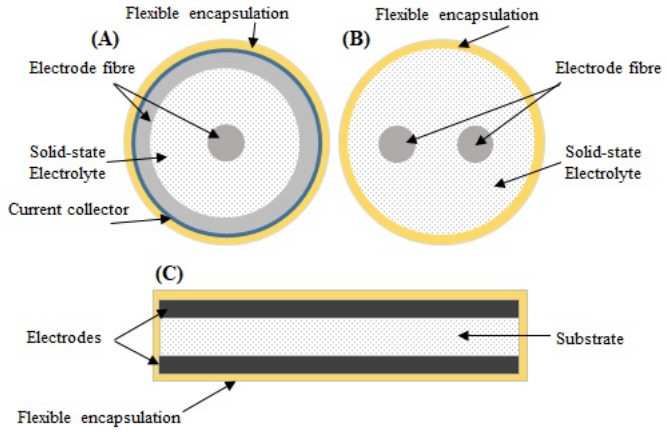

FIGURE 2.7: A schematic of the different textile supercapacitor topologies. (A) and (B) illustarte two forms a yarn TSC can take, coaxial and paired electrodes respectively. The paired form of the yarn TSC can either be parallel or twisted. (C) shows the side profile of a textile supercapacitor with a parallel plate configuration

Due to concerns over the production scalability and the added complications of having to then weave the fibers into a textile, this thesis will not explore the yarn style supercapacitor. Though excellent in-lab results have been demonstrated with yarn supercapacitors the ability to utilise established textile production techniques (such as

screen printing, spray deposition and roll pressing) for the multi-layered configuration presents the greater opportunity. However, that is not to say that the multi-layered configuration is simpler. Challenges with encapsulation and prevention of the active materials wicking away from the printing area are far from trivial. Also, as stated in section 2.2, the textile substrate itself will have an influence over the production method and the final electrochemical results, so further complexity is added by using the multi-layered configuration. However, it is believed that the added complexity of the multi-layered approach has a simpler final solution when considering the final product.

2.3.1 Materials

The electrode materials for textile supercapacitors must fulfil a number of design requirements, some of which are not considered for traditional supercapacitors. As well as being:

- Electrochemically stable throughout the operating potential window.
- Electrically conductive through the bulk of the electrode.
- stable over $> 10^5$ cycles.
- Compatible and wettable with the chosen electrolyte.

They must also be highly flexible and resilient, safe for the end user and must adhere well to the textile substrate. The active material, electrode ink formulation and production methodology all play pivotal roles in the overall performance of the device. Detailed below are a number of key textile supercapacitor materials.

Activated carbon is a highly porous form of carbon that has been extensively used for supercapacitor applications due to its exceedingly high surface area (up to 3000 m^2g^{-1} [59, 60]).These carbons are produced by 'activating' a biomass derived hydrothermal carbon or a pyrochar. The biomass precursor can take many forms, from coconut shells to agriculture, human or wood waste [61] with the activation

stage being in the form of a physical or chemical process. The biomass initially undergoes a pyrolysis stage in an inert atmosphere [62] (as in the case of pyrochar) or in the presence of subcritical water [63] (as in the case of the hyrdothermal carbon). This is then followed by either physical activation, where the carbon is oxidised in a gaseous or steam environment at elevated temperatures [64] or chemical activation, where the carbon is exposed to an activating chemical (such as Zinc Chloride ($ZnCl_2$) [65] or Potassium Hydroxide (KOH) [66]). With the quantity of precursor choices, pyrolysis settings (temperature, ramp rate, environments, etc) and activation options the selection of appropriate material is far from trivial [67–70]. The hydrothermal process is advantageous over tradition pyrolysis due to its ability to process 'wet' biomass without the need for energy dense drying stages but the resulting carbon can suffer from low porosity and electrical conductivity [68]. Chemical activation is seen to produce high porosity and high surface area but suffers from a high cost and energy-dense washing stages to rid the carbon of the chemical activator [71]. Activated carbons are seen as a favourable material due to their customisability with the limiting factor being the low conductivity (due to the high porosity) which can be overcome by conductive additives.

One of the earliest examples of activated carbon TSCs was demonstrated by Jost *et al.* [72]. In this work, activated carbon was combined with Liquitex^{TM} matte medium and water to form the carbon slurry. The slurry was applied to cotton and polyester fabrics fabrics through dip coating and screen printing for comparison. The dip coating methodology did not significantly impregnated the fabric and as such, only the screen printed samples were characterised. The cotton-based devices were found to have a gravimetric capacitance of 90 $F.g^{-1}$ compared to 83 $F.g^{-1}$ for the polyester-based device, characterised in 2 M Lithium Sulphate (Li_2SO_4) electrolyte via Galvanostatic Charge Discharge (GCD) at 20 mA. The cotton substrate devices were found to have a lower Equivalent Series Resistance (ESR) than the polyester substrate, however this was later improved by approximately a factor of 3 through the addition of 10%$_{wt}$ of carbon onions. Though the Liquitex^{TM} binder is misciple in water, the water base of this slurry probably impaired the impregnation of the carbon into the textile due to slight hydrophobicity of the textile substrate (see Figure 5.11 in

Chapter 5). Later, in the work of Xue *et al.* [73] produced a device with directly carbonised cotton electrodes. These devices achieved an areal capacitance of 0.7 $mF.cm^{-2}$ at a discharge current of 11.2 $\mu A.cm^{-2}$ in a 1 M Sodium Sulphate (Na_2SO_4) electrolyte. The drop in performance compared to the work of Jost, is attributed to a low specific surface area (<10 $m^2.g^{-1}$. Though the devices were claimed to be 'arbitrarily foldable' they also suffered from a bulky form factor. Su *et al.* [74] improved the performance of Activated Carbon Fabrics (ACFs) (steam activated) through the implementation of a heat treatment stage in a nitrogen atmosphere. By treating the ACF at 1500°C the specific surface area rose from 1000 to 1500 $m^2.g^{-1}$. At higher rate scan rates (250 $mV.s^{-1}$ the devices were found to have a higher capacitance (86 compared to 17 $F.g^{-1}$). However, at low scan rates (5 $mV.s^{-1}$) the ACF_{1000} was found to have a higher capacitance than the ACF_{1500} (263 compared to 175 $F.g^{-1}$). This is attributed to a greater proportion of mesopores forming during the heat treatment, improving the performance at the higher rates but impairing the capacitance at the slower rates where the micropores dominate the energy storage mechanism, as discussed in section 2.1.

The use of activated carbon as the primary active material for TSC applications then seems to fall out of fashion within the community, except for its use as the negative electrode in asymmetric devices [75–77]. The drop in research interest was due to concerns over the electrical resistance of the activated carbon electrodes and the increased interest in 1D and 2D carbon structures, pseudocapacitive materials and binary, and tertiary electrode formulations. However, in 2017, Xiao *et al.* [78] developed cotton and flax based TSCs which had undergone carbonisation at 550 - 850°C. Under Cyclic Voltammetry (CV) characterisation at 2 $mV.s^{-1}$ the $flax_{850}$ device achieved an areal capacitance of 97 $mF.cm^{-2}$ compared to 38 $mF.cm^{-2}$ for the $cotton_{850}$. The performance of the flax device was subsequently impproved through the addition of Polypyrrole (PPy), raising the capacitance to 860 $mF.cm^{-2}$. Where the flax only device was microporous the flax-PPy device showed both micro and meso porosity, again illustrating the importance of the pore structure and not only the total surface area for capacitance performance. Following this return to the investigation of activated carbon for TSC applications, Zhang *et al.* [79] in 2019 and Yang *et al.* [80] in

2020 further developed the use of activated carbon. Zhang, directly carbonised cotton fabric at 800° under a nitrogen atmosphere before activating, again at 800°C, in the presence of KOH. The electrode achieved a capacitance of 1026 $mF.cm^{-2}$, with a quasi solid-state device achieving 153 $mF.cm^{-2}$ with a PVA/KOH electrolyte. Yang, deviated from the direct activation of the textile substrate methodology, by dip drying fiberglass cloth in an activated carbon - asphalt dispersion before carbonising at 800 - 1000°C.The best performing solid-state device achieved 85.4 $mF.cm^{-2}$ at 0.5 $mA.cm^{-2}$. though lower than the results from Zhang, the power capability was higher 1.23 $mW.cm^{-2}$ compared to 0.54 $mW.cm^{-2}$. These two recent works demonstrated that activated carbon materials can achieve good electrochemical performance without the need for exotic materials, and in the case of Yang, was even able to use recycled material.

Other carbon materials for textile electrodes include graphene, Carbon Nanotubes (CNTs) and nanostructured carbons. Graphene is the monolayer of graphite and can be produced via chemical vapour deposition, mechanical exfoliation, colloidal suspensions or epitaxial growth on electrically insulating surfaces [81]. With desirable characteristics, graphene sets the gold standard for potential EDL supercapacitors with a theoretical capacitance limit of 550 $F.g^{-1}$ [82]. However, the performance is very dependent upon the purity and size of the sheets and the production methods that enable high purity also have high costs and low yields. This can be mitigated by the production of reduced graphene oxide instead (as this is far simpler to make in bulk) but the properties are diminished. CNTs are a higher dimensional form of graphene and can be classified as zigzag, armchair or chiral, depending upon the orientation of the rolled up graphene sheet [83]. Chemical vapour deposition is seen as the most promising large scale production methodology [84]. Sharing similar properties to graphene the use of CNTs in supercapacitor applications is widely reported. They are however seen as a power (rather than energy) dense electrode material due to the reduced surface area of their geometry. Further issues with contamination hinder wide spread adoption, though this can be reduced via additional stages in the production process [85]. Often CNTs (and in fact graphene as well) are used as an additional active material, improving the conductivity of activated carbon electrodes and aiding structural integrity [86]. Templated carbon offers a very controllable

production method for nanostructured carbons. Ordered pore structures and controlled pore distribution are all very possible, making them appealing for supercapacitor applications [87, 88]. These carbons are produced by filling a template (often produced from silica) with carbon in a fluid suspension then carbonizing the whole. The template is later removed through acid dissolution, leaving behind a highly structured carbon. However, complex and costly production limit the commercial opportunities shown by these materials. Carbon aerogels offer a high surface area and good electrical conductivity. Produced via the sol-gel method [89] aerogels are characterized by a highly-porous meso scale pore network. Unlike the activated carbon however, different pore sizes are not possible and meso scale pores are the only available ones. These carbons can be used as a precursor material for further activation or functionalisation.

Carbon (and its many allotropes) are the material of choice for supercapacitors with the EDL storage mechanism. However, as discussed in section 2.1.4 other forms of capacitance exists and for pseudocapacitor electrodes, conductive polymers and metal oxides are the materials of choice. Conductive polymers obtain their conductivity due to a conjugated bond along the backbone of the polymer chain. They can be used as a supercapacitor electrode due to the doping of the polymers, either oxidation or reduction. With good intrinsic conductivity (much better than many metal oxides), comparatively cheap costs and capacitance values in excess of carbon materials [90], conductive polymers are a promising electrode material. The three main polymers used in supercapacitor applications are PPy, Polyaniline (PANI) and Polyiophene (PT). The advantages and disadvantages of these three are nicely summarised by Meng, *et al.* [91]. Conductive polymers do however suffer from a low charge-discharge rate due to slower diffusion, which limits the power capability [92]. Additionally the cycle life of these polymers is poor due to mechanical stress during each cycle [93]. With the addition of carbon, the cycle lives of these devices are greatly increased, as well as overall electrochemical performance. Capacitance values of these 'binary systems' can be double that of the pure polymer equivalent [94]. Various metal oxides have been researched for their use in pseudocapacitors however, MnO_2 is by far the most prevalent in the literature. This is likely due to exceptional capacitance

values while also being relatively inexpensive and environmentally safe [95]. With a theoretical capacitance limit of 1370 $F.g^{-1}$ [96] the performance of MnO_2 is exceedingly promising but is let down by poor conductivity. Ruthenium oxide does not suffer from the same conductivity issues but its cost is prohibitively expensive. Carbon can be used to mitigate the problems of conductivity by acting as the conductive path, while the MnO_2 acts as the active material. The MnO_2 can be deposited onto CNT arrays [97] or porous carbon [98], creating a thin film on or around the carbon (unlike conductive polymers where the carbon is a filler and not a structural base). This thin coating is preferential as the redox reactions only occur in the first few nanometers of the material [99].

2.3.2 Electrolytes

The electrolyte is a fundamental component of the TSC and is the source of ions that form the EDL. Electrolytes are typically produced from a solvent and a salt, with the choice of solvent defining the family and the voltage window in which the device can operate within. It is important that the electrolyte can adequately wet the electrode material, to enable the full use of the high surface area of many of the electrode materials. It is also paramount that the electrolyte has a high ionic conductivity, does not degrade the textile substrate and is safe for the end user. The three families of electrolyte are:

- Aqueous
- Organic
- Ionic

Aqueous electrolytes are formed from a salt dissolved in water. These electrolytes can be characterised by good ionic conductivity (based upon the molar concentration, temperature and pressure of the electrolyte) but a low working potential window. The decomposition voltage of water is 1.23 V [100] limiting the safe to a $\sim$1 V. As the energy stored in the capacitor is related to V^2 (equation 2.2) this is a limiting feature

for improving the energy density of the TSC. Common examples of aqueous electrolytes are Sulphuric Acid (H_2SO_4) [101], Phosphoric Acid (H_3PO_4) [102] or KOH [103]. Fluidic aqueous electrolytes suffer in textile supercapacitors due to the need to encapsulate the whole device to prevent wicking and electrolyte evaporation.

Organic electrolytes increase the potential window beyond that of aqueous electrolytes (up to 3.5 V [104]) but suffer from significantly greater ionic resistance and higher viscosity. More costly production requirements to reduce the water content to $<$5 ppm further complicates the decision over electrolyte. Typical organic electrolytes would be tetrafluoroborate salt dissolved in Acetonitrile (ACN) or Propylene Carbonate (PC), though it must be remarked that ACN is toxic and not suitable for e-textiles. Examples of organic electrolytes for TSC applications include: Poly(vinylidenefluoride-hexfluoropropylene) (PVDF-HFP)-Tetraethylammonium Tetrafluoroborate ($TEABF_4$) with PC as the solvent [105],Lithium Perchlorate ($LiClO_4$)-Poly(Methyl Methacrylate) (PMMA) with a PC and ACN blended solvent [106, 107] and Lithium Bis(trifluoromethanesulphonyl)imide (LiTFSI)-PMMA with a duel solvent of Adiponitrile (ADN) and Succinonitrile (SN) [108]. It is interesting to note that both Keum *et al.* [106] and Park *et al.* [107] both used ACN, regardless of the toxicity. The duel solvent approach both papers took was to tailor the viscosity of the electrolyte with a 2:1 (PC:ACN) ratio having the lowest viscosity. Though this increased the wettability of the electrode (and had the highest electrochemical performance) it also prevented the formation of a solid-state electrolyte and was not taken forward for the real-world device.

Ionic electrolytes are pure salts that contain no solvent. For supercapacitor applications, room temperature ionic liquids are of particular interest with the largest potential window of the three electrolytes (up to 4.5 V [109]) and good stability. A further benefit of these fluids is the lack of solvent, making them more appealing from an environmental standpoint. Again, however, cost and the maturity of the technology in this application hold it back from the commercial scale but designer ionic electrolytes could prove highly successful for future high-energy supercapacitors.

Testing of textile electrodes is generally performed in the presence of a fluidic electrolyte in a three-electrode system. However, for real world devices it is accepted that a higher viscosity is required, and this is achieved through the introduction of a polymer. Within the literature these electrolytes are called solid-state, quasi solid state, gel electrolyte, hdyrogel or polymer electrolyte almost interchangeably. However, there is a difference between them. Solid-state polymer electrolytes are a polymer-salt complex and the ionic conductivity is from the migration of the cations and anions along the backbone of the polymer upon the application of an electric field. Gel polymer electrolytes on the other hand make use of the polymer matrix as a host for the liquid, trapping it in place [110]. Typically, the latter of the two kinds is seen in the literature, with a polymer added during the electrolyte preparation step. Though convenient from a practical perspective (electrolyte evaporation reduction, safety for the end user and use as an intrinsic separator), the addition of a polymer reduces the electrochemical performance of the devices by increasing the ionic resistance, reducing the mobility of the ions. As such, a careful balance must be struck in the preparation of electrolytes for TSC applications.

In a review of the current literature, 777 papers between 2017-2021 from the search 'Textile Supercapacitor' were reviewed (as seen in Figure 2.5). Of these 777 papers, 446 were down selected for critical review. The exclusion criteria for the down selection included:

- Review paper
- Only characterised in a three-electrode system
- Relevance to an adjacent field of research (eg: focusing on the conductive functionalisation of the textile)
- Paywalls or unreachable papers
- Where multiple electrolytes were presented only the best one was considered

It was found that 307 (69%) of the papers focused on just three electrolytes (H_2SO_4, H_3PO_4 and KOH). 317 papers were found to use an electrolyte with a polymer

additive and of these, PVA was the polymer of choice in 292 of the papers (92%). A full year-by-year breakdown can be seen in Table 2.2. Other popularly researched electrolytes were, Lithium Chloride (LiCl) (40) and Na_2SO_4 (33). Their popularity is due to the electrolytes being a neutral which is important in pseudocapacitive devices with MnO_2, as it reacts with acids [111]. Though this quantitative exercise was not an exhaustive meta analysis, it does demonstrate the monopoly a few electrolyte formulation have within the community and the lack of diversity in the research. This gives great scope to performance improvements for classical electrode structures, especially those that do not require a specific electrolyte type. In particular, the development of an electrolyte with a wider potential window would greatly improve the energy density of the TSCs.

TABLE 2.2: Quantitative review of the electrolytes seen within the literature from a 'Textile Supercapacitor' key word search in Web of Science [55] between 2017 - 2021.

Year	Papers	Relevant Papers	'Typical' Electrolyte	Polymer	PVA
2017	127	57	41	44	41
2018	154	92	62	62	55
2019	160	94	69	62	59
2020	159	103	75	80	77
2021	177	100	60	69	60

2.4 State of the Art

As can be seen by the increase in publication number the field of TSCs is certainly growing. With the different electrode materials, electrolytes and manufacturing methods there is a large variation in performance and intended end use. This section reviews the state of the art over the previous five years. Where possible, the key performance indicators are given in terms of cm^{-2}, determined via GCD characterisation and only two electrode systems have been considered. Both EDL and pseudocapacitors have been considered to better understand the full community and

not limit the search to only carbon-based devices. In the following tables (Table 2.3, 2.4, 2.5, 2.6 and 2.7) the electrode material, electrolyte, production methodology, substrate and electrochemical performance are all noted.

TABLE 2.3: State of the art review of e-textile supercapacitors in 2017

Reference	Substrate	Active Material	Electrolyte	Fabrication	$C_{Specific}$ ($F.g^{-1}$)	C_{Areal} ($mF.cm^{-2}$)	Power Density	Energy Density
[103]	Carbon fiber	MnO_2; Molybdenum Trioxide (MoO_3)*	KOH/PVA	Electrodeposition	-	4.86	0.53 $mW.cm^{-2}$	2.7 $\mu Wh.cm^{-2}$
[112]	Cotton	Reduced Graphene Oxide (rGO)	H_2SO_4/PVA	Screen printing	257	2.5	-	-
[113]	Ni coated Cotton	Multi-walled Carbon Nanotube (MWCNT) and rGO	LiCl/PVA	Filtration	-	2675	-	0.2 $mWh.cm^{-2}$ $^{\alpha}$
[114]	Nondescript fabric	PPy nanowires	H_2SO_4/PVA	Templating and transfer	-	7.2	-	0.3 $\mu Wh.cm^{-2}$ $^{\alpha}$
[115]	CNT film	MnO_2; PPy*	KOH/PVA	Electrochemical Deposition	7.72	60.43	-	18.8 $\mu Wh.cm^{-2}$
[116]	Carbon Cloth	Activated Carbon fibers	LiCl/PVA	Electrochemical Oxidation	-	18.5 $^{\alpha}$	14 $\mu W.cm^{-2}$ $^{\alpha}$	10 $\mu Wh.cm^{-2}$ $^{\alpha}$
[78]	Flax fabric	Porous carbon	H_2SO_4	Carbonisation	-	97	-	8.6 $\mu Wh.cm^{-2}$ $^{\alpha}$
[78]	Flax fabric	Nitrogen doped porous carbon	H_2SO_4	Carbonisation	-	860	-	76 $\mu Wh.cm^{-2}$ $^{\alpha}$

* Asymmetric device, $^{\alpha}$ Calculated

TABLE 2.4: State of the art review of e-textile supercapacitors in 2018

Reference	Substrate	Active Material	Electrolyte	Fabrication	$C_{Specific}$ ($F.g^{-1}$)	C_{Areal} ($mF.cm^{-2}$)	Power Density	Energy Density
[117]	Carbon fiber	Metal organic framework, PPy	LiCl/PVA	Electrodeposition	-	206	2.1 $mW.cm^{-2}$	12.8 $\mu Wh.cm^{-2}$
[101]	Polyester	Tungsten Trioxide (WO_3) and Graphene; Graphene*	H_2SO_4/PVA	Dip-drying, electrodeposition	-	167.6 $mF.cm^{-3\beta}$	60 $\mu Wh.cm^{-3}$	2.3 $mW.cm^{-3}$
[118]	Nickel Fiber	Copper foam,Graphene sheets and Layered double hydroxiees; Activated carbon*	KOH/PVA	Dip-drying, electrodeposition	-	351	750 $\mu W.cm^{-2}$	110 $\mu Wh.cm^{-2}$
[119]	Electrospun Carbon Nanofiber	Ni-Mn-O Nanosheets	KOH/PVA	Electrospinning, Hydrothermal Reaction	75.1	-	700 $W.kg^{-1}$	20 $Wh.kg^{-1}$
[120]	CNT Fiber	Mxene	LiCl/PVA	Chemical Vapour Deposition (CVD), drop-casting	-	22.7 $F.cm^{-3\beta}$	46 $mW.cm^{-3}$	2.55 $mWh.cm^{-3}$
[121]	Activated Carbon Cloth	rGO;MnO_2*	Na_2SO_4/PVA	Microwave Irridation, Dip-coated	-	115^{α}	1 $mW.cm^{-2}$	64 $\mu Wh.cm^{-2}$
[122]	Carbon Nanofiber coated Cotton	Activated Carbon; MnO_2*	Na_2SO_4	Dip-drying	134	-	-	12 $Wh.kg^{-1}$
[123]	Cotton	Nitrogen-doped Porous CNT	H_2SO_4/PVA	Templating, Calcination	263	-	91.4 $W.kg^{-1}$	23.4@$Wh.kg^{-1}$

* Asymmertic device, $^{\alpha}$ Calculated, $^{\beta}$ No dimensions given to calculate.

TABLE 2.5: State of the art review of e-textile supercapacitors in 2019

Reference	Substrate	Active Material	Electrolyte	Fabrication	$C_{Specific}$ ($F.g^{-1}$)	C_{Areal} ($mF.cm^{-2}$)	Power Density	Energy Density
[124]	Copper and Nickel coated Polyester Yarn	rGO/CNT;Nickel Cobalt-Bimetallic Oxyhydroxide (NiCo-BOH)*	KOH/PVA	Hydrothermal co-self-assembly, Electrodeposition	-	80	14 $mW.cm^{-2}$	78 $\mu Wh.cm^{-2}$
[79]	Cotton	Activated Carbon	KOH/PVA	Carbonisation, Chemical Activation	-	153	543 $\mu W.cm^{-2}$	21.2 $\mu Wh.cm^{-2}$
[125]	Nondecript Fabric	Silk Fibron Sheathed CNT	H_3PO_4/PVA	3D Printing	-	26	32 $\mu W.cm^{-2}$	0.33 $\mu Wh.cm^{-2}$
[126]	Carbon Cloth	Co-Ni Layered Double Hydroxide, rGO	KOH/PVA	Hydrothermal Synthesis	151	-	1500 $W.kg^{-1}$	30 $\mu Wh.kg^{-1}$
[127]	Gold coated Cotton Yarn	$NiCo_2S_4$	KOH/PVA	Hydrothermal, Electrodeposition	-	37	163 $\mu W.cm^{-2}$	3.6 $\mu Wh.cm^{-2}$
[128]	Cotton Yarn	Mxene	H_2SO_4/PVA	Dip-coating	-	1865	-	93 $\mu Wh.cm^{-2}$ $^{\alpha}$
[129]	Carbon Cloth	Graphene-Lignosulfonate-PANI hyrdogel	H_2SO_4/PVA	Hydrothermal, Polymerisation	-	1223	1$mW.cm^{-2}$	161 $\mu Wh.cm^{-2}$
[130]	Carbon Cloth	Nickel Cobalt Oxide ($NiCo_2O_4$) nanowires and Ni-Metal organic framework; Activated carbon*	KOH/PVA	Hydrothermal, Solvothermal	-	-	250 $W.kg^{-1}$ $^{\rho}$	20 $Wh.kg^{-1}$ $^{\rho}$

* Asymmetric device, $^{\alpha}$ Calculated, $^{\rho}$ Estimated

TABLE 2.6: State of the art review of e-textile supercapacitors in 2020

Reference	Substrate	Active Material	Electrolyte	Fabrication	$C_{Specific}$ ($F.g^{-1}$)	C_{Areal} ($mF.cm^{-2}$)	Power Density	Energy Density
[131]	-	Activated Carbon	LiTFSI/ PVDF	Fiber Drawing	-	240	3.6 $mW.cm^{-2}$	43 $\mu Wh.cm^{-2}$
[132]	Polyacrylonitrile (PAN) Fiber Cloth	O, N functionalised Carbon Fiber; Mxene*	H_2SO_4/PVA	Oxidation, Dip-coating	46	780	0.6 $mW.cm^{-2}$	0.3 $mWh.cm^{-2}$
[133]	Polyester Cloth	PEDOT:PSS	Artificial Sweat	Drop-casting	7.64	8.45	0.4 $mW.cm^{-2}$	1.6 $\mu Wh.cm^{-2}$
[134]	Polyester-Cotton Fabric	Graphene	H_2SO_4/PVA	Pad-Dry-Cure	-	2.7	-	0.1 $\mu Wh.cm^{-2\alpha}$
[80]	Carbon Fiber Cloth	Asphalt, Activated Carbon	H_2SO_4/PVA	Dip-drying, Carbonisation	-	85	0.1 $mW.cm^{-2}$	7.6 $\mu Wh.cm^{-2}$
[135]	Zeolitic Imidazole Framework coated Carbon Cloth	Nickel Cobalt Sulfide ($NiCo_2S_4$); N-doped Carbon Nanorods*	KOH/PVA	Sulfide Conversion, Carbonisation	120	-	2.23 $kW.kg^{-1}$	37.5 $Wh.kg^{-1}$
[136]	Graphene Oxide (GO) Fibers	PANI	H_3PO_4/PVA	Polymerisation	-	56	-	8 $\mu Wh.cm^{-2\alpha}$
[136]	GO Fibers	PANI	1-ethyl-3-methylimidazolium Bis(trifluoromethyl-1-sulfonyl)imide (EMITFSI)/PVDF-HFP	Polymerisation	-	88	0.2 $mW.cm^{-2}$	12 $\mu Wh.cm^{-2}$

* Asymmetric device, $^{\alpha}$ Calculated

TABLE 2.7: State of the art review of e-textile supercapacitors in 2021

Reference	Substrate	Active Material	Electrolyte	Fabrication	$C_{Specific}$ ($F.g^{-1}$)	C_{Areal} ($mF.cm^{-2}$)	Power Density	Energy Density
[137]	Carbon Cloth Yarns	MnO_2; Activated Carbon*	Na_2SO_4/PVA	Dip-drying	-	11.7 $F.cm^{-3}$	-	6.5 $mWh.cm^{-3}$
[138]	Polypropylene Fabric	PPy	H_2SO_4/PVA	Inkjet Printing	72.3	30.5	-	2.7 $\mu Wh.cm^{-2\alpha}$
[139]	Cotton Fabric	Au coated rGO	H_2SO_4/PVA	Dip-drying	295	-	125 $W.kg^{-1}$	34.6 $Wh.kg^{-1}$
[140]	Carbon Fibers	Surface Engineered Carbon	H_3PO_4/PVA	Chemical Activation	-	25	4 $\mu W.cm^{-2}$	3.5 $\mu Wh.cm^{-2}$
[141]	Hierarchical Fabric	Graphene, PANI	H_2SO_4/PVA: Polyacrylamide (PAM)	Spray-coating, Polymerisation	-	708	0.39 $mW.cm^{-2}$	63 $\mu Wh.cm^{-2}$
[142]	Ni coated Polyester Yarn	Iron Oxide (Fe_2O_3)	KOH/PVA	Hydrothermal	7	-	-	0.6@$mWh.g^{-1\alpha}$
[143]	Cotton/Spandex Fabric	PPy	LiCl/PVA	Polymerisation	-	979	0.38 $mW.cm^{-2}$	80.3 $\mu Wh.cm^{-2}$
[144]	Carbon Fibers	N-doped rGO	H_2SO_4/PVA	Pyrolysis	-	22.4@ $mF.cm^{-3}$	10 $mW.cm^{-3\rho}$	2 $mWh.cm^{-3\rho}$

* Asymmetric device, $^{\alpha}$ Calculated, $^{\rho}$ Estimated

Tables 2.3, 2.4, 2.5, 2.6 and 2.7 again show the diversity in approach to developing TSCs. A number of fabrication processes and active materials have been demonstrated but, as discussed in section 2.3.2, very little diversity in electrolyte selection. The orders of magnitude differences in the electrochemical performances show varying rationales within the community, with some wanting to achieve the highest performance performance and others considering particular applications. What is interesting to note is the number of times values had to be estimated or back calculated and shows that there is no clear standard for presenting ones results. This is typified in the works of Yu *et al.* [120] and Qin *et al.* [116]. Yu *et al.* presented their results normalised to volume but gave no obvious indication as to how to get to cm^{-2} normalised. This would not have been a problem in common textile systems but as this was a yarn style device it made calculation challenging as it was not clear whether the area was the area of the yarn or the total area of the device, including the separation. Qin *et al.* presented an 'ultrahigh energy density' but when the values were calculated to be area normalised the results were found to be comparable to other works of the time.

The work of Yang *et al.* [113] stands out in terms of electrochemical performance, especially considering this is a much earlier work than others. The filtration methodology also offers an interesting production methodology that is likely to be scalable. However, this method will only be possible for textile electrodes, and a multi-layered device would always have to be produced, limiting the application. The waterproof-packaged final device was large, limiting the final integration, and wearability would be a concern for this style device.

The fabrication of directly activated textile [78,79] offers an interesting binderless electrode structure. The removal of the need for a polymer binder has distinct advantages, especially the proportion of active material and an inherent conductivity functionalisation. However, much like the work of Yang *et al.* [113], these devices are limited to multi layer designs and it is not clear how this methodology could be applied to a single-layer device.

Khudiyev *et al.* [131] successfully produced long-length yarn TSCs. The 100 m draw

and exceptional electrochemical performance is attributed to the novel thermal drawing process of the electrode and electrolyte gels. This led to high ionic conductivity across the interface boundary. When combined with the porous conductive polymer-metal nanowire current collect this meant that great lengths could be drawn without a loss in performance. This solution poses a legitimate step change in performance for yarn style TSCs, however, future work is needed to see whether they have appropriate weavability via typical textile processes for large scale real-world devices.

Though the electrochemical performance was relatively low, Afroj *et al.* [134] presented a pad-dry-cure process and scalable microfluidisation exfoliated graphene production method that poses a very scalable solution (up to $\sim$150 m.min^{-1}) for future TSCs. devices up to 20 cm^{-2} were produced, while maintaining the areal capacitance value. The selection of 0.6 V as the cut off voltage is unclear whether it was to protect the electrolyte or whether there is an intrinsic charging issue for the device. However, the development of a different electrolyte should greatly increase the energy density and offer a real-world, scalable solution.

2.5 Application Defined Design

The development of TSCs for e-textile applications does not occur in isolation. The role of a supercapcitor within an e-textile is temporary energy storage and power management, acting as a energy accumulator and supply and demand de-coupler. Other technologies must be developed, and operate seamlessly with, the TSCs to achieve a wireless and self-charging e-textile. In particular these technologies include energy harvesters, sensors, actuators and information transfer.

Energy harvesting is action of taking wasted, or indirect, energy sources and converting them into a useful form of energy/power, often in the form of electricity. Examples of energy harvesters developed for e-textile applications include:

- Piezoelectric

- Ferroelectric
- Triboelectric
- Thermoelectric
- Photovoltaic
- Radio Frequency

This section will review the state of the art in e-textile energy harvesting, with a typical performance review found in Table 2.8.

Material that exhibit piezoelectric effects can convert mechanical energy into electrical, with the effect also working in reverse. The phenomena occurs due to the coupling between the stress state of the crystal structure and the electrical polarisation of the material [145]. Traditionally, ceramics such as Lead Zirconate Titanate (PZT) have been the piezoelectric material of choice, due to a large piezoelectric response and good temperature stability [146]. However, for e-textile applications, lead is a restricted material. Lead-free ceramics can be substituted, such as Barium Titanate ($BaTiO_3$) or Potassium Sodium Niobate ($KNaNbO_3$), however, these still suffer from brittleness [147] making large scale production challenging and concerns over their lifetime within a textile limit their widespread adoption.Piezo-polymers offer a flexible, cheaper and process-friendly alternative to the ceramics. Poly(vinylidenefluoride) (PVDF) has good stability and high piezoelectric properties when in the β crystalline phase [148]. In this phase, the polymer is in a planar all-tans conformation [149] (a zig-zag pattern) which means all of the dipoles are in one direction, hence the large spontaneous polarisation. Other polymers include PVDF co-polymers [150] and Nylon 11 [151]. Despite a considerable amount of research, the wide spread adoption has not been seen, with expensive manufacturing and low production capacities. Low power output efficiencies further hinder the technology.

Ferroelectric materials also exhibit piezoelectric effects however for e-textile applications this is often in the form of a ferroelectret material. In these materials a porous polymer is subjected to a corona polarisation, which breaks down the air

trapped in the voids and induces a permanent internal dipole moment [152]. The combination of the permanent dipole moment and the porous structure lead to a large piezoelectric effect. Typical ferroelectret materials for e-textiles are porous PPs [153], in particular Fluorinated Ethylene Propylene (FEP) [154]. Degradation of the material over time in e-textile applications [154] and concerns over a mismatch of optimal frequency and the frequency of human movement (5 - 30 Hz compared to 3-17 Hz) has impaired wide spread adoption of the technology.

Triboelectric energy harvesters have seen the most significant research interest, with Triboelectric Nanogeneratorss (TENGs) being seen as a key harvesting technology due to its compatibility with every day life (moving, running, walking etc.).
Triboelectricity is the phenomena of electron movement from an electron losing material to an electron gaining material during contact. The mechanical energy of the contact and the different operating modes (sliding, single-electrode, free standing and contact separation) all effect the output of the TENG [155]. TENGs can come in a number of formats, including: skin-like [156–158], fiber [159–161], yarn [162, 163] and textile [164, 165] (see Figure 2.8).

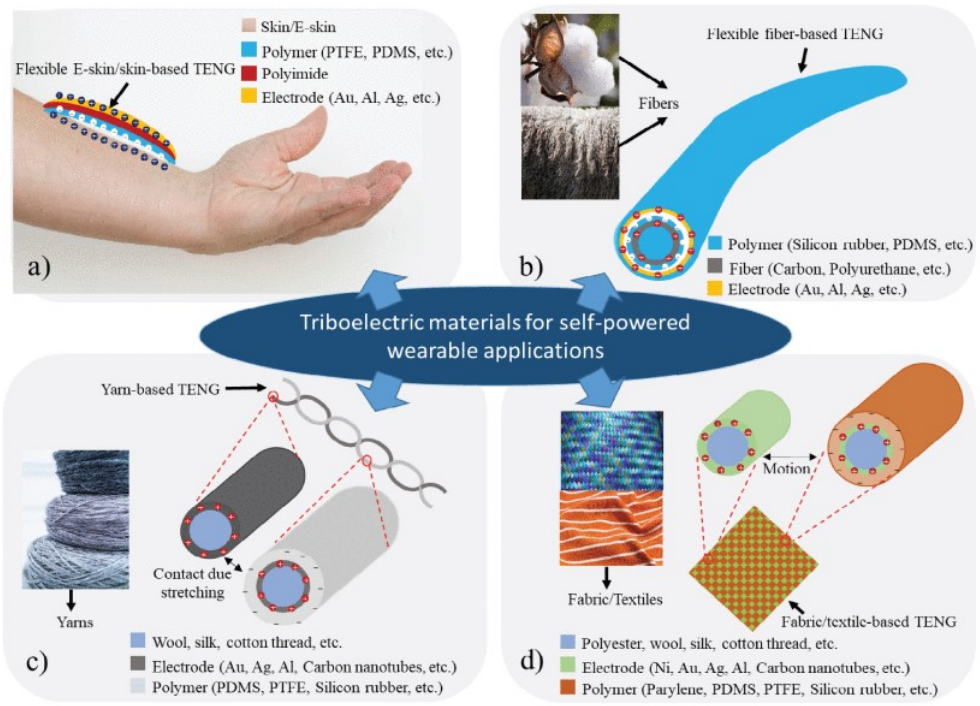

FIGURE 2.8: Typical TENG configurations and materials for the different applications. a) Skin and polymer TENG, b) A fiber based TENG with contact between the fiber and the conductor, c) Yarn-based TENG with yarn-to-yarn contact and d) Tetxile-based TENG with contact between the textiles. Image taken from [147].

TENG devices are typified by high voltages and low current output, with the voltage across the reviewed papers being $\sim$ mV to 1000's V, currents $\sim$ nA to μA and power densities of $\sim$ nW.cm^{-2} to $\sim$ mW.cm^{-2}. The highly transient nature of the output further complicates the capture of the harvested energy.

Thermoelectric energy harvesters convert heat flow to electrical current, through the Seebeck effect. In this effect two dissimilar conductors, or semiconductors, are brought together in a junction and heat applied to one one of the them. This induces the valence electrons to travel to the 'cold' side, generating the electrical current. Typical materials for thermoelectric generators are Lead Telluride (PbTe) or Bismuth Telluride (Bi_2Te_3), however, like the piezoelectric ceramics these materials suffer from toxicity. Though organic conjugated polymers have been shown to work and offer a low cost, safe and highly processable opportunity [166], thermoelectric generators suffer from an intrinsic weakness; the temperature gradient generated between the human body and the ambient conditions is just too low, limiting the power generation to $\sim$nW for non-toxic materials [167].

One could make the argument that photovoltaics are not energy harvesters, having been used as large scale energy generators for decades. However, for e-textile applications, the implementation of photovoltaic harvests solar energy that would otherwise be inaccessible to typical applications. Early examples of textile photovoltaics attached flexible solar panels onto outer wear in patches [168]. However, to fully integrate the photovoltaics into the e-textile significant scientific development was required to achieve the appropriate flexibility and wearability. Dye-sensitised Solar Cells (DSSCs) and Organic Solar Cells (OSCs) are a new generation of photovoltaics and offers a low weight solution, that does not impair the wearability of the garment for the end user. Liu *et al.* [169] demonstrated a DSSC fabricated on woven polyester-cotton and high temperature glass fiber. First, an interface layer was screen printed onto the polyester-cotton before curing under UV. Following this, the active films (silver, Titanium Dioxide (TiO_2) and dye) were built up, before sandwiching with a Indium Tin oxide coated Polyethylene Terephthalate (ITO-PET) electrode. The curing temperature for the polyester-cotton was limited to 150°C whereas the glass fiber could be cured at 2000°C. With this high-temperature processing the roughness of the layers could be reduced and this improved projection increased the efficiency from 1.03% to 4.04%. Arumugam *et al.* produced an integrated OSC in polyester-cotton via solution based processes (spray coating and doctro blading). Initially an interface layer was deposited before the silver nanowires were spray coated through a mask to created the electrodes. A Zinc Oxide (ZnO) nanoparticle layer was then doctor bladed before a layer of Poly(3-hexylthiophene):Indene-C_{60} Bisadduct (P3HT:ICBA) and a layer of Poly(3,4-ethylenedioxythiophene) Polystyrene Sulfante (PEDOT:PSS) were spray deposited.The use of spray coating was found to produce highly reliable and repeatable devices and achieved an efficiency of 1.23%. The use of solution based processes was also important as other methodologies seen in the literature are incompatible with traditional textile processes.

Radio frequency energy harvesting looks to scavenge stray RF radiation from the environment through the use of rectennas (antennas with a rectifier). E-textile rectennas have the same design metrics as traditional antennas but must also contend

with the mounting of lumped components, lossy dielectric properties of textile and the reliability of being on a flexible substrate. The primary limiting factor for these rectennas is the efficiency of the rectifier. However, Wagih *et al.* [170] has recently demonstrated a textile rectenna with over 50% efficiency. This was achieved through photolithography with features down to 150 μm achievable on thin polyimide sheets. Typically, the rectennas are themselves produced on flexible filaments and inserted into a disguised fabric pouch [171, 172]. All-textile examples have been seen in the literature [173] but these tend to suffer with poor flexible and rigid parts of the system (eg: connectors).

TABLE 2.8: Typical power output for e-textile energy harvesters.

Energy Harvester	Power Output
Piezoelectric	5.1 μW.cm^{-2} [174]
Ferroelectret	5.6 μW.cm^{-2} [175]
Triboelectric	0.2 mW.cm^{-2} [165]
Thermoelectric	44.4 μW.cm^{-2} [176]
Photovoltaic	10 μW.cm^{-2}, PCE$^{\alpha}$ = 10% [177]
Radio Frequency	0.25 μW.cm^{-2} @ 820 MHz, PCE = 50.5% [170]

$^{\alpha}$ PCE is the power conversion efficiency.

Often within the literature the TSC or e-textile energy harvester are characterised in isolation and the results are presented as future options for e-textile applications. However, a number of e-textile power modules, with both a harvester and energy storage, have been presented in literature. Yong *et al.* [154] combined a ferroelectret (FEP) with an carbon TSC. The ferroelectret achieved a voltage of 10 V, with an instantaneous power of 0.86 μW.cm^{-2} across a 70 MΩ load. This could charge the 5.55 mF.cm^{-2} TSC to 0.45 V in 3600 s while the ferrolectret was exposed to a 350 N, 1 Hz cyclic load. In the work of Pu *et al.* [102] the authors used a woven TENG made from nickel-polyester and parylene-nickel-polyester to charge yarn-style TSCs. The reduced graphene oxide-nickel supercapacitor yarns had a capacitance of 49.4 mF.cm^{-2} determined via GCD testing at a 1 mA.cm^{-2} discharge current. The TENG textile

delivered 40 V and 2 μW.cm^{-2} of power at a testing frequency of 5 Hz. Once connected, the TENG-TSC power module made of 3 TSCs connected in series could be charged to 2.1 V in 2009 s at 5 Hz. Arguably the most interesting e-textile power module recently was developed by Yin *et al.* in 2021 [178]. In this work the authors looked to combine a TENG with Microbial Biofuel Cells (BFCs) for the synergistic harvesting of power from movement and sweat. The TENG delivered 160 V at a power of 0.02 W (no area given for normalisation). Each BFC module could deliver 21.5 μW at a discharge voltage of 0.5 V. The micro-grid was tested using a 75 μF planar TSC during a period of 10 minutes of running. The TENG on its own took approximately 9 minutes to charge the TSC to 5.1 V, the BFC on its own took approximately 7 minutes and together took approximately 5 minutes. Once the activity stopped, the voltage over the TSC dropped for the TENG only test but maintained for the other two trials as long as sweat was present. This sensible and considered design for the end system greatly improved the performance of each component and acts as a sign to the community that the combination of e-textile energy harvester and energy storage should be chosen with an application in mind.

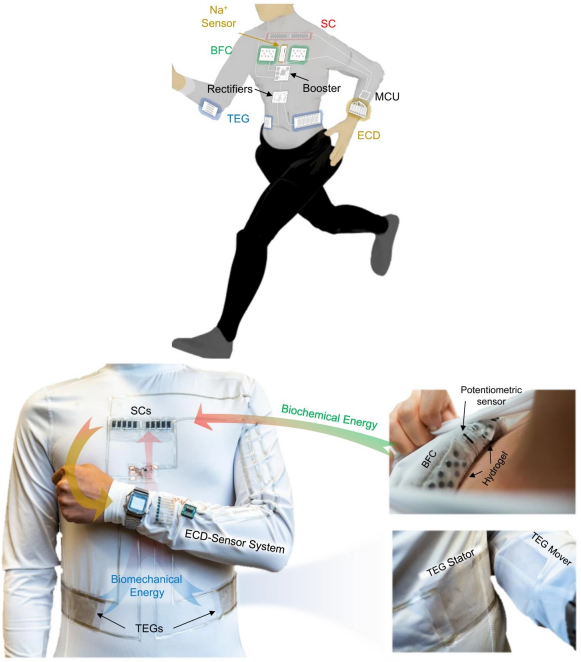

FIGURE 2.9: Schematic and images of the TENG and BFC microgrid. The full system includes energy harvesters/generators, storage and end use applications.The synergistic consideration of the movement and sweat produced via running makes this arguably the most advanced e-textile power module seen in the literature. Image modified from [178]

2.6 Discussion

This chapter has reviewed the literature within the field of TSCs, from fundamental principles and material selection to electrolyte selection and real-world system integration. It is clear from the literature that electrochemical performance, primarily of the electrode materials, is the focus of the research effort. However, what these electrochemical performance metrics should be and how best they should be characterised remains an open question within the community. This makes direct comparison of research unnecessarily challenging.

TSCs have seen a significant amount of research over the previous decade, demonstrating their significance to the e-textile community as a power management component for future applications. Underpinned by the decades of research into traditional energy storage devices, the unique challenges of wearabaility, flexibility and production methods have all been addressed to some extent, though clear challenges still remain.

With the focus on improving the electrochemical performance, advanced electrode materials and structures have been developed, with remarkable performance. Binary and ternary electrodes and advanced functionalisation have all been developed but the production methodologies limit the devices to laboratory scale demonstrators at best. Very few groups use processes familiar to the textile industry, and those that do broadly rely on dip-drying which limits the final device architecture. More work is required to develop sensible production methodologies that can be scaled, with electrode materials that have a clear supply chain and are sustainable.

The choice of electrolyte for TSCs seems to have been driven by historical research and consensus with a dominance of relatively few electrolytes and polymers. The orthodoxy surrounding the electrolyte selection requires a challenge. This is especially true when one remembers that the electrolyte, and not the electrode, is the constituent part of the TSC which defines the operating voltage of the device and has the greater influence over the energy density.

Integration of the TSC into a wider e-textile system is clearly the next significant challenge for the community. The TSC must be compatible with the energy harvester and end use application to achieve a wireless e-textile. Some groups have certainly delivered progress in this area, with end-to-end demonstrators produced from a range of system architectures. However, much of the research stops at the metrological characterisation, or at best, demonstrates the lighting of a series of LEDs. It is not clear how these devices will respond to imperfect charging or whether the testing conditions (discharge current, voltage sweep rate, etc.) are truly representative of real world conditions. Certainly, more interdisciplinary research is required in this area.

Chapter 3

Electrical Theory and Characterisation

Where the previous chapter introduced the physical mechanisms of the supercapacitor (Helmholtz layers, diffuse region, etc) this chapter will present the electrical theory of the supercapacitor. This is important to understand as it will underpin the metrological techniques used throughout the work. The scope of this thesis will limit the number of measurement techniques to GCD, CV and Electrochemical Impedance Spectroscopy (EIS) which will all be explored within this chapter. Physical characterisation (Scanning Electron Microscope (SEM), particle size analysis, Brunauer-Emmett-Teller (BET) and Barret-Joyner-Halenda (BJH) surface area analysis) were also employed as secondary analysis techniques and will be discussed at the end of this chapter.

3.1 Electrical Theory

The theory of supercapacitors presented in chapter 2 was built from a physical perspective. This was crucial to form an understanding of the fundamental nature of the devices and to assess what properties of electrode and electrolyte materials needed to be investigated to obtain the best overall performance. The electrical theory presented in this chapter will be less 'physically' real and will present a simplified

framework to best analyse the performance of the devices. The vast complexities of the system can be simplified through the use of equivalent circuit theory. In this theory, the textile supercapacitor performance/response can be characterised as a two-terminal network of simple electrical components, resistors, capacitors and inductors (to name the most common elements) [179]. Though simplified when compared to a physical model, this theoretical framework can still grow to great complexity and some debate over the required complexity exists within the community. Fletcher *et al.* [180] makes the distinction between a model for electrical engineers (that duplicates the response at a single frequency) and that of a model for electrochemists (that duplicates the response at multiple frequencies). The work of Fletcher *et al.* goes further than defining the models and actually calls out 'egregious examples' of incorrect use of the models within the literature. Fortunately, the classical models (plural as there will be a difference between AC and DC measurements) are sufficient to adequately underpin the characterisation of the symmetrical devices produced in this work.

The equivalent circuit theory under DC conditions for a supercapacitor is relatively straight forward. Within the device there will be two capacitance terms (one at each electrode-electrolyte interface), series resistance terms (made up of the resistance within the electrolyte and any resistances at the contacts) and a parallel resistance term that models any leakage [181].The series resistances can be modelled as a lumped resistance term known as the ESR and the capacitances can be combine into a single capacitance term, with the model being shown in figure 3.1a. This model can be further simplified when one takes into account that under characterisation, the timescales are short and the device is not left at open circuit, therefore we can ignore the Equivalent Parallel Resistance (EPR) as there will be negligible leakage [182] (as seen in figure 3.1b).

For an ideal capacitor, the current across it is given by:

$$I(t) = C\frac{dV}{dt} \tag{3.1}$$

where I is the current, C is the capacitance and dV/dt is the rate of change of voltage.

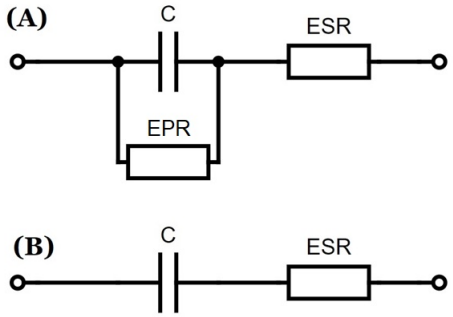

FIGURE 3.1: (A) Classical equivalent circuit model for a symmetric electrostatic supercapacitor, containing a capacitance (C), equivalent series resistance (ESR) and an equivalent parallel resistance term (EPR). (B) the simplified classical model used for characterisation where EPR has been neglected.

This equation shows that for an ideal capacitor under constant current (galvanostatic) conditions the capacitance is inversely proportional to the slope of the voltage time graph (figure 3.2). However, as we have shown in figure 3.1 the supercapacitor is not ideal and we must consider the ESR. As such if we integrate equation 3.1, (remembering that in constant current mode, I is independent of time) we reach:

$$\int_0^t Idt = C\int_0^t \frac{dV}{dt}dt \tag{3.2}$$

$$\frac{It}{C} = V(t) - V(t=0)$$

$$V(t) = \frac{It}{C} + V_0 \tag{3.3}$$

This time independent voltage (V_0) is equal to the voltage over the resistor. This changes the shape of the graph in Figure 3.2A by the introduction of an immediate drop (or rise) in voltage (as seen in Figure 3.2B). Importantly however, when one considers the two stages (charge and discharge) as two separate graphs, the line obeys the simple $y = mx + c$ relationship and the capacitance of the device can still be characterised from the reciprocal of the gradient, while the ESR can be calculated from the instantaneous voltage drop (V_0), (which is in effect the new y-intercept, c, of the discharging plot, figure 3.2B) divided by the the change in current (ΔI). In this instance, ΔI is the charging current minus the discharging current, which is simply 2I.

Though this first order approximation is appropriate for GCD and CV

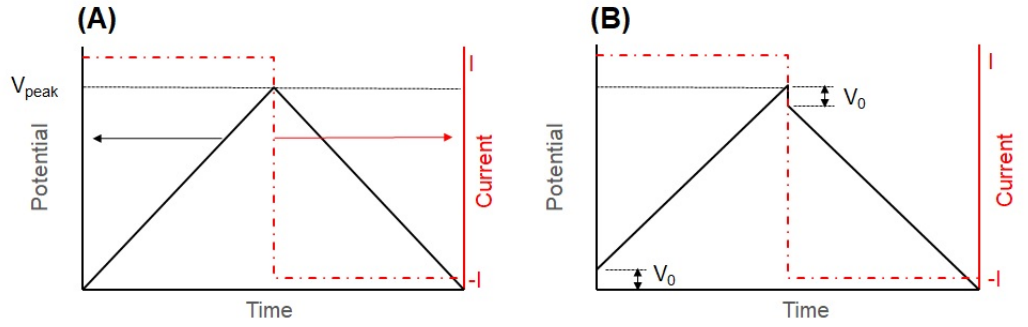

FIGURE 3.2: (A) The voltage profile for an ideal supercapacitor under a constant current charge (+I) and constant current discharge (-I). (B) the same voltage profile but taking into account the equivalent series resistance of the device.

characterisation, this simple Resistor-Capacitor (RC) model is not sufficient to explain the temporary decrease in voltage (under open circuit conditions) after charging or increase after discharge (a phenomena known as charge redistribution [183]). Nor can it explain the linear region of a Nyquist plot, where the real and imaginary impedances are plotted, see section 3.2.3.These phenomena are due to the highly porous nature of carbon electrodes used for supercapacitors. The simple RC model is representative of the surface, but does not taken into account the ions diffusing into the pores. To account for this, the complexity of the model is increased and a series of n RC are combined into a transmission line, figure 3.3. Each RC pair has a different time constant and discharges/charges at different rates. At high frequencies the transmission is approximately a single RC pair and reflects the short time the ion has to diffuse in and out of the pore. However, at lower frequencies the ions can diffuse further, effectively travelling further along the transmission line. The overall frequency response of the transmission line can be approximated by a Warburg element with a 45° phase angle.

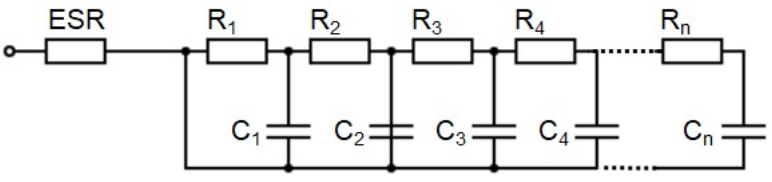

FIGURE 3.3: Transmission line of n RC components

For AC characterisation, this extends the model seen in figure 3.1 by simply added an extra term in series, figure 3.4. The effect that this has on the shape of the Nyquist plot

is discussed in detail in section 3.2.3.

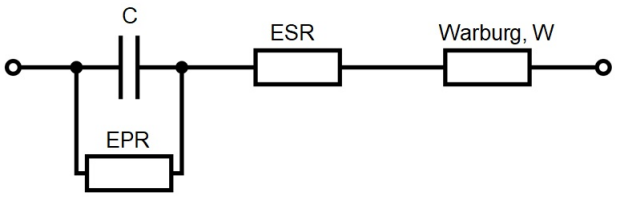

FIGURE 3.4: The AC equivalent circuit mode for a supercapcitor with highly porous electrodes. The addition of the Warburg element models the different diffusion rates into the different pores within the network. At very high frequency the ions don't have chance to diffuse and at very low frequencies (quasi-DC) these effects are not relevant, as such this is a medium to low frequency phenomena and dominates in this frequency range

For clarity, it is important to have a momentary aside regarding the RC network. The Warburg element used in this work is used to model the effect of all of the pores within the bulk of the electrode, as seen in Gourdin *et al.* [184]. However, a finite (or semi finite) RC transmission line can also be used to model the behaviours of individual pores [185], taking into account their geometry [186], size [187] and whether they are open or closed [188]. For example, in the works of Black *et al.* [186, 189] the transmission line is used to model the solution resistance in a conic pore, where the mouth of the pore charges faster than the base, resulting in different charging rates throughout the pore.

3.2 Characterisation Techniques

The characterisation of supercapacitors is fairly straightforward but the community differs in approach and care must be taken. Described below are the characterisation techniques employed throughout this work but it must be noted that all quoted values of capacitance, ESR, energy and power are obtained from GCD traces, as this technique is widely accpeted to be the most reliable [190]. CV and EIS measurements are made to gain a better understanding of the performance of the devices and to characterise parameters not obtainable from the GCD measurement, such as the ionic conductivity of electrolytes. It is also important to note that throughout this work the devices will be characterised as a two electrode system with a *Solatron 1470E* battery analyser (unless explicitly stated otherwise).

3.2.1 Galvanostatic Cycling

Galvanostatic cycling is a constant current charge-discharge measurement technique. The measurement involves charging the device to a specific voltage with a constant current before discharging the device by applying a constant negative current. An ideal voltage response for a supercapacitor undergoing GCD testing can be seen in figure 3.2, though some rounding may be seen in real devices due to the leakage current at higher voltages. From the theory section it has been shown that the capacitance of the device can be obtained from the reciprocal of the gradient of the voltage-time graph from GCD cycling. The British Standards Institution (BSI) measurement standard BS EN6291-1:2016 [191] bounds the appropriate region to take the gradient as 80% to 40% of the peak voltage, and this will be followed in this work.

The ESR of the device is obtained by dividing the instantaneous voltage drop (ΔV) by the change in current (ΔI = 2I). From equation 2.2, the energy stored within a supercapacitor (E) is equal to:

$$E = \frac{1}{2 \cdot 3600} C V_{peak}^2 \tag{3.4}$$

where C is the capacitance, characterised via the slope of the GCD trace, V_{peak} is the peak voltage (and limit of the test) and the $1/3600$ is the conversion from joules (J) to watt hours (Wh). The peak voltage is selected by the user and is related to the voltage window (sometimes called the Electrochemical Stability Window (ESW)) exhibited by the electrolyte of the device. For aqueous solutions seen in this work V_{peak} is kept to 0.8 V which is appropriately below the breakdown voltage of water (1.23 V). It is a commonly adopted voltage limit seen within the community so also allows fair comparison to works seen in literature [192]. For devices made with non-aqueous electrolytes the voltage limit is varied depending upon the particular experiment and as such are defined within the appropriate section.

The power delivered by the supercapacitor during its full discharge (sometimes called the average power) is given by:

$$P = \frac{E}{t} \tag{3.5}$$

where E is the energy of the device and t is the discharge time in hours. The peak power (impedance matched) deliverable by the device is given by:

$$P_{peak} = \frac{V_{peak}^2}{4 \cdot R_{ESR}} \tag{3.6}$$

where V_{peak} is the peak voltage and R_{ESR} is the ESR. These two definitions of power are very different and some works in the literature do not make a distinction. It is best to identify which power is being quoted, to give a more accurate reflection of the performance of the device. Within this work, power is used for any Ragone plots and for quoted values. P_{peak} is used to show the pulse power capabilities and will always be noted as P_{peak} to avoid confusion.

To be able to compare the performance of the devices created within this work and those with different designs, topologies and active materials it is required to normalise the absolute characteristics presented previously. Often this normalisation is performed in reference to dimensional characteristics (length for 1D (m), area of 2D (m^2) and volume for 3D (m^3) or the mass (kg)). For full devices as seen in this work it is the opinion of the author that normalising against mass is dangerous and should be avoided. When one is investigating the fundamental storage capacity of a material (often in a three-electrode system), the capacitance per kg is of paramount importance. However, in a full device should one normalise against the active material or the full device? This ambiguity can lead to confusion or, unfortunately, purposeful obfuscation of the true performance of the device. Given how small the mass of electrodes and electrolyte is for the single-layer TSC seen in this work the limiting factor for the end user would be the available area on the garment, and not the total mass. Considering the implications for erroneous reporting, and the end user limitations values presented in this work will be normalised against the geometric surface area of the electrodes.

3.2.2 Cyclic Voltammerty

Cyclic voltammetry is used to investigate electrochemical activity across a potential window, ΔV and device reversibility. The measurement differs from GCD measurements by controlling the voltage and measuring the output current. The voltage is increased from a starting voltage to a maximal voltage (the voltage window) at a constant sweep rate (ν= dV/dt) while recording the current response. From equation 3.1 it can be seen that for a constant sweep rate and a given capacitance, the current should also be constant. For an ideal supercapacitor this results in a box shape current response, throughout the potential window, increasing in area with increasing scan rate as shown in figure 3.5.

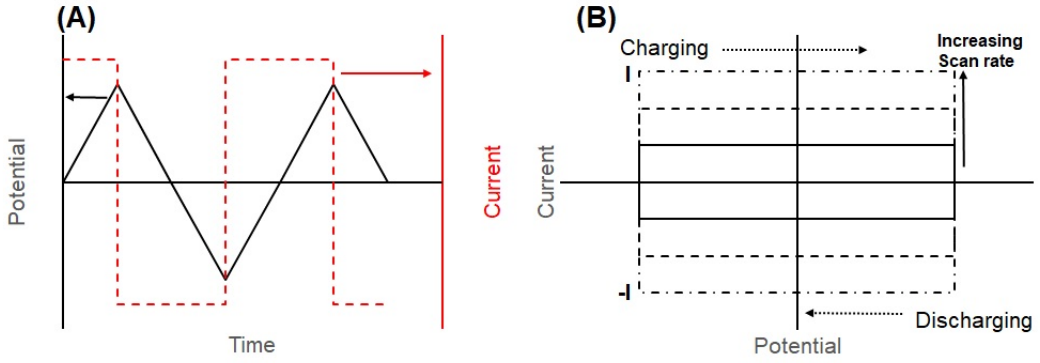

FIGURE 3.5: (A) The current and voltage response over time for a CV measurement. (B) The classical current versus voltage response seen for an ideal supercapacitor for a CV measurement.

However, supercapacitors are not ideal and the ESR will result in a time dependent result around the transient points (eg: when the voltage sweep reverses direction). This correction can be seen in equation 3.7.

$$I = \nu C(1 - e^{\frac{-t}{\tau}}) \tag{3.7}$$

where ν is the sweep rate, C is the capacitance, t is the time and τ is the product of the R_{ESR} and C, known as the time constant.

At t=0, the exponential is 1 showing that there is no current flow. At small t (compared to τ), the current is $< \nu$C but for large t the exponential tends to zero and the current tends towards the ideal case of νC. This has the effect of turning the rectangular graph

into a curved parallelogram. In cases of higher ESR the shape will form more of a pointed rugby ball shape (as seen in Chapter 4) due to the increase time constant. If the potential window exceeds that of the voltage stability of the electrolyte, peaking may also occur at the top right and bottom left of the curve as the electrolyte begins to breakdown and secondary reactions occur.

For a purely EDL supercapacitor the current response should be flat whereas for pseudocapacitors and certainly batteries, distinct peaks should be present at the voltage associated with the particular faradic reaction. Where the peaks for a battery are sharp and far apart, the peaks for a pseudocapacitor will be broader and symmetric, Figure 3.6. Additionally, the peak current of a pseducapacitor is linearly related with the voltage sweep rate whereas the peak current in a battery follows a $\nu^{0.5}$ relationship, differentiating between a surface based process and a diffusion based process. CV measurements in this work will be used as a secondary electrochemical measurement to assess the stability of the devices over the require voltage window and to investigate the impact of the ESR at differing sweep rates. It will not be used to characterise the capacitance as it has been reported that lower scan rates can overestimate the capacitance [190]. Unless stated otherwise the CV measurements used in this work are performed using a Solartron 1470E Cell test system at room temperature.

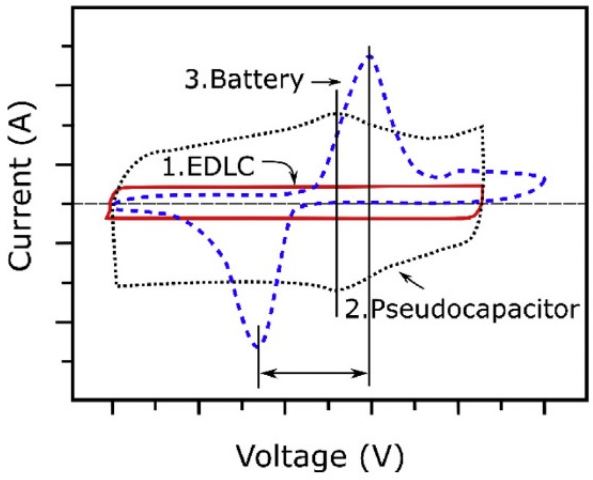

FIGURE 3.6: Cyclic voltammetry curves for an electric double layer capacitor, pseudocapacitor and battery. All three exhibit significantly different profiles making CV measurements a strong tool for understanding the nature of different energy storage devices. As can be seen from the additional lines the peaks for the battery are far apart whereas the peaks for the pseudocapacitor are symmetric. Image edited from [190].

3.2.3 Electrochemical Impedance Spectroscopy

The final electrochemical measurement technique used throughout this work is electrochemical impedance spectroscopy. This technique differs from the previously mentioned techniques as it is an AC based measurement. A small sinusoidal excitation is applied to the device and the response recorded over a range of frequencies (mHz – MHz). The impedance response is then typically presented via Nyquist plot (real impedance (Z′) against imaginary impedance (-Z″)), figure 3.7. For an EDL supercapacitor the Nyquist plot exhibits a semi-circle at higher frequencies before moving into the linear region associated with the Warburg element (transmission line) discussed in section 3.1.

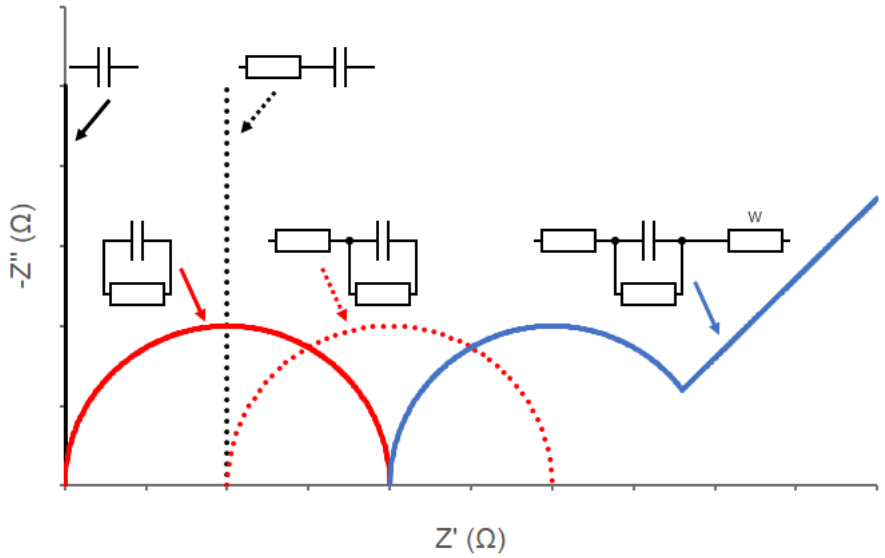

FIGURE 3.7: Representative Nyquist plots for a typical equivalent circuits. This includes a capacitor, a series resistor-capacitor, a parallel resistor-capacitor, a parallel resistor-capacitor with a series resistance and a parallel resistor-capacitor with a series resistance and a Warburg element. The frequency is going from high to low (left to right)

For real-world devices, especially those with a rough or highly porous electrode [193], the simple elements shown in figure 3.7 are not sufficient to describe a frequency dispersion in the impedance measurements. This dispersion is related to the inhomogeneity of the current across the electrodes, which then leads to variation in the solution resistivity or concentration across the interface. This tangles the bulk resistance of the electrolyte and the interfacial capacitance (or C_{dl} from equation 2.3). This manifests as having to replace the capacitor in the equivalent circuit with a Constant Phase Element (CPE). First reported by Fricke in 1932 [194], the constant phase element captures this deviation from the ideal, with the elements impedance (Z_{CPE}) being given by:

$$Z_{CPE} = \frac{1}{Q_{CPE}(i\omega)^{\alpha_{CPE}}} \tag{3.8}$$

where Q_{CPE} ($\mu F cm^{-2} s^{\alpha_{CPE}-1}$) is the CPE parameter, α_{CPE} is the CPE exponent in the range $0 \leq \alpha_{CPE} \leq 1$, where 0 is a resistor and 1 is an ideal capacitor and ω is the angular frequency.

The introduction of a new element should not be of concern as the Warburg element,

introduced in section 3.1, is a special case of the CPE with α_{CPE} being 0.5. However, care must be given to the physical representation of this CPE. Though models that make use of an CPE improve the quality of the fit, there remains ambiguity to the physical origin [195]. As such, for this work, the models fitted to EIS data making use of CPEs in chapter 5 will be used as a comparative study only.

The final use of EIS is for the characterisation of the ionic conductivity of an electrolyte. As can be seen in figure 3.7 for a series resistor-capacitor there is a non-zero crossing point with the x-axis. The position of this crossing point is associated with the series resistance. For e-textile applications this can be used to measure the ionic conductivity of electrolytes within a given fabric. If the fabric substrate is saturated in the electrolyte and placed between the two poles of a Swagelok text cell, the Nyquist plot will give the resistance of the electrolyte (as shown in the the work of Huang *et al.* [196] and He *et al.* [197]. From the resistance one can then calculate the ionic conductivity:

$$\sigma = \frac{T}{RA} \tag{3.9}$$

where σ is the ionic conductivity, T is the thickness of the textile, R is the resistance determined from the crossing point of the Nyquist trace and A is the area of the sample.

3.2.4 Physical Characterisation

The physical characterisation utilised within this thesis includes SEM, particle size distribution, BET and BJH.

SEM is a microscopy technique that makes use of a focused beam of electrons to 'look' at materials. The accelerated electrons interact with the target and give off various signals (secondary electrons, back scattered electrons, diffracted back scattered electrons) and from these signals an image can be produced. Within this work, the SEM is largely used to assess the structure of the materials and final device and as such it is the secondary electrons that are of most interest.

The particle size distribution of the activated carbons can be assessed through laser diffraction particle sizing (*Malvern Mastersizer Hydro 2000SM*). In this technique a dilute dispersion made from an appropriate solvent and the carbon is passed through a cavity, a laser is shone through the cavity and the flowing dispersion. The different sizes particles will scatter the laser differently, with the angle of scatter increasing with decreasing particle size. The different scattering angles are recorded by a detector enabling the distribution of particle size within the dispersion to be made.

The BET theory links the physical adsorption of gas at a surface to the surface area of the solid. By measuring the volume of adsorbed gas (nitrogen) at a number of partial pressures at the boiling point of the nitrogen, the surface area of the solid can be calculated, along with the pore size distribution. Like the BET characterisation, the BJH characterisation uses the experimental isotherms but instead of calculating the total surface area it calculates the pore size distribution of the material. Given the complex interaction at the boundary between the electrode surface and the electrolyte, it is imperative that both the surface area and pore size distribution are analysed.

Chapter 4

Electrode Design

Supercapacitors of any form are made up of three constituent elements, the electrode, the electrolyte and the separator. This chapter will focus on the work delivered to formulate, understand and develop the carbon based electrodes that will be utilised throughout the remainder of this thesis. Considering the ethos of sustainability, scalability and safety that underpins this thesis, only commercially available activated carbon materials have been considered. The three carbons, *Kurray YP 80-F*, *Cabot Norit GSX* and *Cabot Norit SX Ultra* were selected based upon their availability, material precursor and activation process. At least two different precursor materials were desired while the activation process was fixed to be the same (physical). The YP80F carbon has a coconut shell precursor and was activated with CO_2, while the SXU and GSX carbons had a peat precursor and underwent steam activation. Carbons prepared through chemical activation were discounted due to the large volumes of acids required, negatively impacting the long term sustainability of the product, and going against the ethos of this work. This approach sets the work apart from many contemporaries who are focused more on the material science, and the desire for increasingly energy dense electrode materials.

Within this chapter the deposition methodology is also investigated, with the results informing the experimental methodology for the later chapters. A spray distance, pressure and number of coating layers are all established and the effect on the electrode structure explored. It is found that at four layers of spray deposition, a

consistent electrode is formed, with a weave dependent thickness variation of 50 - 150 μm. Considering the multi-scale nature of the electrodes (four orders of magnitude between the textile structure and the conductive additive), the formation of the electrode was also explored. When the electrochemical results and the physical characterisation of the material are compared for the best performing devices it was found that they differ by a factor of 2, demonstrating that the electrode is behaving as a consistent 'plate' and not a complex network of connected capacitors.

Of the three commercial activated carbons tested throughout this chapter, one material in particular performed well. When formulated into a 9:1 by weight material ratio electrode ink, and deposited via the optimal spray methodology, devices produced using the *Kurray YP 80-F* activated carbon achieved an areal capacitance of 23.6 $mF.cm^{-2}$ and power and energy densities of 0.59 $mW.cm^{-2}$ and 2.1 $\mu Wh.cm^{-2}$ respectively. This demonstrated an order of magnitude improvement over the other selected carbon materials. Physical characterisation and microscopy techniques were utilised to elucidate the reason behind this stark difference in electrochemical performance.

This chapter has been presented in-part, in two published works [198] and [199]. Thanks must be given to Dr. N Zhelev for their help with the BET and BJH measurements and Aran Amin for their help with many of the SEM micrographs.

4.1 Activated Carbon Textile Supercapacitors

The selection of electrode material is driven primarily by application; in this case a smart bandage, discussed at length in chapter 6. Within section 2.1 the two families of supercapacitor were discussed, each with their own advantages and disadvantages. For this work, it was decided early in the design life cycle that a purely EDL based device would be optimal for the integration into a energy harvester driven textile power module due to the longer cycle lifetime and fast response rate. With this in mind, metal oxides, conducting polymers and exotic materials were quickly ruled out, as were any binary or tertiary electrode systems containing these materials.

Fundamentally, this left the decision of which electrode material to a decision over carbon materials. Section 2.3.1 details and reviews the different carbon materials used for electrode materials within the community from a physical and electrochemical perspective. What is not discussed however, is the scalability and economic consideration over the materials. Though graphene (and other low dimensional carbon structures) showed exceptional performance within supercapacitors, the scalability of the material production must be questioned. Though some within the community have proposed improved yield methodologies, such as Del Rio Castillo *et al.*'s wet-jet milling (mechanical exfoliation) [200] and Zhou *et al.*'s electrochemical exfoliation [201], the reality of today's market shows that activated carbon is ~ 3 orders of magnitude less expensive than graphene (£0.12 per gram compared to £600 from Sigma Aldrich [202]). Activated carbon's wide use in water purification, wastewater treatment, gas filters, green gas capture as well as other energy storage technologies [203–208] makes it a cost effective and readily available electrode material, making it an ideal candidate for this work.

With this work being device focused, an experimental investigation into the production of the activated carbon, and the impact of different source materials, is outside of the scope and as such three commercially available activated carbons have been selected: *Kurray YP-80F* (YP80F), *Cabot Norit GSX* (GSX) and *Cabot Norit SX Ultra* (SXU), with no further modification made.

4.1.1 Carbon Inks

Activated carbon is a good EDL material due to its highly porous nature. However, with this porosity comes problems, in particular the electrical conductivity of the material. As the surface area of the carbon particles goes up the quantity of carbon material within each particle logically reduces. This results in less pathways for electron mobility and an increase in the resistance. To overcome this, a conductive additive is required to boost the conductivity of the bulk electrode. For this project 40 nm carbon black from *Chevron Phillips* was chosen. However, with an increase in conductive additive the percentage mass of the active, energy storing, material goes

down. Intuitively, there must be an optimisation where one retains enough of the active material to store the electrical charge but with enough conductive additive to reduce ohmic losses within the device.

Additionally to the consideration of the ratio of active material to additive is the consideration of how will the electrode material within the ink adhere to the textile fibers. Though some electrostatic attraction will likely be present, a polymer binder is also required within the ink. It is important to keep the percentage weight of the polymer within the ink to a minimum to not impact the conductivity of the electrode or displace the activated carbon material.

The final significant consideration for the ink formulation is the device production methodology. The two scalable textile compatible printing/deposition processes are screen printing or spray deposition. Akin to the rationale to not use exotic or expensive electrode materials, laboratory scale deposition methodologies such as CVD [209], facile templating [210] or *in situ* polymerisation [211] have not been considered. Screen printing inks are thixotropic, to enable the ink to be spread evenly by the blade and the squeegee to push the ink through the mesh screen, with the printed shape retained post printing. If the ink is too fluid it will pass through the mesh and not stay within the confines of the printing area. To achieve an appropriate viscosity a polymer base is required. Typically this is then either cured at an elevated temperature to sure the binder or large amounts of polymer are used (sacrificing the by-weight percentage of the active material) to form a a polymer matrix [212]. Neither of these situations are appropriate so a spray deposition methodology has been chosen, which requires a loose ink to be produced. This is achieved via the selection of an appropriate solvent. This solvent must be able to incorporate the polymer, forming a polymer-polymer fluid, and easily aerosolised during the deposition.

With all of these considerations to parametise, the electrode ink formulation was based around a 5 ml solution with 1 g of dry materials. 0.85 g of the dry mass was the two carbons with 0.15 g being the polymer binder. The polymer selected for this work was EVA, which had shown demonstrated good adhering properties in previous work and good chemical stability. The solvent selected was 1,2,4-Trichlorobenzene (1 2 4-TCB) as

it can readily dissolve the EVA. Concerns over the solvent are mitigated by the fact that it is driven off during the manufacturing process. As long as the production is undertaken in an appropriate manner (ventilation, PPE, etc) the solvent will not affect the end use of the device. Of interest to this work, the ratio of activated carbon to carbon black along with the choice of activated carbon.

4.1.2 Device Production

Along with the two variables under investigation in the ink itself, the production methodology for the electrodes was also experimentally investigated by varying the number of spray layers (and therefore material loading). With three different ratios of carbon materials and three activated carbons and three spray layers the experimental program constituted a 3^k factorial experimental design (where k is the number of variables, in this case 3). To reduce this complexity it was decided that the experimental work would be split into two sections. The first section would investigate the different activated carbons and the number of spray layers. For the three spray layers, 2, 4 and 6 were selected. Previous work in this area [56], had demonstrated promising performance from 4 layers of deposition and formed the reference for this study. The upper bound of 6 layers was justified through initial experiments demonstrating failure due to total ink penetration. The lower bound of 2 layers was selected after trials with 1 layer showed visibly incomplete coverage of the carbon ink on the surface, which would have resulted in low electrical conductivity of the carbon current collector, biasing any electrochemical results. The best performing activated carbon and spray method were then taken and the ratio of activated carbon to carbon black varied. The ratios of activated carbon to carbon black were 80:20, 90:10 and 100:0. The ratio of 90:10 was used in the the work of Sheng *et al.* [56], which was used as the reference for this study. The 100:0 ratio was chosen as the upper bound to investigate the relevance of the conductive additive within the electrode. The ratio of 80:20 was selected as the lower bound to investigate whether an increase in electrical conductivity would balance the loss of active material. Steps of 10 in the ratios were selected due to the resolution of the scales and the practical consideration of the handling of the carbon material. Reducing the ratio step would have incurred greater

uncertainty during the production of the carbon inks. The two step experimental strategy reduces the number of experiments from 3^3 to 3^2+2, reducing the number of experiments from 27 to 11. The naming convention and parameters for the first phase of the work can be seen in table 4.1.

The electrode inks were produced via a one-pot methodology. 0.15 g of the EVA was dissolved in 5 ml of the 1 2 4-TCB (both from *Sigma Aldrich*) under constant stirring on a hotplate at 80 °C until all of the polymer was visibly dissolved. This was then added to the 0.85 g carbon mixture and mixed at 1000 rpm for 1 minute in a *Hauschild Engineering* speed mixer, this was repeated two further times. The speed rpm was selected so to not allow the ink to rise beyond the lip of the plastic mixing pot during speed mixing.The ink then underwent 1 hour of sonication in a *Branson 1510* ultrasonic bath to disperse any aggregation of the carbon particles before one final speedmixer run.

TABLE 4.1: The naming convention for the textile supercapacitors produced in this chapter with their associated production variables

Name	Activated Carbon	$\%_{wt}$ Activated Carbon	No. of Ink Layers
YP80F_2_90	YP80F	90	2
YP80F_4_90	YP80F	90	4
YP80F_6_90	YP80F	90	6
SXU_2_90	SXU	90	2
SXU_4_90	SXU	90	4
SXU_6_90	SXU	90	6
GSX_2_90	GSX	90	2
GSX_4_90	GSX	90	4
GSX_6_90	GSX	90	6

The device was produced via spray deposition of the aforementioned ink onto both

sides of the textile, forming the TSC from a single layer of textile. Throughout the project the same plain weave cotton was used. The cotton was ∼0.43 mm thick with 33 ends per inch (13 per cm) and 38 picks per inch (15 per cm) [20]. Each textile sample was dried at 100 °C for 10 minutes and weighed before and after the electrode deposition to characterise the loading of carbon on the devices. Figure 4.1 shows an SEM micrograph of the cotton at a magnification of 50x. The general plain weave pattern of the textile is plain to see with a loose fibres structure, which is ideal to act as a scaffold for the deposited carbon inks.

To limit the ink permeating throughout the bulk of the textile (figure 4.15) the spray distance and air pressure of the spray gun must be closely monitored. This was achieved by mounting the spray gun 7.5 cm away from the substrate and the air pressure set to 138 kPa (20 psi), see figure 4.2. The spray gun itself was gravity fed and had a nozzle width of 0.5 mm. This nozzle width had to be increased from 0.2 mm to accommodate all of the carbons used in this study and reduce blockages. To create the 1 cm diameter (0.785 cm^2) circle electrodes, which will be used throughout this work, the cotton substrate was mounted within an aluminium shadow mask (see figure 4.3) which could produced six devices at a time. The aluminium mask was then mounted on an automated conveyor belt (see figure 4.2) to standardise a single deposition layer. The belt speed was set such that each electrode would pass through the spray arc of the air gun for 0.5 s. Each pass through the spray arc counted as one layer. Following the deposition the samples were placed into an oven at 100 °C for 15 minutes to drive off any excess solvent and the samples weighed.

The electrolyte used within this experiment was an aqueous gel electrolyte produced from Ammonium Dihydrogenphosphate (ADP) and PVA, both from *Sigma Aldrich* and used as received. ADP was chosen as the electrolyte due to its to its strong 1 : 1 dissociation, making it a strong electrolyte [213] like KOH and H_3PO_4. Its use as an electrolyte for TSCs has also been shown previously [56]. 0.5 g of PVA (high molecular weight, Mw = 85,000 - 124,000) was dissolved in 5 ml of deionised water under constant stirring and heating (200 °C until the temperature of the fluid reached 85 °C). 0.3 g of ADP was dissolved in 1 ml of deionised water, this was then added dropwise to the polymer solution under constant stirring but with the heat turned off. The

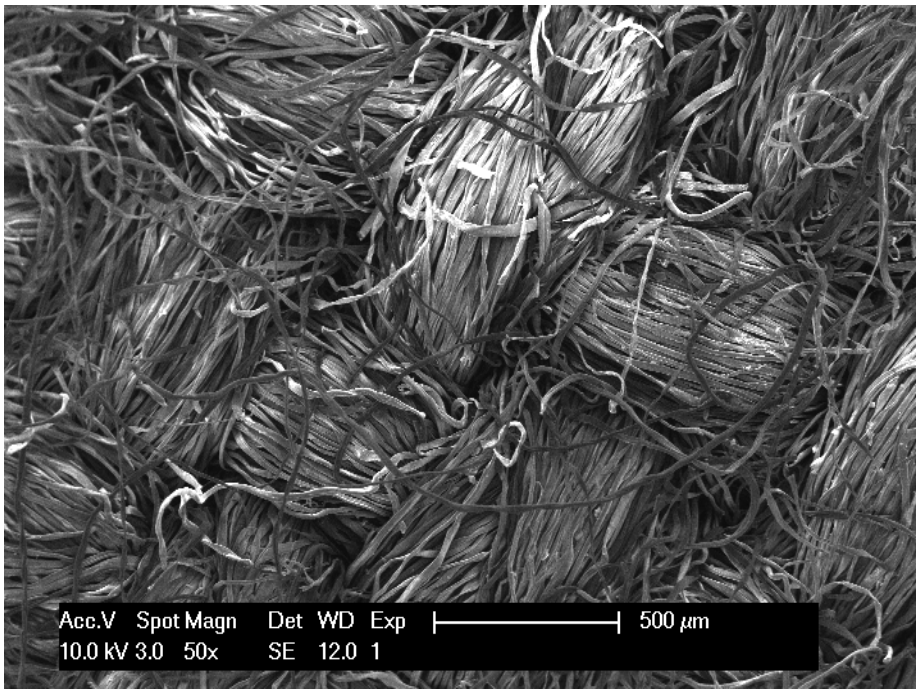

FIGURE 4.1: SEM image of the cotton substrate used throughout this project at a magnification of 50x. The general plain weave pattern is clear but the loose fibrous nature of the cotton adds a loose surface layer of stray fibres, known as pilosity

electrolyte was subsequently degassed under vacuum. Following this, the TSCs were submerged in the electrolyte and vacuum impregnated under 50 mbar for 20 minutes. This was done to drive the air out of the loose structure of the cotton (see figure 4.4) and improve the wetting of the electrodes.

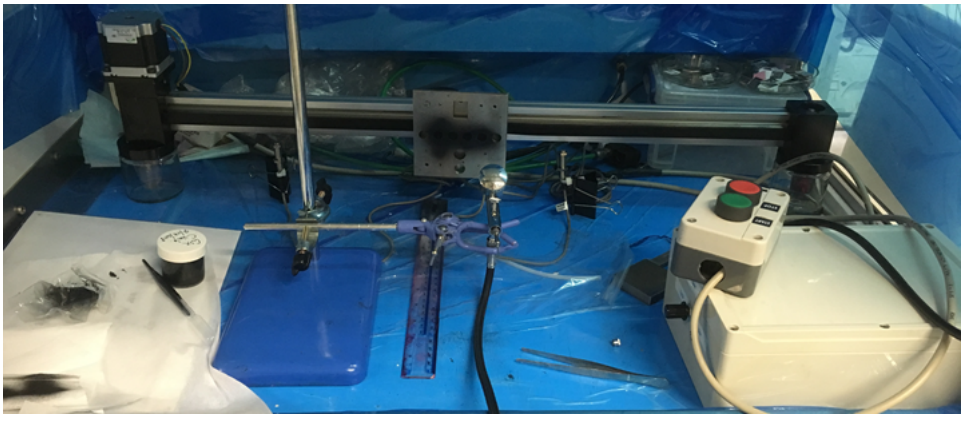

FIGURE 4.2: Photo of the spray set up used in the creation of the TSCs. In the foreground the spray gun is held in place via a clamp stand, positioned along the central line of aluminium mask and 7.5 cm away. The automatic belt in the background is long enough to allow the attached aluminium mask to fully exit the spray arc between each deposition

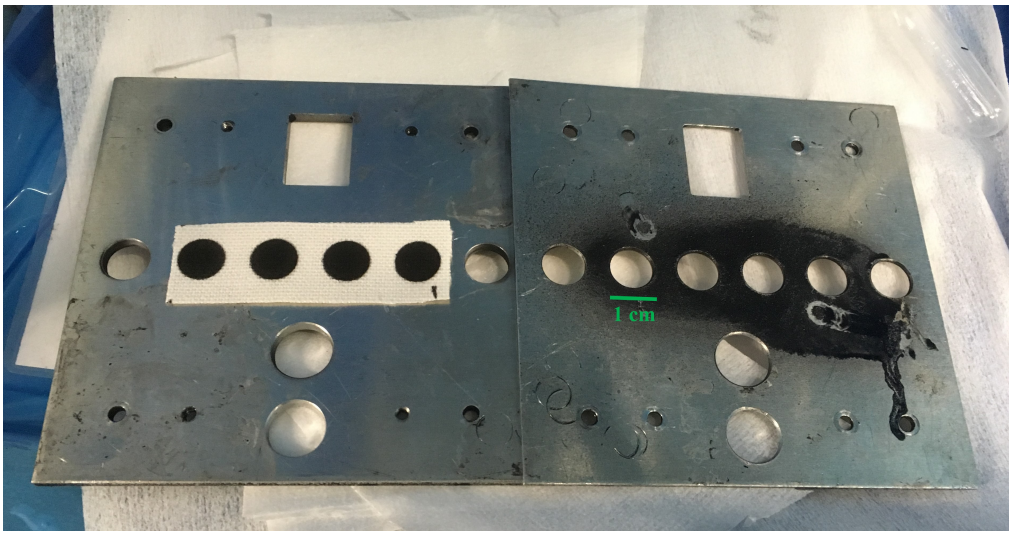

FIGURE 4.3: Photo of the aluminium shadow mask used in the spray deposition of the electrodes. The mask is made of two pieces held together with bolts and allows the deposition of the electrodes on both sides of the textile substrate. Pictured is a typical substrate with the carbon deposited. Green 1 cm bar for scale.

FIGURE 4.4: Textile supercapacitors immersed in polymer electrolyte undergoing vacuum impregnation. Bubbles can clearly be seen on the surface of the electrode and then detach and float to the top of the electrolyte volume.

4.1.3 Testing

As discussed in chapter 3, all of the devices underwent GCD and CV electrochemical testing. Each device was housed within a Swagelok test cell (see figure 4.5). The

Swagelok is constructed from two stainless steel electrodes and a spring (to maintain constant pressure and to prevent over tightening) housed within a screw fitting. All of the devices were initially screened with 0.25 mA.cm^{-2} (0 to V_{peak} 0.8 V) GCD and a 50 mV.s^{-1} (-0.8 to 0.8 V) CV measurements before undergoing repeated 0.25, 0.5, 1, 2 and 3 mA.cm^{-2} and 5, 25, 50, 100, 200 mV.s^{-1} measurements. Measurements were repeated 5 times.

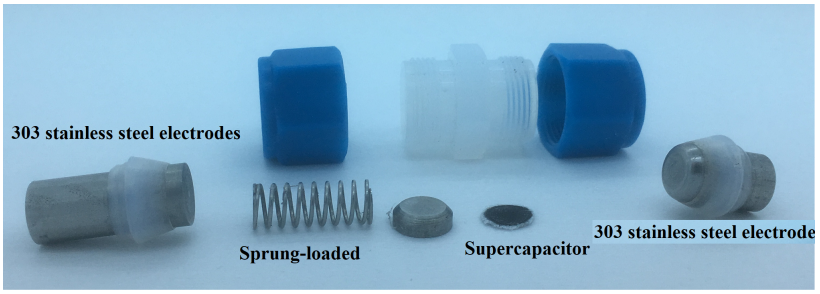

FIGURE 4.5: An exploded view of a Swagelok test cell used for the characterisation of the textile supercapacitors

For the SEM characterisation the surface of the carbon electrodes were sputtered with 10 nm of gold to prevent any charge build. For the cross section microgrpahs, the samples were initially frozen in liquid nitrogen before being cut with a scalpel. This was done to limit the crushing of the soft sample, and to prevent smearing the carbon into the unpregnated central region of the cotton.

For the particle size distribution measurement the *Malvern* Mastersizer optic section was first removed and cleaned. After the reinsertion of this section the system was filled with ethanol (the working fluid) and a baseline measurement was taken. A solution of ethanol and the three carbons was produced and sonicated for 30 minutes to ensure good dispersion of the carbon. This solution was then added dropwise to the circulating ethanol until the instrument showed that the concentration of carbon was within the measurement limits. Following the measurement, the ethanol-carbon solution was drained, the system flushed and the optics cleaned. This was repeated three times for all three carbons.

For the BET and BJH measurement 1 g of each carbon was degassed at 80°C overnight and the N_2 adsorption measurement was performed using a *Micromeritics Tristar 3020* at a bath temperature of 77.3 K.

The surface profile of the carbon was characterised via a *Tencor P-11* surface profiler. Akin to an Atomic Force Microscope (AFM) a needle is drawn across the surface of the sample and is deflected by physical features, giving a 1D vertical profile. The sample was first stuck to a glass slide to flatten it. Following this, the sample was placed in the centre of the measurement region. The measurements were taken across 2000 μm of travel with three of the measurements occurring through the carbon (400 μm of cotton and 1600 μm of carbon) and one just of the cotton as a baseline.

4.2 Results

4.2.1 Electrode Formation

The construction of the electrodes involves materials of various length scales, from the textile at 100s of μm to the conductive additive at nm. This poses complexities worthy of discussion before moving onto the physical and electrochemical results. From figure 2.7 it is assumed that for TSCs the electrodes will deposit as plates. However, given the complexities in the nature of the textile and its interaction with the carbon ink, this is not necessarily the case. The different lengths scales exhibited within the electrode are presented in figure 4.6. It is seen that the deposition forms a weave dependent, irregular electrode, as some of the ink is absorbed by the cotton material forming a layer while more of the ink pools in the gap between the woven warp and weft yarns. This illustrates the importance of a tight weave, as a looser woven fabric would allow the ink to penetrate too far, causing a short circuit.

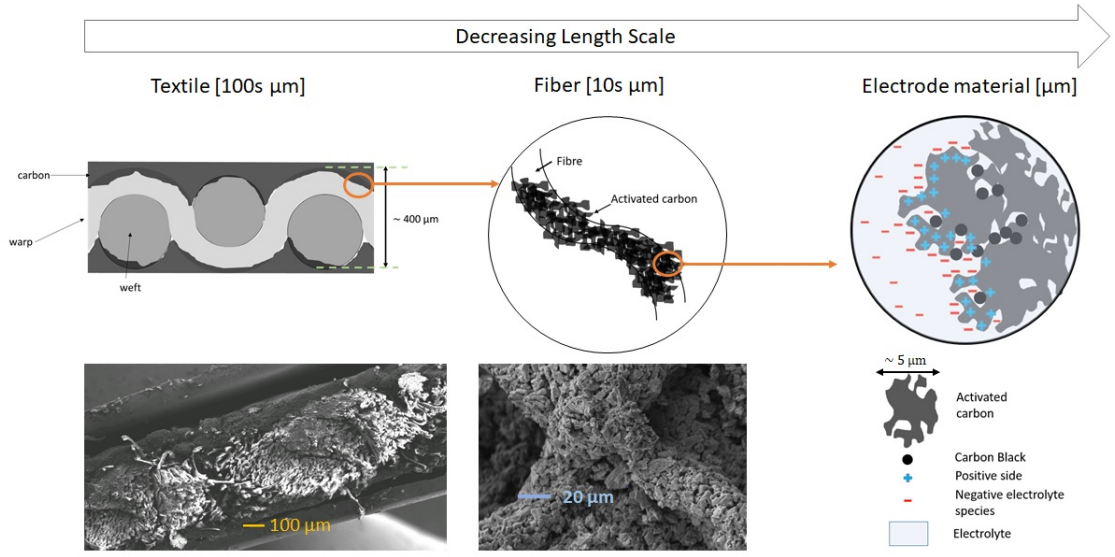

FIGURE 4.6: Multi-scale cross sectional diagram of the TSC. Left, the TSC cross section at the device scale (100s of μm). In the SEM image pooling of the carbon ink between warp and the weft can be seen, as well as absorption of the ink by the fibres. This is illustrated in the schematic above. Middle, at a reduced length scale (10s μm) it can be seen that the ink adheres uniformly to the fibers. The final image, right, shows schematically the highly porous nature of the electrode material themselves. The conductive additive bridges the gaps between the porous carbon flakes, generating the electrical network. The build up of the charge close to the electrode is more dense, with the charge density reducing as the distance from the electrode increases.

The electrode thickness is characterised to be 50 - 150 μm across the width of the device (characterised from figure 4.15). However, what is challenging to discern from the SEM images is the height of the electrode protruding above the textile. To understand this further a profile measurement was performed at three locations on the carbon electrode. The results are shown in figure 4.7 where the white sections of (B)-(E) show where the measurement was over cotton and the grey section is where it was characterising the electrode. In (B) there appears to be an edge as the measurement needle deflects at $\sim$40 μm, and goes on to have a series of high peaks. However this is not replicated in (C) or (D). Additionally, as well as large peaks there are also a number of large troughs, at $\sim$100 μm in (B) and at $\sim$60 μm in (C). If the carbon film was thick above the surface, one would expect less variation. When the control case of just the cotton (E) is taken into account one can see that a variable profile is typical of the cotton surface, including peak vertical displacements comparable to the peaks seen on the electrode itself. This suggest that the carbon ink is almost fully absorbed into the surface of the cotton and the thin film of exposed carbon (as seen in figure 4.12) contours with the weave, yarns and fibres. Given the nature of the measurement, this control measurement is of paramount importance. With the loose natural structure of the cotton, as seen in figure 4.1 the needle could have a tendency to drag these fibres. Where a harder material could be characterised as an absolute measurement, the measurement within this work was a relative measurement.

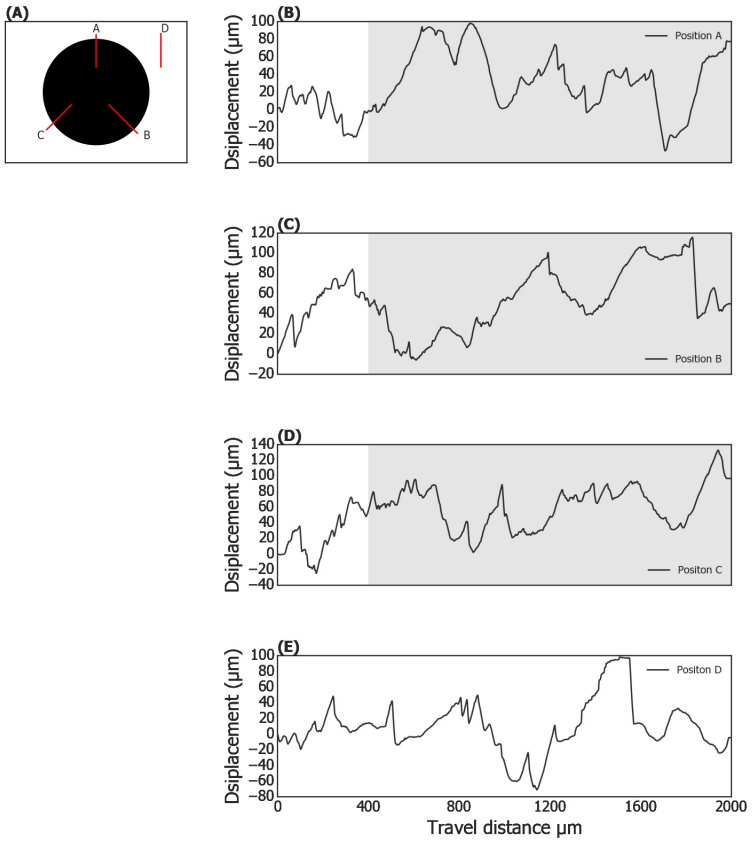

FIGURE 4.7: The surface profile of the carbon electrode for one of the textile supercapacitors.The profile was taken from 3 positions as shown in (A) along with a Representative all cotton measurement.Plots (B)-(E) show the surface profile relative to the starting position of the needle. The grey shaded regions represent the position of the transition from cotton to carbon.

4.2.2 Physical Results

The three carbons were physically characterised via BET and BJH. The adsorption and desorption isotherms are presented in figure 4.8 and the pore size distributions presented in figure 4.9. All three of the isotherms exhibit a type 1b characteristic [214, 215] which demonstrates a microporous structure within the three carbons but with a broader pore size distribution than a conventional type 1. There could be an argument that the GSX and SXU carbons exhibit a type 2 characteristic due to the steepening as the isotherm reaches a partial pressure of 1. This implies a macroporous structure. It is the belief of the author that though they are steeper (adsorbing 100's $cm^2.g^{-1}$ between 0.5 and 1 p/p_0 instead of 10's) than the other YP80F isotherm, it is not enough to be classed as a type 2 and that is supported by the pore size distribution in figure 4.9. The hysteresis seen between 0.5 and 1 partial pressure in

all of the carbons suggests there is also a proportion of mesoporous structure. The shape of the hysteresis is typical of a H4 classification, implying that the micropores within the carbons are 'slit-like' in shape [216]. The hysteresis in the GSX and SXU carbons is more pronounced, implying a greater proportion of meso scale pores. This mix of micro and mesoporous structure is advantageous to supercapacitor applications.Though all three of the carbons exhibit this form it is immediately clear that there are differences between the three. The YP80F carbon adsorbed almost double of that of the other two carbons and this is represented in the surface area characteristics presented in table 4.2. The single point surface area is determined from a single point (P/P_0 = 0.3) whereas the BET surface area is determined from at least 3 points between $0.025 < P/P_0 < 0.3$. A partial pressure higher than 0.5 suffers from capillary condensation, reducing the veracity of the calculation. The single point surface area has been included for completeness, with the BET surface area being used henceforth.

The pore size distribution characterisation supports the assertion that the GSX and SXU carbons possessed a greater proportion of meso scale pores than the YP80F carbon. Where the YP80F has a dominant peak between 1.6 - 2.7 nm, straddling the micro- and mesopore boundary ($\sim$ 2 nm), the other carbons show a flatter distribution, predominately in the 10 - 18 nm range. The SXU carbon does exhibit a peak at $\sim$1.8 nm, with the GSX carbon exhibiting a smaller peak at $\sim$2.2 nm. From figure 4.9B it is seen that there are negligible pore widths above 4 nm for the YP80F, whereas the SXU peaks at 13 nm and the GSX at 15 nm. From chapter 2 this would imply that the YP80F should deliver higher energy density but the other two should be more power dense, with the ion mobility enhanced with a greater portion of larger pores.

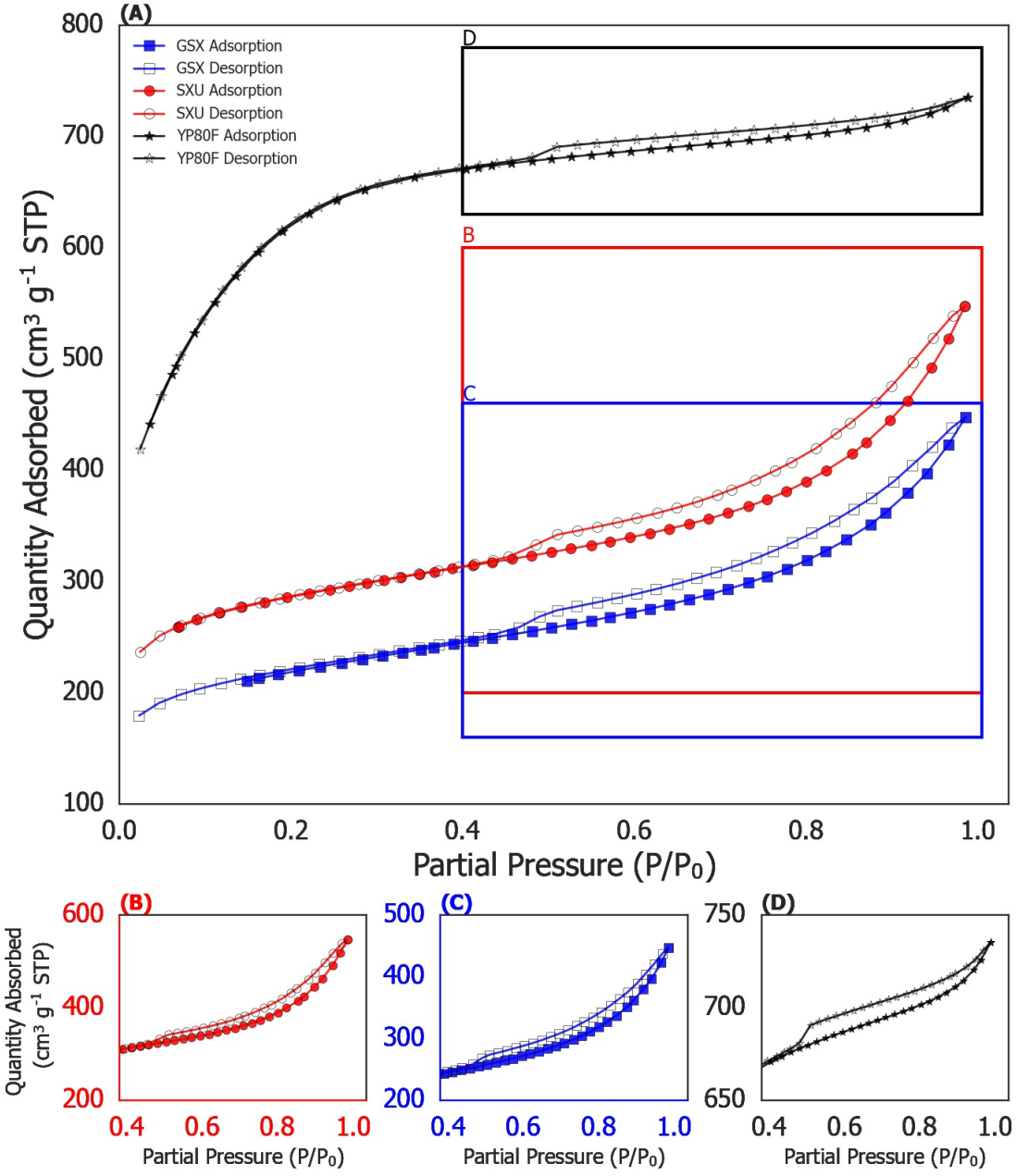

FIGURE 4.8: Nitrogen adsorption-desorption isotherms of the three carbons.The closed markers are adsorption and the open markers are the desorption.The hysteresis portion of the plots is magnified in (B), (C) and (D) for the SXU, GSX and YP80F carbons respectively.

TABLE 4.2: The single point and BET surface areas for the YP80F, SXU and GSX activated carbons

Carbon	Single Point Surface Area at $P/P_0 = 0.3$ (m^2g^{-1})	BET Surface Area (m^2g^{-1})
YP80F	2028.2	1874.2
SXU	907.0	833.0
GSX	703.1	653.0

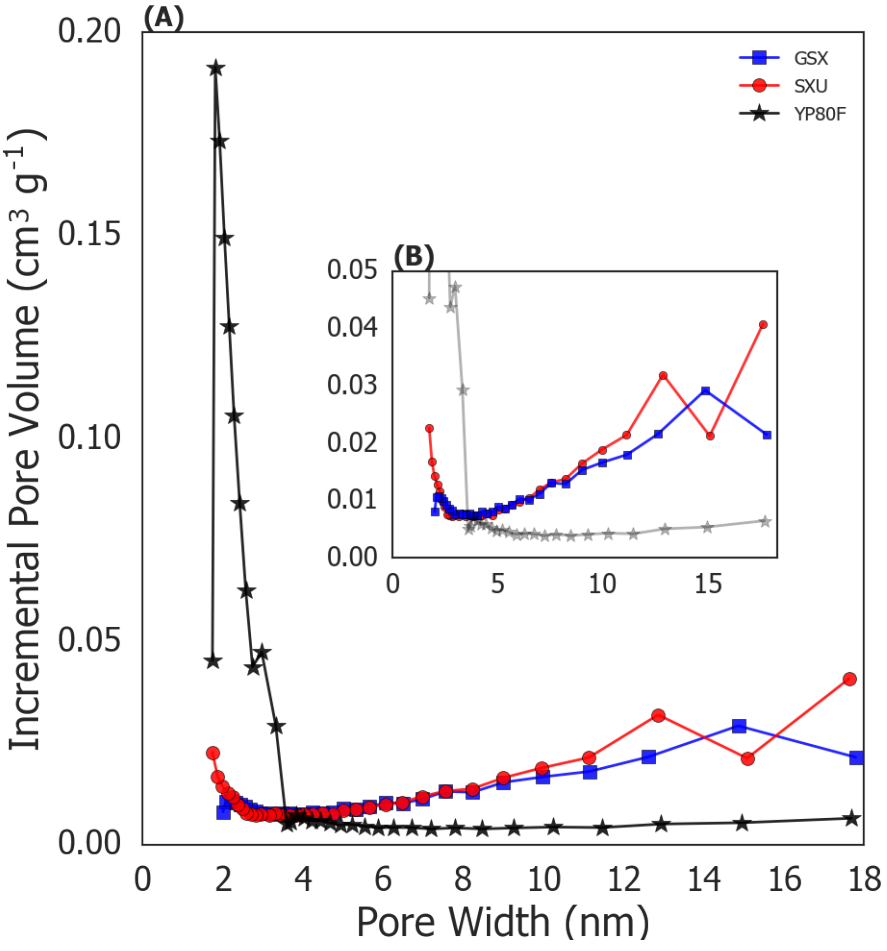

FIGURE 4.9: Pore size distribution for the three activated carbons. (A) The full results for all three. (B) Magnified view to show the SXU and GSX activated carbon results in more clarity

Following the characterisation of the surface area and the pore widths, the physical characterisation jumped a length scale to investigate the particle size and morphology of the carbon and its adherence to the cotton. This was undertaken through laser diffraction and SEM. The particle size distribution can be seen in figure 4.10 and the morphology can be seen in figures 4.11 and 4.12. The particle size characteristic can be seen in table 4.3. What is clear, is the narrow distribution of the YP80F compared to the other carbon materials. With a peak particle size of 5.0 μm the YP80F its particle size is also considerably smaller than the other two carbons. The narrow distribution suggests a very uniform powder. The GSX and SXU carbons show a very broad distribution (137.4 and 362.4 μm, respectively) with some large particle size peaks outside of the main distribution for the SXU carbon.

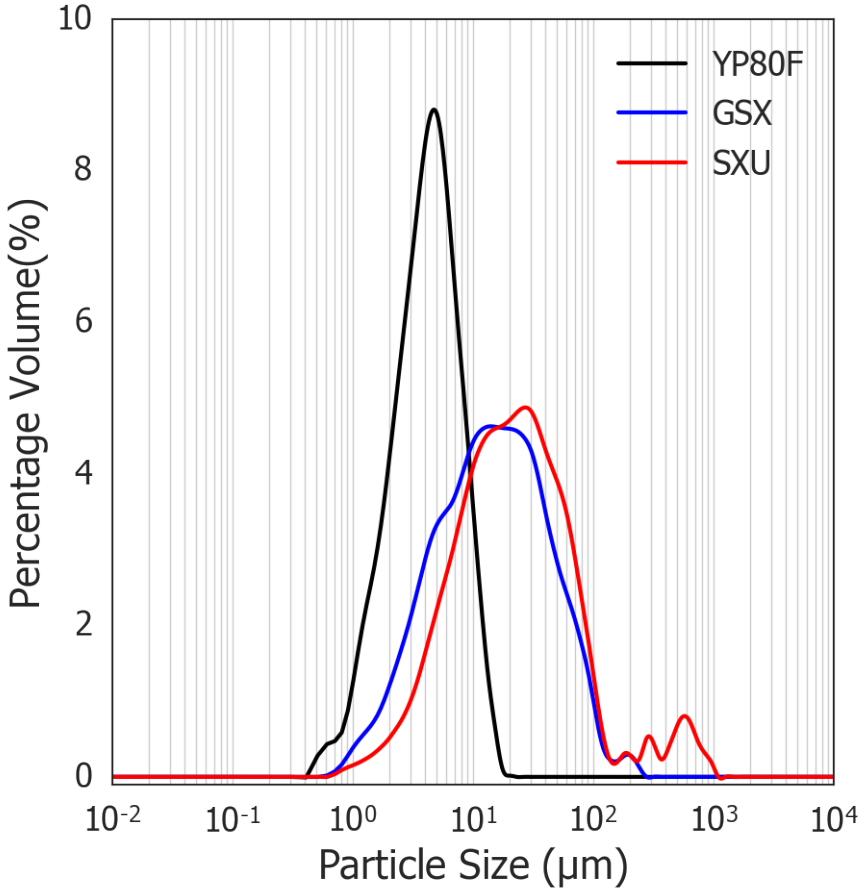

FIGURE 4.10: Particle size distribution of the three activated carbons.

TABLE 4.3: The peak particle size, associated percentage volume and distribution width for the YP80F, SXU and GSX activated carbons

Carbon	Peak Particle Size (μm)[a.]	Volume Percentage (%)[b.]	Distribution Width (μm)
YP80F	5.0 $\pm$0.7	8.7 $\pm$ 0.5	19.5
SXU	26.3 $\pm$3.6	4.9 $\pm$ 0.1	362.4
GSX	14.2 $\pm$1.0	4.6 $\pm$ 0.3	137.4

a. The uncertainty is half the bin width for that particle size

b. The uncertainty is the standard deviation of three repeat measurements

The uniformity, or lack of, will have an effect on the stacking of the carbons during deposition. In figure 4.11 the deposition of all three carbons are compared at a 50 μm length scale. The SXU carbon sample shows a number of the larger particle flakes. It can also be seen to be a chaotic stacking structure onto the fibres, leaving some exposed and some attached by only a small portion of the carbon particle. The GSX micrograph displays a considerable amount of exposed fibre, and again shows a number of these larger carbon flakes. In stark contrast, the YP80F sample shows a smooth and even coverage of carbon across all of the fibres. This suggests the smaller and more uniform particle size is optimal for a uniform coating. To investigate this further another series of SEM micrographs were performed on the YP80F sample at a magnification of 502x (figure 4.12). From (A) it can be seen that the uniformity of deposition goes beyond that of the individual fibres and a film is formed on the surface of the cotton, creating a consistent electrode surface. (B) again shows a very consistent deposition onto the fibres but at a 20 μm length scale.

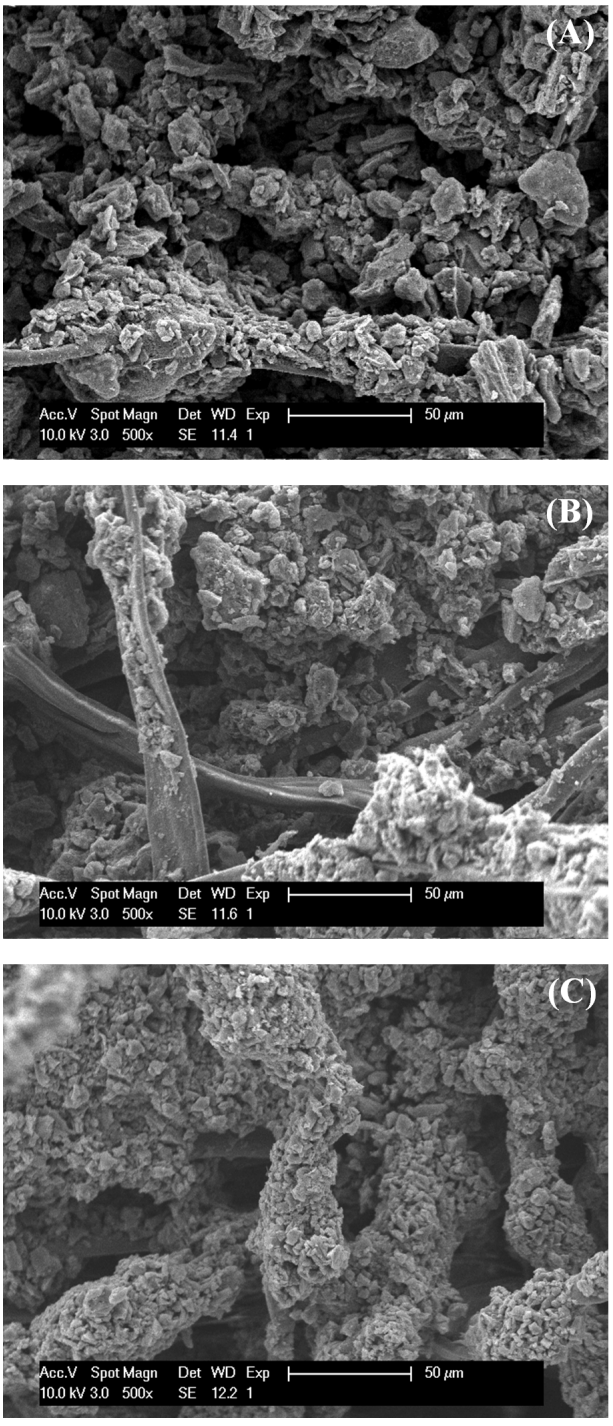

FIGURE 4.11: SEM micrographs of an electrode produced from each of the activated carbons at a magnification of 500x. Each electrode have 4 deposition layers and a 9:1 carbon ratio. (A) SXU, (B) GSX and (C) YP80F

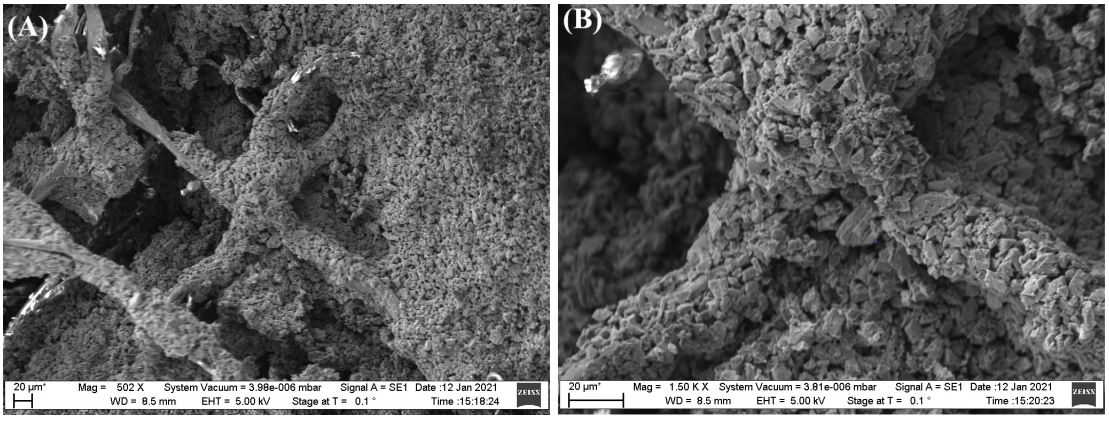

FIGURE 4.12: SEM micrographs of an electrode produced from YP80F activated carbon. (A) shows a a zoomed out view of the electrode, demonstrating the even coating of the electrode in the right of the image. (B) is a more magnified image and corroborates the SEM from figure 4.11.

4.2.3 Electrochemical Results

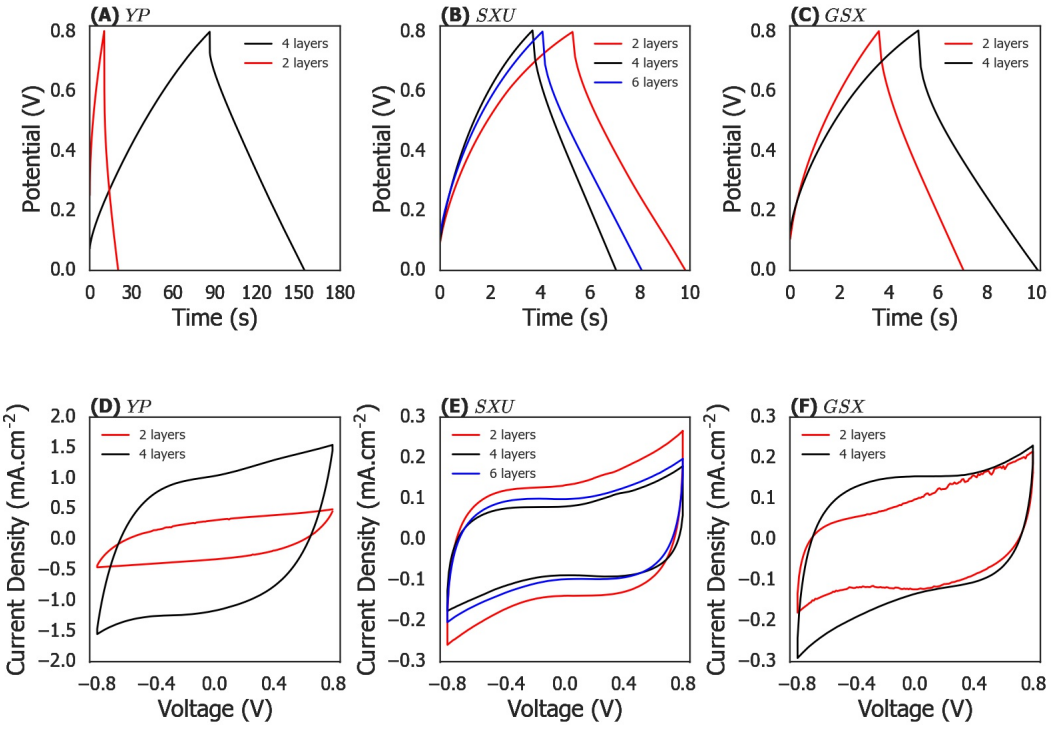

FIGURE 4.13: Electrochemical results for the three different activated carbons under differing deposition conditions. (A) GCD measurement at a 0.25 mA.cm^{-2} charge and discharge current of the YP80F activated carbon with 2 and 4 layers, devices with 6 depositions layers failed.(B) GCD measurement at a 0.25 mA.cm^{-2} of the SXU activated carbon with 2, 4 and 6 layers.(C) GCD measurement at a 0.25 mA.cm^{-2} of the GSX activated carbon with 2 and 4 layers, devices with 6 deposition layers all failed. (D) CV measurement at 50 mV/s for the YP80F activated carbon with 2 and 4 layers. (E) CV measurement at 50 mV/s for the SXU activated carbon with 2, 4 and 6 layers. (F) CV measurement at 50 mV/s for the GSX activated carbon with 2 and 4 layers.

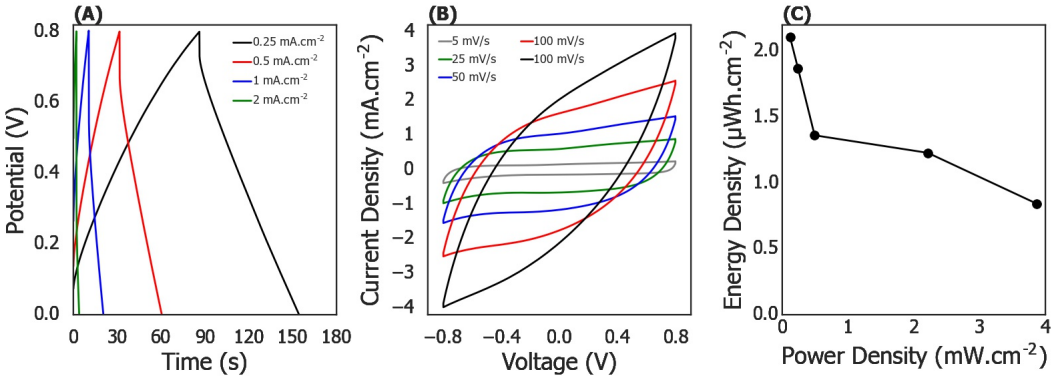

FIGURE 4.14: Extended electrochemical results for the YP80F TSCs. (A) GCD measurements at 0.25, 0.5, 1 and 2 mA.cm^{-2} for the YP80F with 4 layers, 3 mA.cm^{-2} has been omitted for clarity. (B) CV measurements at 5, 25, 50 100 and 200 mV/s for the Y80F with 4 layers. (C) Ragone plot derived from the results presented in (A). The standard deviation for both power and energy density is $\pm$ 0.1 (μWh.cm^{-2} and mW.cm^{-2} respecitvely) from 5 repeats.

Following the physical characterisation the electrochemical performance of the three carbons, in an ink ratio of 9:1, was evaluated. The graphical results can be seen in Figures 4.13 and 4.14 with the numeric results in table 4.4.

TABLE 4.4: Areal capacitance, energy density and peak power density of the three activated carbons determined via GCD measuremnts at a charge/discharge current of 0.25 mA.cm^{-2}. The uncertinty is the standard deviation of 5 repeats

Sample	Areal Capacitance (mF.cm^{-2})	Energy Density (μWh.cm^{-2})	Peak Power Density (x10^{-4} W.cm^{-2})
YP80F_2_90	2.7 $\pm$ 0.08	0.24 $\pm$0.06	2.4 $\pm$ 0.7
YP80F_4_90	23.6 $\pm$ 0.05	2.1 $\pm$0.1	5.9 $\pm$ 0.7
YP80F_6_90	-	-	-
GSX_2_90	1.4 $\pm$ 0.08	0.12 $\pm$0.08	8.3 $\pm$ 0.2
GSX_4_90	1.6 $\pm$ 0.03	0.15 $\pm$0.02	6.7 $\pm$ 0.1
GSX_6_90	-	-	-
SXU_2_90	1.5 $\pm$ 0.01	0.14 $\pm$0.01	10.0 $\pm$ 0.2
SXU_4_90	1.2 $\pm$ 0.03	0.11 $\pm$0.03	8.6 $\pm$ 0.2
SXU_6_90	1.4 $\pm$ 0.01	0.13 $\pm$0.01	9.5 $\pm$ 0.2

In figure 4.13 all of the GCD traces show triangular profiles, typical of EDL supercapacitors. However, some curving towards the peak voltage for the SXU and suggest an increase in leakage current at the higher voltage in the form of a parasitic current. The x-axis in figure 4.13(A) is significantly larger than that of (B) or (C), suggesting that the YP80F has a far greater energy storage capability and that is shown explicitly in the areal capacitance and the energy density. The CV traces for the YP80F show a good square shape, with no additional peaks. This again shows that the material has produced a good EDL textile supercapacitor. The CV trace for the SXU carbon (figure 4.13(E) on the other hand shows 'peaking' as the voltage window approaches $\pm$0.8 V. This suggests that the electrolyte is beginning to break down. As this was not observed in the case of the YP80F carbon, it suggest there is a

contaminant (perhaps a surface group) in this carbon which is also goes some way of explaining the curving of the associated GCD trace. This 'peaking' is also replicated in the GSX (4 layers) device, again implying some from of contaminant. Also in figure 4.13(F) the 2 layer device shows an asymmetry which was unexpected. This is attributed to an asymmetric loading of the electrodes and is discussed further in section 4.3. With such disparity in the performance of the carbons (23.6, 1.6 and 1.2 $mF.cm^{-2}$ for the YP80F, GSX and SXU respectively) it was decided to only perform further characterisation on the YP80F devices. In figure 4.14(A) and (B) the GCD and CV results at the varying current densities and scan rates are displayed. It is seen that between 0.25 and 3 $mA.cm^{-2}$ there is a decrease in areal capacitance from 23.6 to 9.2 $mF.cm^{-2}$. At the higher current discharge this shows that there is a drop in capacitance. This, however, is not unexpected as the capacitance has a time dependence that is widely acknowledged. At low current densities the ions have time to diffuse into (and deeper) into the pores of the carbon. At higher currents, this isn't the case (especially considering the small pore widths seen in the YP80F carbon) and the charge storage becomes even more of a surface effect, only utilising a portion of the total surface area of the carbon.

As seen in figure 4.6, the structure of the TSCs is complex and to validate the capacitance values presented in table 4.4 the results were compared to the expected values when calculated from the parallel plate equation (equation 2.1). If one assumes a Helmholtz distance of 2 nm (value d, in equation 2.1) and a permittivity of 10, a calculation for the expected active area of the capacitor can be found and compared to the results in table 4.2. The total capacitance of a supercapacitor is the combination of two parallel plate capacitors in series, as seen in figure 2.3, therefore, if the measured capacitance was approximately 20 mF for the YP80F_4_90 devices then each of the electrodes had a capacitance of approximately 40 mF.

$$
\begin{aligned}
C &= \frac{\epsilon_0 \epsilon_r A}{d} \\
\therefore A &= \frac{Cd}{\epsilon_0 \epsilon_r} \\
&\approx \frac{40 \times 10^{-3} \cdot 2 \times 10^{-9}}{10 \cdot 8.9 \times 10^{-12}} \\
&\approx 0.9\ m^2
\end{aligned}
\tag{4.1}
$$

Taking the mass of a single electrode and the BET surface area of the YP80F carbon, one would expect the area of the electrode to be approximately 1.9 m^2. The two values for the expected area of the electrode are a factor of 2 different. Considering the approximations required to perform the calculation, this is a very close agreement. The calculated value for the area from the capacitance is smaller than the direct characterisation of the area of the carbon, this is to be expected as it is unlikely that all of the surface area is utilised in a real world system. Importantly for this work, the close agree also suggests that each electrode is working as a consistent electrode. This rules out any concerns of the carbon network on the individual fibers within the yarn acting as as isolated capacitors, distributed in a series chain through the thickness of the electrode.

The YP80F device is seen to have an energy density of 2.1 μWh.cm^{-2} at a power density of 0.11 mW.cm^{-2} and an energy density of 0.84 μWh.cm^{-2} at a power density of 3.9 mW.cm^{-2}. This is enough to power and Radio Frequency Identification (RFID) platform for $\sim$1 minute (based on the power demand of 168.3 μW) from the work of Lemey *et al.* [217] or for $\sim$0.6 s for a e-textile proximity sensor (as displayed in the work of Ojuroye *et al.* [218], based on 13.5 mW). This shows that though appropriate for low power e-textiles more work is required to fully integrate these devices into real-world e-textile power modules.

The second phase of the electrode work was to investigate the ratio of active material to conductive additive. As such two new inks were made with an 80:20 ratio and a 100:0 ratio. In this phase only the YP80F carbon was selected and devices produced from the 4 layer deposition methodology were evaluated. For the 100% activated

carbon devices, none of them were stable enough for the quantities to be extracted from the measurements. The 80% activated carbon ink produced devices with a capacitance of 10.9 mF.cm^{-2}. This shows the importance of an optimised ink formulation. The 100% activated carbon was too resistive, causing the device to fail and the higher percentage of carbon black in the 80:20 formulation restricted the available surface for the EDL to form.

4.3 Discussion

From figures 4.13 and 4.14 and table 4.4 it is clear that there is a 'Goldilocks' ink formulation and deposition process. When one considers the physical characteristics of the individual carbons it is not a surprise to see that the YP80F carbon outperformed the other two carbons. With the more uniform particle size and greater number of micropores it would have been surprising if this were not the case. This combination of physical characteristics is significant and demonstrates the importance of considering all of the lengths scales when designing a supercapacitor electrode. The volume of micropores enables a much higher theoretical energy density while the particle size has more practical ramifications. The more uniform and smaller particle size of the YP80F (figure 4.10) enabled the particles to stack more evenly, building up the layers during deposition and avoiding clumping. This improves the coverage and consistency of the electrode (as seen in figure 4.11). The lack of agglomeration of the smaller more uniform particles, benefits the electrolyte penetration into the electrode. The peak power density further supports the physical data, with the carbons with a greater percentage of mesopores demonstrating a better peak power due to the improved ion diffusion compared to those of the smaller pores seen in the YP80F carbon. What is interesting to note however is there does not appear to be a trend in the peak power density. While the YP80F carbon increased in peak power with a greater degree of loading, the GSX ans SXU carbons were more variable. As peak power is highly dependent on the ESR (see equation 3.6) these results show the complexity of this parameter. Though relatively easy to characterise, it is a lumped parameter that is based upon the electrical contact resistance and the electrolyte

resistance (ion mobility/diffusion). With the greater loading of SXU and GSX carbon onto the cotton the electrical network within the electrode likely improved but due to the large variation in particle size (figure 4.10) and pore width it is thought that the tortuosity [219] of the ion diffusion varied greatly. This is in contrast to the YP80F, where an increased loading (up to a point) only improved the ESR (506 to 343 Ω).

The failure of the 6 layered devices for the YP80F and the GSX carbons is also interesting. Once produced the TSCs look very alike and it is hard to know why one would be prone to failure over another. As such one of the YP80F 6 layered electrodes was view under the SEM and the resulting micrograph is displayed in figure 4.15. As can be seen in figure 4.15(A) for one of the 4 layered devices a clear all textile separating layer can be seen. Though variation in the separation is present across the length of the cross section, there is a consistent carbon free layer. When this is compared to figure 4.15(B) it is clear to see why these devices failed. The carbon ink has permeated the full thickness of the textile, creating a constant electrical pathway across the electrodes, leading to short circuits. When the mass loading of the devices is compared (2 layer ∼1 mg, 4 layer ∼2 mg and 6 layer ∼4 mg) the increase from 4 to 6 layers is greater than expected. This is attributed to the repeated deposition pushing the ink further into the textile, instead of building a thicker layer on the surface of the electrode. Relating this back to the surface profile measurement, it is clear that there exists an optimal deposition procedure. One that deposits enough carbon to permeate partially through the carbon, forming only a thin surface layer of carbon. This means, that the bulk of the carbon network is within the textile itself (bound to the individual fibres of the cotton, figure 4.11), showing the advantages of using a natural fibre as the scaffold for the electrodes. The thin layer of carbon that protrudes the height of the textile is important to form the electrical contact with the test equipment (in this case) and with electrical interconnection in a real-world device.

The final interesting result is the asymmetry of the 2 layer CV trace for the GSX carbon. As can be seen in the other traces it would be expected to be symmetrical. Given the low total loading of the electrodes of the two layer devices, it is thought this asymmetry in the electrochemical results is a result of a slight asymmetry in the mass loading of the individual electrodes. The ionic species within the ADP electrolyte

(NH_4^+ and $H_2PO_4^-$) have different ionic radii (1.45 Å [220] and 2.69 Å [221] respectively) and this different size can cause the ions to behave differently at the surface boundary. When an electrolyte system has ions of different radii the larger ion may be blocked in small pore width carbons reducing the concentration at that electrode, as discussed in Bates *et al.* [222] and Andres *et al.* [223]. Bates found an asymmetry in electrochemical results in a $TEABF_4$ electrolyte system, which was attributed to the different desolvation of the ionic species when entering small pore widths, while Andres postulated that under or over coverage of the ions at the electrolyte-electrode boundary harms the devices performance. To verify that claim, Andres purposefully changed the mass loading of the electrodes in a symmetric electrode device to better match the ion size of the electrolyte (sodium hydroxide, NaOH), with a 10% improvement in capacitance. The difference in ion size in NaOH is 0.58 Å whereas in ADP, the difference is 1.45 Å, immediately, it seems clear that the asymmetry shown in the CV trace could be due to loading. This effect is dominated in the low voltage region of the potential window. It would have been entirely appropriate to repeat the manufacture of the devices to ascertain the truth if the results were closer to that of the YP80F however, due to the poor performance in total for the GSX carbon it was decided to not repeat this work.

As discussed in section 4.2.3 the performance of the device is sufficient to power some e-textile applications but is limited to the low power devices. When compared to similar TSC seen in literature it outperforms the work of Abelkader *et al.* [112]

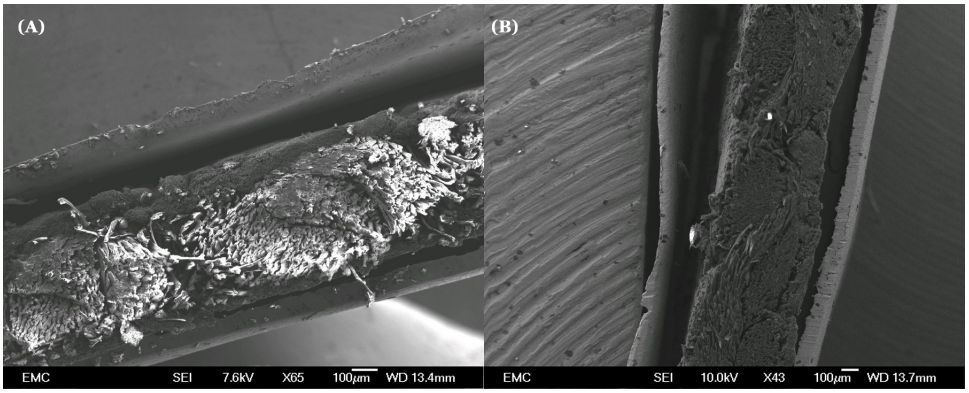

FIGURE 4.15: Cross-sectional SEM micrographs of a YP80F_4_90 (A) and a YP80F_6_90 (B) textile supercapacitor. It is clear to see the carbon free seperation layer in (A) however, in (B) the ink has permeating the whole way through the textile.

(2.5 mF.cm^{-2}, reduced graphene oxide electrodes and H_2SO_4 electrolyte), Lam *et al.* [224] (<20 mF.cm^{-2} for calligraphy ink electrodes, with loading 6 mg.cm^{-2} or less, and lithium chloride electrolyte) and Zopf *et al.* [225] (20 mF.cm^{-2}, for activated carbon electrodes and 1-ethyl-3-methylimidazolium tetracyanoborate electrolyte).The device even outperforms a pseudocapacitive device, detailed in the work of Zhang *et al.* [226] (19.2 mF.cm^{-2} for MnO_2 coated carbon microsphere electrodes with H_3PO_4 electrolyte). However, it falls behind many state-of-the-art devices in terms of performance. Chen *et al.* [227], reported an asymmetrical aqueous TSC (doped carbon anode and PANI cathode) with a capacitance of 3.6 F.cm^{-2}, energy density of 1.1 mWh.cm^{-2} and power density of 21 mW.cm^{-2}. Wei *et al.* [228] have also recently reported an asymmetric TSC (activated carbon and $NiCo_2O_4$) with a capacitance of 2.2 F.cm^{-2}, energy density of 3.4 mWh.cm^{-2} and power density of 24.6 mW.cm^{-2}. Recent development of zinc-ion hybrid capacitors have also showed exceptional performance, with the work of Chen *et al.* [229] producing an oxygen and fluorine doped CNT nanobundle device that had a capacitance of 1.6 F.cm^{-2}. Though questions over the scalability of such devices remains, it is clear that more work is required to be comparable to the state-of-the-art. Further work to increase the capacitance and energy density via the study of novel electrolytes will be undertaken in Chapter 5.

4.4 Conclusion

This chapter has shown that a single layer TSC can be readily produced from unprocessed commercial activated carbon via spray deposition. This offers a scalable and cost effective alternative to laboratory produced electrode materials currently seen widely in the literature. An optimised ink formulation of 90%$_{wt}$ activated carbon to 10%$_{wt}$ is seen to give the best performance, balancing available surface area with electrical conductivity. Through a series of experimental trials it has been found that a four layer deposition (equating to $\sim$2 mg of electrode mass) of the YP80F carbon gave the most uniform coating of the electrodes, thus creating a good electrical network. With the premier physical characteristics (exceptional surface area, good pore size distribution and particle size) the YP80F devices produced with 4 layers showed the

best performance with an areal capacitance of 23.6 mF.cm^{-2}, energy density of 2.1 μWh.cm^{-2}, power density of 0.11 mW.cm^{-2} and a peak power density of 5.9 mW.cm^{-2}. The reasons behind this best in class performance has been rationalised through the use of physical and electrochemical characterisation, with both micro and macro scale measurements. This multi-scaled approach brings confidence to the conclusions made within this body of work.

This chapter has answered the original research questions with regard to commercial activated carbons, optimised ink formulation and deposition process and electrochemical performance. Single layered EDL TSCs have been successfully demonstrated and the work within this chapter will underpin the rest of the thesis. No changes will be made to the electrodes and increases in performance will be made via new electrolytes and through the integration into textile power modules.

Chapter 5

Electrolyte

As discussed in section 2.3.2, the electrolyte selection for TSCs defines the maximum operating voltage and is of crucial importance to the overall device performance. Surprisingly, research into different electrolytes is minimal and focuses on just three: H_3PO_4, H_2SO_4 and KOH (Chapter 2). It is important to challenge the assumptions and habits of the community. Within this work, three different electrolyte families have been investigated, see Figure 5.1, including an ADP-PVA electrolyte (Chapter 4), a series of very low toxicity edible electrolytes and a high performance ACN-free organic electrolyte.

As discussed in chapter 2 the three primary families of electrolyte are aqueous, organic and ionic, all with different operating voltages and characteristics (see table 5.1). It was reasoned to investigate three separate electrolyte classes within this thesis, two aqueous and one organic. Ionic electrolytes were discounted due to their commercial immaturity and challenging chemistry. The first electrolyte for dedicated research was the ADP electrolyte used for the carbon study in chapter 4. After demonstrating its electrochemical performance, more real-world testing was undertaken in the form of aging. This was intended to act as a benchmark for the other electrolyte systems and to provide continuity across the work delivered in the thesis. The second class of electrolyte was a benign series of edible aqueous electrolytes. Though aqueous electrolytes are understood to be the safest of the electrolytes, many systems seen within the literature make use of high molarity acids

and alkalies, which are less conducive to wearable applications. To investigate the applicability of truly safe aqueous electrolytes, everyday commercial ingredients and beverages were investigated. It had been initial thought that PVA would be the gelling agent across both aqueous electrolyte systems, however, following the aging study it was rationalised that the PVA was the cause of the poor aging performance (discussed below and later in the chapter) and so two natural gelling agents were selected. Aqueous electrolytes have many benefits but suffer from a low potential stability window due to the water as the solvent. As such, the third electrolyte investigated was a higher voltage organic electrolyte. The challenge with organic electrolytes for wearable applications is the flammability of many of the solvents, in particular acetonitrile. As such, the research focused around developing an organic electrolyte that did not make use of this solvent.

In section 5.1, the ageing characteristics of the aqueous, PVA, electrolyte used within Chapter 4 is evaluated. Following significant performance degradation after three days and a total failure after five days, the validity of a PVA based system was called into question. The primary rationale for an aqueous system is the safety for the end user, with PVA being used as the gelling agent due to its ubiquity and its water solubility. However, with the evidenced failure over time the search for further, low hazard, electrolytes is of paramount importance. In section 5.2, four benign electrolytes are evaluated, these include: two LoSalt® solutions, an isotonic sports drink and an energy drink. For the best performing electrolyte two natural gelling agents (agar agar and κ-carrageenan) were investigated for gel electrolytes. These electrolytes are completely harmless to the end user and the wider environment. It is seen that a 1 M LoSalt® (KCL and NaCl blend) performs comparatively to more traditional electrolytes and can be made into a gel electrolyte through the inclusion of κ-carrageenan. The final research theme, presented in section 5.3, looks to move away from the low voltage window (which hampers all aqueous electrolytes), through the investigation of an organic electrolyte. This section presents an organic electrolyte using a 'green' solvent that significantly increases the lifetime and and increases the energy density of the devices produced in chapter 4 by nearly an order of magnitude.

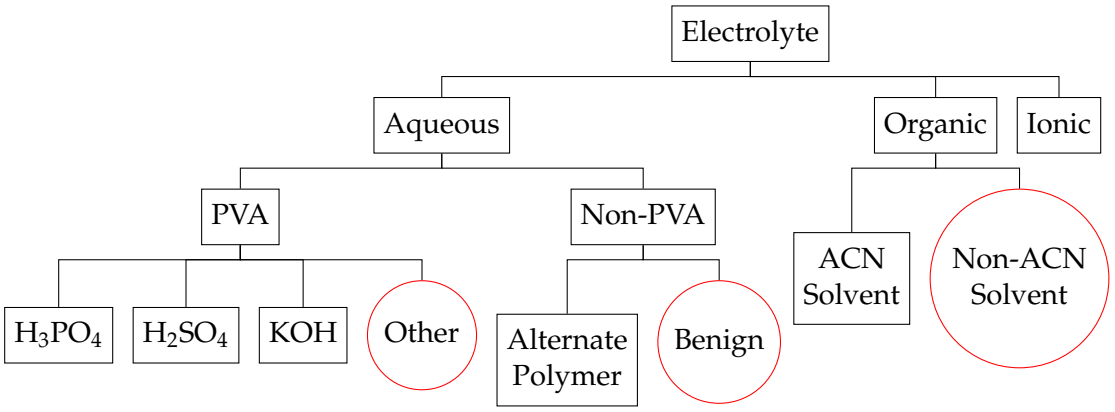

FIGURE 5.1: The possible electrolytes for textile supercapacitors. Research within the community has predominantly focused on aqueous electrolytes (H_3PO_4, H_2SO_4 or KOH) with a PVA gelling agent. This work has focused on three new areas of research: non-traditional aqueous PVA electrolytes, edible aqueous electrolytes and non-acetonitrile organic electrolytes (highlighted in red).

TABLE 5.1: Comparison of the three primary electrolyte families of supercapacitor electrolytes

Electrolyte	Potential Window (V)	Pros	Cons
Aqueous	1 - 1.23	• High conductivity • Non-flammability • Lower cost	• Low potential window • High solvation • poor absorption by hydrophobic textiles
Organic	2 - 2.5	• Higher potential window • Commercialised	• Lower conductivity • Flammability of some solvents • Sensitivity to water
Ionic	4.5	• Highest potential window • Low solvation • Low volatility	• Immaturity • Low conductivity • High viscosity

Alongside the research into the different electrolytes, this chapter presents characterisation methodologies that are not seen within the e-textile community (such as long duration voltage hold testing), strengthening the evaluation of the electrolyte performance.

The work within this chapter has been presented in-part in three publications [199, 230, 231].

5.1 The Trouble with PVA

Where chapter 4 focused on the carbon electrodes of the TSC, this chapter focuses on the electrolyte, and particularly in the long term behaviour, stability and practicality in real-world devices. Chapter 4 demonstrated the excellent performance of the YP80F carbon in comparison to the other two carbon, and the literature. However, under observation, older TSCs were visually different to freshly made ones, appearing a lot drier and more rigid. This drew concern over the long term performance of the device. As such, the initial investigation into the electrolyte was an ageing study. Ageing studies of TSCs have been seen in literature, such as the work of Bharathidasan *et al.* [232], Lee *et al.* [108] and Luo *et al.* [233]. Bharathidasan was investigating the addition of nanoparticles to extend the voltage capability of their aqueous electrolyte (as discussed further in section 5.3). They evaluated how the electrolyte aged over a 60 day period. However, this study focused solely on the electrolyte (in particular the stability of the nanoparticles in within the electrolyte) and did no age the devices themselves. The testing of the zeta potential, conductivity and visual appearance of the electrolyte is of significant interest but it does not give information on electrolyte retention, potential parasitic reactions or electrochemcial degradation of the electrode and substrate when exposed to the electrolyte for an extended period of time. Lee *et al.* [108] produced a packaged, stretchable planar device, with a mixed solvent organic electrolyte with PMMA polymer binder. Over a 30 day period, there appeared to be negligible change in the Nyquist plot for the device after being stored in air between measurements. However, this was certainly a secondary study within the work and given the vast difference between these devices and those documented here, direct

comparison is challenging. Luo *et al.* [233] produced an all textile packaged device, with a H_3PO_4||PVA electrolyte. This device is the closest to that of this work, and stored the device for $\sim$ 4 months between testing. At a 20 $mV.s^{-1}$ scan rate the device saw an almost 50% reduction in specific capacitance. However, there is no discussion on how the device was stored between testing and there is no incremental measurements over the testing period.

Inspired by the above studies, but differing, the author's single layer TSCs were evaluated at intervals over a 30 day period. Significantly, the devices are also unpackaged to gain a better understanding of the intrinsic properties of the electrolyte within a device setting. Additionally a number of 'test' environments were also investigated, designed to mimic typical real-world use cases for an e-textile.

5.1.1 Ageing Experimental Design

The devices and electrolyte were produced as discussed in Chapter 4. The produced devices were separated into 5 groups and stored under different environmental conditions, including one control condition of staying within the Swagelok test cell for the duration of the testing. The full list of the groups and associated storage conditions can be seen in table 5.2.

TABLE 5.2: Storage conditions for the assessment of failure mechanisms during ageing of ADP||PVA based textile supercapacitors.

Identifier	Storage Description
A	Stored within a Swagelok test cell, under compression.
B	Stored within a sealed container.
C	Stored between glass plates under compression from two Neodymium Iron BoronNdFeB permanent magnets
D	Stored within a sealed container in a fridge.
E	Stored as B but dipped into deionised water for 5 minutes and then dried at 50°C for 10 minutes before testing.

As discussed, group A is acting as a control group. Group B is to mimic storage in ambient but in a close container to limit any external interference. Group C is to investigate if pressure is a driving mechanism to failure. Group D is mimic exposure to colder climates and to limit evaporative loss of the electrolyte. Group E is to mimic a wash cycle and is the most extreme of the testing environments considering the test is on un-packaged devices.

The characterisation utilised for this study was GCD and EIS tests. They were both delivered as discussed in Chapter 3 with the GCD being performed between 0 and 0.8 V at a charge/discharge current density of 0.25 mA.cm^{-2} and the EIS being performed between 1 and 250 kHz at a 10 mV amplitude. 0.25 mA.cm^{-2} was chosen as the testing current to limit any degradation of the devices due to testing which may mask any degradation due to ageing. The capacitance was calculated via equation 3.1 and the ionic conductivity was calculated via quation 3.9 with the substrate samples being 0.785 cm^2 in area and 430 μm thick.

5.1.2 Results & Discussion

Figure 5.2, presents the length of time each device survived (defined as the time at which the devices could no longer be characterised) in the differing storage methods. As expected, the control test in the Swagelok cell had the longest lifetime. However, what is surprising is the discrepancy between that and the other methods. This may imply that the device held in the Swagelok and the devices that were stored externally may have different failure methods. This is supported by visual inspection of the devices post testing with group A having no visual difference whereas group B to E were clearly dryer. The dryer appearance of the devices implies some form of dehydration, interestingly though, even the device stored below ambient conditions showed this behaviour. This is however attributed to crystallisation of the polymer base at these lower temperatures. To explore the dehydration of the aqueous electrolyte, plain cotton samples were impregnated with electrolyte and the ionic conductivity investigated over a five day period. The results can be seen in figure 5.3, with the conductivity seen to fall to 0.00 S/m within three days (a nearly five orders of

magnitude drop). The other storage mechanisms were not selected for further testing due to the poor results. The ionic conductivity is shown to sharply decrease over the initial five days, from 9.4 $S.m^{-1}$ to 0.001 $S.m^{-1}$ before stabilising at this level. This significant drop is attributed to dehydration, drastically reducing the ionic transport and leads to the total failure at day 5 due to the high internal resistance. This demonstrates the unsuitably of this electrolyte for this application outside of a laboratory environment, something not covered in the work of Yong *et al.* [56].

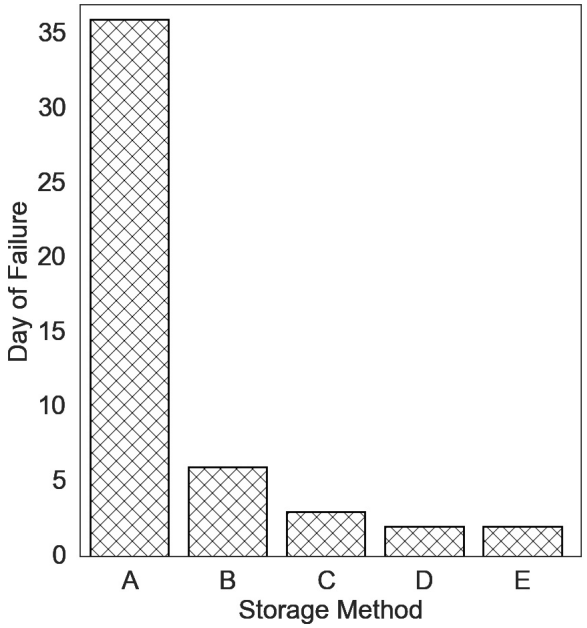

FIGURE 5.2: The date of failure of the textile supercapacitors stored in each of the five storage methods.

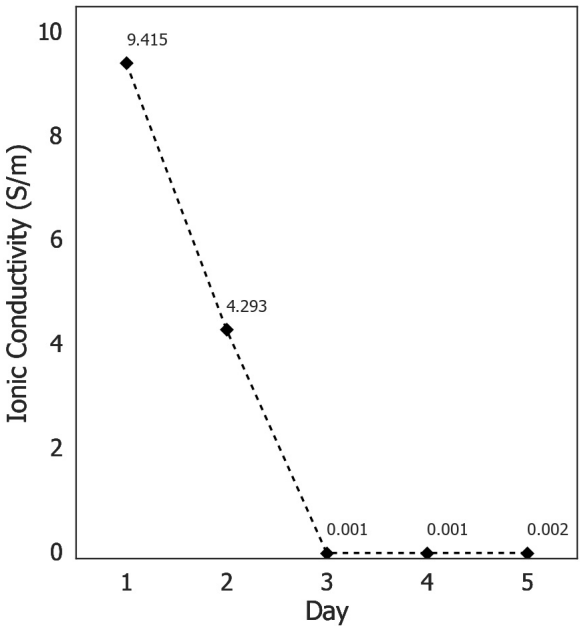

FIGURE 5.3: The ionic conductivity degradation of the PVA||PVA electrolyte over a period of 5 days, stored in a sealed vessel. The points have a standard deviation of $\pm$ 0.02 S/m from 5 repeat measurements.

The control group (A)'s performance was investigated further, with the 30 day results shown in Figure 5.4. It was observed that the device goes through a number of regions. In this case, it is seen there is an initial stabilisation period (common for electrochemical systems), a steady region where the variation around the mean (C/C_0 = 1.1) was $<$9% and finally the unstable region which saw a 100% increase in capacitance on day 35 but then total failure at day 36. This instability is hypothesised to be due to carbon migration through the textile substrate, with the variability being seen as the breaking and remaking of electrical networks within the bulk structure of the electrode. To confirm that these results were not caused by the repeated testing, a group A device underwent 450 GCD cycles (figure 5.5), the same number as the total number of measurements in the first study. Within these tests, the capacitance fell by $<$2% showing that the ageing of the device was a degradation mechanism and not an artifact of the characterisation.

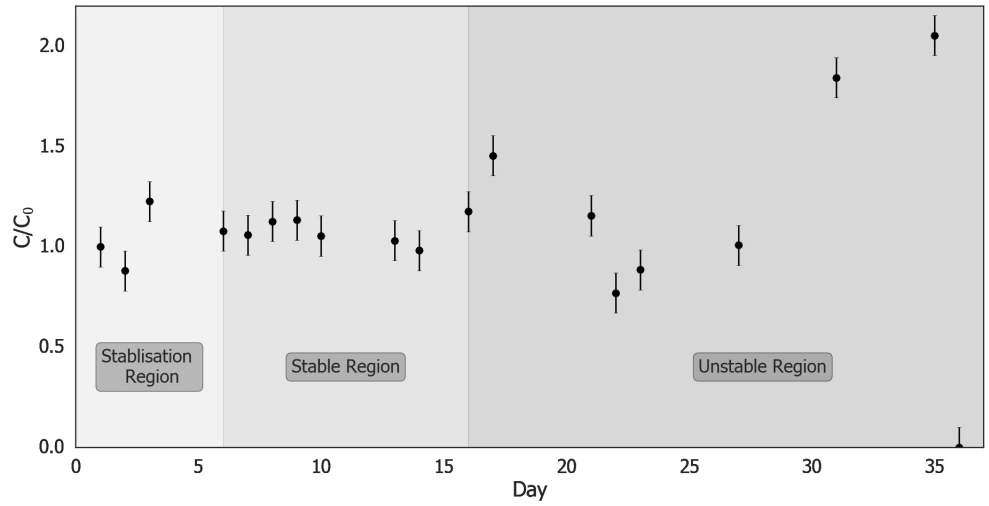

FIGURE 5.4: The capacitance retention of the device stored within the Swagelok. Each point is the average of 10 cycles, with the error calculated from the standard deviation

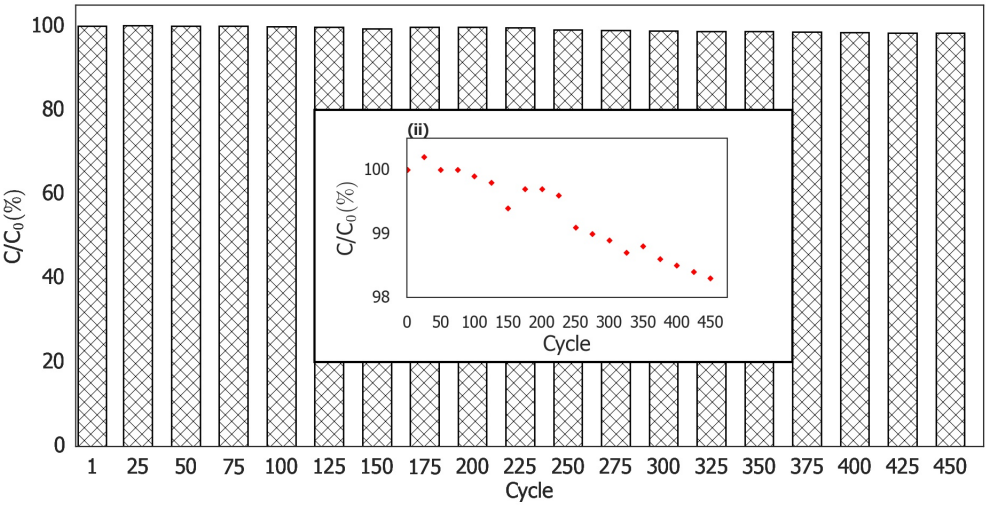

FIGURE 5.5: The capacitance retention over 450 cycles at 0.25 mA.cm^{-2}. The secondary graph (ii) is a magnified view of the retention, showing a <2% drop over these cycles.

These series of tests has shown the incompatibility of the ADP||PVA electrolyte for real-world devices. Even in the most controlled of environments, the devices produced failed after a month. The ethos of this thesis is to develop the TSC from a laboratory device to one that could be deployed in the a real-world power module and this electrolyte is not appropriate. Other works in the literature, such as Gao *et al.* [234], have also observed long term instability of PVA based devices. This significantly challenges the status quo of the communities understanding and the likelihood of commercial adoption of such devices. Though further work could be

undertaken to develop the PVA based electrolyte further, such as polymer crosslinking [235, 236], it was decided to transition away from aqueous PVA based gel electrolytes. The ubiquity, and ease of production of PVA is certainly attractive to the community but for this all textile, single-layer TSC it has been concluded to be inappropriate outside of the laboratory. Aside from the use of a fluidic ADP electrolyte for prototyping in section 6.3 and as a benchmark for section 5.2 this electrolyte will not be subsequently researched in this thesis.

5.2 Beyond PVA

With the analysis from section 5.1 it was seen that to develop the electrolyte portion of these TSCs beyond a laboratory device a non-PVA electrolyte had to be found. One of the rationales behind the use of aqueous electrolytes is the safety to the end user. However, one could readily argue that the commonly used electrolytes are not intrinsically safe in themselves, with all of them requiring advanced packaging to safeguard the user from irritation or harm. This has led to the investigation of low-hazard, benign electrolytes, inspired by the biomedical field.

5.2.1 Culinary Inspired Electrolytes

Taking inspiration from the works of Na *et al.* [237] and Wang *et al.* [238], this section presents the feasibility of food based electrolytes within TSC applications. In the work of Na [237], an Sodium Chloride (NaCl) and egg white based electrolyte was incorporated within a membrane to create a green, carbon-based, quasi-gel electrolyte supercapacitor; achieving an ionic conductivity of 7.6 $mS.cm^{-1}$ and capacitances of 214 $F.g^{-1}$ at a discharge current density of 0.2 $A.g^{-1}$. Wang [238] took the idea of a food based supercapacitor further and constructed a fully edible supercapacitor from cheese, seaweed, gold leaf, charcoal and Gatorade. The Gatorade electrolyte had an ionic conductivity of >2 $mS.cm^{-1}$ and the final device (with the addition of Monosodium Glutamate (MSG) in the electrolyte) had a capacitance of 129 $F.g^{-1}$. Other food based electrolytes were also presented (such as BBQ sauce, Monster

energy® drink and vegetable juices) and showed the viability of these electrolytes for real-world applications. The electrolytes being investigated in this section are Grenade Energy®, Euro Shopper isotonic drink and two solutions (0.5 and 1 M) of LoSalt® which is a reduced sodium table salt made from Potassium Chloride (KCl) and NaCl. The energy drink contains KCl, NaCl and magnesium citrate, while the isotonic drinks contains magnesium chloride, calcium chloride and potassium phosphate. For real world TSC applications the electrolyte must be in a gel, or gel-like, form. As such the best performing electrolyte was tested in a gel form via the addition of Agar Agar and κ-carrageenan. Agar Agar is a mixed polymer of agarose (linear polysaccharide) and agaropectin while κ-carrageenan is a singularly sulfated polysaccharide. Both are extracted from red algae and are commonly used within the food industry. Agarose has been demonstrated as a gelling agent for supercapacitor electrolytes in the work of Moon *et al.* [239] while κ-carrageenan has been used in bio-polymer electrolytes for zinc ion batteries [240]. To act as a reference for the performance of the edible electrolytes, TSC with ammonium dihydrogen phosphate (ADP) were constructed.

5.2.2 Experimental

The κ-carrageenan was purchased from *Sigma Aldrich* and the agar agar was purchased from *NKD Living*.

The electrodes were prepared as described in chapter 4. The 1 M and 0.5 M LoSalt® electrolyte solutions (with an assumption of a 2:1 ratio of KCl to NaCl) were prepared by dissolving 0.342 and 0.171 g of LoSalt® respectively in 5 ml of de-ionized water. The Euro Shopper isotonic drink was found to not be suitable upon purchase (with all devices produced with it as the electrolyte failing) and was reduced by 30% by weight via constant heating. The Grenade Energy® drink was left to decarbonate and was then used as purchased. A 0.5 M solution of ADP was produced by dissolving 0.288 g of ADP in 5 ml of de-ionized water. The gel electrolytes were produced by adding 0.52 and 0.67 g of the Agar Agar and κ-carrageenan respectively, to 5 ml of 1 M LoSalt solution under heating and constant stirring.

GCD was performed at charge-discharge currents 0.5, 1, 2 and 3 mA.cm^{-2} from 0 to 0.8 V and cyclic voltammetry was performed at 5, 25, 50, 100 and 200 mV.s^{-1} sweep rates across the potential window of 0 to 0.8 V. Electrochemical impedance spectroscopy measurements were performed from 10 kHz to 100 mHz with an amplitude of 10 mV for the full cell testing and 250 kHz to 1 kHz for the characterisation of the ionic conductivity of the electrolytes. The capacitance, energy density, power density and conductivity were calculated from equations 3.1, 3.4, 3.5 and 3.9 respectively.

5.2.3 Results & Discussion

The results for the four different electrolytes, and the ADP electrolyte, can be found in figure 5.6, 5.7 and 5.8. Figure 5.6 shows the EIS characterization of the full TSC as well as the individual conductivities of the electrolyte soaked cotton substrate. With a conductivity of 18.9 mS.cm^{-1} the 1 M LoSalt® electrolyte demonstrated the least resistance of the 4 edible electrolytes and outperformed the 0.5 M ADP electrolyte and electrolyte discussed in section 5.1. It also outperformed the conductivity of the both edible electrolytes from the work of Wang [238] and Na [237]. The isotonic drink was the least conductive and the magnification of the Nyquist plot in Fig 5.6B shows a much larger semi-circle in the high frequency region, indicating a reduced ionic transport.

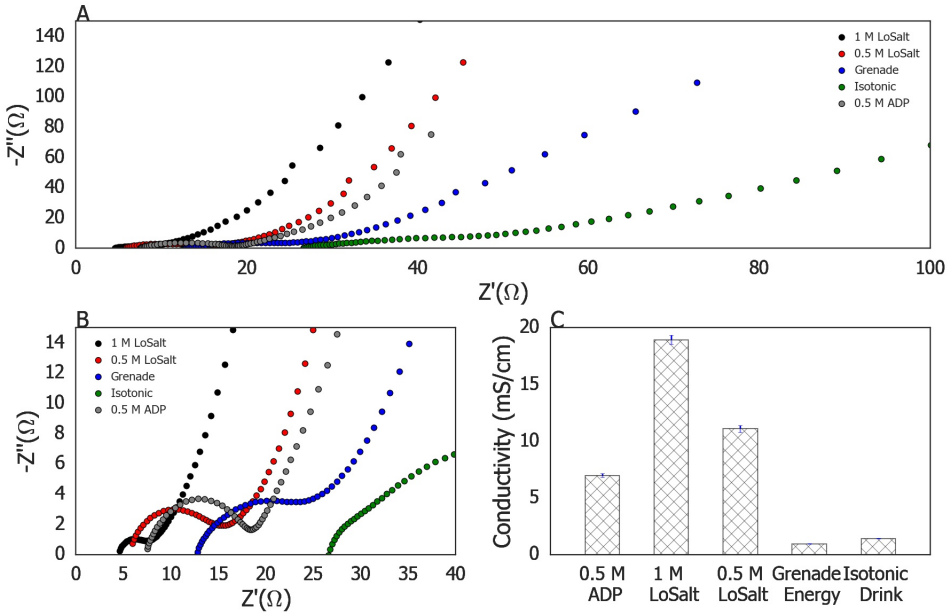

FIGURE 5.6: (A) Nyquist plot of the 4 edible electrolytes and the ADP electrolyte as full cells with (B) presenting a magnification of the high frequency region. (C) is the conductivity of the 5 electrolytes, the uncertainty is the standard error of 9 measurements over three samples.

Figure 5.7 shows the CV data for the electrolytes with a comparison of all of 5 of the electrolytes at 50 $mV.s^{-1}$ presented in figure 5.7f. As expected from the previous measurements in figure 5.6, the LoSalt® and ADP electrolytes showed superior performance with quasi-rectangular CV plots. The curves of the Grenade Energy® and the isotonic drinks resemble that of a rugby ball, demonstrating the effect of the increased resistance found in the conductivity study (figure 5.6). The LoSalt® TSCs showed a squarer shape than the ADP but the area contained within the curves were similar, and therefore having similar capacitances. This was confirmed by the GCD measurements.

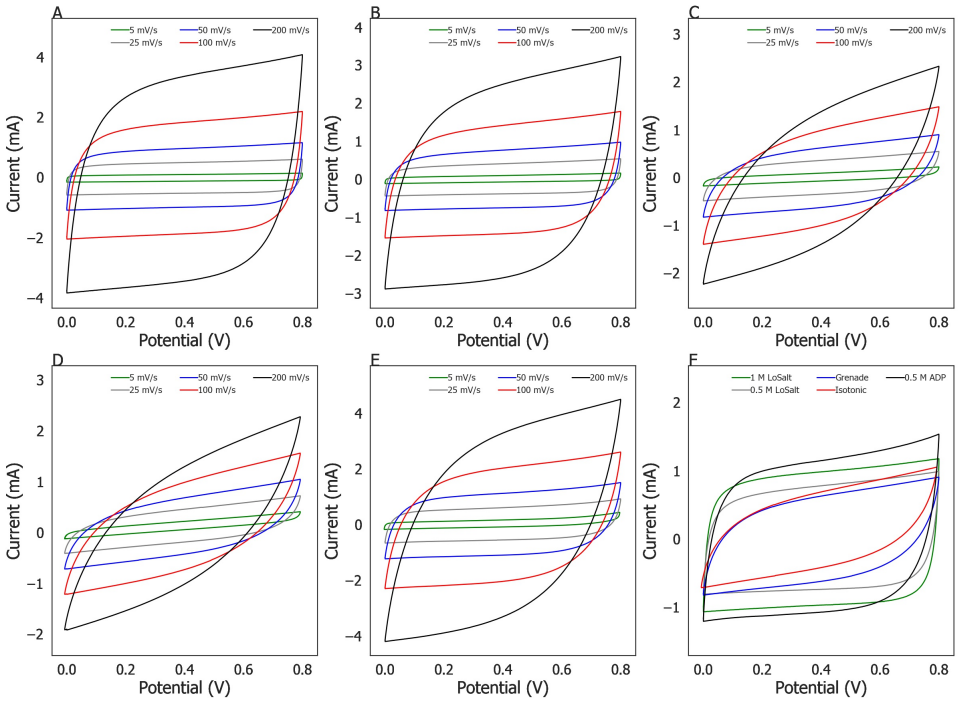

FIGURE 5.7: CV plots for the 5 electrolytes from 0 to 0.8 V at 5, 25, 50, 100 and 200 mV.s^{-1} sweep rates. (A) 1 M LoSalt® (B) 0.5 M LoSalt® (C) Grenade Energy ® (D) Isotonic Drink (E) 0.5 M ADP (F) is a comparison of all 5 electrolytes at 50 mV.s^{-1} sweep rate.

Figure 5.8 shows the GCD measurements of the differing electrolytes and the degradation of capacitance with increasing current density. The LoSalt® solution and the ADP show near symmetric triangular responses whereas the Grenade Energy® and isotonic drink electrolytes show rounding as they approach 0.8 V, showing the effect of the increased ionic resistances that were measured in figure 5.6, and an increase in the leakage current. The equivalent series resistance of these electrolytes (88 and 93 Ω respectively) was significantly higher that of the other electrolytes (1 M LoSalt® 19 Ω, 0.5 M LoSalt® 31 Ω and ADP 35 Ω). The 1 M LoSalt® electrolyte had the best performance at 0.5 mA.cm^{-2} with a capacitance of 25.7 mF.cm^{-2} and energy and power densities of 2.3 µWh.cm^{-2} and 0.2 mW.cm^{-2}. However, with increasing current density this dropped to 22.8 mF.cm^{-2} at 3 mA.cm^{-2} with the ADP electrolyte achieving 24.0 mF.cm^{-2} at 3 mA.cm^{-2}. When the mass of the activated carbon is taken into consideration instead of the area of the TSC the 1 M LoSalt® achieved a specific capacitance of 13.2 F.g^{-1}. This is lower than that reported by Wang or Na and shows that more work is needed to translate these biomedical based electrolytes into TSCs.

However, with no further improvements this TSC could power a low-power application such as the RFID tag presented in the work of Lemey *et al.* and is comparable to the calligraphy ink based device (36 mF.cm^{-2} Lam *et al.* [224]) and outperformed an activated carbon based device (20 mF.cm^{-2} Zopf *et al.* [225]) and the work seen in section 5.1.

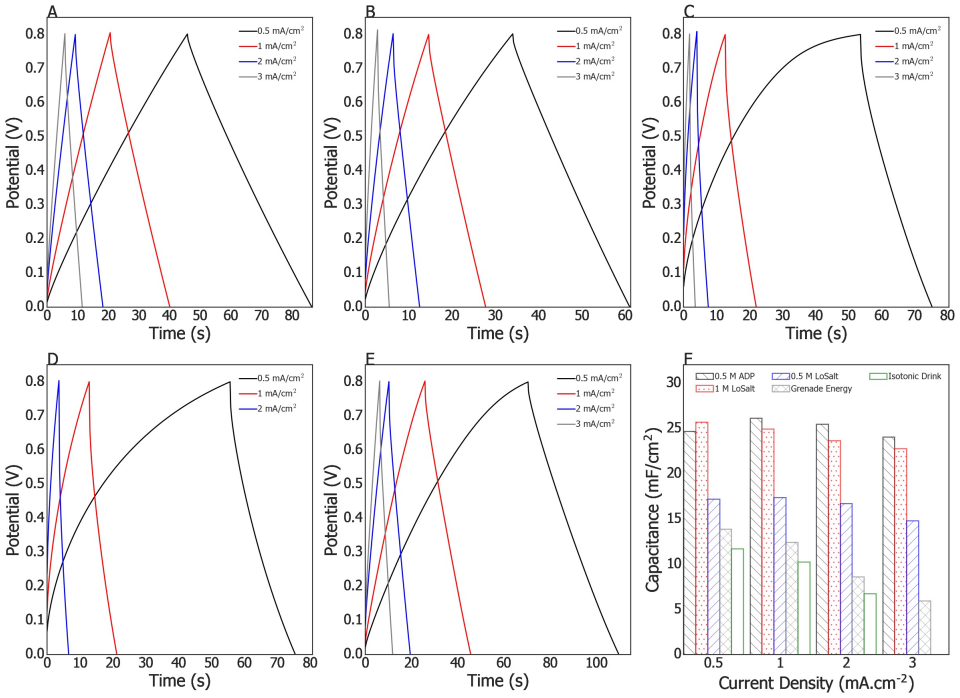

FIGURE 5.8: GCD measurements for the different electrolytes with charge-discharge current densities of 0.5, 1, 2 and 3 mA.cm^{-2}. (A) 1 M LoSalt® (B) 0.5 M LoSalt® (C) Grenade Energy® (D) Isotonic Drink (E) 0.5 M ADP and (F) is degradation in capacitance with increasing current density. The isotonic drink failed at the highest current density, thus only three results are displayed for 3 mA.cm^{-2}.

With the 1 M LoSalt® electrolyte achieving the highest performance it was selected to be made into a gel-like electrolyte. The GCD, CV and EIS results from this are presented in figure 5.9. The Agar Agar based LoSalt® gel electrolyte was found to be comparatively resistive with an ESR of 183 Ω, compared to 84 Ω for the κ-carrageenan based gel, and was not tested further. The increase in resistance between the fluidic electrolyte and the κ-carrageenan electrolyte can be seen in figure 5.9B and 5.9C, with significant curving in the CV plot and a much larger semi-circle in the high frequency region of the Nyquist plot; illustrating an increased bulk resistance of the electrolyte and a less optimal electrode-electrolyte boundary. However, the addition of the

κ-carrageenan only lowered the capacitance from 25.7 to 22.5 mF.cm^{-2} demonstrating its potential for real world TSCs.

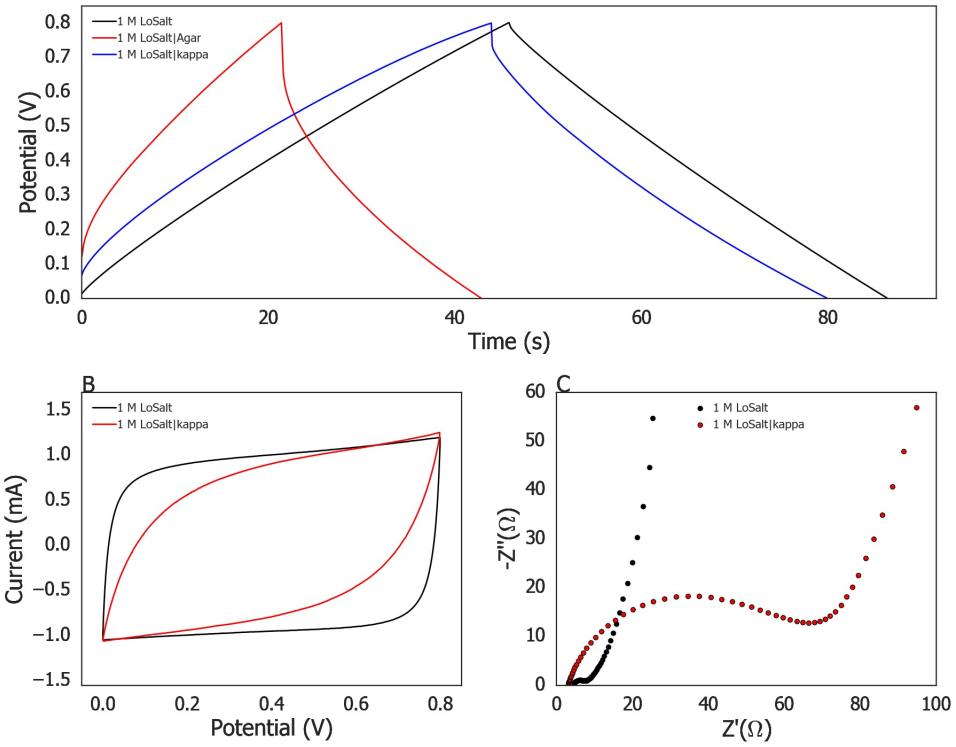

FIGURE 5.9: (A) GC plot of the 1 M LoSalt® electrolyte as a fluid and in the agar agar and κ-carrageenan gel form. (B) and (C) are the CV and EIS for the fluidic and κ-carrageenan gel devices.

The devices produced in this section certainly demonstrated the possibility of using truly benign electrolytes for TSC applications. The results of the 1 M LoSalt® with κ-carrageenan in fact out performed that of the best devices produced in chapter 4 (22.5 vs 21.0 mF.cm^{-2} at 0.5 mA.cm^{-2}). However, they still suffer from the low voltage potential of all aqueous electrolytes and would require many devices to achieve a high enough energy density and working voltage for the real-world applications presented in chapter 6. This requirement for low component number (for power module simplicity) means that though the devices improved upon the PVA based electrolyte it is still not enough and a mindset change is required.

5.3 Beyond Aqueous Electrolytes

The use of water as a solvent for aqueous electrolytes has distinct advantages, such as high ionic conductivity once the salt is added and improved safety for the end user as discussed previously in this chapter. However, the potential window of the aqueous electrolytes are restricted by the electrolysis voltage of water, 1.23 V. In practical applications this means multiple TSCs must be connected in series to achieve an appropriate voltage to operate with energy harvesters or the end use technology. This further limits the energy density by reducing the available capacitance as the total capacitance is the sum of the reciprocals of the individual devices. Wagih et al. [171], for example, had to connect three TSCs in series in their textile power module, driven by a RF-harvesting rectenna. While Dong et al. [163] incorporated two yarn TSCs in series in their triboelectric nanogenerator system, though proposed the use of up to four. With more devices comes more complexity and consideration must be taken over the balancing within the TSC string. To increase the operating window for aqueous electrolytes, groups have made use of additives, (such as Bharathidasan et al. [232] use of dispersed SiO_x nano particlescite) or asymmetric electrodes (such as Guo et al. [234] use of nitrogen doped carbon sheets and $CoNiO_2$). The SiO_x nanoparticles led to a three times improvement in the energy density, while the asymmetric electrodes increased the potential window of the KOH electrolyte to 1.5 V. However, these strategies again add complexity to the system.

As discussed in Chapter 2, organic electrolytes can achieve voltage windows as high as 2.8 V [241] but suffer from lower ionic conductivity and flammability of the solvents.This has led to the majority of TSCs with organic electrolytes being seen in yarn-type supercapacitors due to the inherent encapsulation provided during the production process. Choi *et al.* [105] used a $TEABF_4$ electrolyte with PC as the solvent. This asymmetric yarn had an exceptional voltage range, up to 3.5 V, and achieved a capacitance of 171 $mF.cm^{-2}$. Keum *et al.* [106] developed a symmetric, twisted-wire, yarn supercapacitor with a lithium perchlorate electrolyte with a dual solvent of PC and ACN. This device had a voltage window of 1.5 V, achieving a capacitance of 5.23 $mF.cm^{-2}$. Park *et al.* [107] also made use of a $LiClO_4$ electrolyte with a dual

solvent, within their TSC-biosensor device. Importantly, this device was not a yarn and was constructed as a multi-layered device, with further encapsulation used as a barrier between the end user and the ACN/PC solvent. This TSC had a maximum operating voltage of 2 V but was found to be optimal at $\sim$ 1.4 V and achieved a capacitance of 33.8 mF.cm^{-2}. It is clear that the benefits of organic electrolytes, namely, high energy density and large operating potential, warrants further research focus than has been currently seen in the literature.

5.3.1 Tetraethylammonium Tetrafluoroborate

This section presents a novel organic electrolyte, one which makes use of Dimethyl Sulfoxide (DMSO) (considered a green solvent [242]) as the solvent instead of ACN or PC. Much like the work of Choi [105], $TEABF_4$ has been chosen as the salt and polyacrylamide (PAM) will be the polymer element. $TEABF_4$ was chosen as the electrolyte salt, not simply due to good results seen in literature but also due to good ion radii size matching with the carbon pore widths. Within the electrolyte, the TEA^+ ion is the largest with a bare ion radii of $\sim$ 4 Å (estimated from a number of papers with possible quoted values within the range 0.339 – 0.425 nm [243, 244]), when one considers the solvation shell (which could double the size of the ion [245]) the pore size distribution and ion size are seen to be highly compatible, with the predominant ion sizes approaching the length scale of the ions. It is widely seen (and discussed further in chapter 2) that a gel polymer electrolyte is beneficial for TSCs, with the polymer helping to retain the liquid element, both in terms of reducing wicking throughout the bulk of the textile and to reduce evaporation. Polyvinyl alcohol (PVA) has been seen as the polymer of choice for many groups, owing to its solubility in water and ubiquity. However, previous work in this chapter demonstrated catastrophic ageing (total failure after 3 days) of the TSCs made from a PVA based electrolyte. Gao *et al.* [246] also demonstrated poor ageing of PVA based systems, attributed to dehydration of the electrolyte. The electrolytes were shown to crystallize with age, leading to a higher activation energy barrier for the ion transport. Whereas, PAM based electrolytes have shown good stability over time [141] and have also been successfully realized in other electrochemical systems [247–249]. The performance of

the electrolyte will be benchmarked directly against previous works seen in Chapter 4 to compare against an identical electrode system, as well as the wider community. Importantly, absolute performance will not be the only test and a true ageing study will also be performed to investigate the ageing of an un-encapsulated device.

5.3.2 Experimental

The electrolytes were prepared in similar ways. For the $TEABF_4|_{PAM}$ electrolyte, 0.125 g of PAM was initially allowed to soak in 4 ml of DMSO overnight before being heated under constant stirring via a magnetic bead set at 400 rpm until fully dissolved. Once fully incorporated, a 2 ml solution of $TEABF_4$ and DMSO was added dropwise with the direct heat turned off but the stirring continuing. This was allowed to cool to room temperature. For the 0.1, 0.5 and 1 M electrolyte solutions 130, 650 and 1300 mg of $TEABF_4$ was used respectively.

All devices underwent electrochemcial characterisation as detailed in chapter 3, with the exception of the peak voltage voltage increasing from 0.8 V to 2.0 V to account for the increased solvent breakdown volatge of the organic electrolyte. The CV measurements were performed within the potential window of 0 – 2.0 V at scan rates of 5, 25, 50, 100 and 200 $mV.s^{-1}$, while the GCD measurements had a maximum voltage of 2.0 V and current densities of 0.25, 0.5, 1, 1.5, 2 and 3 $mA.cm^{-2}$. The EIS measurements were performed over the frequency range of 250 kHz – 0.1 Hz with a voltage amplitude of 10 mV. The ionic conductivity of the electrolytes was characterised as described previously within this chapter and as desmonstrated by Huang *et al.* [250] and He *et al.* [197] by soaking, under vacuum, samples of the cotton (0.785 cm2, 430 µm thick) in the electrolyte before housing between stainless steel electrodes within a Swagelok cell to perform the EIS measurement. The conductivity is calculated from equation 3.9 The electrochemical stability of the electrolyte was characterized through a potentiostatic hold measurement at 2.0 and 2.4 V, with GCD cycling every 10 hours. The performance of the aged device was characterised via GCD at 1 $mA.cm^{-2}$ with the device stored in air at 0 V in between measurements. The storage of the un-encapsulated device in air, under ambient conditions, was to

demonstrate a worst case ageing and would be expected to be less severe in a packaged system.

Mechanical bending of the devices is the reserve of Chapter 6 and has not been considered within this work.

5.3.3 Results & Discussion

Electrochemical properties of the 0.1, 0.5 and 1 M electrolytes ($TEABF_4\|PAM_{0.1}$, $TEABF_4\|PAM_{0.5}$ and $TEABF_4\|PAM_1$) are presented in figure 5.10. Figure 5.10A-F show that all three of the electrolytes behave very much as expected for EDL supercapacitors. The GCD curves (Figure 5.10A-C) demonstrate symmetric isosceles shaped profiles, with varying voltage drops at the point of current reversal. The voltage drop is associated with the ESR of the devices and was found to decrease with increased molar concentration (from 210 Ω at 0.1 M to 55 Ω at 1.0 M). These ESRs are lower than that of the devices produced in chapter 4, even though the the electrolyte is organic, compared to aqueous and is attributed to better wetting of the electrodes, see figure 5.11. The higher ESR in the device made from the 0.1 M electrolyte caused instability at the highest discharge currents and limited the characterization to 2 $mA.cm^{-2}$. The CV curves (Figure 5.10D-F) show smooth, curved rectangular shapes with no obvious redox peaks. These curves are much squarer than those observed in figure 4.13 (especially the SXU and GSX carbons), suggesting a much improved performance and stability compared to the devices produced with the ADP electrolyte. Figure 5.10G shows the conductivity of the electrolyte impregnated cotton substrate/separator. The conductivity is seen to increase with increasing molarity, however, doubling the molarity from 0.5 to 1 M only saw an increase of 0.6 $mS.cm^{-1}$. Figure 5.10H and 5.10I present the capacitance decay with increasing current density and the Ragone plot (respectively) for all three molarities. It can be seen that the $TEABF_4\|PAM_1$ device achieved an excellent areal capacitance of 34.0 $mF.cm^{-2}$ at 0.25 $mA.cm^{-2}$, reducing to 28.3 $mF.cm^{-2}$ at 3 $mA.cm^{-2}$. Though there is a decay in the overall capacitance due to the inability to utilize the full surface area of the electrode at the faster measurement rates, the device still performed well at higher current

densities. The $TEABF_4||PAM_{0.5}$ electrolyte achieved ∼78% of this performance with a maximum capacitance of 26.5 $mF.cm^{-2}$ and the $TEABF_4||PAM_{0.1}$ achieving ∼52% of the 1 M performance, with a maximum capacitance of 17.6 $mF.cm^{-2}$. The $TEABF_4||PAM_1$ electrolyte is seen to have an exceptional energy density for its class (18.9 $\mu Wh.cm^{-2}$ at 0.24 $mW.cm^{-2}$ or 15.8 $\mu Wh.cm^{-2}$ at 3.2 $mW.cm^{-2}$), with this attributed to the good capacitance and large operating potential window.

When these results are compared against the work in chapter 4 it can be seen that the new electrolyte not only improves the energy density, due to the increased operating voltage, but also improves the capacitance. The differences in performance can be seen in table 5.3. As can be seen, there is a ∼44% increase in capacitance but a 9x increase in energy density. The power densities (both average and peak) are also significantly increased, owing to the higher energy density and lower ESR respectively. The small variation in the peak power density between the 0.25 $mA.cm^{-2}$ and 3 $mA.cm^{-2}$ measurements is due to small variation in the ESR, but are equivalent when the uncertainty is taken into account. This immediately demonstrates the significance of this electrolyte and shows its benefits for simple carbon/carbon devices. High energy densities and good capacitances can be reached without the need for structured/exotic materials or difficult manufacturing processes. The increase in capacitance seen between the two works is attributed partially to better ion-pore size matching but mostly to the wetting of the electrode by the electrolyte. With the electrolyte better soaked into more of the pores, there will be better ion mobility, especially important at higher rates of charge-discharge.

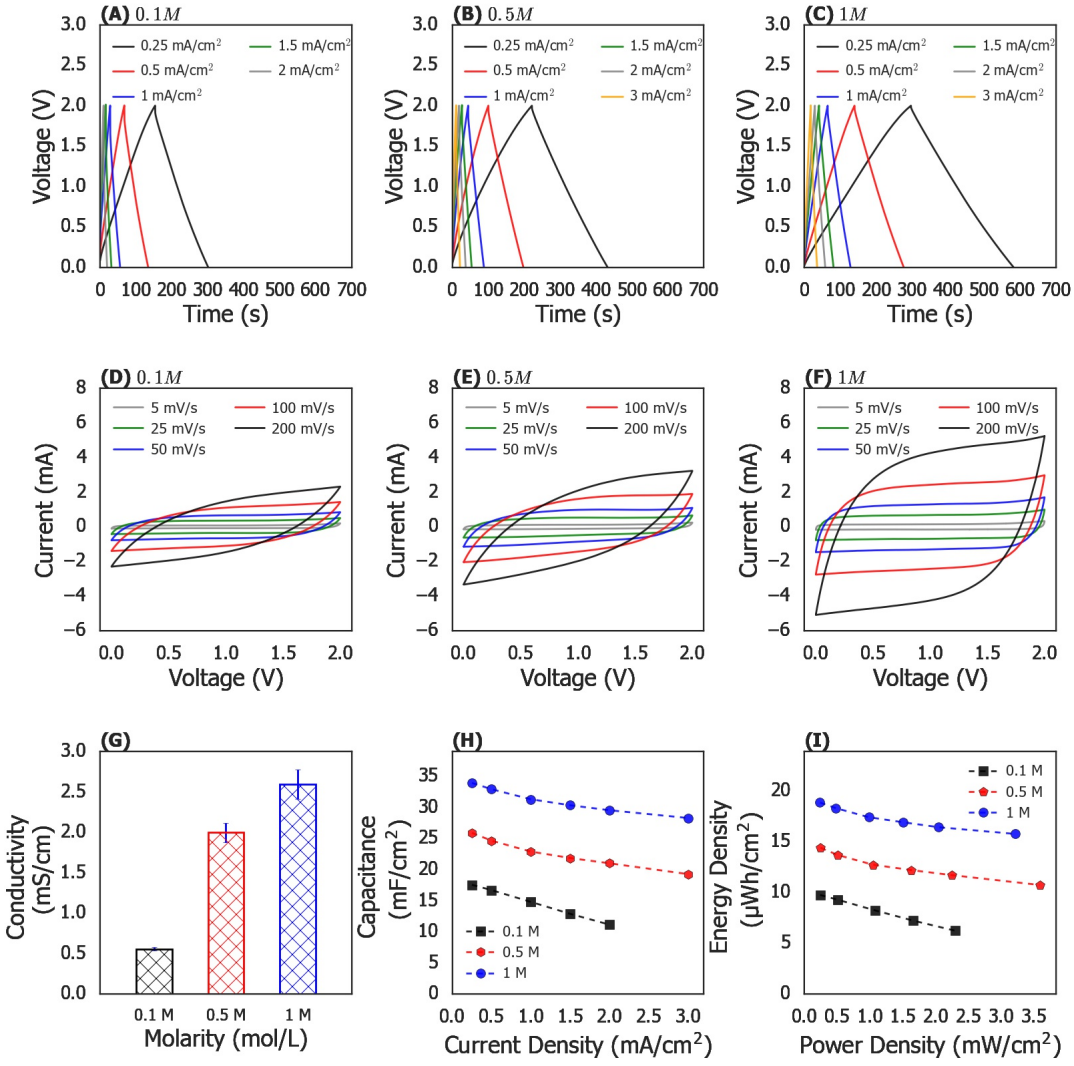

FIGURE 5.10: Electrochemical properties of the activated carbon/activated carbon TSCs with varying molarities of the $TEABF_4$||PAM electrolyte. GCD curves of (A) 0.1 M, (B) 0.5 M and (C) 1 at current densities of 0.25 – 3 $mA.cm^{-2}$. CV curves of (D) 0.1 M, (E) 0.5 M and (F) 1 M at scan rates of 5 – 200 $mV.s^{-1}$. (G) is the ionic conductivity of the electrolyte soaked cotton substrate characterized via EIS, there error bars are the standard error from three samples with 5 repeats each. (H) Capacitance degradation with increasing measurement current (I) Ragone plot of the devices made from the three molarities of electrolyte.

TABLE 5.3: Areal capacitance, energy density, power density and peak power density for devices made from ADP and $TEABF_4$ electrolytes at 0.25 $mA.cm^{-2}$ charge/discharge current density. The uncertainty is the standard deviation of 5 repeats.

Electrolyte	Areal Capacitance ($mF.cm^{-2}$)	Energy Density ($\mu Wh.cm^{-2}$)	Power Density ($mW.cm^{-2}$)	Peak Power Density ($mW.cm^{-2}$)
YP80F_4_90	23.6 ± 0.05	2.1 ± 0.1	0.1 ± 0.03	0.6 ± 0.7
$TEABF_4 \| PAM_1$	$34.0 \pm 0.03^{\epsilon}$	18.9 ± 0.01	0.24 ± 0.01	23.0 ± 0.08
	$28.3 \pm 0.03^{\zeta}$	15.8 ± 0.04	3.22 ± 0.01	24.8 ± 0.2
$TEABF_4 \| PAM_{0.1}$	17.6 ± 0.02	9.8 ± 0.01	0.24 ± 0.01	6.1 ± 0.01
$TEABF_4 \| PAM_{0.5}$	26.5 ± 0.01	14.7 ± 0.01	0.24 ± 0.01	9.0 ± 0.02

ϵ values from 0.25 $mA.cm^{-2}$ measurment, ζ values from 3 $mA.cm^{-2}$ measurement.

Figure 5.11 shows a qualitative evaluation of the wetting of the electrodes with the PVA‖ADP electrolyte (Figure 5.11(Left)) and the $TEABF_4$‖PAM electrolyte (Figure 5.11(Right)). For both electrodes a single drop of the electrolyte was dropped onto the surface and the image taken 5 seconds after that. As can be seen, the water based electrolyte forms a bead on the surface of the electrode while the organic electrolyte almost immediately wets the full electrode. There is clearly some hydrophobicity, probably caused by the rough surface of the electrode. This means greater effort is required to fully impregnate the electrode with the electrolyte and longer time is required for the TSC to be under vacuum for the aqueous system. Even then, it is difficult to know whether all of the small pores are fully filled with the electrolyte.

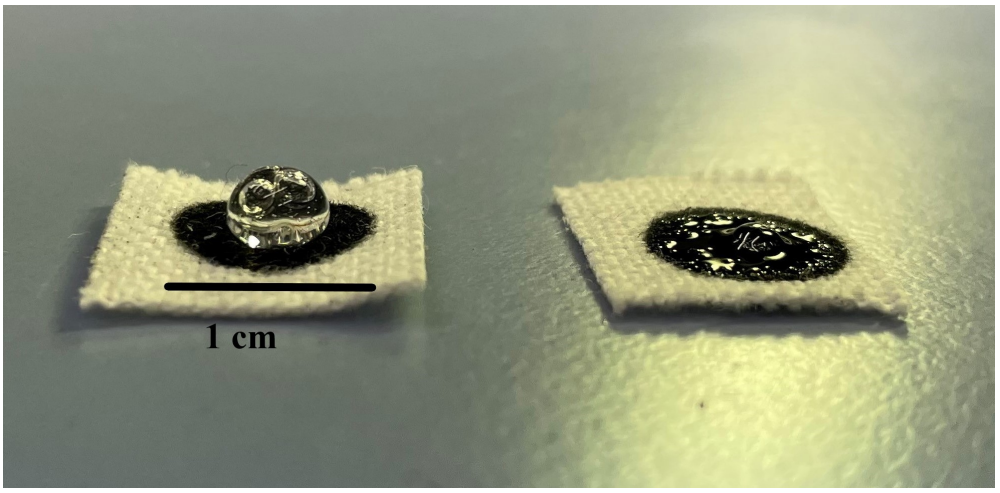

FIGURE 5.11: Image of a qualitative wetting experiment between aqueous ammonium dihydrogenphophate||PVA electrolyte (Left) and $TEABF_4$||PAM electrolytes (Right) on two representative carbon electrodes produced identically as those used for the devices in this work.

To further evaluate the 1 M electrolyte, devices were characterised via GCD at a cut off voltage of 2.2 and 2.4 V, with the coulumbic efficiency and energy density shown in Figure 5.12A and B respectively. Increasing the voltage threshold significantly increased the energy density, from 18.9 to 31.4 μWh.cm^{-2}. However, as the voltage limit increased the coulombic efficiency at the lower current levels decreased, with a minimum of 91.4% at 2.4 V while under a 0.25 mA.cm^{-2} charge/discharge current density. This reduction of coulombic efficiency for textile supercapacitors is not uncommon at the lower current levels (for example, in the work of Yang *et al.* [80], their activated carbon coated fiberglass cloth had a charging time of $\sim$300 s compared to a total charge cycle of $\sim$565 s at 0.5 mA.cm^{-2}). This is often attributed to impurities within the device that are challenging to remove at the laboratory scale and higher intrinsic losses when compared to traditional supercapacitors. However, it is also seen in more traditional supercapacitors that use activated carbon electrodes, as in the work of Cheng *et al.* [251] where their activated carbon/nano-carbon traditional supercapacitor achieved a coulombic efficiency of 93% at 0.5 A.g^{-1} rising to $\sim$100% only at 10 A.g^{-1}.

To investigate the effect of this efficiency drop on the long term behavior of the device an ageing study and two voltage hold tests were performed (at 2.0 and 2.4 V). Voltage hold tests are seen as more rigorous for determining the stability of a supercapacitor

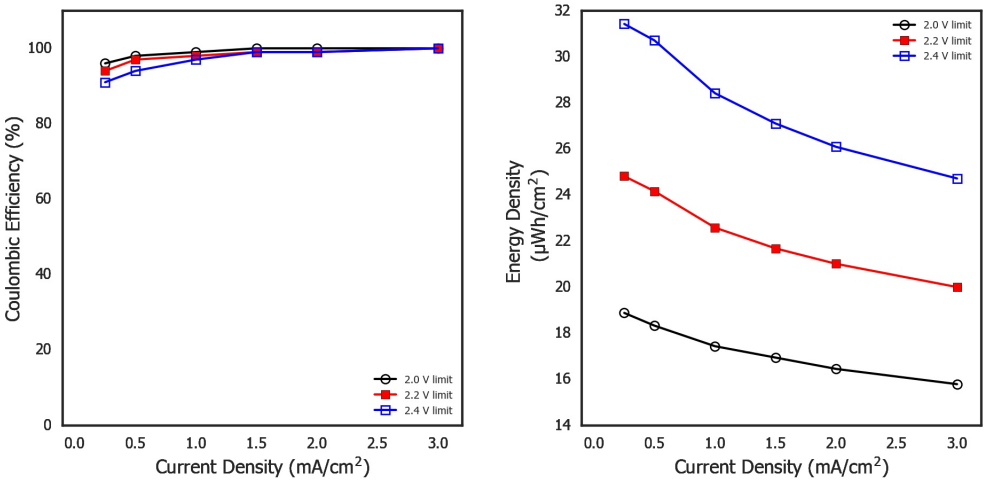

FIGURE 5.12: Coulombic effiency and energy density of the 1 M devices when characterised via GCD measurements at cut off voltages of 2.0, 2.2 and 2.4 V.

compared to CV or Linear Sweep Voltammetry (LSV) testing as the device is held at the operating point, instead of temporarily entering the partially unstable voltage region during cycling tests (as discussed in the works of Ruschhaupt *et al.* [252] and Weingarth *et al.* [253]). Figure 5.13 shows the result of 90 hours of hold testing at the two voltage limits. Both voltages see an initial drop after 10 hours before the 2.0 V measurement plateaus above 70% capacitance retention for the remaining 80 hours, with an ESR increase of $<$40%. After 1 week of relaxation the device was re-measured and found to have retained 94% of the original capacitance, indicating the degradation was not permanent and unlikely to be decomposition of the electrolyte. The 2.4 V device however falls to an unstable plateau around 27% capacitance retention and a 360% increase in ESR, returning to a 54% capacitance after 1 week of rest. To the authors knowledge the use of the voltage hold characterization technique is the first for textile supercapacitors, and should be used more frequently within the community. These tests showed that though the device can operate at 2.4 V, long term exposure to this voltage level could have significant effects to the device's lifetime and the wearable technology it is attached to, whereas, the device appears stable if operated up to 2.0 V.

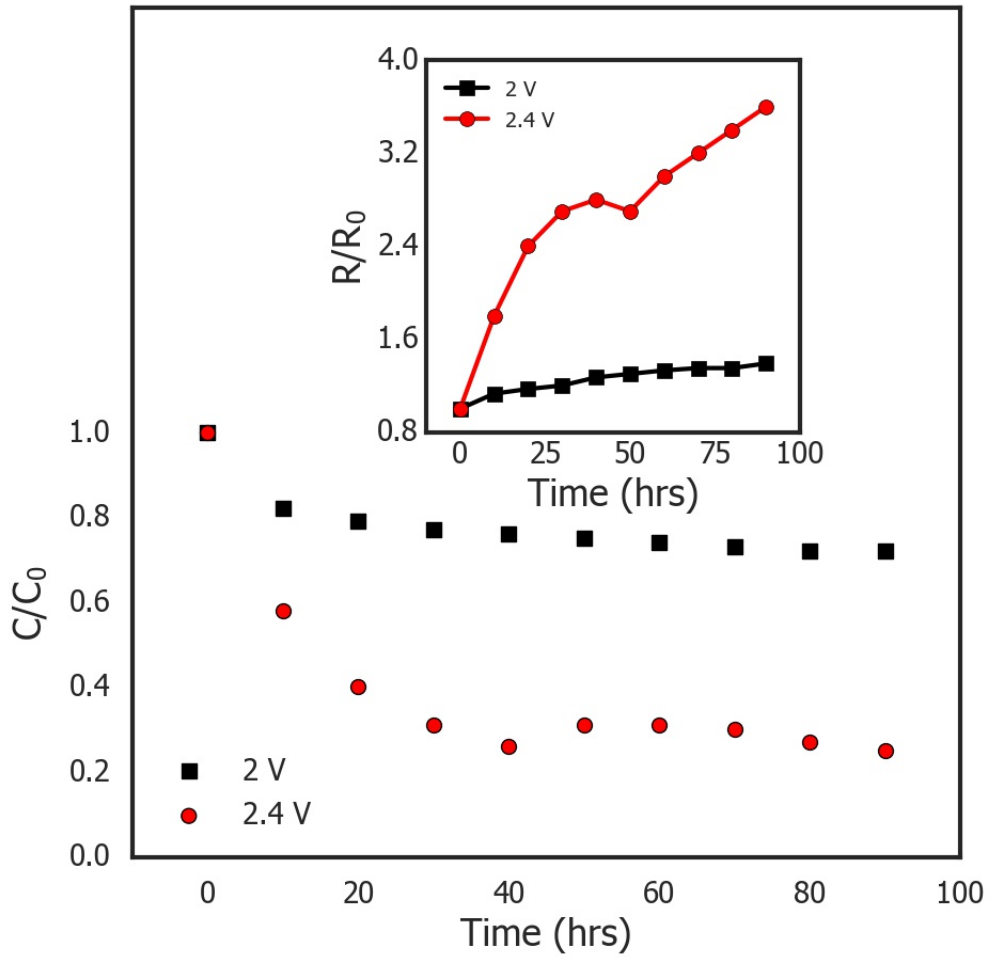

FIGURE 5.13: Capacitance degradation during voltage hold testing at 2.0 and 2.4 V over a 90 hour period. The insert is the ESR of the devices characterized over the same cycles as the capacitance. All values are the average of five cycles.

Finally, ageing was chosen instead of cycle stability (to assess the stability of the electrolyte) as the effect of ageing is rarely characterized but has a more fundamental effect on the device, and is more representative of the real world usage, complementing the voltage hold testing. The device was tested after 1 day, 2 days, 1 week, 2 weeks, 1 month and 2 month intervals and between tests was stored in air. The GCD results can be seen in Figure 5.14, and further EIS analysis shown in Figure 5.15. It can be seen that the device was still operational after the two month period, with a capacitance retention of 48%, while the coulombic efficiency fell from 97% to 88%. When this is compared to section 5.1 this is a vast improvement ($>$ 19 times) as previous devices failed (zero capacitance) after only three days of being

exposed to similar ageing tests. The equivalent series resistance was found to rise from 56 Ω to 254 Ω over the period of investigation and suggests a partial dehydration of the electrolyte, leading to an increase in resistance. This is supported by the EIS measurements that show only a small increase in the initial resistance of the device (the Z' intercept) but a large increase in the electrolyte resistance. The high frequency region of the EIS plot shows a depressed semi-circle, which is best modelled as a constant phase element and resistor in parallel, sometimes referred to as a Cole element. The CPEs impedance is seen in equation 3.8 with the α_{CPE} ($0 < \alpha_{CPE} < 1$) term representing the behavior of the device with 0 being a resistor and 1 an ideal capacitor. Within the device this value dropped from 0.66 to 0.49 and the parallel resistance rose from 39.4 Ω to 685 Ω. Though ageing is seen within the device, it is far less catastrophic than that seen in previous studies and sets a good benchmark for future electrolytes and TSC devices. The use of both ageing and voltage hold testing are seen as complementary techniques and when combined give a greater understanding of the electrochemical and temporal stability of the TSC.

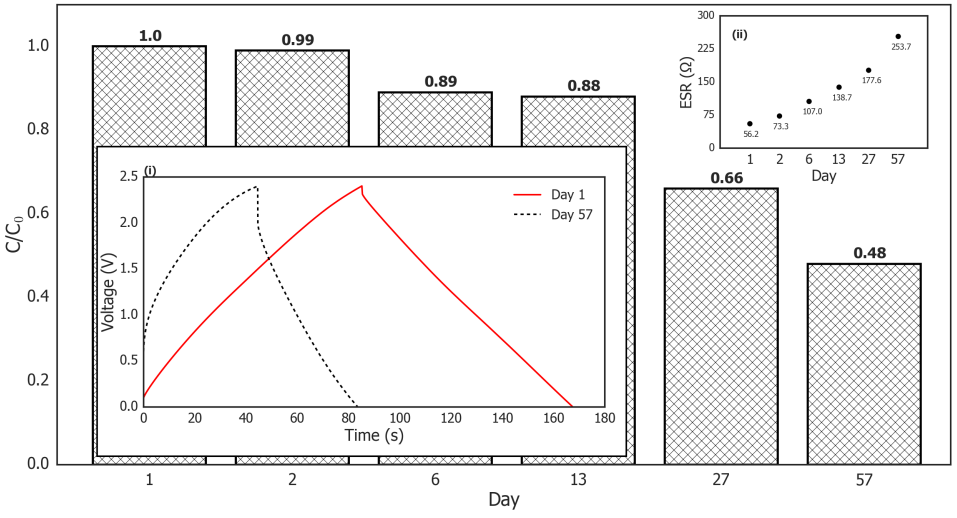

FIGURE 5.14: Normalised capacitance determined from GCD testing of a $TEABF_4||PAM_1$ device at 1 $mA.cm^{-2}$ at intervals over a two month period. The insert (i) is the GCD trace on the first day versus that of the 57th day. Insert (ii) is the ESR change over the two month period.

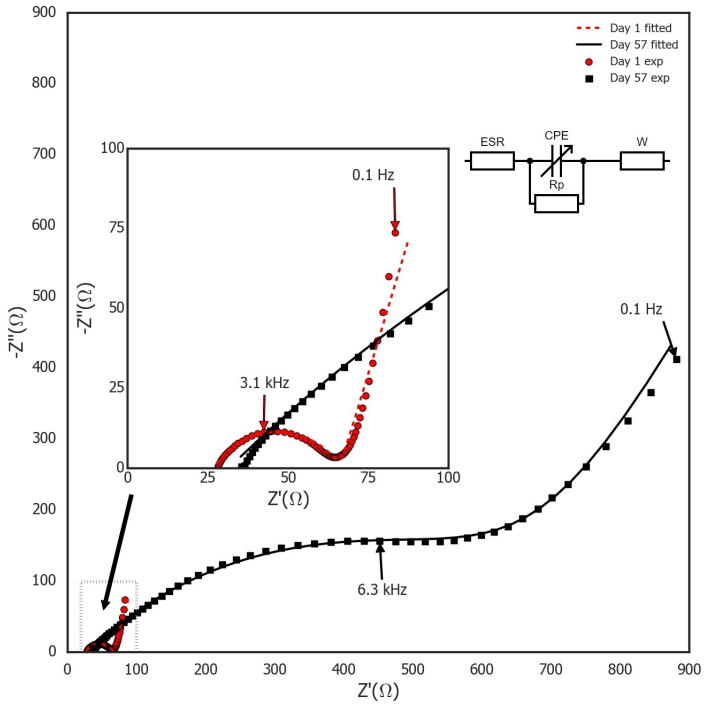

FIGURE 5.15: EIS measurement for the $TEABF_4||PAM_1$ device at day 1 and day 57. The insert is a magnified view of the graph over the range 0 – 100 Ω with the fitting model also shown on the figure.

Direct comparison with previous work of similar devices is important to validate the absolute improvement in the device performance due to the electrolyte alone, however, comparison with devices within the community is also required. Table 5.4 shows a detailed comparison with similar devices while Figure 5.16 benchmarks the device against the results of the wider community, not just porous carbon devices. Though similar devices achieved higher capacitances than the values reported in this work, the energy densities were lower due to the exceptional performance of the $TEABF_4||PAM$ electrolyte compared to those used in the other works. From Figure 5.16 it can be seen that the devices produced within this work are comparable to the highest energy density devices seen in literature. It is only the work of Shang *et al.* [254] and Yang *et al.* [113] that shows significant improvement but these make use of soft hybrid scaffolding and multi-walled carbon nanotubes-reduced graphene oxide (respectively). These are expensive techniques and materials compared to the ones used within this study, questioning their viability for real-world devices.

TABLE 5.4: Areal capacitance, energy density, power density and peak power density for devices made from the $TEABF_4$ electrolytes compared to advanced devices seen in the literature.

Reference	Electrode Material	Electrolyte	Areal Capacitance ($mF.cm^{-2}$)	Energy Density ($\mu Wh.cm^{-2}$)
Yang *et al.* [80]	Activated carbon and asphalt	H_2SO_4‖PVA	85.4	7.6
Zhang *et al.* [79]	Activated carbon	KOH‖PVA	153	21.2
Tan *et al.* [255]	Carbon nanofibers	KOH	150	15
Xiao *et al.* [78]	Cotton derived porous carbon	H_2SO_4	38	3.4^{α}
	Cotton-flax derived porous carbon	H_2SO_4	97	8.6^{α}
This work	Activated carbon	$TEABF_4$‖PAM	34.0^{β}	18.9
			39.3^{Γ}	31.4

α Calculated using the potential window 0.8 V., β Peak voltage of 2.0 V, Γ Peak voltage of 2.4 V.

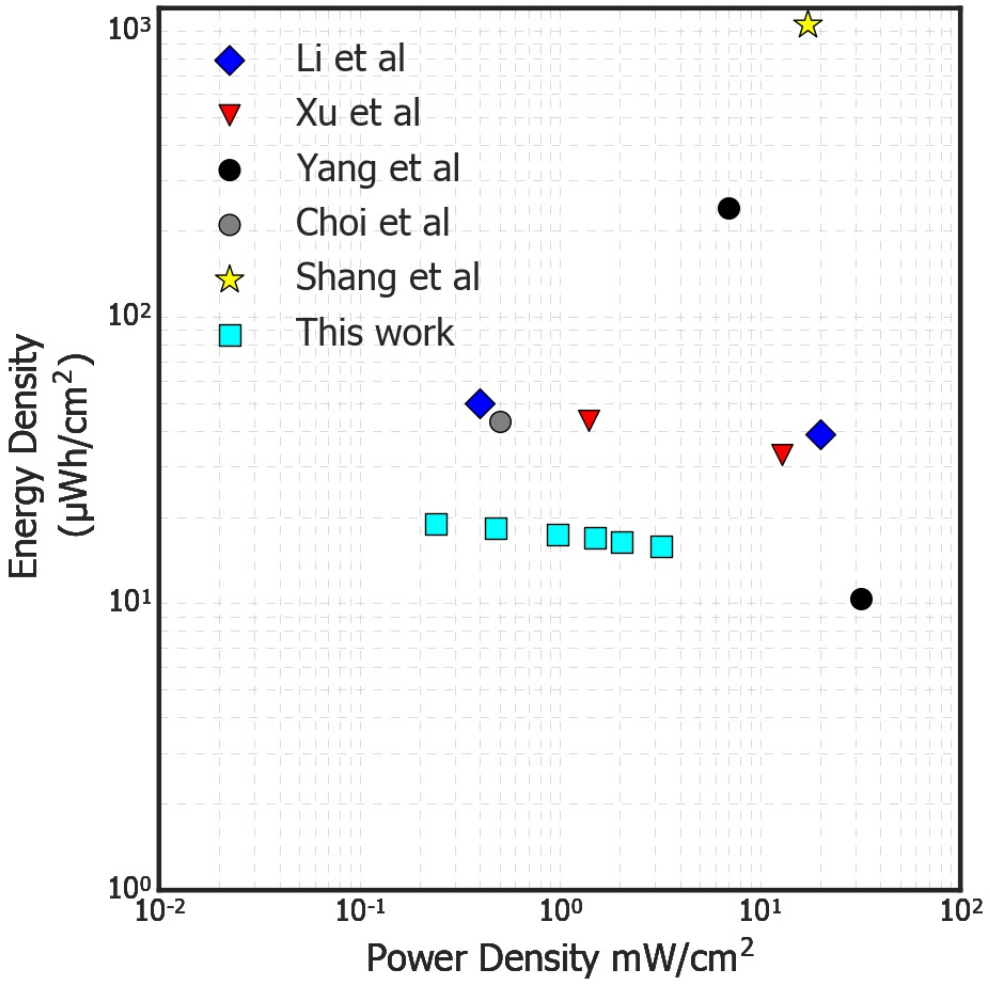

FIGURE 5.16: Ragone plot of high energy density textile supercapacitors. Data taken from Li *et al.* [256], Xu *et al.* [257], Yang *et al.* [113], Choi *et al.* [105] and Shang *et al.* [254]

5.4 Conclusion

This chapter has presented a wide breadth of research covering electrolytes for TSC applications. Within the chapter, a logical progression has been seen starting with benchmarking of the ageing of a traditional aqueous electrolyte, followed by the investigation of PVA-free benign electrolytes before finishing on the development of a low hazard organic electrolyte. The work has continuously, and purposefully, stepped away from common consensus within the e-textile community and has made use of rarely seen characterisation techniques in a novel combination.

Section 5.1 benchmarked the performance of the laboratory level electrolyte used in

chapter 4. Within this section it was shown that the electrolyte is unsuitable for future TSC applications due to poor ageing due to dehydration of the electrolyte. As such, the research was forced to move onto other options.

Section 5.2 investigated aqueous benign electrolytes inspired by the biomedical research field. Four edible electrolytes were investigated, with the 1 M LoSalt® electrolyte showing excellent performance with a capacitance of 25.7 $mF.cm^{-2}$ at 0.5 $mA.cm^{-2}$. With the addition of κ-carrageenan a gel electrolyte was develoepd with a capacitance of 22.5 $mF.cm^{-2}$ at 0.5 $mF.cm^{-2}$ which was greater than that of the original ADP||PVA electrolyte (21.0 $mF.cm^{-2}$). Progression in performance of the TSCs was seen but arguably not enough for the real world power module envisaged in chapter 6 but certainly has some niche applications.

Finally, section 5.3 developed upon the previous sections, and by taking inspiration from traditional supercapacitor research developed a low hazard, high voltage organic electrolyte that can be produced in a one-pot methodology. Devices produced from this electrolyte were found to have a capacitance of 34.0 $mF.cm^{-2}$ and an energy density of 18.9 $\mu Wh.cm^{-2}$, a 9x increase compared to the best results in chapter 4. The use of voltage hold and ageing testing enabled the evaluation of a safe operating window (2.0 V) and demonstrated the improved ageing compared to the ADP||PVA electrolyte. This combination of measurements give far greater detail on the stability of the devices (both electrochemically and temporally) compared to LSV or CV tests, and should be more widely adopted by the community.

Though further work in this area is certainly required beyond this thesis, the research within this chapter has answered or progressed all of the original research questions laid out in chapter 1.

Chapter 6

Practical Applications

The integration of TSCs into full e-textile systems is a paramountly important area of research to enable the wider adoption of the technology. To better integrate the devices into future systems knoweldge of how they will react under real-world conditions and how compatible they are with the other systems within the e-textile.

This chapter presents simulated real-world testing (temperature and physical deformation) and the effect it has on the electrochemical performance of the unpackaged carbon-$TEABF_4$ devices. It is important to understand the performance of unpackaged devices to give a benchmark to future encapsulation research and to understand the performance in case of failure. It was found that the unpackaged devices were still operation after 1750 mechanical bends and were still safe to operate after both bisect cutting and puncturing.

Following this, the devices were integrated into a proof of principle energy harvester - energy storage power module. When considering a real world demonstrator it is important to have an application in mind. Many works have focused on movement driven e-textiles, making use of triboelectric or ferroelectret energy harvesters for sport or commercial markets. However, for this thesis, the target application is a smart bandage for point of care treatment and monitoring in healthcare. As such, movement will be limited, reducing the benefits of a mechanically induced energy harvesters. Therefore, an RF rectenna harvester has been selected for this work. Though lower

peak power than other harvesters, in a built environment such as a hospital, there are an abundance of RF signals (routers, communications, etc) which can be harvested while the patient is static, charging the supercapacitor while they are being monitored. TSCs are seen as an advantageous energy store for such an application due to their conformity to the body, breathability and integrated nature. Though packaging is out of the scope of this thesis, it is imagined that only the active material would have to be packaged, reducing the amount of non-breathable packaging as compared to a traditional small pouch cell (the devices within this thesis are only 0.785 cm^2 each). Additionally, if one were to use a small pouch cell then that is an additional discrete component that must be integrated into the bandage, where discrete components are challenging to attach to flexible substrates due to cracking at the joint [258]. The manufacturing process of spray coating the textile (allowing high manufacturing volumes with little modification to the process) is favourable compared to that of the battery industry. For point of care treatment, e-textiles are seen as beneficial over common place wearables such as a smart watch due to their lower cost, discretion for the patient and integration. If a bandage or patch is already required then functionalising the required medical device is favourable as compared to having to attach another item to the patient. Additionally, e-textiles can be tailored specifically to the required biomonitoring [259].The work presented shows that a literature leading efficiency was achieved through the integration of a flexible rectenna and series of TSCs. This concept was progressed through to minimal viable product through the use of the devices discussed in Chapter 5, with this power module capable of powering a Bluetooth data transfer application.

The work within this chapter has been presented in-part in three publications [171, 260, 261].

6.1 Durability

The durability of TSCs is rightly a concern for real-world applications. The device must last at least as long as the lifetime of the garment it is integrated into. Traditionally, the lifetime and 'durability' of the device has been demonstrated

elctrochemically through repeated cycling. However, external stresses (in the form of bending, twisting or impact) on the device can also degrade the lifetime. Often, the flexibility (and therefore implicitly the durability) is characterised through bending of the device at various angles [80, 103, 114, 127, 142] or through bending cycling [79, 101, 113, 116, 117, 120, 123, 124, 129, 132, 139, 141]. Manjakkal *et al.* [133] stands out amongst the literature through the use of a bending radius, which not only bends the device but also imparts an element of contact and abrasion not seen in two-point bending tests.

This section presents the electrochemical results from a series of bending tests through the use of a mandrel to mimic both bending and contact abrasion. Additionally to the bending tests, samples were tested before and after cutting and puncturing. For real-world devices it is imperative that the TSC is safe and will not catastrophically fail in the case of mechanical damage.

6.1.1 Experimental

The devices tested in this section were prepared as described in Chapter 5. The electrochemical properties were characterised via GCD testing set the peak voltage to 1.8 V. An *Autolab* potentiostat was used for the characterisation. This voltage was selected to be under the normal operating window determined in Chapter 5 to remove any potential measurement artefacts (or degradation) from the cycling. Electrochemical testing was performed before and at intervals throughout the bending process, up to 1750 bends, and 5 measurements were taken at each time.

The testing was all completed within one day, with no device being left half tested overnight. It was decided to space out the testing to evaluate whether there was any influence on the mechanical durability due to the time between manufacture and test. As such, device 1 was tested on the day of production, device 2 was tested 2 days after manufacture (kept within the electrolyte during this time) and device 3 was tested 1 month after manufacture (again, kept within the electrolyte during this period).

The mechanical bending was performed using an in-lab bending set up (Figure 6.1). The sample was housed within a stitched pocket and clamped at either end via to 3D printed jaws. Within the pocket, the TSC was wrapped in a loose polymer film to avoid any electrolyte wicking into the polyester pocket. One end of the textile pocket was attached to a a sliding platform, which was driven by a stepper motor. The other end was attached to a 100 g tension weight. The stepper motor was controlled through a pre-programmed Arduino, which controlled the bending frequency to 1 Hz. The travel of the sliding platform was set as to allow the TSC within the pocket to start and end each cycle completely off of the mandrel. The mandrel's radius was 10 mmm.

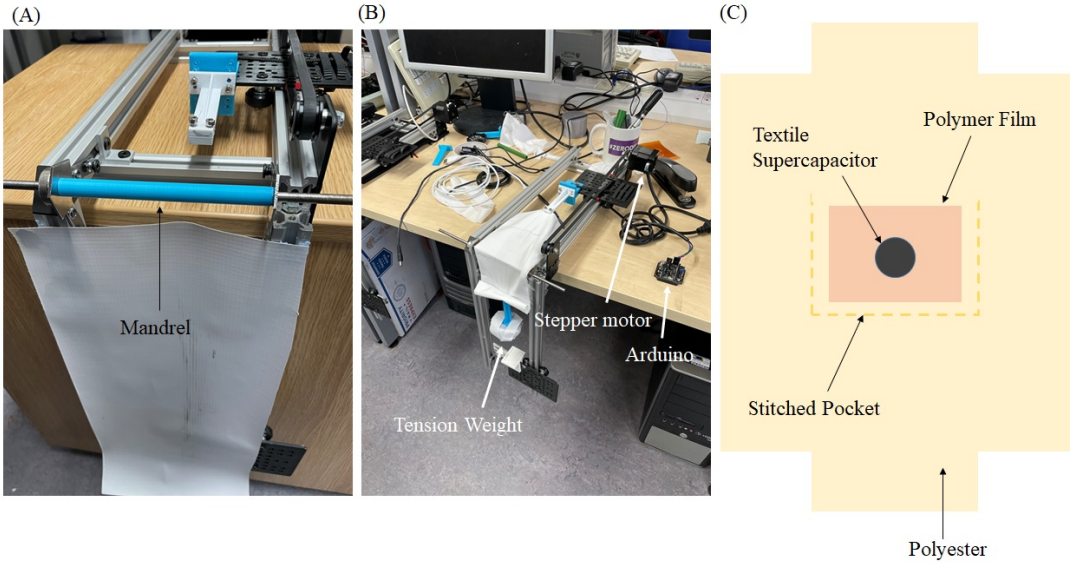

FIGURE 6.1: Images and schematic of the test set up for the mechnical bending. (A) Front view of the 10 mm radius mandrel and attachment point. (B) Loaded test rig detailing the stepper motor, 100 g tension weight and Arduino control board. (C) Schematic of the stitched polyester pocket used to house the TSC during bending.

To evaluate whether mechanical damage would lead to a catastrophic failure, one sample was initially tested before being cut in half and then half again, testing each time with the same testing regime as the bending test, though the charge/discharge current was changed to maintain a nominal 1.5 $mA.cm^{-2}$ current density. A second sample was then punctured with a laboratory pick, with a conical frustum shaped tip. The sample was characterised before and after puncture.

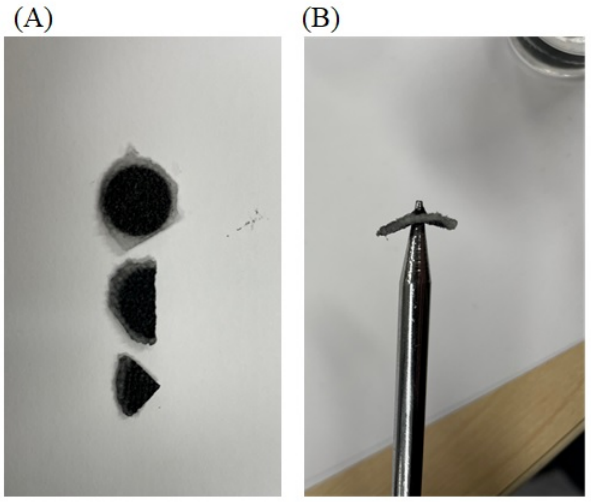

FIGURE 6.2: Images of the cut and punctured devices characterised during the safety investigation. (A) The half and quarter samples post cut in reference to a pristine reference TSC, samples are 10 mm diameter. (B) Punctured sample with the tip of the pick clearly protruding through the sample.

6.1.2 Results

The capacitance degradation of the three samples can be seen in Figure 6.3. On average there is 20% drop in capacitance over the first 50 bending cycles and a 40% drop over the first 200 cycles. After this the capacitance degradation plateaus before falling below 50% after 1750 cycles. This is matched by an increase in R/R_0 from 1 to 1.2 after 50 cycles and 2 after 200. After 1750 bending cycles R/R_0 was 3. The initial loss in performance is attributed to a shearing of the outer layers of carbon from the bulk electrode. This is supported by the images taken before and after bending (Figure 6.4) where the carbon has smeared into the pristine fabric surrounding the deposited electrode. However, the carbon that seems to separate from the bulk of the electrode is not lost but seems to form new conductive paths, hence the chaotic nature of the results (particularly seen in device 3, after 250 cycles). It is additionally interesting to note that though all three devices share similar initial performance (with a starting capacitance variance of ± 1 mF.cm^{-2}) and overall trends, they behave differently, implying that the detachment is not at a specific region of the electrode and further work is required to fully elucidate the mechanism. This would take the form of a batch to batch study, including a larger number of samples that was out of scope for this thesis. With the larger sample size more physical analysis could be undertaken

and the statistical relevance of unusual devices (such as device 2 can be established. This phenomena is similar to the results seen in Chapter 4 where the 6-layer electrodes seemed to not make use of all of the available active material. It is postulated that the inner layers form a coherent and well bonded electrode network, while the outer layers of carbon form a more fragile network which is easily detached during mechanical stress.

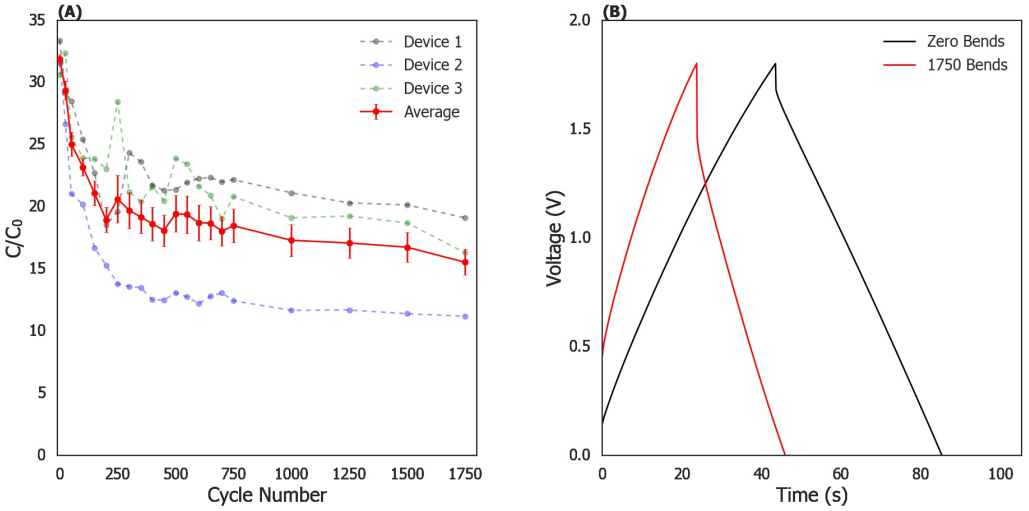

FIGURE 6.3: Capacitance degradation over 1750 mechanical bending cycles. (A) Capacitance degradation for device 1, 2 and 3 (dashed) and the average of all three devices. The error bars are the standard error of 15 measurements at each point. (B) The GCD traces for the original device and then after 1750 bending cycles.

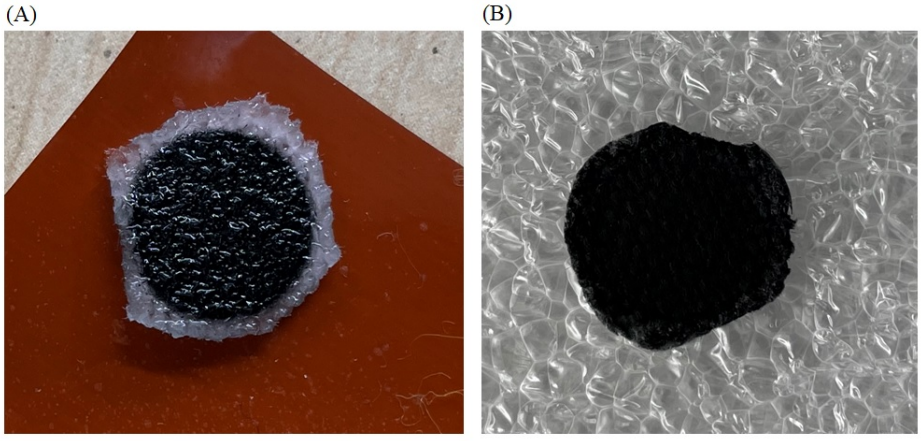

FIGURE 6.4: Pre and post images of one of the TSC's under test. In (A) there is a clear ring of pristine textile while in (B) that is no longer clear. Devices are 10 mm in diameter.

When the bending results are compared to literature they fall below the reported values. For example, in the work of Karami *et al.* [139] the device lost 11% of its

capacitance over 1000 bending cycles and in the work of Yang *et al.* [113] the capacitance rose after 10,000 cycles. However, it is important to note that the device developed by Yang was packaged whereas the device tested within this thesis was purposefully unpackaged, to gain an understanding of the inherent durability of the device. There is also a certain level of confirmation bias as only a subset of the publications seen in the literature quote bending results, leading to a comparison against the very best devices and not all devices. It is also challenging to compare the results from one bending test to another without replicating the conditions of both. It is the opinion of the author that a mandrel based bending test is more akin to the wear seen in real-world devices but more work is required to understand the differences between the testing set ups.

What this measurement has demonstrated is that the TSCs developed as part of this thesis can maintain operation in excess of 1750 bending cycles in their unpackaged form. Future work should develop packaging solution that limits this degradation through the application of compression [262] to maintain the integrity of the inner and outer electrode structure.

The cutting and puncture testing can be seen in Figure 6.5. All of the devices are seen to remain operational even after significant mechanical damage. The drop in performance during the cutting (16% for the half and 41% for the quarter) is attributed to stresses caused during the cut and an imprecise estimation of the actual surface area. The device that was punctured was still fully operational, demonstrating that the single layer design is resistant to carbon migration and subsequent short circuits during extreme mechanical damage.

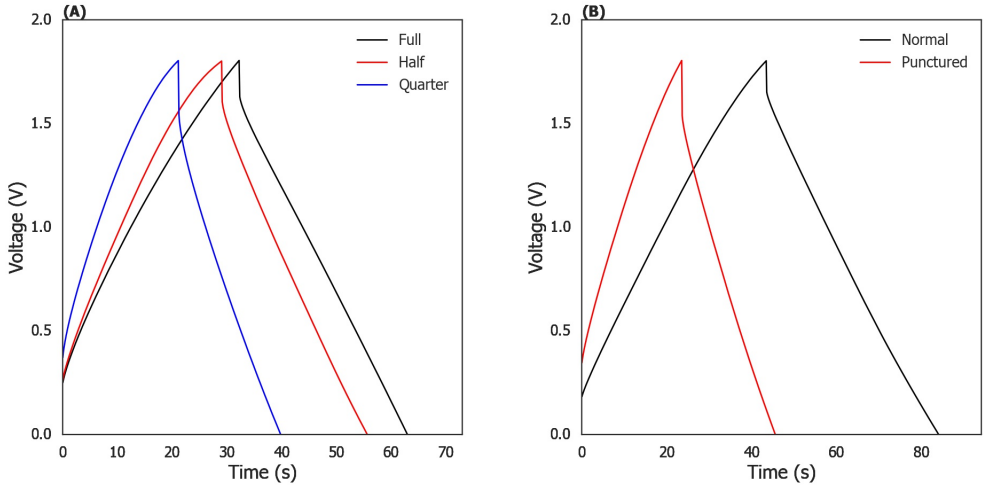

FIGURE 6.5: Electrochemical results pre and post cutting and puncturing. (A) Shows the results of the full device, cut in half and cut into a quarter. (B) Shows the results of a TSC before and after being punctured.

Testing of this kind is relevant for wearable devices that are likely to be exposed to environmental conditions which could cause such damage. The flexibility of textiles is a great advantage, however, the lightweight nature and flexibility makes it prone to damage and integrated TSCs must be shown to not catastrophically fail upon such damage. Within the literature, there is little documented research into the reliability of devices under extreme mechanical conditions. Wang *et al.* [263] stand out as their work does include cutting and puncturing. Their cuts, however, did not bisect the device. The puncture testing was also done with a fine needle ($\sim$60 μm) and was to evaluate the enhancement of breathability of the device, whereas in the aforementioned testing in this section the puncture testing was to evaluate mechanical resiliency. It is clear that more resiliency and safety testing is required within the community.

6.2 Temperature Stability

TSCs must be able to operate whereever the end user wishes to go. As such, the device will face different environmental conditions and must be able to still deliver the power management for the e-textile. In this section the temperature stability of the carbon-TEABF$_4$ devices is characterised using a modified Swagelok test cell. The devices were tested from room temperature up to 60°C to expose the devices to

temperatures well in excess of anything expected within real-world use. Unlike aqueous electrolyte based devices, which improve their electrochcemial performance with increasing temperature due to a reduction in charge-transfer resistance [264], organic electrolytes are shown to degrade with elevated temperature [265]. Considering the proximity to the human body (and its radiative heat) and the desired application of in-door use, near to an RF energy source (for built environment and office/work/military platform applications) characterisation below room temperature was not considered.

6.2.1 Experimental

The devices were produced as detailed in Chapter 5 and underwent the same electrochemical testing as detailed in section 6.1. The temperature measurements were made with a customised Swagelok cell (Figure 6.6) which allowed a thermocouple to be placed on the surface of the device during test, allowing for in-situ characterisation. To achieve this, a small hole was drilled through the length of the shortest current collecting rod, allowing the thermocouple to reach the interior of the test cell. Any gap was then sealed and the thermocouple secured in place. The customised Swagelok was placed within an oven and the temperature ramped slowly to allow for stabilisation. The temperature was held at each testing temperature and the device was allowed to soak for 10 minutes at the testing temperature (measured at the surface of the device) prior to testing.

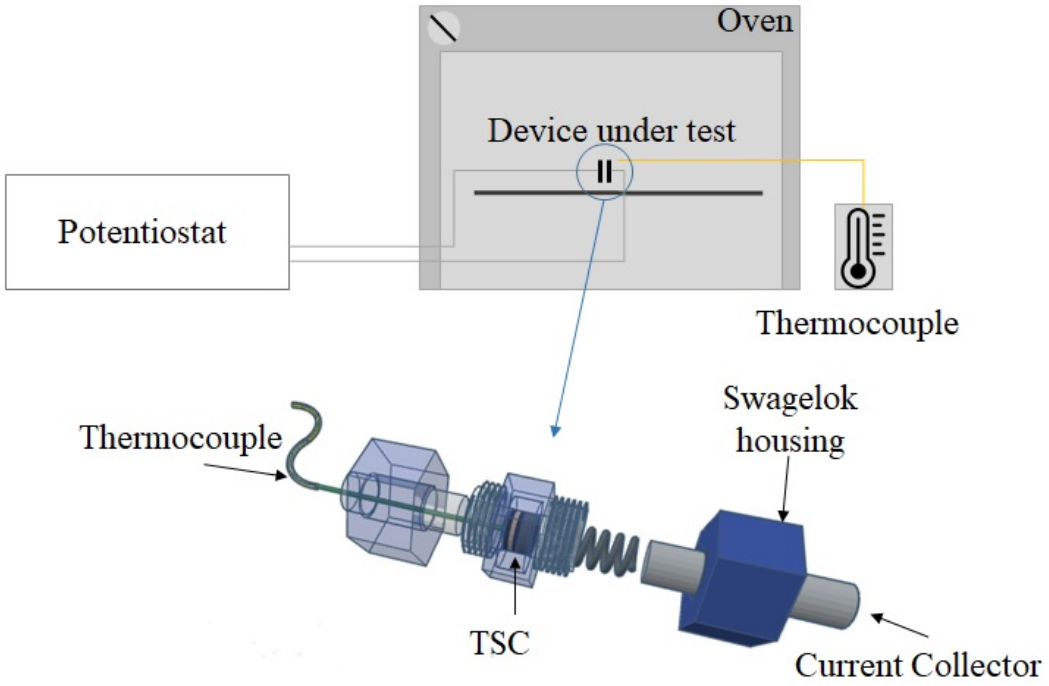

FIGURE 6.6: Testing rig for elevated temperature testing. The device is placed in the customised Swagelok (blown out CAD representation at the bottom of the image) and then put within the oven to ramp the temperature. The GCD characterisation is performed while the device is held at the testing temperature.

6.2.2 Results

The electrochemical results are shown in Figure 6.7. There is seen to be 0.23%/°C degradation from room temperature to 60°C. There remained a <5% change up to 45°C. It was also observed that there was a small 1.5% hysteretic change when the device was allowed to return to room temperature. This suggests that there was damage done to the device. However, 60°C was purposefully chosen as an extreme temperature for e-textiles and it is expected that under normal conditions this permanent degradation would not be present. For specialist high temperature applications further work is required to fully understand the impact of elevated temperatures on the lifetime of the device.

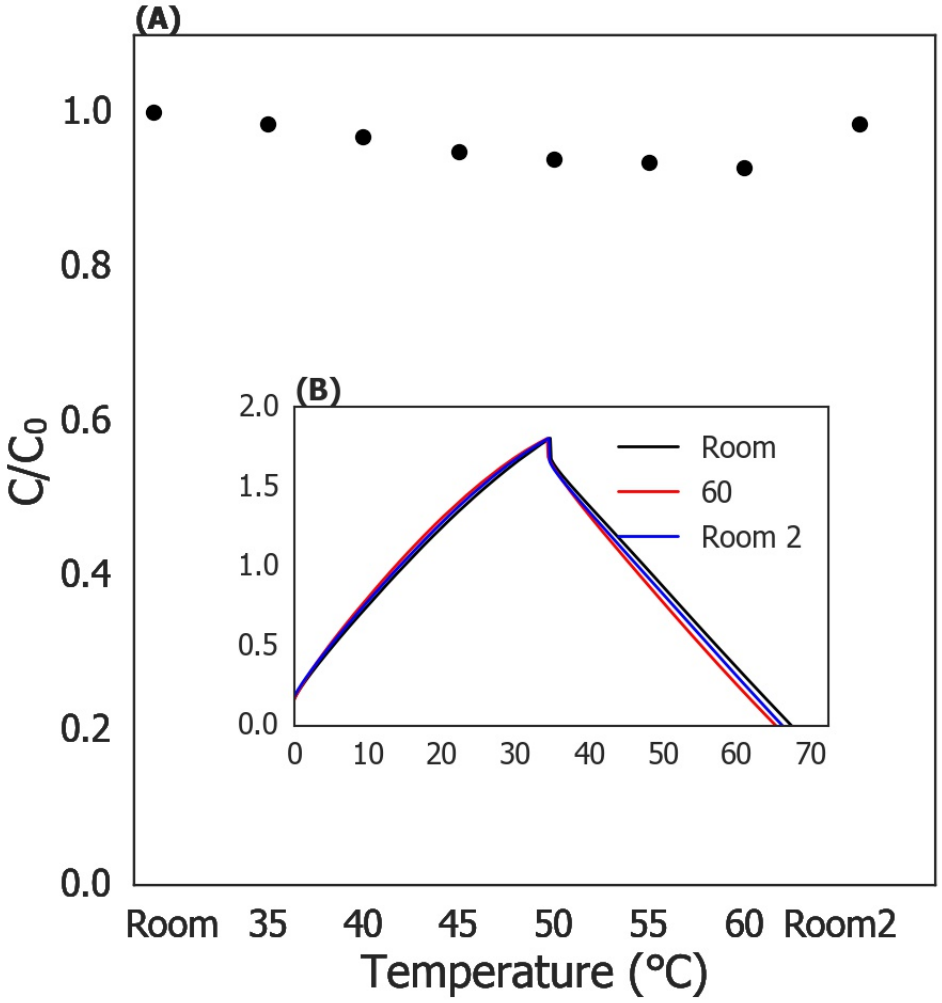

FIGURE 6.7: Electrochemical results at elevated temperatures. (A) Capacitance degradation at elevated temperatures normalised to the results at room temperature. Each point is the average of 5 measurements, with an error of ± 0.01 for the normalised value calculated from the standard deviation. (B) Insert showing the GCD curves for the room, 60°C and return to room temperature. They compare well, showing only a small degradation at extreme temperature conditions.

6.3 Proof of Principle Textile Power Module

Durability and safety are key considerations for practical e-textiles, however, so is compatibility and system integration. Within this section and section 6.4 the TSCs will be incorporated into power modules.

E-textiles need a reliable power source, disconnected from permanent connections and ideally self powered. Ideally, this power source should be compact, limiting the inconvenience to the end user. As discussed in Chapter 2 there have been a number of

designs for an e-textile power modules, including ferroelectric [154] and micro-fuel cells [178]. However, by far and away the most prevalent format seen within the literature is to pair a triboelectric energy harvester with a TSC [102, 124, 158, 163]. For movement based applications, such as a runner's clothing, a triboelectric-TSC power module makes a lot of sense. However, not all applications have sufficient movement, or any movement at all, and generation would be low. Additionally, the output signal from triboelectric devices is transient and more components are required to sufficiently harvest the energy. For applications in the built-environment or immobile applications (such as in hospital or movement impaired individuals) a ready source of stray power to harvest is in the form of sub-GHz radiation from applications such as wireless networks. In an office or workplace environment, this would enable energy harvesting while stationary.

As such, a textile power module based upon a rectenna-TSC is presented. The appropriately designed rectenna is compact and can provide continuous power for the wearable application. The TSC acts as a power reservoir, accumulating the harvesting power before delivering it to the application. This is especially important for higher power applications or for devices which require a higher voltage for operation. Additionally the TSC can act as a supply-and-demand buffer in the case of lost harvesting due to misalignment, range or body shadowing [266, 267]. The combination of flexible rectenna and energy storage is not new, with examples charging lumped supercapacitors/capacitors [268, 269]. However, these systems require a Power Management Integrated Circuit (PMIC) which are made from a large number of lumped components (Okba *et al.* [270] and Assimonis *et al.* [271] both required $>$20 components, Li *et al.* [269] needed $\sim$23 and Zhao *et al.* [272] needed $\sim$45). This number of lumped components and the use of an integrated circuit are not conducive to wearable applications. As such, a first all textile system is proposed with a flexible rectenna and TSC

The proposed rectenna is a meandered monopole-Coplanar Waveguide (CPW) antenna and a voltage doubler rectifier, connected to a series of carbon based aqueous TSCs. The antenna and rectifier design is out of scope of this thesis and will be treated as a black box charging source. Technical characterisation will only be reported where

the device connects to the TSC. More details of the design of the antenna and rectifer are presented in [170–172].

6.3.1 Experimental

TSC fabrication

The TSC were produced via the procedure discussed in Chapter 4 and were found to have a mass loading of 2 mg. The cells in this power module are connected in series and will be self balancing, with no external circuitry. As such, each TSC was printed on separate plain woven cotton substrates to allow for device replacement in case one of the devices did not match the performance of the others. The electrolyte selected for this prototype was a fluidic 0.5 M ADP electrolyte. It was decided to not add a polymer to the electrolyte for this trial to mitigate any complications due to increased resistances. The electrolyte was impregnated into the electrodes through vacuum impregnation. Each device was immediately stored within a Swagelok test cell to guarantee the long term stability of the devices, limiting any time-variant effects that may have jeopardised the characterisation.

TSC Characterisation

The TSCs were characterised via GCD. The single TSC's were characterised at 0.25 - 2 $mA.cm^{-2}$ (0.2 - 1.6 mA, which corresponds to the anticipated DC output of the rectenna for various power levels) with a cut off voltage of 0.8 V while the series connected cells had a 2.4 V cut off voltage. All measurements were performed using a *Solartron 1470E* Cell Test system.

TSC Chargeability Characterisation

Typical rectifiers are characterised using a resistive load, however, the TSC presents a resistive and capacitive load and it was important to characterise the chargeability of the system, s-parameter (S_{11}) and the charging efficiency of the rectifier-TSC. S_{11} is the single port reflection coefficient and represents how much power is reflected, and therefore not transmitted. The characterisation of the RF charging, S_{11} and charging efficiency were all performed with a 50 Ω RF power source (to match the rectifier) and

Rhone & Schwarz Vector Network Analyser (VNA). This means the power source uncertainty is ∼0.1 dB [273]. The VNA was swept across power levels of -4 - 14 dBm (dBm is decibel-milliwatts and equates to 0 dBm = 1 mW). The VNA was in continuous wave mode with a frequency of 10 Hz, leading to the TSCs being charged with a pseudo-10 Hz square wave after rectification. The TSCs were charged up to a cut-off voltage of 2.9 V (the peak voltage was kept significantly below the 3.6 V breakdown voltage as no protection circuit was present to prevent overcharge) or for 180 s, whichever was first. The devices were subsequently discharged across a 1 MΩ load, resulting in a ∼2 μA current draw to replicate the current draw from a low-power micro controller in sleep mode [274]. The charging efficiency (or Power Conversion Efficiency (PCE)) was calculated from equation 6.1.

$$PCE_{charging} = \frac{CV_{peak}^2}{2} \times \frac{1}{t} \times \frac{1}{P_{RF}} \tag{6.1}$$

where C is the capacitance, V_{peak} is the peak voltage, t is time and P_{RF} is the available RF power.

It is important to clarify the relevance of PCE as an appropriate figure of merit. The PCE is the characterisation of the the efficiency of the available power to be transferred to the supercapacitor. For example, when connected to the VNA, the PCE shows the efficiency of the rectifier to take the power and transfer it to the supercapacitor (taking into account the inefficiencies of the rectifier and of the supercapacitor, along with any change of impedance). For measurements at distance (as seen in sections 6.3.2 and 6.4.2) the efficiency is not calculated from the source power (an end-to-end efficiency) but from the available radiated power at that distance, which is discussed later in equations 6.2 and 6.3. Varying the power from the VNA in the initial experiments is used to mimic the likely power seen at distance to validate whether the power module will work function away from an RF source. The use of this PCE as a figure of merit is widely used in the RF harvesting community [170, 275–280]

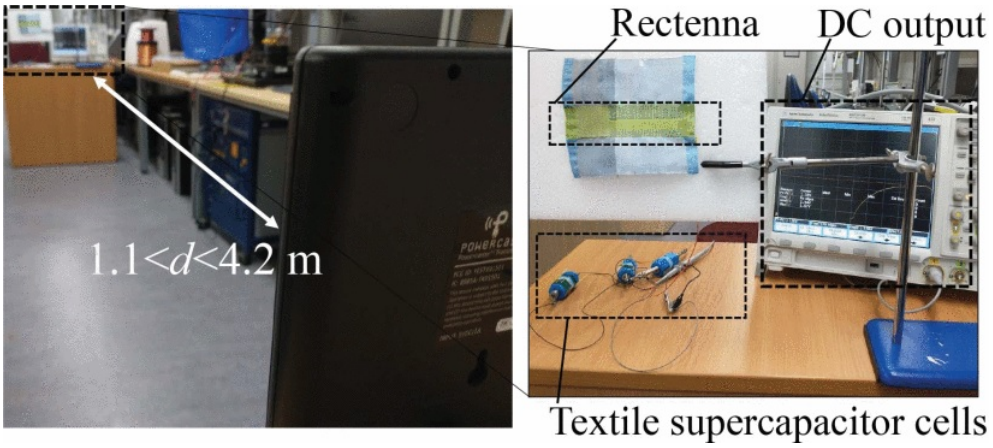

FIGURE 6.8: Wireless characterisation set up with the 915 MHz Powercast set up at varying distances from the rectenna held within a textile pocket. Image taken from [171]

Frequency Dependence Characterisation

Though the wireless charging was intended to be performed at 915 MHz, there are a number of other potential frequency bands of interest to the wider RF community, including 940-960 MHz GSM (Global System for Mobiles) and 4G/5G bands down to 700 MHz as well as the 868/915 MHz ISM (Instrument, Scientific and Medical) band. As such the charging efficiency across a frequency band is characterised with a RF source. The TSC is charged for 10 s at both 5 and 10 dBm and the charging efficiency and peak voltage recorded.

Wireless Charging Characterisation

For the wireless charging tests, a 915 MHz 3 W Effective Isotropic Radiated Power (EIRP) Powercast transmitter was placed at varying distances (1.1 - 4.2 m) from the rectenna, Figure 6.8. The rectenna was housed within a textile pocket to establish real-world conditions. The TSC were then charged to 2.9 V and the time recorded.

6.3.2 Results

Electrochemical Results

The GCD results are presented in Figure 6.9. The individual TSCs were found to have capacitances of 19.6, 19.3 and 20.6 $mF.cm^{-2}$ characterised at 1 $mA.cm^{-2}$. The series

connected devices was found to 7.6, 7.4, 7.2, 6.9 an 6.7 mF.cm^{-2} at discharge currents of 0.25, 0.5, 1, 2 and 3 mA.cm^{-2} respectively. This is a capacitance degradation of 12% across the range of characterisation. There is seen to be an ESR of 71.9 Ω, calculated from the initial voltage drop at discharge and the discharging current. The capacitance of the three series supercapacitor module is higher than expected from perfect series-connected capacitors and implies some balancing is taking place during charge/discharge. However, from Figure 6.9 (A) the devices behave broadly as expected when connected together, with no significant variation in the cycle time.

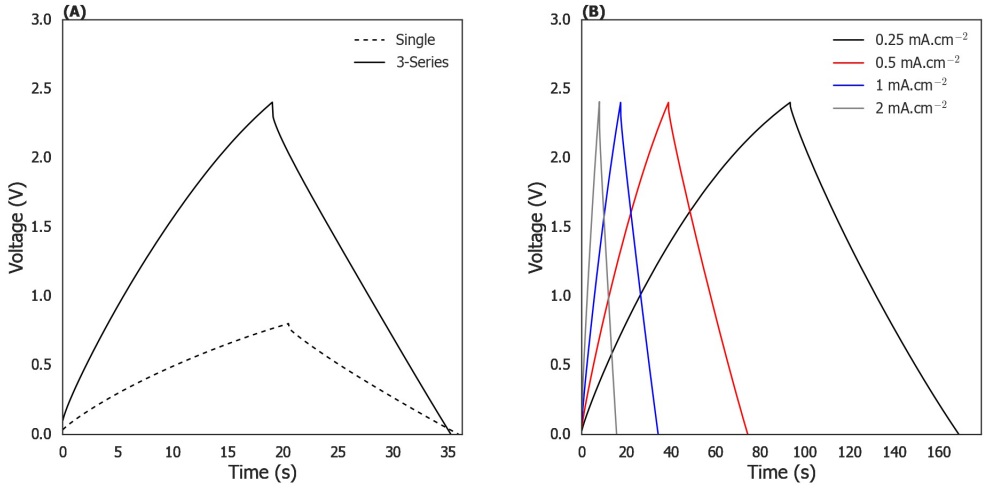

FIGURE 6.9: GCD results for the series connected TSC used in the prototype power module. (A) A comparison of the GCD measurement at 1 mA.cm^{-2} charge/discharge current density for a single TSC and the three connected in series. (B) Full characterisation measuremenst for the series connected TSC module.

Charging Results

The charging of the TSC at varying power levels is presented in Figure 6.10. For power inputs >0 dBm the peak voltage of 2.9 V can be reached in <180 s. The jagged lines seen in Figure 6.10 (B) is due to the non-continuous input from the rectified system. In the 'off' periods the TSC slightly discharges due to the TSC's charge redistribution [183]. Upon discharge across the 1 MΩ resistore the discharge curves are very shallow and maintained a voltage level >1.5 V for >180 s.

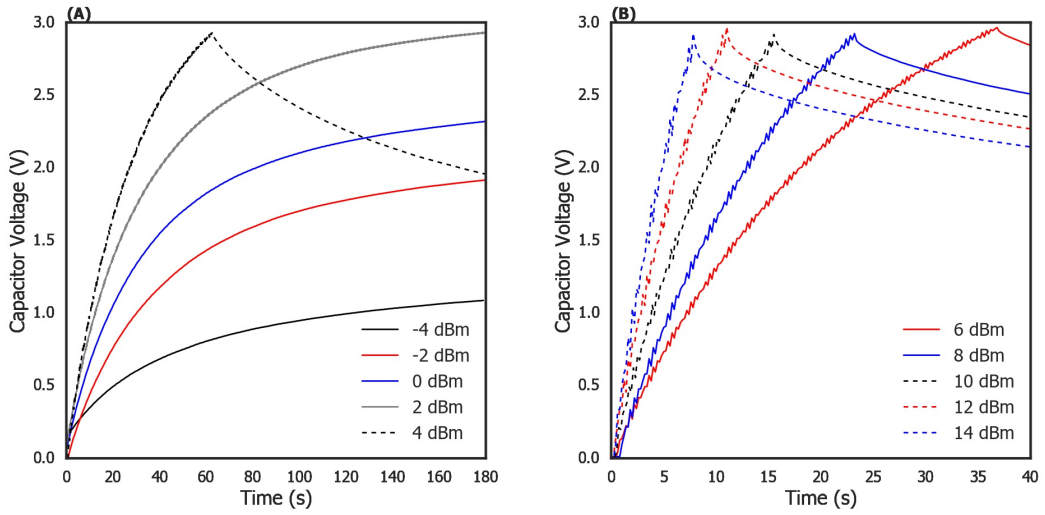

FIGURE 6.10: Charging curves of the series TSCs by the rectifier at varying power levels. (A) Charging curves at power levels <6 dBm, with -4,-2, 2 and 0 dBm power levels unable to reach the cut off voltage of 2.9 V. (B) Charging curves for power levels >6 dBm

From the data presented in Figure 6.10 the PCE could be characterised using equation 6.1 and is presented in Figure 6.11. For the time, t, 30 s was used for power levels <8 dBm so as to remain in the linear charge region of the curve and to negate erroneous effects caused due to self-discharge of the TSC. For power levels of 8 dBm and above, the time taken to reach 2.9 V was used. It is seen that the rectifier-TSC maintains a charging efficiency >20% from -2 to 8 dBm (with the trend implying this would remain at 9 dBm). The loss in efficiency is attributted to impedance mismatch at the connection between the rectifier and TSC and the rectifier approaching the diode's breakdown voltage for power levels above 8 dBm. As discussed previously, the characterised PCE is expected to be lower than in the real-world test due to the intermittency of the 10 Hz square wave, and the values in Figure 6.11 are seen to be lower boundary estimates for the true chargeability. The TSC can be charged to 1 V in 30 s with power levels as low as -2 dBm.

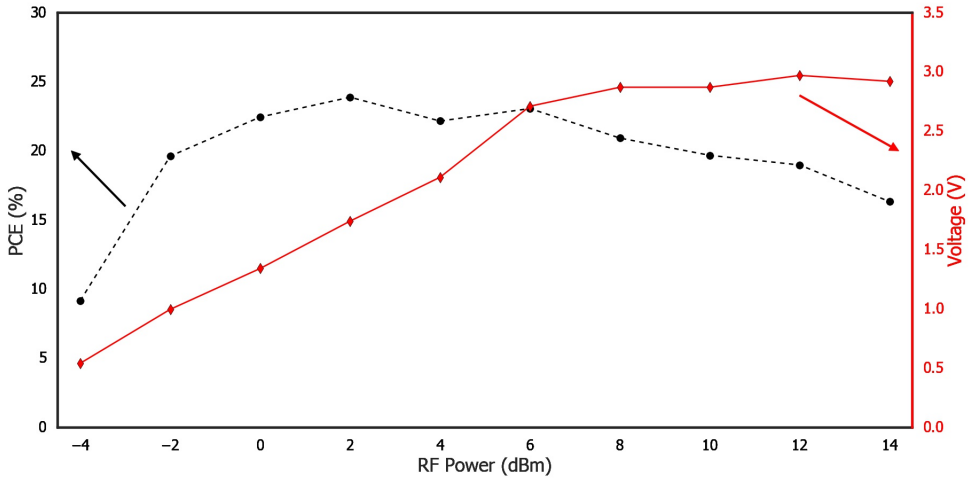

FIGURE 6.11: The measured voltage and PCE of the rectifier-TSC at varying power levels.

The PCE for the rectifier-TSC is seen to be lower than when the rectifier is connected to a purely resistive load [171]. This is not surprising when one considers other works looking into capacitor connected energy harvesters show a similar trend [170, 269]. However, it does warrant further investigation. The S_{11} parameter was characterised at 0 dBm and the equivalent load seen by the rectifier found by calculating the changing current (I(t)) from equation 3.1, with the results presented in Figure 6.12. It is assumed for this calculation that all of the current drawn by the TSC induces a voltage change.

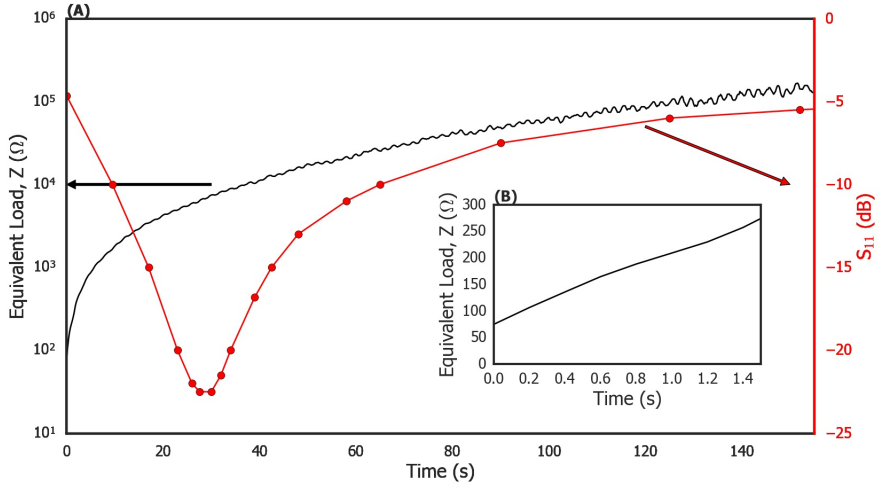

FIGURE 6.12: Characterised S_{11} of the rectifier while charging the series connected TSCs at 0 dBm. (A) The S_{11} parameter and equivalent load, Z, seen by the rectifier at 0 dBm. (B) The equivalent load during the first 1.5 s of charging.

At the beginning of the charge (Figure 6.12 (B)) the only load seen by the rectifier is the ESR of the TSC. In this measurement the ESR is seen to be 74 Ω, matching closely the 71.9 Ω characterised from the GCD measurement. Upon charging, the current draw begins to change, significantly increasing the load seen by the rectifier. This load quickly reaches the optimal load for the rectifier and remains within this region for ∼55 s. This is seen by the reflection coefficient, S_{11} being below -10 dBm between 5 and 60 s (at -10 dBm the reflected power is less than 10%). After 60 s the charging of the TSC is reaching the maximum and the current draw is small, resulting in a large equivalent load and an increase in reflected power. Though this variation in load could be mitigated through the use of maximum power point tracking with an integrated circuit, this would limit the efficiency of the system and is not required in this instance.

Frequency Sweep Results

The frequency response of the rectifier-TSC is presented in Figure 6.13. The capacitor voltage after 10 s and the charging PCE are shown. At 10 dBm input power the TSC can charge to at least 1 V up to 1600 MHz and 0.5 V for 5 dBm. For frequencies above 700 MHz the half-power bandwidth (centre frequency = 1050 MHz) is found to be ∼73%, during the period of testing. When this is compared to the half-power bandwidth found from when connected to a resistive load (57% [171]) the direct connection of the rectifier to the supercapacitor is seen as beneficial and this system could cover the full frequency range discussed in section 6.3.1.

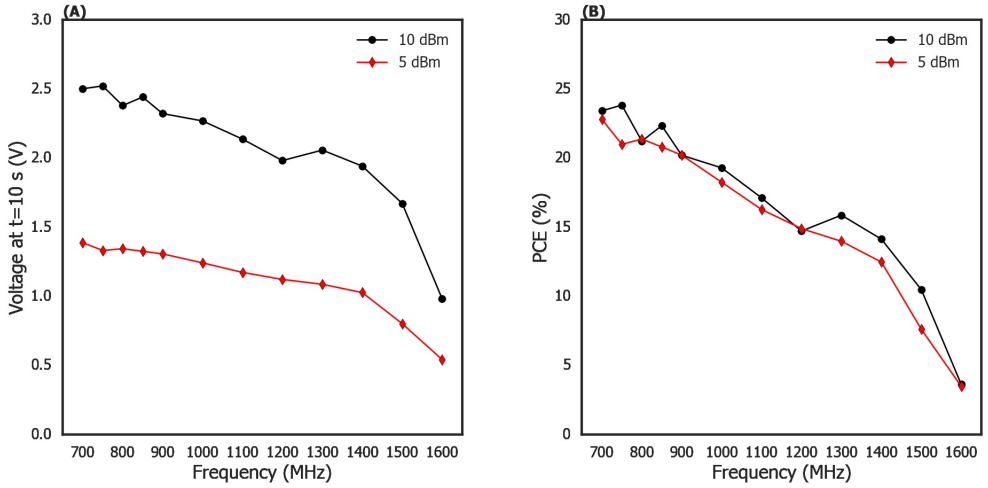

FIGURE 6.13: Frequency response of the rectifier-TSC. (A) Voltage over the TSC after 10 s of charging. (B) PCE of the rectifier-TSC. The system exhibits a 73% half-power bandwidth.

Distance Measurement Results

The characterisation of the full rectenna and TSC is presented in Figures 6.14. The power density, S, seen by the rectifier at the different distances is 19.7, 7.4, 4.9 and 1.35 μW.cm^{-2} at 1.1, 1.8, 2.2 and 4.2 m respectively, calculated from equations 6.2 and 3.

$$S = \frac{E^2}{120\pi} \tag{6.2}$$

$$E = \frac{\sqrt{30 P_T G_T}}{d} \tag{6.3}$$

where S is the power density, E is the electric field, P_T and G_T is the transmitters power and gain and d is the separation. 120π is the free space impedance, Z_0.

At the highest power density (1.1 m) the TSC charged in 45 seconds, while at 4.2 m the device is charged to 1.5 V in 4 minutes. The subsequent PCE are presented in Figure 6.14(B). It is seen that the peak efficiency is 38% at a distance of 1.8 m. At 1.1 m the power available is greater than 10 dBm, resulting in the rectifier having to operating in its breakdown region. At 4.2 m the efficiency drops to 17%, showing that even at the low power levels/larger distances the power module could still harvest energy successfully.

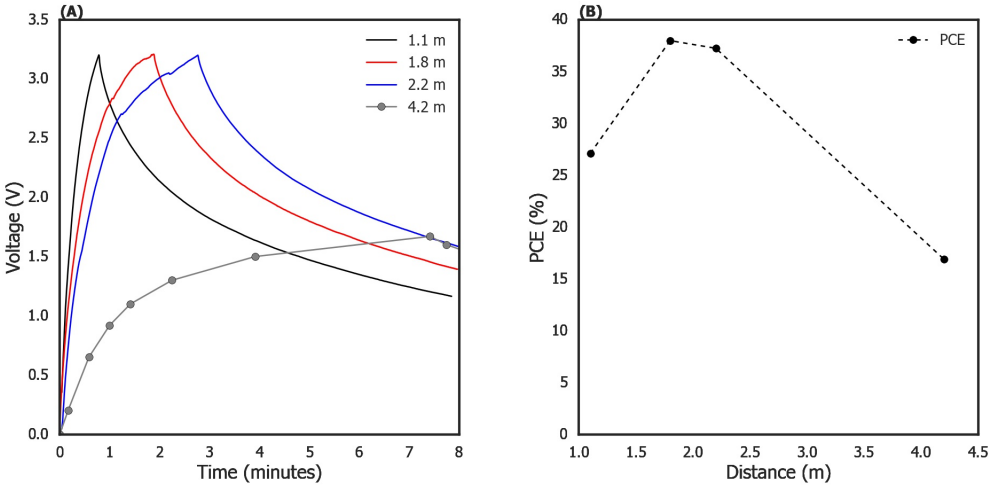

FIGURE 6.14: Charging curves and PCE of the rectenna-TSC at a range of distances with a 915 MHz 34.77 dBm Transmitter as the source.

6.3.3 Discussion

It is seen that the TSC is compatible with the rectifier, ad considering the time variant load seen throughout the charge cycle demonstrates a good bandwidth response across a range of input frequencies. The initial characterisation of the rectifier-TSC presents a lower limit to the PCE due to the 'off' periods in the rectified square wave input to the TSC. This is evidenced by the superior PCE during the wireless testing. The initial measurement is, however, still important as the use of the VNA gives a calibrated evaluation of the performance and ability to characterise the S_{11} while charging and acts as a good benchmark of the performance expectations of the final device.

When the power module is compared to the literature the 38% PCE and ability to charge the TSC to 3.2 V (28.7 mJ) in under 2 minutes stands out amongst the e-textile energy harvesting community, especially considering the simplicity of the design. A comparison to some of the current literature is presented in Table 6.1. The device presented here is the only reported e-textile that can harvest mJ from μW.cm^{-2} power densities in under 4 minutes.

TABLE 6.1: Comparison of e-textile (or e-textile adjacent) power modules

Work	Energy Harvester	Energy Storage	Substrate	S (μW.cm^{-2})	Charging Time (minutes)	Capacitor Voltage (V)
[268]	Sub GHz Rectenna	Supercapacitor	PCB	12.6	6	1.9 (12.6 mJ)
[269]	Sub GHz Rectenna	Capacitor	PCB	23.8	0.02	4 (0.12 mJ)
[281]	2.4 GHz Rectenna	Capacitor	Printed Enclosure	0.8	3	1.5 (0.11 mJ)
[272]	Sub GHz Rectenna	Battery	PCB	31.8 *	50	0.71 (490 mJ)
[154]	Ferroelectret	TSC	Textile	31 μW†	60	0.4 0.16 mJ)
[163]	Triboelectric yarn	TSC	Textile yarn	8.5 μW†	1.7	1.1 (0.1 mJ)
This Chapter	Sub GHz Rectenna	TSC	Textile	7.3	1.8	3.2 (28.7 mJ)

* Calculated, † Instantaneous DC Power

6.4 Co-Design of a Full Power Module and Application

The power module discussed in section 6.3 demonstrated a first of its kind combination of flexible rectenna and TSC, achieving an impressive end-to-end efficiency. The work demonstrated the advantages of directly connected the rectenna to the supercapacitor and was comparatively simple in its construction compared to similar systems. However that is not to say that the design is without flaws. For example, the voltage limit of the aqueous electrolyte will always impair its real world use. A significant number of TSCs would be required in series to reach a voltage that could be used for a wide array of applications. This would subsequently reduce the energy storage potential and would add complication as a balancing circuit would be required, whereas in section 6.3 self balancing was sufficient for a string of three.

As such, an enhanced rectenna-TSC textile power module was proposed with two organic electrolyte TSCs (from Chapter 5). This TSC system can be charged to 4.8 V, and very safely charged to 4 V, sufficient to power a Bluetooth Low Energy sensor node for more than 100 s. The power module is also tested with a second far-field antenna (disc) and the use of a near-field wire antenna is demonstrated, with the stray signal from a walkie-talkie sufficient to charge the TSC to 4 V in $<$25 s.

6.4.1 Experimental

TSC Fabrication

The TSCs were fabricated as discussed before. The electrolyte was a 0.5 M $TEABF_4$-PAM organic electrolyte. 0.5 M was selected to enable fairer comparison with the results from section 6.3 and a polymer was used to form a gel electrolyte to best replicate what would be required in a real-world device. Due to the increased voltage operating from the use of the organic electrolyte, only two TSCs were required to be produced for the power module.

TSC Characterisation

The TSCs were characterised via GCD testing up to a V_{peak} of 4.8 V at current densities 0.25, 0.5, 1, 2 and 3 $mA.cm^{-2}$ and CV characterisation across the voltage window of 0 - 4.8 V at scan rates of 5, 25, 50, 100 and 200 $mV.s^{-1}$. Due to the long term capacitance loss seen when operated at 2.4 V for extended periods in Chapter 5 the CV measurements were performed to establish the stability of this TSC module.

TSC Chargeability Characterisation

Due to the different electrochemistry of these TSCs compared to the ones in section 6.3 it was required to evaluate the chargeability of the TSC by the rectifier. This was done in a similar manner to the previous testing with the rectifier connected to the VNA via a matched 50 Ω load and the TSC directly connected to the rectifier. A sweep of powers (from -16 to 15 dBm) was then performed, again with the signal reaching the TSC being a rectified pseudo 10 Hz square wave.

Wireless Testing

The wireless testing for the far-field rectenna (meander and disc) were performed using the same 915 MHz transmitter as previously. The meandered monopole is the same as in section 6.3 and technical details of the disc monopole can be found in [170]. The rectenna was placed 1 m from the source (S = 23.9 $\mu W.cm^{-2}$) and connected to the TSC. The TSC was subsequently connected to the Bluetooth sensor node. The node was based on a microcontroller and the Bluetooth Low Energy transceiver system and

was purchased from Texas Instruments. A cold-start circuit based on two XC61C voltage monitors and a latch switch MOSFET was included in the circuit. Though for this demonstrator these were placed on a rigid development board, examples of fully flexible solutions have been seen in the literature [282] and could be implemented for future applications. The transmitter was programmed to transmit every 1000 ms, at a power level of 0 dBm (enough to communicate up to 100 m). The voltage was monitored across the TSC and the current draw from the sensor node was monitored across a 10 Ω sense resistor. Each test consisted of an RF charging period, followed by a brief pause before connecting the sensor node. Following the electrochemical characterisation discussed below, the TSCs charge will be limited to ∼4.1 V.

For the near-field test a Walkie-Talkie was positioned ∼ 12 cm (to mimic realistic conditions) from the wire antenna and the same monitoring was performed. Charging was performed by manual depression of the Walkie-Talkie's speak button.

6.4.2 Results

Electrochemical Results

The GCD and CV results can be seen in Figure 6.15. The series connected TSCs were found to have an areal capacitance of 18.0 $mF.cm^{-2}$ at 0.25 $mA.cm^{-2}$, falling to 14.3 $mF.cm.cm^{-2}$ at a current density of 3 $mA.cm^{-2}$. The ESR was determined to be 149 Ω.The CV show square like profiles, however, some minor peaking is observed towards the higher voltage. As such the wireless charging was limited to ∼4.1 V in the following tests.

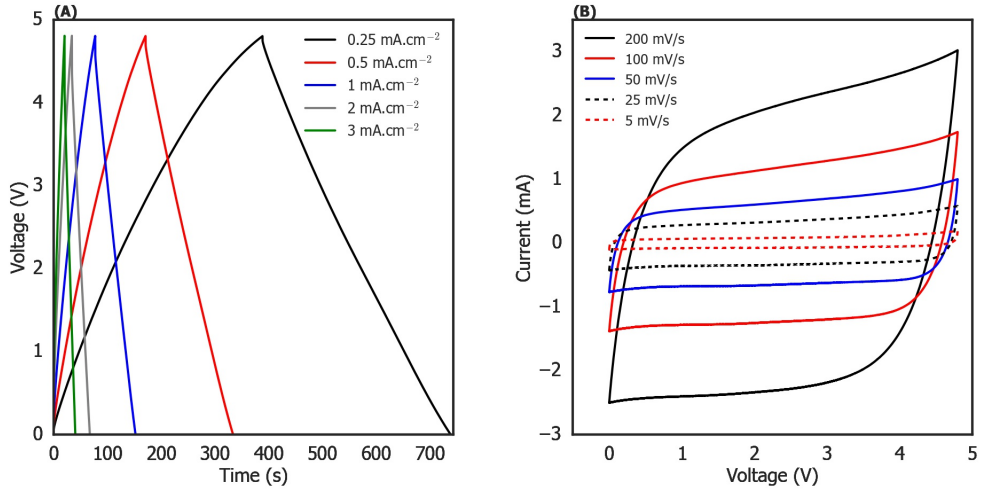

FIGURE 6.15: Electrochemical performance of the the series connected 0.5 M $TEABF_4$-PAM TSCs. (A) shows the GCD results from 0.25 - 3 $mA.cm^{-2}$ charge/discharge current densities. (B) CV traces at varying sweeprates from 5 to 200 mV/s.

TSC Chargeability Results

The chargeability of the TSC by the rectifier is presented in Figure 6.16. The peak PCE is seen to be 28% which is larger than that observed in the aqueous based power module. The TSC is also possible to charge with input powers as low as -16 dBm, reaching a voltage of 0.05 V (18 μJ of energy) within 30 s of charging. At a power input of 10 dBm, the TSC was able to be charged to 3.4 V (82 mJ of energy accumulated) in 30 s.

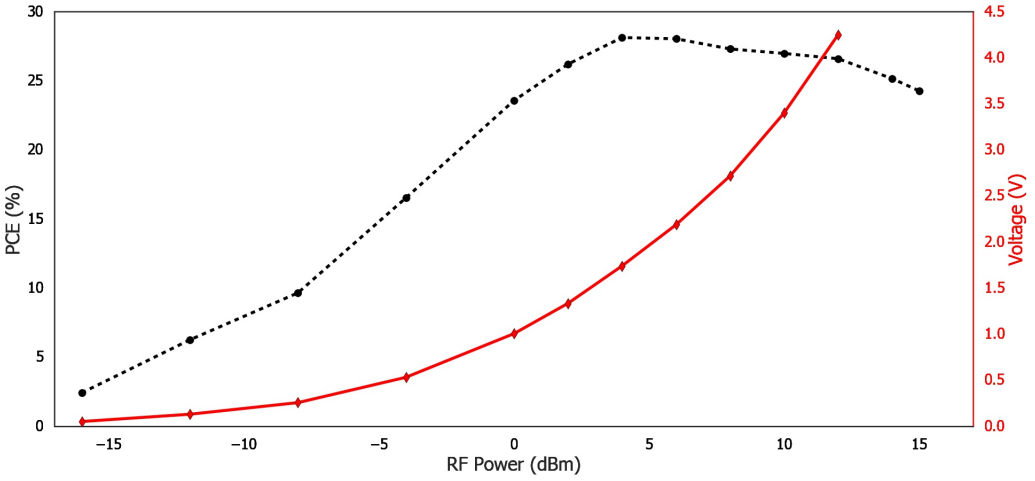

FIGURE 6.16: PCE and voltage (at t=30 s) for the rectenna-organic electrolyte TSC power module across a power range of -16 - 16 dBm. The voltages for >12 dBm have been ommitted as they reached the cut off voltage before 30 s

Wireless Testing Results

Prior to full wireless testing the rectifier was connected to the Bluetooth node directly, without the TSC. During open circuit the rectfier could deliver 8 V however as soon as the load was started the voltage fell below <1.8 V, meaning the Bluetooth node could not operate. This quick assessment displays the importance of the TSC in the power module.

The wireless charging of the TSC by the meandered and disc monopole is presented in Figure 6.17(A) and 6.18 respectively. It can be seen that both rectennas easily charge the TSC to >4 V in 83 and 88 s for the meandered and disc monopoles respectively. The final cut off for the tests was 4.2 and 4.1 V. The calculated PCEs were calculated from equation 6.1 and was found to be 46% and 45% respectively. This remarkable efficiency is greater than that seen in section 6.3 and the wider community.

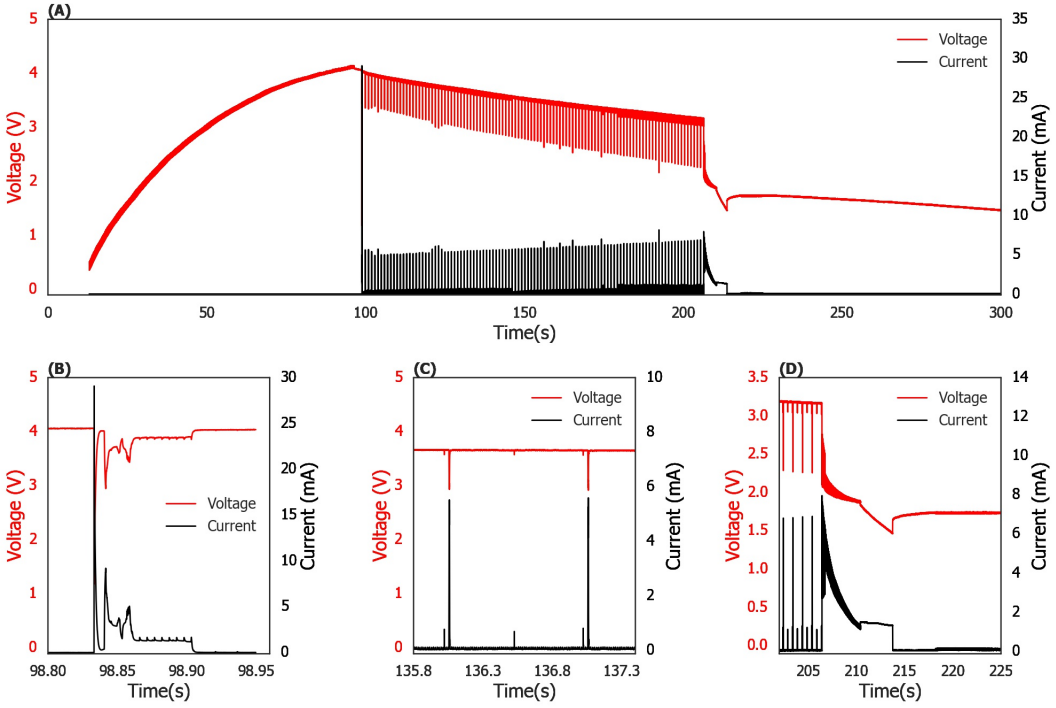

FIGURE 6.17: The voltage across the TSC during charge and discharge and the current drawn by the load during operation for the meandered monopole-TSC power module. (A) Charge and discharge voltgae and current. (B) Capacitor voltage and current drawn during start-up. (C) Two duty cycles of the node, during operation. (D) System shutdown following the fall of the capacitors voltage below 1.8 V.

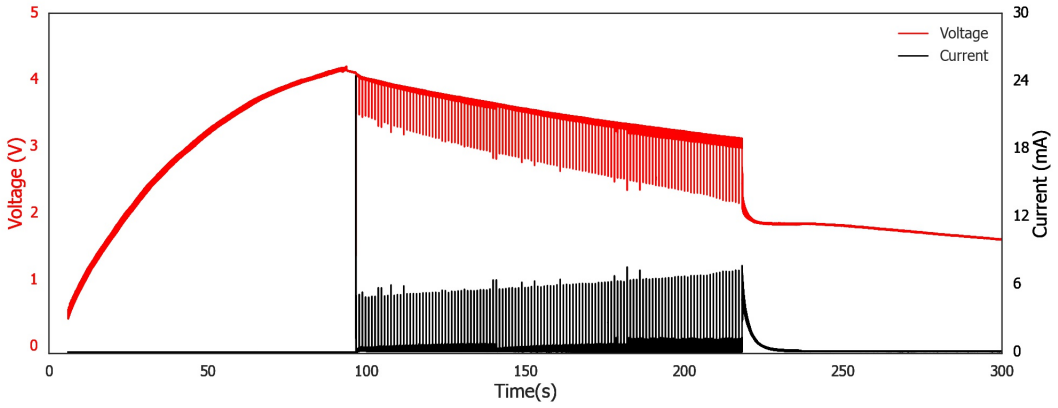

FIGURE 6.18: The voltage across the TSC during charge and discharge and the current drawn by the load during operation for the disc monopole-TSC power module.

It was observed that the TSC could subsequently power the Bluetooth node for 108 s and 121 s for the meandered and disc rectennas. The different powering times is attributed to the slightly differing peak voltages reached during the charging stage. The ratio of charge time to power time shows a favourable duty ratio, with the charge and discharge being of comparable lengths. In Figure 6.17(B) the current and voltage during switch on can be seen. There is a large (nearly 30 mA) transient current draw which drops the TSC's voltage below the operation voltage of the Bluetooth node (1.8 V). However, given the transient nature of the pulse, the current draw returns to the more manageable level of 6 mA rapidly. The TSC was able to handle this pulse with the voltage returning to the voltage level proceeding the current draw (curve to the right of current pulse in Figure 6.17(B)) due to the charge redistribution characteristics of the porous carbon electrodes.

The pulses seen in the current data are the data package transmission periods, drawing $\sim$6 mA. In Figure 6.17(C) two of these pulses are shown, with the time interval of 1000 ms. The data could be received by the receiving mobile two offices away from the laboratory, or approximately 30 m away.

As the voltage of the TSC approached 1.8 V a ringing can be seen in the voltage and the current, Figure 6.17(D). At the boundary of the voltage switch on level, the Bluetooth node attempts to start but the current draw drops the voltage below 1.8 V, thus not turning on and the TSC voltage returns to a higher level which in turn allows the node to try to start up again. This repeats in a damped oscillation fashion until the

voltage permanently falls below 1.8 V. However, it must be noted that while unloaded the voltage across the TSC will remain at ∼1.8 V for a while, only discharging through self-discharge of the device. This will enable subsequent charges to be quicker, resulting in a better duty-ratio for subsequent charge/discharge cycles.

The final experiment for the TSC in a power module was with a wire based rectenna, operating in the near-field driven by the signal from a walkie-talkie. Due to the complexities associated with near-field propagation, rigorous analysis was not performed and the results are presented (Figure 6.19) as a demonstration of capability only. Three charge-discharge cycles are performed. This is representative of an individual making a number of subsequent communications across the walkie-talkie, for example giving and receiving instructions for the police/fire service. The first charge to ∼4 V took 21 s with the subsequent charge taking 10 s. The TSC could then power the Bluetooth node as previously. One could readily think of an application where data from an individual would need to be sent (health, temperature, etc.) and they would be using a walkie-talkie like device, such as the fire brigade when they are at the scene of a fire.

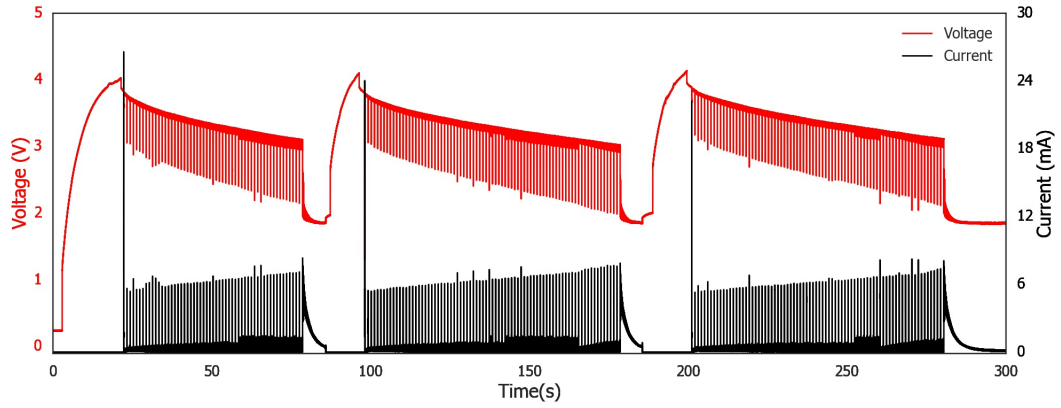

FIGURE 6.19: Charge discharge cycles of the near-field power module, powered by close proximity to a walkie-talkie during transmission

6.4.3 Discussion

The power modules produced with the organic TSCs have shown excellent performance, being able to be charged from a number of rectenna configurations, withstand the initial current spike from the Bluetooth node and then power the node

for >100 s. Very little difference is seen in the performance of the power modules in terms of performance. However, one must consider the end use of such a power module and the size and weight of any textile power module will effect the final product. To enable a fairer comparison of power modules a new figure of merit is proposed [261] which takes into account the area of the power module. The Power Harvesting Efficiency (PHE) is defined as:

$$PHE = \frac{P_{DC}}{S.A_{Physical}} = \frac{CV^2}{2} \times \frac{1}{t} \times \frac{1}{S.A_{Physical}} \tag{6.4}$$

where P_{DC} is the rectenna's DC power output, S is the incident power density and $A_{Physical}$.

The meandered monopole has an area of 4.55 cm^2 and the disc monopole has an area of 124 cm^2. This led to a PHE of 13.2 and 0.47 respectively.

6.5 Conclusion

This chapter has presented research into the durability and safety of the TSC and their integration into a textile power module.

While employing testing methodologies with bespoke apparatus, the mechanical and thermal stability of the TSC was characterised. It was seen that the device was still operational after 1750 bending cycles, with a capacitance degradation of 50%. The thermal stability from room temperature to 60°C was evaluated to be -0.23%/°C. The devices were also seen to still be operational after both cutting and puncturing damage.

Two textile power modules were produced using a rectenna as the energy harvester and the TSC as the energy storage. The first system, based upon an aqueous electrolyte, was able to be charged to 3.2 V (31 mJ) in under 4 minutes at distances up to 2.2 m from a 915 MHz 3 W EIRP source. An PCE efficiency of 38% was found. This was then improved upon by making an organic TSC power module. In this work, the

power module was able to charge to $>$ 4V in $<$100 s and was able to power a Bluetooth node for in excess of 100 s before another charge was required. The PCE efficiency of this power module was determined to be 45%, making it a literature leading e-textile power module.

From an practical application perspective, the ability to power a Bluetooth data transmission protocol (the largest power share in wireless sensing technologies [259]) for in excess of 100 s is certainly long enough to transmit the required medical data to a centralised monitoring hub or warning system. Also, when state-of-the-art e-textile biomedical sensors are reviewed the voltage, and power and energy densities are found to be applicable for the later adoption into a full biomedical smart bandage. Electrochemical transistor based textile moisture sensors are seen to require less than 1 V for an operating voltage [259] which can be readily delivered by this power module. Mattana *et al.* [283] developed a capacitive woven moisture sensor that utilised an AD7150 capacitive converter which only required 2.7 V at 100 μA. This system could also enter sleep mode, enabling pulsed characterisation. In the work of Yamashita *et al.* [284] a moisture sensor system was powered by a microbial fuel cell. In this example the sensing and data transmission required only 3.06 μJ, 4 orders of magnitude lower than the energy stored within rectenna powder TSC after less than 100 s of charging at a distance of 1 m. A higher power example seen in the literature is the work of Xu *et al.* [285] who developed a graphene base moisture sensor system that was demonstrated using an NFC NT3H211 chip and embroidered coil as the power source. This was estimated to harvest 6.2 mW. With appropriate low power circuit design and physical scaling of the TSCs the proposed power module could deliver the required power for the system.

Chapter 7

Conclusions

This thesis has presented the technological development of a single layer all-carbon textile supercapacitor from a laboratory concept to a device capable of integration into a textile power module capable of power a real-world device. Simple production methodologies and commercially available materials were used throughout the work, enabling seamless scale-up, compatible with the textile industry. This practical minded approach has challenged some of the commonly held views within the e-textile community and the use of a wide range of characterisation techniques has shone a light on the performance of the these devices, as well as challenged the community to adopt their use.

Commercially available activated carbons were evaluated as the active material for the electrode ink with the ratio of active material and conductive additive optimised. The YP80-F activated carbon at a ratio of 9:1 (weight ratio of active material to additive) was found to be the optimal formulation. The pore size distribution of this carbon was found to match the ion size of the electrolytes well, with the mixture of micro and meso pores enabling good energy and power densities. This ink can be simply implemented via a spray deposition methodology to achieve a single layer supercapacitor within a cotton substrate. Areal capacitance of 23.6 $mF.cm^{-2}$, energy density of 21. $\mu Wh.cm^{-2}$, average power density of 0.11 $mW.cm^{-2}$ and peak power density of 5.9 $mW.cm^{-2}$ were achieved.

The orthodoxy around electrolyte selection, especially the use of PVA as the gelling agent, has limited research into others. This work sort to understand the impact of the electrolyte on the device performance, not only from the perspective of electrochemical performance but also real-world considerations such as lifetime. The PVA electrolyte was initially tested for calendar lifetime and found to fail after only 5 days while stored in air, which was attributed to electrolyte dehydration. When housed within a Swagelok cell, the device failed after 35 days showing that even under optimal conditions the PVA electrolyte is not compatible with this e-textile application. A benign aqueous electrolyte was subsequently investigated, and a series of fully edible electrolytes were produced (a first study within the TSC community). The electrolytes were user-friendly and delivered results comparable or better to more traditional electrolytes, achieving a capacitance of 22.5 $mF.cm^{-2}$ at a current density of 0.5 $mA.cm^{-2}$. However, the voltage limit of the aqueous based electrolytes remained a problem for real-world applications. This challenge was overcome through the development of an organic electrolyte that did not use ACN or PC as the solvent and utilised PAM as the polymer instead of PVA. The devices produced from this electrolyte achieved an areal capacitance of 34.0 $mF.cm^{-2}$ but more importantly an energy density of 18.9 $\mu Wh.cm^{-2}$ at a voltage of 2.4 V, a 9x increase from the previous work.

The durability and safety of the unpackaged devices was evaluated and the devices were found to still be operational after 1750 bends around a 10 mm radius mandrel and were still operational after being cut and punctured. The temperature stability was characterised via the use of a bespoke Swagelok cell and an in-situ temperature measurement. The stability of the device was found to be -0.23%/°C, with the device still operation at a temperature of 60°C.

The research of the carbon electrodes and electrolyte developed a TSC capable of powering real-world devices and this was established in the delivery of two textile power modules (a proof of principle and a minimal viable product), designed for built environment and static applications. Both achieved end-to-end efficiencies which were higher than previously reported in the literature. The proof of principle power module made was a rectenna-aqueous electrolyte system that was able to be charged

from a 915 MHz 3 W EIRP source up to 4.5 m away. This system achieved an end to end charging efficiency of 38% and reached a peak voltage of 2.9 V in under 2 minutes. The minimal viable product improved and simplified the previous module by using the organic electrolyte, reducing the number of TSCs required while also increasing the safe operating voltage range. Charged by a number of far and near field rectennas the TSC could be charged to $>$4 V in under 100 s and could power a Bluetooth sensor node (transmitting an information packet every 1000 ms) for over 100 s between each charge. The end-to-end effiency of this power module was found to be 45%.

Chapter 8

Future Work

Though this thesis has progressed the development of TSCs there still remain challenges that must be overcome. To continue the work presented in this thesis, and develop a fully real-word device, the recommended research areas to focus on are the energy density, packaging and the electrical interconnection.

Within this thesis the energy density of an all carbon TSC has been improved through the introduction of a high voltage electrolyte. However, when compared to the state-of-the-art (section 4.3 and figure 5.16), these devices are substantially lower. The achieved energy density of the TSCs in chapter 5 was demonstrated in chapter 6 to be sufficient for the intended application but with the development of new technology, higher energy densities will be required. Within this thesis the increase of energy density was through the increase in the voltage as seen in equation 3.4. However, when one considers the parallel plate equation (equation 2.1) increasing the area of the devices would increase the capacitance, and therefore the energy density. In a porous carbon device the area is dominated by the pores of the material. To increase the area a greater mass of the carbon could be deposited or a larger device area of could be deposited. From chapter 4 it is seen that increasing the mass loading without increasing the device area poses technical problems with ink penetration. Additionally, even if one could increase the loading significantly without short circuiting the device, there is a question over how much carbon is at the electrode-electrolyte boundary. Increasing the loading alone is likely to result in an

under utilisation of the carbon material's surface area. The second option of increasing the devices area seems a far more logical route for future work, with large area devices being presented such as Wang *et al.* [286] who produced a PPY based TSC with dimensions 16 x 14 cm^2. However, it must be noted that the physical scaling of the devices is not challenge free. In the work of Sun *et al.* [287] the team produced rGO/PANI/polyester TSCs at various length scales, ranging from 4 to 100 cm^2. This large area was achieved through a dip coating and polymerisation process for the active materials and the use of a highly conductive current collecting grid of silver ink. However, at large grid areas the performance decreased, thought to be due to a hindrance in the electron transport. When scaling the devices, careful research is required to understand the uniformity of the deposition and the distribution of electrical current across the the electrode to avoid islanding or hot spots forming which would degrade the performance of the device and potentially harm the user.

The energy density of these devices can also be increased via the addition of pseudocapacitive material. When the devices produced in this thesis are compared to the state-of-the-art they fall behind those contemporaries making use of materials that exhibit fast redox reactions. The development of these complex electrodes is challenging from both an electrochemical perspective and also the commercialisation perspective. From an electrochemical view, these type of materials (whether metal oxide, conductive polymer or something more exotic such as mxene) all suffer from slower response times and reduced cycle life due to the faradic reactions. The electrode conductivity can also be an issue for these materials. The deposition of these materials onto a highly porous carbon helps mitigate the conductivity problem, acting as a physical and electrical scaffold. Additionally, by using a highly porous scaffold the device still exhibits a high electric double layer capacitance, with the pseudocapacitve material adding to this. Asymmetric devices (hybrid capacitors or supercapatteries) have also seen a lot of research attention and should be considered. Commercial scalability is also challenging with these materials with either complex production or deposition required (as documented in chapters 2 and 4). The development of low cost and scalable production methodologies for these materials poses its own research question and certainly warrants further investigation. The use

of these higher energy density materials should be considered on an application by application basis, where high energy density but fast response time or transient power loads are required (thus ruling out batteries).

The packaging (encapsulation) of the TSC is vital for the protection of the end-user as well as the device. The packaging (expected to be a physical barrier and superhydrophobic coating) should be breathable and flexible, while also protecting the device from abrasion and sweat of the user during operation and washing during cleaning. A further complication is the consideration for the environmental impact of the packaging. Traditionally within the textile industry, C8 chemistries (polymers with eight or more fluorinated carbons) have been used as super hydrophobic coatings. However, these polymers pose health and environmental problems and are no longer used. Brands such as Gore-Tex make use of C8 chemistry in their microporous membrane layer and outer water repellent coatings and are having to phase them out of their product line. A direct alternative to C8 coatings has yet to be established, with the C8 chemistries not only exhibiting superhydrophobicity but also a robustness to mechanical and chemical wear. The important characteristic for any superhydrophobic coating is its roughness, with C8 chemistries achieving their roughness through their long fluorinated chains. C6 chemistries (polymers with 6 or less fluorinated carbons) have been suggested due to greater environmental friendliness but their shorter chains suffer from time-dependent wetting, with a saturation of the polymer backbone over time. Alternatives such as silane and silicone, beeswax and nanoparticles have also been suggested within the literature.

Aside from the superhydrophobic coating, adherence of the physical barrier to the textile and the production methodology are further open questions that must also be overcome.

The electrodes produced within this thesis also serve as the current collector and conductive portion of the device. However, as the systems in which the TSC are integrated into get more complex the problem of reliable electrical interconnections becomes pronounced. Having to be as flexible, wearable and resilient as the energy storage device and packaging, the interconnections must also have a low resistance so

as to not impair the operation of the energy storage, harvester or final application. Textile functionalisation, conductive transfer or weaved metallic threads are all possible research routes.

An obvious solution to both the packaging and the interconnection is through the implementation of a multi-layered textile patch that on one side has a conductive track and the other a superhydrophobic coating. However, this goes against the design ethos of hidden functionality. As such, as far as possible this should be avoided.

With the development of appropriate packaging and encapsulation of the TSC, focus can be spent on application informed design, and the optimisation of the TSC with further energy harvesters, sensors and displays can be made; enabling the realisation of on-body, autonomous nano-grids.

References

[1] J. Kim, A. S. Campbell, B. E.-F. de Ávila, and J. Wang, "Wearable biosensors for healthcare monitoring," *Nature biotechnology*, vol. 37, no. 4, pp. 389–406, 2019, doi:10.1038/s41587-019-0045-y.

[2] T. Luczak, R. Burch, E. Lewis, H. Chander, and J. Ball, "State-of-the-art review of athletic wearable technology: What 113 strength and conditioning coaches and athletic trainers from the usa said about technology in sports," *International Journal of Sports Science & Coaching*, vol. 15, no. 1, pp. 26–40, 2020, doi: 10.1177/1747954119885244.

[3] H. Shi, H. Zhao, Y. Liu, W. Gao, and S.-C. Dou, "Systematic analysis of a military wearable device based on a multi-level fusion framework: Research directions," *Sensors*, vol. 19, no. 12, 2019, dOI: 10.3390/s19122651.

[4] R. Wright and L. Keith, "Wearable technology: If the tech fits, wear it," *Journal of Electronic Resources in Medical Libraries*, vol. 11, no. 4, pp. 204–216, 2014, doi:10.1080/15424065.2014.969051.

[5] K. Bayoumy, M. Gaber, A. Elshafeey, O. Mhaimeed, E. H. Dineen, F. A. Marvel, S. S. Martin, E. D. Muse, M. P. Turakhia, K. G. Tarakji *et al.*, "Smart wearable devices in cardiovascular care: where we are and how to move forward," *Nature Reviews Cardiology*, vol. 18, no. 8, pp. 581–599, 2021, doi: https://doi.org/10.1038/s41569-021-00522-7.

[6] J. Lee, H. Kwon, J. Seo, S. Shin, J. H. Koo, C. Pang, S. Son, J. H. Kim, Y. H. Jang, D. E. Kim, and T. Lee, "Conductive fiber-based ultrasensitive textile pressure

sensor for wearable electronics," *Advanced Materials*, vol. 27, no. 15, pp. 2433–2439, 2015, doi: https://doi.org/10.1002/adma.201500009.

[7] M. Sibinski, M. Jakubowska, and M. Sloma, "Flexible temperature sensors on fibers," *Sensors*, vol. 10, no. 9, pp. 7934–7946, 2010, doi: https://doi.org/10.3390/s100907934.

[8] J. Deng, W. Zhuang, L. Bao, X. Wu, J. Gao, B. Wang, X. Sun, and H. Peng, "A tactile sensing textile with bending-independent pressure perception and spatial acuity," *Carbon*, vol. 149, pp. 63–70, 2019, doi: https://doi.org/10.1016/j.carbon.2019.04.019.

[9] W. A. D. M. Jayathilaka, K. Qi, Y. Qin, A. Chinnappan, W. Serrano-García, C. Baskar, H. Wang, J. He, S. Cui, S. W. Thomas *et al.*, "Significance of nanomaterials in wearables: a review on wearable actuators and sensors," *Advanced Materials*, vol. 31, no. 7, p. 1805921, 2019, doi: https://doi.org/10.1002/adma.201805921.

[10] N.-S. Jang, K.-H. Kim, S.-H. Ha, S.-H. Jung, H. M. Lee, and J.-M. Kim, "Simple approach to high-performance stretchable heaters based on kirigami patterning of conductive paper for wearable thermotherapy applications," *ACS applied materials & interfaces*, vol. 9, no. 23, pp. 19 612–19 621, 2017, doi: https://doi.org/10.1021/acsami.7b03474.

[11] W. H.-S. Huang, Y.-C. Wang, P.-C. Hsu, W.-C. Wang, A. Cavalier, T.-H. Huang, and C.-L. Shen, "Flexible led displays for electronic textiles," in *2018 International Flexible Electronics Technology Conference (IFETC)*. IEEE, 2018, pp. 1–3, doi: https://doi.org/10.1109/IFETC.2018.8583963.

[12] H. Baskan, H. Acikgoz, R. Atakan, H. Eryuruk, N. Akalın, H. Kose, Y. Li, S. K. Bahadir, and F. Kalaoglu, "Running functional sport vest and short for e-textile applications," in *IOP Conference Series: Materials Science and Engineering*, vol. 254, no. 7. IOP Publishing, 2017, p. 072004, doi: https://doi.org/10.1088/1757-899X/254/7/072004.

[13] A. Rabbitt, I. Horsfall, and D. Carr, "Effect of ballistic impacts on batteries and the potential for injury," *BMJ Mil Health*, vol. 166, no. 5, pp. 330–335, 2020, doi: http://dx.doi.org/10.1136/jramc-2018-001113.

[14] S. Lee, W. Ko, Y. Oh, J. Lee, G. Baek, Y. Lee, J. Sohn, S. Cha, J. Kim, J. Park *et al.*, "Triboelectric energy harvester based on wearable textile platforms employing various surface morphologies," *Nano Energy*, vol. 12, pp. 410–418, 2015, doi: https://doi.org/10.1016/j.nanoen.2015.01.009.

[15] Z. Tian, J. He, X. Chen, Z. Zhang, T. Wen, C. Zhai, J. Han, J. Mu, X. Hou, X. Chou *et al.*, "Performance-boosted triboelectric textile for harvesting human motion energy," *Nano Energy*, vol. 39, pp. 562–570, 2017, doi: https://doi.org/10.1016/j.nanoen.2017.06.018.

[16] F. Mokhtari, J. Foroughi, T. Zheng, Z. Cheng, and G. M. Spinks, "Triaxial braided piezo fiber energy harvesters for self-powered wearable technologies," *Journal of Materials Chemistry A*, vol. 7, no. 14, pp. 8245–8257, 2019, doi: https://doi.org/10.1039/C8TA10964H.

[17] A. Almusallam, Z. Luo, A. Komolafe, K. Yang, A. Robinson, R. Torah, and S. Beeby, "Flexible piezoelectric nano-composite films for kinetic energy harvesting from textiles," *Nano Energy*, vol. 33, pp. 146–156, 2017, doi: https://doi.org/10.1016/j.nanoen.2017.01.037.

[18] S. Arumugam, Y. Li, M. Glanc-Gostkiewicz, R. N. Torah, and S. P. Beeby, "Solution processed organic solar cells on textiles," *IEEE Journal of Photovoltaics*, vol. 8, no. 6, pp. 1710–1715, 2018, doi: https://doi.org/10.1109/JPHOTOV.2018.2871334.

[19] N. Hillier, S. Yong, and S. Beeby, "The good, the bad and the porous: A review of carbonaceous materials for flexible supercapacitor applications," *Energy Reports*, vol. 6, pp. 148–156, 2020, doi:10.1016/j.egyr.2020.03.019.

[20] S. Yong, N. Hillier, and S. Beeby, "The influence of textile substrate on the performance of multilayer fabric supercapacitors," *Journal of Industrial Textiles*, vol. 50, no. 9, pp. 1397–1408, 2021, doi:10.1177/1528083719865038.

[21] F. Scholz, "From the leiden jar to the discovery of the glass electrode by max cremer," *Journal of Solid State Electrochemistry*, vol. 15, no. 1, pp. 5–14, 2011, doi: https://doi.org/10.1007/s10008-009-0962-7.

[22] H. Kishi, Y. Mizuno, and H. Chazono, "Base-metal electrode-multilayer ceramic capacitors: past, present and future perspectives," *Japanese journal of applied physics*, vol. 42, no. 1R, p. 1, 2003, doi: https://doi.org/10.1143/JJAP.42.1.

[23] A. Morley and D. Campbell, "Electrolytic capacitors: Their fabrication and the interpretation of their operational behaviour," *Radio and Electronic Engineer*, vol. 43, no. 7, pp. 421–429, 1973, doi: https://doi.org/10.1049/ree.1973.0066.

[24] D. Goad and H. Uchi, "Modelling the capacitance of dc etched aluminium electrolytic capacitor foil," *Journal of applied electrochemistry*, vol. 30, no. 3, pp. 285–291, 2000, doi; https://doi.org/10.1023/A:1003527316173.

[25] K. S. Jang, B. Moon, E. J. Oh, and H. Lee, "Characteristics of tantalum electrolytic capacitors using soluble polypyrrole electrolyte," *Journal of power sources*, vol. 124, no. 1, pp. 338–342, 2003, doi: https://doi.org/10.1016/S0378-7753(03)00594-9.

[26] Y. Pozdeev, "Reliability comparison of tantalum and niobium solid electrolytic capacitors," *Quality and reliability engineering international*, vol. 14, no. 2, pp. 79–82, 1998, doi: https://doi.org/10.1002/(SICI)1099-1638(199803/04)14:2⟨79::AID-QRE163⟩3.0.CO;2-Y.

[27] H. Chen, T. N. Cong, W. Yang, C. Tan, Y. Li, and Y. Ding, "Progress in electrical energy storage system: A critical review," *Progress in natural science*, vol. 19, no. 3, pp. 291–312, 2009, doi: https://doi.org/10.1016/j.pnsc.2008.07.014.

[28] H. Ibrahim, A. Ilinca, and J. Perron, "Energy storage systems—characteristics and comparisons," *Renewable and sustainable energy reviews*, vol. 12, no. 5, pp. 1221–1250, 2008, doi: https://doi.org/10.1016/j.rser.2007.01.023.

[29] R. E. Araujo, R. de Castro, C. Pinto, P. Melo, and D. Freitas, "Combined sizing and energy management in evs with batteries and supercapacitors," *IEEE*

Transactions on Vehicular Technology, vol. 63, no. 7, pp. 3062–3076, 2014, doi: https://doi.org/10.1109/TVT.2014.2318275.

[30] L. Qu and W. Qiao, "Constant power control of dfig wind turbines with supercapacitor energy storage," *IEEE Transactions on Industry Applications*, vol. 47, no. 1, pp. 359–367, 2011, doi: 10.1109/TIA.2010.2090932.

[31] C. V. M. Gopi, R. Vinodh, S. Sambasivam, I. M. Obaidat, and H.-J. Kim, "Recent progress of advanced energy storage materials for flexible and wearable supercapacitor: From design and development to applications," *Journal of Energy Storage*, vol. 27, p. 101035, 2020, doi: https://doi.org/10.1016/j.est.2019.101035.

[32] M. Ren, J. Di, and W. Chen, "Recent progress and application challenges of wearable supercapacitors," *Batteries & Supercaps*, vol. 4, no. 8, pp. 1279–1290, 2021, doi: https://doi.org/10.1002/batt.202000333.

[33] C. Lu and X. Chen, "Latest advances in flexible symmetric supercapacitors: From material engineering to wearable applications," *Accounts of Chemical Research*, vol. 53, no. 8, pp. 1468–1477, 2020, doi: https://doi.org/10.1021/acs.accounts.0c00205.

[34] L. L. Zhang and X. S. Zhao, "Carbon-based materials as supercapacitor electrodes," *Chem. Soc. Rev.*, vol. 38, pp. 2520–2531, 2009, doi: https://doi.org/10.1039/B813846.

[35] A. Davies and A. Yu, "Material advancements in supercapacitors: From activated carbon to carbon nanotube and graphene," *The Canadian Journal of Chemical Engineering*, vol. 89, no. 6, pp. 1342–1357, 2011, doi: https://doi.org/10.1002/cjce.20586.

[36] O. Barbieri, M. Hahn, A. Herzog, and R. Kötz, "Capacitance limits of high surface area activated carbons for double layer capacitors," *Carbon*, vol. 43, no. 6, pp. 1303–1310, 2005, doi: https://doi.org/10.1016/j.carbon.2005.01.001.

[37] D. Qu, "Studies of the activated carbons used in double-layer supercapacitors," *Journal of Power Sources*, vol. 109, no. 2, pp. 403–411, 2002, doi: https://doi.org/10.1016/S0378-7753(02)00108-8.

[38] J. Gamby, P. Taberna, P. Simon, J. Fauvarque, and M. Chesneau, "Studies and characterisations of various activated carbons used for carbon/carbon supercapacitors," *Journal of Power Sources*, vol. 101, no. 1, pp. 109–116, 2001, doi: https://doi.org/10.1016/S0378-7753(01)00707-8.

[39] J. Chmiola, G. Yushin, R. Dash, and Y. Gogotsi, "Effect of pore size and surface area of carbide derived carbons on specific capacitance," *Journal of Power Sources*, vol. 158, no. 1, pp. 765–772, 2006, doi: https://doi.org/10.1016/j.jpowsour.2005.09.008.

[40] C. Largeot, C. Portet, J. Chmiola, P.-L. Taberna, Y. Gogotsi, and P. Simon, "Relation between the ion size and pore size for an electric double-layer capacitor," *Journal of the American Chemical Society*, vol. 130, no. 9, pp. 2730–2731, 2008, doi: https://doi.org/10.1021/ja7106178.

[41] J. Marañón Di Leo and J. Marañón, "Hydration and diffusion of cations in nanopores," *Journal of Molecular Structure: THEOCHEM*, vol. 729, no. 1, pp. 53–57, 2005, doi: https://doi.org/10.1016/j.theochem.2005.02.070.

[42] B. Conway, V. Birss, and J. Wojtowicz, "The role and utilization of pseudocapacitance for energy storage by supercapacitors," *Journal of Power Sources*, vol. 66, no. 1, pp. 1–14, 1997, doi: https://doi.org/10.1016/S0378-7753(96)02474-3.

[43] B. Conway and W. Pell, "Double-layer and pseudocapacitance types of electrochemical capacitors and their applications to the development of hybrid devices," *Journal of Solid State Electrochemistry*, vol. 7, no. 9, pp. 637–644, 2003, doi: https://doi.org/10.1007/s10008-003-0395-7.

[44] M. Zhi, C. Xiang, J. Li, M. Li, and N. Wu, "Nanostructured carbon–metal oxide composite electrodes for supercapacitors: a review," *Nanoscale*, vol. 5, pp. 72–88, 2013, doi: https://doi.org/10.1039/C2NR32040A.

[45] T. Brousse, D. Bélanger, and J. W. Long, "To be or not to be pseudocapacitive?" *Journal of The Electrochemical Society*, vol. 162, no. 5, pp. A5185–A5189, 2015, doi: https://doi.org/10.1149/2.0201505jes.

[46] V. á Augustyn, J. á Come, M. á Lowe, J. á Kim, and P. á Taberna, "High-rate electrochemical energy storage through li intercalation pseudocapacitance," *Nat. Mater*, vol. 12, p. 518, 2013, doi: https://doi.org/10.1038/nmat3601.

[47] E. Herrero, L. J. Buller, and H. D. Abruña, "Underpotential deposition at single crystal surfaces of au, pt, ag and other materials," *Chemical Reviews*, vol. 101, no. 7, pp. 1897–1930, 2001, doi: https://doi.org/10.1021/cr9600363.

[48] B. Conway and H. Angerstein-Kozlowska, "Interaction effects in electrodeposited monolayers and the role of the "electrosorption valency" factor," *Journal of Electroanalytical Chemistry and Interfacial Electrochemistry*, vol. 113, no. 1, pp. 63–77, 1980, doi: https://doi.org/10.1016/S0022-0728(80)80511-0.

[49] J. T. Mefford, W. G. Hardin, S. Dai, K. P. Johnston, and K. J. Stevenson, "Anion charge storage through oxygen intercalation in lamno3 perovskite pseudocapacitor electrodes," *Nature materials*, vol. 13, no. 7, pp. 726–732, 2014, doi: https://doi.org/10.1038/nmat4000.

[50] J. P. Zheng and T. R. Jow, "A new charge storage mechanism for electrochemical capacitors," *Journal of The Electrochemical Society*, vol. 142, no. 1, pp. L6–L8, jan 1995, doi: https://doi.org/10.1149/1.2043984.

[51] J. Wen and Z. Zhou, "Pseudocapacitance characterization of hydrous ruthenium oxide prepared via cyclic voltammetric deposition," *Materials Chemistry and Physics*, vol. 98, no. 2, pp. 442–446, 2006, doi: https://doi.org/10.1016/j.matchemphys.2005.09.079.

[52] B. Ütebay, P. Çelik, and A. Çay, "Effects of cotton textile waste properties on recycled fibre quality," *Journal of Cleaner Production*, vol. 222, pp. 29–35, 2019, doi: https://doi.org/10.1016/j.jclepro.2019.03.033.

[53] S. Yong, N. Hillier, and S. P. Beeby, "Phase-inverted copolymer membrane for the enhancement of textile supercapacitors," *Polymers*, vol. 14, no. 16, 2022, doi: https://doi.org/10.3390/polym14163399.

[54] G. Xia, W. Han, Z. Xu, J. Zhang, F. Kong, J. Zhang, X. Zhang, and F. Jia, "Complete recycling and valorization of waste textiles for value-added

transparent films via an ionic liquid," *Journal of Environmental Chemical Engineering*, vol. 9, no. 5, p. 106182, 2021, doi: https://doi.org/10.1016/j.jece.2021.106182.

[55] Clarivate. (2022) Web of science. [Online]. Available: https://www.webofscience.com/wos/woscc/basic-search

[56] S. Yong, J. Owen, and S. Beeby, "Solid-state supercapacitor fabricated in a single woven textile layer for e-textiles applications," *Advanced Engineering Materials*, vol. 20, no. 5, p. 1700860, 2018, doi: https://doi.org/10.1002/adem.201700860.

[57] C. Choi, J. W. Park, K. J. Kim, D. W. Lee, M. J. de Andrade, S. H. Kim, S. Gambhir, G. M. Spinks, R. H. Baughman, and S. J. Kim, "Weavable asymmetric carbon nanotube yarn supercapacitor for electronic textiles," *RSC Adv.*, vol. 8, pp. 13 112–13 120, 2018, doi: http://dx.doi.org/10.1039/C8RA01384E.

[58] L. Kou, T. Huang, B. Zheng, Y. Han, X. Zhao, K. Gopalsamy, H. Sun, and C. Gao, "Coaxial wet-spun yarn supercapacitors for high-energy density and safe wearable electronics," *Nature communications*, vol. 5, no. 1, pp. 1–10, 2014, doi: https://doi.org/10.1038/ncomms4754.

[59] T. Otowa, Y. Nojima, and T. Miyazaki, "Development of koh activated high surface area carbon and its application to drinking water purification," *Carbon*, vol. 35, no. 9, pp. 1315–1319, 1997, doi: https://doi.org/10.1016/S0008-6223(97)00076-6.

[60] Y. M. Shulga, E. N. Kabachkov, V. I. Korepanov, I. I. Khodos, D. Y. Kovalev, A. V. Melezhik, A. G. Tkachev, and G. L. Gutsev, "The concentration of c(sp3) atoms and properties of an activated carbon with over 3000 m2/g bet surface area," *Nanomaterials*, vol. 11, no. 5, 2021, doi: https://www.mdpi.com/2079-4991/11/5/1324.

[61] J. A. Libra, K. S. Ro, C. Kammann, A. Funke, N. D. Berge, Y. Neubauer, M.-M. Titirici, C. Fühner, O. Bens, J. Kern, and K.-H. Emmerich, "Hydrothermal carbonization of biomass residuals: a comparative review of the chemistry,

processes and applications of wet and dry pyrolysis," *Biofuels*, vol. 2, no. 1, pp. 71–106, 2011, doi: https://doi.org/10.4155/bfs.10.81.

[62] M. Pecchi and M. Baratieri, "Coupling anaerobic digestion with gasification, pyrolysis or hydrothermal carbonization: A review," *Renewable and Sustainable Energy Reviews*, vol. 105, pp. 462–475, 2019, doi: https://doi.org/10.1016/j.rser.2019.02.003.

[63] A. Funke and F. Ziegler, "Hydrothermal carbonization of biomass: A summary and discussion of chemical mechanisms for process engineering," *Biofuels, Bioproducts and Biorefining*, vol. 4, no. 2, pp. 160–177, 2010, doi: https://onlinelibrary.wiley.com/doi/abs/10.1002/bbb.198.

[64] N. Mohamad Nor, L. C. Lau, K. T. Lee, and A. R. Mohamed, "Synthesis of activated carbon from lignocellulosic biomass and its applications in air pollution control—a review," *Journal of Environmental Chemical Engineering*, vol. 1, no. 4, pp. 658–666, 2013, doi: https://doi.org/10.1016/j.jece.2013.09.017.

[65] G. Cruz, M. Pirilä, M. Huuhtanen, L. Carrión, E. Alvarenga, and R. L. Keiski, "Production of activated carbon from cocoa (theobroma cacao) pod husk," *J. Civ. Environ. Eng*, vol. 2, no. 2, pp. 1–6, 2012, doi: http://dx.doi.org/10.4172/2165-784X.1000109.

[66] J. Romanos, M. Beckner, T. Rash, L. Firlej, B. Kuchta, P. Yu, G. Suppes, C. Wexler, and P. Pfeifer, "Nanospace engineering of koh activated carbon," *Nanotechnology*, vol. 23, no. 1, p. 015401, dec 2011, doi: https://doi.org/10.1088/0957-4484/23/1/015401.

[67] A. Jain, R. Balasubramanian, and M. Srinivasan, "Hydrothermal conversion of biomass waste to activated carbon with high porosity: A review," *Chemical Engineering Journal*, vol. 283, pp. 789–805, 2016, doi: https://doi.org/10.1016/j.cej.2015.08.014.

[68] M.-M. Titirici, R. J. White, C. Falco, and M. Sevilla, "Black perspectives for a green future: hydrothermal carbons for environment protection and energy

storage," *Energy Environ. Sci.*, vol. 5, pp. 6796–6822, 2012, doi: http://dx.doi.org/10.1039/C2EE21166A.

[69] M. A. Yahya, Z. Al-Qodah, and C. Z. Ngah, "Agricultural bio-waste materials as potential sustainable precursors used for activated carbon production: A review," *Renewable and Sustainable Energy Reviews*, vol. 46, pp. 218–235, 2015, doi: https://doi.org/10.1016/j.rser.2015.02.051.

[70] S. Román, J. Libra, N. Berge, E. Sabio, K. Ro, L. Li, B. Ledesma, A. Álvarez, and S. Bae, "Hydrothermal carbonization: Modeling, final properties design and applications: A review," *Energies*, vol. 11, no. 1, 2018, doi: https://doi.org/10.3390/en11010216.

[71] A. M. Abioye and F. N. Ani, "Recent development in the production of activated carbon electrodes from agricultural waste biomass for supercapacitors: A review," *Renewable and Sustainable Energy Reviews*, vol. 52, pp. 1282–1293, 2015, doi: https://doi.org/10.1016/j.rser.2015.07.129.

[72] K. Jost, C. R. Perez, J. K. McDonough, V. Presser, M. Heon, G. Dion, and Y. Gogotsi, "Carbon coated textiles for flexible energy storage," *Energy Environ. Sci.*, vol. 4, pp. 5060–5067, 2011, doi: http://dx.doi.org/10.1039/C1EE02421C.

[73] J. Xue, Y. Zhao, H. Cheng, C. Hu, Y. Hu, Y. Meng, H. Shao, Z. Zhang, and L. Qu, "An all-cotton-derived, arbitrarily foldable, high-rate, electrochemical supercapacitor," *Phys. Chem. Chem. Phys.*, vol. 15, pp. 8042–8045, 2013, doi: http://dx.doi.org/10.1039/C3CP51571K.

[74] C.-I. Su, W.-C. Shih, C.-M. Wang, Y.-S. Liu, and S.-P. Wu, "Effect of high temperature treatment on electrochemical properties of activated carbon fabric in supercapacitor application," *Fibers and Polymers*, vol. 14, no. 11, pp. 1808–1816, 2013, doi: https://doi.org/10.1007/s12221-013-1808-6.

[75] D. Kong, W. Ren, C. Cheng, Y. Wang, Z. Huang, and H. Y. Yang, "Three-dimensional nico2o4@polypyrrole coaxial nanowire arrays on carbon textiles for high-performance flexible asymmetric solid-state supercapacitor,"

ACS Applied Materials & Interfaces, vol. 7, no. 38, pp. 21 334–21 346, 2015, doi: https://doi.org/10.1021/acsami.5b05908.

[76] S. Senthilkumar, N. Fu, Y. Liu, Y. Wang, L. Zhou, and H. Huang, "Flexible fiber hybrid supercapacitor with nico2o4 nanograss@carbon fiber and bio-waste derived high surface area porous carbon," *Electrochimica Acta*, vol. 211, pp. 411–419, 2016, doi: https://doi.org/10.1016/j.electacta.2016.06.059.

[77] X. Lu, Y. Bai, R. Wang, and J. Sun, "A high-performance flexible and weavable asymmetric fiber-shaped solid-state supercapacitor enhanced by surface modifications of carbon fibers with carbon nanotubes," *J. Mater. Chem. A*, vol. 4, pp. 18 164–18 173, 2016, doi: http://dx.doi.org/10.1039/C6TA08233E.

[78] P.-W. Xiao, Q. Meng, L. Zhao, J.-J. Li, Z. Wei, and B.-H. Han, "Biomass-derived flexible porous carbon materials and their applications in supercapacitor and gas adsorption," *Materials & Design*, vol. 129, pp. 164–172, 2017, doi: https://doi.org/10.1016/j.matdes.2017.05.035.

[79] W. Zhang, R. Guo, J. Sun, L. Dang, Z. Liu, Z. Lei, and Q. Sun, "Textile carbon network with enhanced areal capacitance prepared by chemical activation of cotton cloth," *Journal of Colloid and Interface Science*, vol. 553, pp. 705–712, 2019, doi: https://doi.org/10.1016/j.jcis.2019.06.048.

[80] C. Yang, L. Hu, L. Zang, Q. Liu, J. Qiu, J. Yang, and X. Qiao, "High-performance all-solid-state supercapacitor based on activated carbon coated fiberglass cloth using asphalt as active binder," *Journal of The Electrochemical Society*, vol. 167, no. 2, p. 020540, jan 2020, doi: https://doi.org/10.1149/1945-7111/ab6bbb.

[81] S. Park and R. S. Ruoff, "Chemical methods for the production of graphenes," *Nature nanotechnology*, vol. 4, no. 4, pp. 217–224, 2009, doi: https://doi.org/10.1038/nnano.2009.58.

[82] Y. Shao, M. F. El-Kady, L. J. Wang, Q. Zhang, Y. Li, H. Wang, M. F. Mousavi, and R. B. Kaner, "Graphene-based materials for flexible supercapacitors," *Chem. Soc. Rev.*, vol. 44, pp. 3639–3665, 2015, doi: http://dx.doi.org/10.1039/C4CS00316K.

[83] N. Karousis, N. Tagmatarchis, and D. Tasis, "Current progress on the chemical modification of carbon nanotubes," *Chemical Reviews*, vol. 110, no. 9, pp. 5366–5397, 2010, doi: https://doi.org/10.1021/cr100018g.

[84] K. A. Shah and B. A. Tali, "Synthesis of carbon nanotubes by catalytic chemical vapour deposition: A review on carbon sources, catalysts and substrates," *Materials Science in Semiconductor Processing*, vol. 41, pp. 67–82, 2016, doi: https://doi.org/10.1016/j.mssp.2015.08.013.

[85] E. Couteau, K. Hernadi, J. Seo, L. Thiên-Nga, C. Mikó, R. Gaál, and L. Forró, "Cvd synthesis of high-purity multiwalled carbon nanotubes using caco3 catalyst support for large-scale production," *Chemical Physics Letters*, vol. 378, no. 1, pp. 9–17, 2003, doi: https://doi.org/10.1016/S0009-2614(03)01218-1.

[86] L. Dong, C. Xu, Q. Yang, J. Fang, Y. Li, and F. Kang, "High-performance compressible supercapacitors based on functionally synergic multiscale carbon composite textiles," *J. Mater. Chem. A*, vol. 3, pp. 4729–4737, 2015, doi: http://dx.doi.org/10.1039/C4TA06494A.

[87] D.-W. Wang, F. Li, M. Liu, G. Lu, and H.-M. Cheng, "3d aperiodic hierarchical porous graphitic carbon material for high-rate electrochemical capacitive energy storage," *Angewandte Chemie International Edition*, vol. 47, no. 2, pp. 373–376, 2008, doi: https://doi.org/10.1002/anie.200702721.

[88] W. Li, D. Chen, Z. Li, Y. Shi, Y. Wan, G. Wang, Z. Jiang, and D. Zhao, "Nitrogen-containing carbon spheres with very large uniform mesopores: The superior electrode materials for edlc in organic electrolyte," *Carbon*, vol. 45, no. 9, pp. 1757–1763, 2007, doi: https://doi.org/10.1016/j.carbon.2007.05.004.

[89] P. Lorjai, T. Chaisuwan, and S. Wongkasemjit, "Porous structure of polybenzoxazine-based organic aerogel prepared by sol–gel process and their carbon aerogels," *Journal of sol-gel science and technology*, vol. 52, no. 1, pp. 56–64, 2009, doi: https://doi.org/10.1007/s10971-009-1992-4.

[90] Y. Han and L. Dai, "Conducting polymers for flexible supercapacitors," *Macromolecular Chemistry and Physics*, vol. 220, no. 3, p. 1800355, 2019, doi: https://doi.org/10.1002/macp.201800355.

[91] Q. Meng, K. Cai, Y. Chen, and L. Chen, "Research progress on conducting polymer based supercapacitor electrode materials," *Nano Energy*, vol. 36, pp. 268–285, 2017, doi: https://doi.org/10.1016/j.nanoen.2017.04.040.

[92] P. Naskar, A. Maiti, P. Chakraborty, D. Kundu, B. Biswas, and A. Banerjee, "Chemical supercapacitors: a review focusing on metallic compounds and conducting polymers," *J. Mater. Chem. A*, vol. 9, pp. 1970–2017, 2021, doi: http://dx.doi.org/10.1039/D0TA09655E.

[93] E. Frackowiak, V. Khomenko, K. Jurewicz, K. Lota, and F. Béguin, "Supercapacitors based on conducting polymers/nanotubes composites," *Journal of Power Sources*, vol. 153, no. 2, pp. 413–418, 2006, doi: https://doi.org/10.1016/j.jpowsour.2005.05.030. [Online]. Available: https://www.sciencedirect.com/science/article/pii/S0378775305007391

[94] H. Wang, Q. Hao, X. Yang, L. Lu, and X. Wang, "Graphene oxide doped polyaniline for supercapacitors," *Electrochemistry Communications*, vol. 11, no. 6, pp. 1158–1161, 2009, doi: https://doi.org/10.1016/j.elecom.2009.03.036.

[95] Q.-Z. Zhang, D. Zhang, Z.-C. Miao, X.-L. Zhang, and S.-L. Chou, "Research progress in mno2–carbon based supercapacitor electrode materials," *Small*, vol. 14, no. 24, p. 1702883, 2018, doi: https://doi.org/10.1002/smll.201702883.

[96] M. Toupin, T. Brousse, and D. Bélanger, "Charge storage mechanism of mno2 electrode used in aqueous electrochemical capacitor," *Chemistry of Materials*, vol. 16, no. 16, pp. 3184–3190, 2004, doi: https://doi.org/10.1021/cm049649j.

[97] J. Liu, J. Essner, and J. Li, "Hybrid supercapacitor based on coaxially coated manganese oxide on vertically aligned carbon nanofiber arrays," *Chemistry of Materials*, vol. 22, no. 17, pp. 5022–5030, 2010, doi: https://doi.org/10.1021/cm101591p.

[98] L. Yuan, X.-H. Lu, X. Xiao, T. Zhai, J. Dai, F. Zhang, B. Hu, X. Wang, L. Gong, J. Chen, C. Hu, Y. Tong, J. Zhou, and Z. L. Wang, "Flexible solid-state supercapacitors based on carbon nanoparticles/mno2 nanorods hybrid structure," *ACS Nano*, vol. 6, no. 1, pp. 656–661, 2012, doi: https://doi.org/10.1021/nn2041279.

[99] N. Liu, Y. Su, Z. Wang, Z. Wang, J. Xia, Y. Chen, Z. Zhao, Q. Li, and F. Geng, "Electrostatic-interaction-assisted construction of 3d networks of manganese dioxide nanosheets for flexible high-performance solid-state asymmetric supercapacitors," *ACS Nano*, vol. 11, no. 8, pp. 7879–7888, 2017, doi: https://doi.org/10.1021/acsnano.7b02344.

[100] K. Fic, G. Lota, M. Meller, and E. Frackowiak, "Novel insight into neutral medium as electrolyte for high-voltage supercapacitors," *Energy Environ. Sci.*, vol. 5, pp. 5842–5850, 2012, doi: http://dx.doi.org/10.1039/C1EE02262H.

[101] L.-N. Jin, P. Liu, C. Jin, J.-N. Zhang, and S.-W. Bian, "Porous wo3/graphene/polyester textile electrode materials with enhanced electrochemical performance for flexible solid-state supercapacitors," *Journal of Colloid and Interface Science*, vol. 510, pp. 1–11, 2018, doi: https://doi.org/10.1016/j.jcis.2017.08.103.

[102] X. Pu, L. Li, M. Liu, C. Jiang, C. Du, Z. Zhao, W. Hu, and Z. L. Wang, "Wearable self-charging power textile based on flexible yarn supercapacitors and fabric nanogenerators," *Advanced Materials*, vol. 28, no. 1, pp. 98–105, 2016, doi: https://doi.org/10.1002/adma.201504403.

[103] J. Noh, C.-M. Yoon, Y. K. Kim, and J. Jang, "High performance asymmetric supercapacitor twisted from carbon fiber/mno2 and carbon fiber/moo3," *Carbon*, vol. 116, pp. 470–478, 2017, doi: https://doi.org/10.1016/j.carbon.2017.02.033.

[104] G. Wang, L. Zhang, and J. Zhang, "A review of electrode materials for electrochemical supercapacitors," *Chem. Soc. Rev.*, vol. 41, pp. 797–828, 2012, doi: http://dx.doi.org/10.1039/C1CS15060J.

[105] C. Choi, J. W. Park, K. J. Kim, D. W. Lee, M. J. de Andrade, S. H. Kim, S. Gambhir, G. M. Spinks, R. H. Baughman, and S. J. Kim, "Weavable asymmetric carbon nanotube yarn supercapacitor for electronic textiles," *RSC Adv.*, vol. 8, pp. 13 112–13 120, 2018, doi: http://dx.doi.org/10.1039/C8RA01384E.

[106] K. Keum, G. Lee, H. Lee, J. Yun, H. Park, S. Y. Hong, C. Song, J. W. Kim, and J. S. Ha, "Wire-shaped supercapacitors with organic electrolytes fabricated via layer-by-layer assembly," *ACS Applied Materials & Interfaces*, vol. 10, no. 31, pp. 26 248–26 257, 2018, doi: https://doi.org/10.1021/acsami.8b07113.

[107] H. Park, J. W. Kim, S. Y. Hong, G. Lee, H. Lee, C. Song, K. Keum, Y. R. Jeong, S. W. Jin, D. S. Kim, and J. S. Ha, "Dynamically stretchable supercapacitor for powering an integrated biosensor in an all-in-one textile system," *ACS Nano*, vol. 13, no. 9, pp. 10 469–10 480, 2019, doi: https://doi.org/10.1021/acsnano.9b04340.

[108] G. Lee, J. W. Kim, H. Park, J. Y. Lee, H. Lee, C. Song, S. W. Jin, K. Keum, C.-H. Lee, and J. S. Ha, "Skin-like, dynamically stretchable, planar supercapacitors with buckled carbon nanotube/mn–mo mixed oxide electrodes and air-stable organic electrolyte," *ACS Nano*, vol. 13, no. 1, pp. 855–866, 2019, doi: https://doi.org/10.1021/acsnano.8b08645.

[109] A. Balducci, R. Dugas, P. Taberna, P. Simon, D. Plée, M. Mastragostino, and S. Passerini, "High temperature carbon–carbon supercapacitor using ionic liquid as electrolyte," *Journal of Power Sources*, vol. 165, no. 2, pp. 922–927, 2007, doi: https://doi.org/10.1016/j.jpowsour.2006.12.048.

[110] C.-y. Hui, C.-w. Kan, C.-l. Mak, and K.-h. Chau, "Flexible energy storage system—an introductory review of textile-based flexible supercapacitors," *Processes*, vol. 7, no. 12, 2019, doi: https://doi.org/10.3390/pr7120922.

[111] Z. Lu, Y. Chao, Y. Ge, J. Foroughi, Y. Zhao, C. Wang, H. Long, and G. G. Wallace, "High-performance hybrid carbon nanotube fibers for wearable energy storage," *Nanoscale*, vol. 9, pp. 5063–5071, 2017, doi: http://dx.doi.org/10.1039/C7NR00408G.

[112] A. M. Abdelkader, N. Karim, C. Vallés, S. Afroj, K. S. Novoselov, and S. G. Yeates, "Ultraflexible and robust graphene supercapacitors printed on textiles for wearable electronics applications," *2D Materials*, vol. 4, no. 3, p. 035016, jul 2017, doi: https://doi.org/10.1088/2053-1583/aa7d71.

[113] Y. Yang, Q. Huang, L. Niu, D. Wang, C. Yan, Y. She, and Z. Zheng, "Waterproof, ultrahigh areal-capacitance, wearable supercapacitor fabrics," *Advanced Materials*, vol. 29, no. 19, p. 1606679, 2017, doi: https://doi.org/10.1002/adma.201606679.

[114] M. Zhu, Y. Huang, Y. Huang, H. Li, Z. Wang, Z. Pei, Q. Xue, H. Geng, and C. Zhi, "A highly durable, transferable, and substrate-versatile high-performance all-polymer micro-supercapacitor with plug-and-play function," *Advanced Materials*, vol. 29, no. 16, p. 1605137, 2017, doi: https://doi.org/10.1002/adma.201605137.

[115] J. Yu, W. Lu, J. P. Smith, K. S. Booksh, L. Meng, Y. Huang, Q. Li, J.-H. Byun, Y. Oh, Y. Yan, and T.-W. Chou, "A high performance stretchable asymmetric fiber-shaped supercapacitor with a core-sheath helical structure," *Advanced Energy Materials*, vol. 7, no. 3, p. 1600976, 2017, doi: https://doi.org/10.1002/aenm.201600976.

[116] T. Qin, S. Peng, J. Hao, Y. Wen, Z. Wang, X. Wang, D. He, J. Zhang, J. Hou, and G. Cao, "Flexible and wearable all-solid-state supercapacitors with ultrahigh energy density based on a carbon fiber fabric electrode," *Advanced Energy Materials*, vol. 7, no. 20, p. 1700409, 2017, doi: https://doi.org/10.1002/aenm.201700409.

[117] K. Qi, R. Hou, S. Zaman, Y. Qiu, B. Y. Xia, and H. Duan, "Construction of metal–organic framework/conductive polymer hybrid for all-solid-state fabric supercapacitor," *ACS Applied Materials & Interfaces*, vol. 10, no. 21, pp. 18 021–18 028, 2018, doi: https://doi.org/10.1021/acsami.8b05802.

[118] L. Gao, J. Song, J. U. Surjadi, K. Cao, Y. Han, D. Sun, X. Tao, and Y. Lu, "Graphene-bridged multifunctional flexible fiber supercapacitor with high

energy density," *ACS Applied Materials & Interfaces*, vol. 10, no. 34, pp. 28 597–28 607, 2018, doi: https://doi.org/10.1021/acsami.8b08680.

[119] D. Tian, X. Lu, G. Nie, M. Gao, and C. Wang, "Direct growth of ni–mn–o nanosheets on flexible electrospun carbon nanofibers for high performance supercapacitor applications," *Inorg. Chem. Front.*, vol. 5, pp. 635–642, 2018, doi: http://dx.doi.org/10.1039/C7QI00696A.

[120] C. Yu, Y. Gong, R. Chen, M. Zhang, J. Zhou, J. An, F. Lv, S. Guo, and G. Sun, "A solid-state fibriform supercapacitor boosted by host–guest hybridization between the carbon nanotube scaffold and mxene nanosheets," *Small*, vol. 14, no. 29, p. 1801203, 2018, doi: https://doi.org/10.1002/smll.201801203.

[121] H. Jeon, J. Jeong, S. B. Hong, M. Yang, J. Park, D. H. Kim, S. Y. Hwang, and B. G. Choi, "Facile and fast microwave-assisted fabrication of activated and porous carbon cloth composites with graphene and mno2 for flexible asymmetric supercapacitors," *Electrochimica Acta*, vol. 280, pp. 9–16, 2018, doi: https://doi.org/10.1016/j.electacta.2018.05.108.

[122] A. Paleo, P. Staiti, A. Brigandì, F. Ferreira, A. Rocha, and F. Lufrano, "Supercapacitors based on ac/mno2 deposited onto dip-coated carbon nanofiber cotton fabric electrodes," *Energy Storage Materials*, vol. 12, pp. 204–215, 2018, doi: https://doi.org/10.1016/j.ensm.2017.12.013.

[123] Y.-N. Liu, H.-T. Wang, X.-H. Kang, Y.-F. Wang, S.-Y. Yang, and S.-W. Bian, "Cotton fabric and zeolitic imidazolate framework (zif-8) derived hierarchical nitrogen-doped porous carbon nanotubes/carbon fabric electrodes for all-solid-state supercapacitors," *Journal of Power Sources*, vol. 402, pp. 413–421, 2018, doi: https://doi.org/10.1016/j.jpowsour.2018.09.052.

[124] M. Liu, Z. Cong, X. Pu, W. Guo, T. Liu, M. Li, Y. Zhang, W. Hu, and Z. L. Wang, "High-energy asymmetric supercapacitor yarns for self-charging power textiles," *Advanced Functional Materials*, vol. 29, no. 41, p. 1806298, 2019, doi: https://doi.org/10.1002/adfm.201806298.

[125] M. Zhang, M. Zhao, M. Jian, C. Wang, A. Yu, Z. Yin, X. Liang, H. Wang, K. Xia, X. Liang, J. Zhai, and Y. Zhang, "Printable smart pattern for multifunctional energy-management e-textile," *Matter*, vol. 1, no. 1, pp. 168–179, 2019, doi: https://doi.org/10.1016/j.matt.2019.02.003.

[126] D. Wang, A. Wei, L. Tian, A. Mensah, D. Li, Y. Xu, and Q. Wei, "Nickel-cobalt layered double hydroxide nanosheets with reduced graphene oxide grown on carbon cloth for symmetric supercapacitor," *Applied Surface Science*, vol. 483, pp. 593–600, 2019, doi: https://doi.org/10.1016/j.apsusc.2019.03.345.

[127] Y.-F. Wang, H.-T. Wang, S.-Y. Yang, Y. Yue, and S.-W. Bian, "Hierarchical nico2s4@nickel–cobalt layered double hydroxide nanotube arrays on metallic cotton yarns for flexible supercapacitors," *ACS Applied Materials & Interfaces*, vol. 11, no. 33, pp. 30 384–30 390, 2019, doi: https://doi.org/10.1021/acsami.9b06317.

[128] S. Uzun, S. Seyedin, A. L. Stoltzfus, A. S. Levitt, M. Alhabeb, M. Anayee, C. J. Strobel, J. M. Razal, G. Dion, and Y. Gogotsi, "Knittable and washable multifunctional mxene-coated cellulose yarns," *Advanced Functional Materials*, vol. 29, no. 45, p. 1905015, 2019, doi: https://doi.org/10.1002/adfm.201905015.

[129] D. Wu and W. Zhong, "A new strategy for anchoring a functionalized graphene hydrogel in a carbon cloth network to support a lignosulfonate/polyaniline hydrogel as an integrated electrode for flexible high areal-capacitance supercapacitors," *J. Mater. Chem. A*, vol. 7, pp. 5819–5830, 2019, doi: http://dx.doi.org/10.1039/C8TA11153G.

[130] G. Li, H. Cai, X. Li, J. Zhang, D. Zhang, Y. Yang, and J. Xiong, "Construction of hierarchical nico2o4@ni-mof hybrid arrays on carbon cloth as superior battery-type electrodes for flexible solid-state hybrid supercapacitors," *ACS Applied Materials & Interfaces*, vol. 11, no. 41, pp. 37 675–37 684, 2019, doi: https://doi.org/10.1021/acsami.9b11994.

[131] T. Khudiyev, J. T. Lee, J. R. Cox, E. Argentieri, G. Loke, R. Yuan, G. H. Noel, R. Tatara, Y. Yu, F. Logan, J. Joannopoulos, Y. Shao-Horn, and Y. Fink, "100 m

long thermally drawn supercapacitor fibers with applications to 3d printing and textiles," *Advanced Materials*, vol. 32, no. 49, p. 2004971, 2020, doi: https://doi.org/10.1002/adma.202004971.

[132] Y. Wang, X. Wang, X. Li, X. Li, Y. Liu, Y. Bai, H. Xiao, and G. Yuan, "A high-performance, tailorable, wearable, and foldable solid-state supercapacitor enabled by arranging pseudocapacitive groups and mxene flakes on textile electrode surface," *Advanced Functional Materials*, vol. 31, no. 7, p. 2008185, 2021, doi: https://doi.org/10.1002/adfm.202008185.

[133] L. Manjakkal, A. Pullanchiyodan, N. Yogeswaran, E. S. Hosseini, and R. Dahiya, "A wearable supercapacitor based on conductive pedot:pss-coated cloth and a sweat electrolyte," *Advanced Materials*, vol. 32, no. 24, p. 1907254, 2020, doi: https://doi.org/10.1002/adma.201907254.

[134] S. Afroj, S. Tan, A. M. Abdelkader, K. S. Novoselov, and N. Karim, "Highly conductive, scalable, and machine washable graphene-based e-textiles for multifunctional wearable electronic applications," *Advanced Functional Materials*, vol. 30, no. 23, p. 2000293, 2020, doi: https://doi.org/10.1002/adfm.202000293.

[135] D. Wang, L. Tian, J. Huang, D. Li, J. Liu, Y. Xu, H. Ke, and Q. Wei, ""one for two" strategy to prepare mof-derived nico2s4 nanorods grown on carbon cloth for high-performance asymmetric supercapacitors and efficient oxygen evolution reaction," *Electrochimica Acta*, vol. 334, p. 135636, 2020, doi: https://doi.org/10.1016/j.electacta.2020.135636.

[136] M. Zhang, X. Wang, T. Yang, P. Zhang, X. Wei, L. Zhang, and H. Li, "Polyaniline/graphene hybrid fibers as electrodes for flexible supercapacitors," *Synthetic Metals*, vol. 268, p. 116484, 2020, doi: https://doi.org/10.1016/j.synthmet.2020.116484.

[137] Y. Mao, Y. Li, J. Xie, H. Liu, C. Guo, and W. Hu, "Triboelectric nanogenerator/supercapacitor in-one self-powered textile based on ptfe yarn wrapped pdms/mno2nw hybrid elastomer," *Nano Energy*, vol. 84, p. 105918, 2021, doi: https://doi.org/10.1016/j.nanoen.2021.105918.

[138] Z. Stempien, M. Khalid, M. Kozanecki, P. Filipczak, A. Wrzesińska, E. Korzeniewska, and E. Sasiadek, "Inkjet printing of polypyrrole electroconductive layers based on direct inks freezing and their use in textile solid state supercapacitors," *Materials*, vol. 14, no. 13, 2021, doi: https://doi.org/10.3390/ma14133577.

[139] Z. Karami, M. Youssefi, K. Raeissi, and M. Zhiani, "An efficient textile-based electrode utilizing silver nanoparticles/reduced graphene oxide/cotton fabric composite for high-performance wearable supercapacitors," *Electrochimica Acta*, vol. 368, p. 137647, 2021, doi: https://doi.org/10.1016/j.electacta.2020.137647.

[140] J. Lee and G. An, "Surface-engineered flexible fibrous supercapacitor electrode for improved electrochemical performance," *Applied Surface Science*, vol. 539, p. 148290, 2021, doi: https://doi.org/10.1016/j.apsusc.2020.148290.

[141] Z. Li, M. Li, Q. Fan, X. Qi, L. Qu, and M. Tian, "Smart-fabric-based supercapacitor with long-term durability and waterproof properties toward wearable applications," *ACS Applied Materials & Interfaces*, vol. 13, no. 12, pp. 14 778–14 785, 2021, doi: https://doi.org/10.1021/acsami.1c02615.

[142] X. Wu, Y. Chen, K. Liang, X. Yu, Q. Zhuang, Q. Yang, S. Liu, S. Liao, N. Li, and H. Zhang, "Fe2o3 nanowire arrays on ni-coated yarns as excellent electrodes for high performance wearable yarn-supercapacitor," *Journal of Alloys and Compounds*, vol. 866, p. 158156, 2021, doi: https://doi.org/10.1016/j.jallcom.2020.158156.

[143] J. Lv, Z. Liu, L. Zhang, K. Li, S. Zhang, H. Xu, Z. Mao, H. Zhang, J. Chen, and G. Pan, "Multifunctional polypyrrole and rose-like silver flower-decorated e-textile with outstanding pressure/strain sensing and energy storage performance," *Chemical Engineering Journal*, vol. 427, p. 130823, 2022, doi: https://doi.org/10.1016/j.cej.2021.130823.

[144] M. S. Islam, S. N. Faisal, L. Tong, A. Roy, J. Zhang, E. Haque, A. I. Minett, and C. H. Wang, "N-doped reduced graphene oxide (rgo) wrapped carbon microfibers as binder-free electrodes for flexible fibre supercapacitors and

sodium-ion batteries," *Journal of Energy Storage*, vol. 37, p. 102453, 2021, doi: https://doi.org/10.1016/j.est.2021.102453.

[145] M. Smith and S. Kar-Narayan, "Piezoelectric polymers: theory, challenges and opportunities," *International Materials Reviews*, vol. 67, no. 1, pp. 65–88, 2022, doi: https://doi.org/10.1080/09506608.2021.1915935.

[146] M. Fang, S. Rajput, Z. Dai, Y. Ji, Y. Hao, and X. Ren, "Understanding the mechanism of thermal-stable high-performance piezoelectricity," *Acta Materialia*, vol. 169, pp. 155–161, 2019, doi: https://doi.org/10.1016/j.actamat.2019.03.011.

[147] A. Komolafe, B. Zaghari, R. Torah, A. S. Weddell, H. Khanbareh, Z. M. Tsikriteas, M. Vousden, M. Wagih, U. T. Jurado, J. Shi, S. Yong, S. Arumugam, Y. Li, K. Yang, G. Savelli, N. M. White, and S. Beeby, "E-textile technology review–from materials to application," *IEEE Access*, vol. 9, pp. 97 152–97 179, 2021, doi: https://doi.org/10.1109/ACCESS.2021.3094303.

[148] W. J. Oh, H. S. Lim, J. S. Won, and S. G. Lee, "Preparation of pvdf/par composites with piezoelectric properties by post-treatment," *Polymers*, vol. 10, no. 12, 2018, doi: https://doi.org/10.3390/polym10121333.

[149] L. Ruan, X. Yao, Y. Chang, L. Zhou, G. Qin, and X. Zhang, "Properties and applications of the β phase poly(vinylidene fluoride)," *Polymers*, vol. 10, no. 3, 2018, doi: https://doi.org/10.3390/polym10030228.

[150] G. Eberle, H. Schmidt, and W. Eisenmenger, "Piezoelectric polymer electrets," *IEEE Transactions on Dielectrics and Electrical Insulation*, vol. 3, no. 5, pp. 624–646, 1996, doi: https://doi.org/10.1109/94.544185.

[151] B. A. Newman, P. Chen, K. D. Pae, and J. I. Scheinbeim, "Piezoelectricity in nylon 11," *Journal of Applied Physics*, vol. 51, no. 10, pp. 5161–5164, 1980, doi: https://aip.scitation.org/doi/abs/10.1063/1.327283.

[152] Y. Zhang, C. R. Bowen, S. K. Ghosh, D. Mandal, H. Khanbareh, M. Arafa, and C. Wan, "Ferroelectret materials and devices for energy harvesting applications," *Nano Energy*, vol. 57, pp. 118–140, 2019, doi: https://doi.org/10.1016/j.nanoen.2018.12.040.

[153] J. Shi and S. P. Beeby, "The effect of fabric properties on the performance of a textile based ferroelectret generator toward human body energy harvesting," *Smart Materials and Structures*, vol. 31, no. 4, p. 045015, mar 2022, doi: https://doi.org/10.1088/1361-665x/ac56b8.

[154] S. Yong, J. Shi, and S. Beeby, "Wearable textile power module based on flexible ferroelectret and supercapacitor," *Energy Technology*, vol. 7, no. 5, p. 1800938, 2019, doi: https://doi.org/10.1002/ente.201800938.

[155] Y. Zi, S. Niu, J. Wang, Z. Wen, W. Tang, and Z. L. Wang, "Standards and figure-of-merits for quantifying the performance of triboelectric nanogenerators," *Nature communications*, vol. 6, no. 1, pp. 1–8, 2015, doi: https://doi.org/10.1038/ncomms9376.

[156] B. Meng, W. Tang, Z.-h. Too, X. Zhang, M. Han, W. Liu, and H. Zhang, "A transparent single-friction-surface triboelectric generator and self-powered touch sensor," *Energy Environ. Sci.*, vol. 6, pp. 3235–3240, 2013, doi: http://dx.doi.org/10.1039/C3EE42311E.

[157] Y. Yang, H. Zhang, Z.-H. Lin, Y. S. Zhou, Q. Jing, Y. Su, J. Yang, J. Chen, C. Hu, and Z. L. Wang, "Human skin based triboelectric nanogenerators for harvesting biomechanical energy and as self-powered active tactile sensor system," *ACS Nano*, vol. 7, no. 10, pp. 9213–9222, 2013, doi: https://doi.org/10.1021/nn403838y.

[158] X. Pu, M. Liu, X. Chen, J. Sun, C. Du, Y. Zhang, J. Zhai, W. Hu, and Z. L. Wang, "Ultrastretchable, transparent triboelectric nanogenerator as electronic skin for biomechanical energy harvesting and tactile sensing," *Science Advances*, vol. 3, no. 5, p. e1700015, 2017, doi: https://doi.org/10.1126/sciadv.1700015.

[159] X. Li, Z.-H. Lin, G. Cheng, X. Wen, Y. Liu, S. Niu, and Z. L. Wang, "3d fiber-based hybrid nanogenerator for energy harvesting and as a self-powered pressure sensor," *ACS Nano*, vol. 8, no. 10, pp. 10 674–10 681, 2014, doi: https://doi.org/10.1021/nn504243.

[160] H. J. Sim, C. Choi, S. H. Kim, K. M. Kim, C. J. Lee, Y. T. Kim, X. Lepró, R. H. Baughman, and S. J. Kim, "Stretchable triboelectric fiber for self-powered kinematic sensing textile," *Scientific reports*, vol. 6, no. 1, pp. 1–7, 2016, doi: https://doi.org/10.1038/srep35153.

[161] X. Yu, J. Pan, J. Zhang, H. Sun, S. He, L. Qiu, H. Lou, X. Sun, and H. Peng, "A coaxial triboelectric nanogenerator fiber for energy harvesting and sensing under deformation," *J. Mater. Chem. A*, vol. 5, pp. 6032–6037, 2017, doi: http://dx.doi.org/10.1039/C7TA00248C.

[162] W. B. Ko, D. S. Choi, C. H. Lee, J. Y. Yang, G. S. Yoon, and J. P. Hong, "Hierarchically nanostructured 1d conductive bundle yarn-based triboelectric nanogenerators," *Advanced Materials*, vol. 29, no. 47, p. 1704434, 2017, doi: https://doi.org/10.1002/adma.201704434.

[163] K. Dong, Y.-C. Wang, J. Deng, Y. Dai, S. L. Zhang, H. Zou, B. Gu, B. Sun, and Z. L. Wang, "A highly stretchable and washable all-yarn-based self-charging knitting power textile composed of fiber triboelectric nanogenerators and supercapacitors," *ACS Nano*, vol. 11, no. 9, pp. 9490–9499, 2017, doi: https://doi.org/10.1021/acsnano.7b05317.

[164] W. Paosangthong, R. Torah, and S. Beeby, "Recent progress on textile-based triboelectric nanogenerators," *Nano Energy*, vol. 55, pp. 401–423, 2019, doi: https://doi.org/10.1016/j.nanoen.2018.10.036.

[165] C. Ning, L. Tian, X. Zhao, S. Xiang, Y. Tang, E. Liang, and Y. Mao, "Washable textile-structured single-electrode triboelectric nanogenerator for self-powered wearable electronics," *J. Mater. Chem. A*, vol. 6, pp. 19 143–19 150, 2018, doi: https;//doi.org/10.1039/C8TA07784C.

[166] V. Jangra, S. Maity, and P. Vishnoi, "A review on the development of conjugated polymer-based textile thermoelectric generator," *Journal of Industrial Textiles*, vol. 51, no. 1_suppl, pp. 181S–214S, 2022, doi: https://doi.org/10.1177/1528083721996732.

[167] N. Klochko, K. Klepikova, D. Zhadan, V. Kopach, S. Chernyavskaya, S. Petrushenko, S. Dukarov, V. Lyubov, and A. Khrypunova, "Thermoelectric textile with fibers coated by copper iodide thin films," *Thin Solid Films*, vol. 704, p. 138026, 2020, doi: https://doi.org/10.1016/j.tsf.2020.138026.

[168] M. B. Schubert and J. H. Werner, "Flexible solar cells for clothing," *Materials Today*, vol. 9, no. 6, pp. 42–50, 2006, doi: https://doi.org/10.1016/S1369-7021(06)71542-5.

[169] J. Liu, Y. Li, M. Li, S. Arumugam, and S. P. Beeby, "Processing of printed dye sensitized solar cells on woven textiles," *IEEE Journal of Photovoltaics*, vol. 9, no. 4, pp. 1020–1024, 2019, doi: https://doi.org/10.1109/JPHOTOV.2019.2899432.

[170] M. Wagih, A. S. Weddell, and S. Beeby, "Omnidirectional dual-polarized low-profile textile rectenna with over 50% efficiency for sub-µw/cm2 wearable power harvesting," *IEEE Transactions on Antennas and Propagation*, vol. 69, no. 5, pp. 2522–2536, 2021, doi: https://doi.org/10.1109/TAP.2020.3030992.

[171] M. Wagih, N. Hillier, S. Yong, A. S. Weddell, and S. Beeby, "Rf-powered wearable energy harvesting and storage module based on e-textile coplanar waveguide rectenna and supercapacitor," *IEEE Open Journal of Antennas and Propagation*, vol. 2, pp. 302–314, 2021, doi: 10.1109/OJAP.2021.3059501.

[172] M. Wagih, Y. Wei, A. Komolafe, R. Torah, and S. Beeby, "Reliable uhf long-range textile-integrated rfid tag based on a compact flexible antenna filament," *Sensors*, vol. 20, no. 12, 2020, doi: https://doi.org/10.3390/s20123435.

[173] F. Silva, R. Almeida, C. Gouveia, C. Loss, P. Pinho, and D. Belo, "Textile rectenna for rf energy harvesting," in *2021 15th European Conference on Antennas and Propagation (EuCAP)*, 2021, pp. 1–4, doi: https://doi.or/10.23919/EuCAP51087.2021.9411039.

[174] N. Soin, T. H. Shah, S. C. Anand, J. Geng, W. Pornwannachai, P. Mandal, D. Reid, S. Sharma, R. L. Hadimani, D. V. Bayramol, and E. Siores, "Novel "3-d spacer" all fibre piezoelectric textiles for energy harvesting applications," *Energy*

Environ. Sci., vol. 7, pp. 1670–1679, 2014, doi: http://dx.doi.org/10.1039/C3EE43987A.

[175] Z. Luo, D. Zhu, J. Shi, S. Beeby, C. Zhang, P. Proynov, and B. Stark, "Energy harvesting study on single and multilayer ferroelectret foams under compressive force," *IEEE Transactions on Dielectrics and Electrical Insulation*, vol. 22, no. 3, pp. 1360–1368, 2015, doi: https://doi.org/10.1109/TDEI.2015.7116323.

[176] A. Nozariasbmarz, H. Collins, K. Dsouza, M. H. Polash, M. Hosseini, M. Hyland, J. Liu, A. Malhotra, F. M. Ortiz, F. Mohaddes, V. P. Ramesh, Y. Sargolzaeiaval, N. Snouwaert, M. C. Özturk, and D. Vashaee, "Review of wearable thermoelectric energy harvesting: From body temperature to electronic systems," *Applied Energy*, vol. 258, p. 114069, 2020, doi: https://doi.org/10.1016/j.apenergy.2019.114069.

[177] X. Fu, H. Sun, S. Xie, J. Zhang, Z. Pan, M. Liao, L. Xu, Z. Li, B. Wang, X. Sun, and H. Peng, "A fiber-shaped solar cell showing a record power conversion efficiency of 102018, doi: http://dx.doi.org/10.1039/C7TA08637G.

[178] L. Yin, K. N. Kim, J. Lv, F. Tehrani, M. Lin, Z. Lin, J.-M. Moon, J. Ma, J. Yu, S. Xu *et al.*, "A self-sustainable wearable multi-modular e-textile bioenergy microgrid system," *Nature communications*, vol. 12, no. 1, pp. 1–12, 2021, doi: https://doi.org/10.1038/s41467-021-21701-7.

[179] S. Fletcher, "Tables of degenerate electrical networks for use in the equivalent-circuit analysis of electrochemical systems," *Journal of The Electrochemical Society*, vol. 141, no. 7, pp. 1823–1826, jul 1994, doi: https://doi.org/10.1149/1.2055011.

[180] S. Fletcher, V. J. Black, and I. Kirkpatrick, "A universal equivalent circuit for carbon-based supercapacitors," *Journal of Solid State Electrochemistry*, vol. 18, pp. 1377–1387, 2014, doi: https://doi.org/10.1007/s10008-013-2328-4.

[181] R. Spyker and R. Nelms, "Classical equivalent circuit parameters for a double-layer capacitor," *IEEE Transactions on Aerospace and Electronic Systems*, vol. 36, no. 3, pp. 829–836, 2000, doi: https://doi.org/10.1109/7.869502.

[182] ——, "Analysis of double-layer capacitors supplying constant power loads," *IEEE Transactions on Aerospace and Electronic Systems*, vol. 36, no. 4, pp. 1439–1443, 2000, doi: https://doi.org/10.1109/7.892696.

[183] J. W. Graydon, M. Panjehshahi, and D. W. Kirk, "Charge redistribution and ionic mobility in the micropores of supercapacitors," *Journal of Power Sources*, vol. 245, pp. 822–829, 2014, doi: https://doi.org/10.1016/j.jpowsour.2013.07.036.

[184] G. Gourdin, A. Meehan, T. Jiang, P. Smith, and D. Qu, "Investigation of the impact of stacking pressure on a double-layer supercapacitor," *Journal of Power Sources*, vol. 196, no. 1, pp. 523–529, 2011, doi: https://doi.org/10.1016/j.jpowsour.2010.06.022.

[185] M. Janssen, "Transmission line circuit and equation for an electrolyte-filled pore of finite length," *Phys. Rev. Lett.*, vol. 126, p. 136002, Mar 2021, doi: 10.1103/PhysRevLett.126.136002. [Online]. Available: https://link.aps.org/doi/10.1103/PhysRevLett.126.136002

[186] J. M. Black and H. A. Andreas, "Pore shape affects spontaneous charge redistribution in small pores," *The Journal of Physical Chemistry C*, vol. 114, no. 27, pp. 12 030–12 038, 2010, doi: https://doi.org/10.1021/jp103766q.

[187] G.-J. Lee, S.-I. Pyun, and C.-H. Kim, "Kinetics of double-layer charging/discharging of the activated carbon fiber cloth electrode: effects of pore length distribution and solution resistance," *Journal of Solid State Electrochemistry*, vol. 8, pp. 110–117, 2004, doi: https://doi.org/10.1007/s10008-003-0392-x.

[188] D. B. Robinson, "Optimization of power and energy densities in supercapacitors," *Journal of Power Sources*, vol. 195, no. 11, pp. 3748–3756, 2010, doi: https://doi.org/10.1016/j.jpowsour.2009.12.004.

[189] J. Black and H. A. Andreas, "Effects of charge redistribution on self-discharge of electrochemical capacitors," *Electrochimica Acta*, vol. 54, no. 13, pp. 3568–3574, 2009, doi: https://doi.org/10.1016/j.electacta.2009.01.019.

[190] J. Xie, P. Yang, Y. Wang, T. Qi, Y. Lei, and C. M. Li, "Puzzles and confusions in supercapacitor and battery: Theory and solutions," *Journal of Power Sources*, vol. 401, pp. 213–223, 2018, doi: https://doi.org/10.1016/j.jpowsour.2018.08.090.

[191] The British Standards Institution, "BS EN 62391-1:2016 Fixed electric double-layer capacitors for use in electric and electronic equipment. Generic specification," The British Standards Institution, London, UK, standard BS EN 62391-1:2016, 2016, doi: https://doi.org/10.3403/30260803.

[192] D. Huang, Q. Zheng, K. Guo, and X. Chen, "Wearable supercapacitor based on polyaniline supported by graphene coated polyester textile," *International Journal of Energy Research*, vol. 45, no. 15, pp. 21 403–21 413, 2021, doi: https://doi.org/10.1002/er.7190.

[193] D. Qu, G. Wang, J. Kafle, J. Harris, L. Crain, Z. Jin, and D. Zheng, "Electrochemical impedance and its applications in energy-storage systems," *Small Methods*, vol. 2, no. 8, p. 1700342, 2018, doi: https://doi.org/10.1002/smtd.201700342.

[194] H. Fricke, "Xxxiii. the theory of electrolytic polarization," *The London, Edinburgh, and Dublin Philosophical Magazine and Journal of Science*, vol. 14, no. 90, pp. 310–318, 1932, doi: https://doi.org/10.1080/14786443209462064.

[195] P. Córdoba-Torres, "Relationship between constant-phase element (cpe) parameters and physical properties of films with a distributed resistivity," *Electrochimica Acta*, vol. 225, pp. 592–604, 2017, doi: https://doi.org/10.1016/j.electacta.2016.12.087.

[196] Q. Huang, D. Wang, H. Hu, J. Shang, J. Chang, C. Xie, Y. Yang, X. Lepró, R. H. Baughman, and Z. Zheng, "Additive functionalization and embroidery for manufacturing wearable and washable textile supercapacitors," *Advanced*

Functional Materials, vol. 30, no. 27, p. 1910541, 2020, doi: https://doi.org/10.1002/adfm.201910541.

[197] T. He, R. Jia, X. Lang, X. Wu, and Y. Wang, "Preparation and electrochemical performance of PVdF ultrafine porous fiber separator-cum-electrolyte for supercapacitor," *Journal of The Electrochemical Society*, vol. 164, no. 13, pp. E379–E384, 2017, doi: https://doi.org/10.1149/2.0631713jes.

[198] N. Hillier, S. Yong, and S. Beeby, "Optimization of carbon electrodes for solid-state e-textile supercapacitors," *Journal of Physics: Conference Series*, vol. 1407, p. 012059, 2019, doi: 10.1088/1742-6596/1407/1/01205.

[199] N. Hillier, S. Yong, A. Cruden, and S. Beeby, "Acetonitrile-free organic electrolyte for textile supercapacitor applications," *Journal of The Electrochemical Society*, vol. 168, no. 8, p. 080520, aug 2021, doi: https://doi.org/10.1149/1945-7111/ac1a58.

[200] A. E. Del Rio Castillo, V. Pellegrini, A. Ansaldo, F. Ricciardella, H. Sun, L. Marasco, J. Buha, Z. Dang, L. Gagliani, E. Lago, N. Curreli, S. Gentiluomo, F. Palazon, M. Prato, R. Oropesa-Nuñez, P. S. Toth, E. Mantero, M. Crugliano, A. Gamucci, A. Tomadin, M. Polini, and F. Bonaccorso, "High-yield production of 2d crystals by wet-jet milling," *Mater. Horiz.*, vol. 5, pp. 890–904, 2018, doi: http://dx.doi.org/10.1039/C8MH00487K.

[201] Q. Zhou, Y. Lu, and H. Xu, "High-yield production of high-quality graphene by novel electrochemical exfoliation at air-electrolyte interface," *Materials Letters*, vol. 235, pp. 153–156, 2019, doi: https://doi.org/10.1016/j.matlet.2018.10.016.

[202] "Sigma Aldrich," https://www.sigmaaldrich.com/GB/en, accessed: 2021-10-09.

[203] R. I. Kosheleva, A. C. Mitropoulos, and G. Z. Kyzas, "Synthesis of activated carbon from food waste," *Environmental Chemistry Letters*, vol. 17, no. 1, pp. 429–438, 2019, doi: https://doi.org/10.1007/s10311-018-0817-5.

[204] B. Ruiz, N. Ferrera-Lorenzo, and E. Fuente, "Valorisation of lignocellulosic wastes from the candied chestnut industry. sustainable activated carbons for

environmental applications," *Journal of Environmental Chemical Engineering*, vol. 5, no. 2, pp. 1504–1515, 2017, doi: https://doi.org/10.1016/j.jece.2017.02.028.

[205] D. Özçimen and A. Ersoy-Meriçboyu, "Removal of copper from aqueous solutions by adsorption onto chestnut shell and grapeseed activated carbons," *Journal of Hazardous Materials*, vol. 168, no. 2, pp. 1118–1125, 2009, doi: https://doi.org/10.1016/j.jhazmat.2009.02.148.

[206] H. Wang, J. Xu, X. Liu, and L. Sheng, "Preparation of straw activated carbon and its application in wastewater treatment: A review," *Journal of Cleaner Production*, vol. 283, p. 124671, 2021, doi: https://doi.org/10.1016/j.jclepro.2020.124671.

[207] M. Danish and T. Ahmad, "A review on utilization of wood biomass as a sustainable precursor for activated carbon production and application," *Renewable and Sustainable Energy Reviews*, vol. 87, pp. 1–21, 2018, doi: https://doi.org/10.1016/j.rser.2018.02.003.

[208] R. T. Ayinla, J. Dennis, H. Zaid, Y. Sanusi, F. Usman, and L. Adebayo, "A review of technical advances of recent palm bio-waste conversion to activated carbon for energy storage," *Journal of Cleaner Production*, vol. 229, pp. 1427–1442, 2019, doi: https://doi.org/10.1016/j.jclepro.2019.04.116.

[209] K. Liu, Y. Yao, T. Lv, H. Li, N. Li, Z. Chen, G. Qian, and T. Chen, "Textile-like electrodes of seamless graphene/nanotubes for wearable and stretchable supercapacitors," *Journal of Power Sources*, vol. 446, p. 227355, 2020, doi: https://doi.org/10.1016/j.jpowsour.2019.227355.

[210] L. Wang, C. Zhang, X. Jiao, and Z. Yuan, "Polypyrrole-based hybrid nanostructures grown on textile for wearable supercapacitors," *Nano Research*, vol. 12, no. 5, pp. 1129–1137, 2019, doi: https://doi.org/10.1007/s12274-019-2360-5.

[211] L.-N. Jin, F. Shao, C. Jin, J.-N. Zhang, P. Liu, M.-X. Guo, and S.-W. Bian, "High-performance textile supercapacitor electrode materials enhanced with three-dimensional carbon nanotubes/graphene conductive network and in situ

polymerized polyaniline," *Electrochimica Acta*, vol. 249, pp. 387–394, 2017, doi: https://doi.org/10.1016/j.electacta.2017.08.035.

[212] G. Paul, R. Torah, S. Beeby, and J. Tudor, "The development of screen printed conductive networks on textiles for biopotential monitoring applications," *Sensors and Actuators A: Physical*, vol. 206, pp. 35–41, 2014, doi: https://doi.org/10.1016/j.sna.2013.11.026.

[213] E. N. Tsurko, R. Neueder, J. Barthel, and A. Apelblat, "Conductivity of phosphoric acid, sodium, potassium, and ammonium phosphates in dilute aqueous solutions from 278.15 k to 308.15 k," *Journal of solution chemistry*, vol. 28, no. 8, pp. 973–999, 1999, doi: https://doi.org/10.1023/A:1022630610419.

[214] M. Ahmed, M. A. Islam, M. Asif, and B. Hameed, "Human hair-derived high surface area porous carbon material for the adsorption isotherm and kinetics of tetracycline antibiotics," *Bioresource Technology*, vol. 243, pp. 778–784, 2017, doi: https://doi.org/10.1016/j.biortech.2017.06.174.

[215] M. Thommes, K. Kaneko, A. V. Neimark, J. P. Olivier, F. Rodriguez-Reinoso, J. Rouquerol, and K. S. Sing, "Physisorption of gases, with special reference to the evaluation of surface area and pore size distribution (iupac technical report)," *Pure and applied chemistry*, vol. 87, no. 9-10, pp. 1051–1069, 2015, doi: https://doi.org/10.1515/pac-2014-1117.

[216] R. Bardestani, G. S. Patience, and S. Kaliaguine, "Experimental methods in chemical engineering: specific surface area and pore size distribution measurements—bet, bjh, and dft," *The Canadian Journal of Chemical Engineering*, vol. 97, no. 11, pp. 2781–2791, 2019, doi: https://doi.org/10.1002/cjce.23632.

[217] S. Lemey, S. Agneessens, P. Van Torre, K. Baes, J. Vanfleteren, and H. Rogier, "Wearable flexible lightweight modular rfid tag with integrated energy harvester," *IEEE Transactions on Microwave Theory and Techniques*, vol. 64, no. 7, pp. 2304–2314, 2016, doi: https://doi.org/10.1109/TMTT.2016.2573274.

[218] O. O. Ojuroye, R. N. Torah, A. O. Komolafe, and S. P. Beeby, "Embedded capacitive proximity and touch sensing flexible circuit system for electronic

textile and wearable systems," *IEEE Sensors Journal*, vol. 19, no. 16, pp. 6975–6985, 2019, doi: https://doi.org/10.1109/JSEN.2019.2911561.

[219] J. Le Houx and D. Kramer, "X-ray tomography for lithium ion battery electrode characterisation — a review," *Energy Reports*, vol. 7, pp. 9–14, 2021, doi: https://doi.org/10.1016/j.egyr.2021.02.063.

[220] A. Voronov, V. Salo, V. Puzikov, V. Tkachenko, and Y. T. Vydai, "Potassium and ammonium dihydrogen phosphates activated with thallium: Growth and luminescence and scintillation properties," *Crystallography Reports*, vol. 51, no. 4, pp. 696–701, 2006, doi: https://doi.org/10.1134/S1063774506040262.

[221] A. Ruf, B. Kanawati, and P. Schmitt-Kopplin, "Dihydrogen phosphate anion boosts the detection of sugars in electrospray ionization mass spectrometry: A combined experimental and computational investigation," *Rapid Communications in Mass Spectrometry*, vol. 36, no. 11, p. e9283, 2022, doi: https://doi.org/10.1002/rcm.9283.

[222] J. Bates, F. Markoulidis, C. Lekakou, and G. M. Laudone, "Design of porous carbons for supercapacitor applications for different organic solvent-electrolytes," *C*, vol. 7, no. 1, 2021, doi: https://doi.org/10.3390/c7010015.

[223] B. Andres, A.-C. Engström, N. Blomquist, S. Forsberg, C. Dahlström, and H. Olin, "Electrode mass balancing as an inexpensive and simple method to increase the capacitance of electric double-layer capacitors," *Plos one*, vol. 11, no. 9, p. e0163146, 2016, doi: https://doi.org/10.1371/journal.pone.0163146.

[224] D. Van Lam, K. Jo, C.-H. Kim, S. Won, Y. Hwangbo, J.-H. Kim, H.-J. Lee, and S.-M. Lee, "Calligraphic ink enabling washable conductive textile electrodes for supercapacitors," *J. Mater. Chem. A*, vol. 4, pp. 4082–4088, 2016, doi: http://dx.doi.org/10.1039/C6TA01341D.

[225] S. F. Zopf and M. Manser, "Screen-printed military textiles for wearable energy storage," *Journal of Engineered Fibers and Fabrics*, vol. 11, no. 3, p. 155892501601100303, 2016, doi: https://doi.org/10.1177/155892501601100303.

[226] H. Zhang, Y. Qiao, and Z. Lu, "Fully printed ultraflexible supercapacitor supported by a single-textile substrate," *ACS Applied Materials & Interfaces*, vol. 8, no. 47, pp. 32 317–32 323, 2016, doi: https://doi.org/10.1021/acsami.6b11172.

[227] R. Chen, H. Tang, P. He, W. Zhang, Y. Dai, W. Zong, F. Guo, G. He, and X. Wang, "Interface engineering of biomass-derived carbon used as ultrahigh-energy-density and practical mass-loading supercapacitor electrodes," *Advanced Functional Materials*, vol. 33, no. 8, p. 2212078, 2023, doi:https://doi.org/10.1002/adfm.202212078.

[228] S. Wei, C. Wan, L. Zhang, X. Liu, W. Tian, J. Su, W. Cheng, and Y. Wu, "N-doped and oxygen vacancy-rich nico2o4 nanograss for supercapacitor electrode," *Chemical Engineering Journal*, vol. 429, p. 132242, 2022, doi: https://doi.org/10.1016/j.cej.2021.132242.

[229] Q. Chen, L. Cao, H. Wang, Z. Zhou, and P. Xiao, "Oxygen/fluorine-functionalized flexible carbon electrodes for high-performance and anti-self-discharge zn-ion hybrid capacitors," *Journal of Power Sources*, vol. 538, p. 231586, 2022, doi: https://doi.org/10.1016/j.jpowsour.2022.231586.

[230] N. Hillier, S. Yong, and S. Beeby, "Calendar life of textile supercapacitors," in *2019 19th International Conference on Micro and Nanotechnology for Power Generation and Energy Conversion Applications (PowerMEMS)*, 2019, pp. 1–5, doi: 10.1109/PowerMEMS49317.2019.82063200604.

[231] ——, "Culinary inspired electrolytes for textile supercapacitors," *Energy Reports*, vol. 7, pp. 81–86, 2021, doi: https://doi.org/10.1016/j.egyr.2021.02.050.

[232] P. Bharathidasan, T. Subramaniam, D. Chandini, S. R. Sivakkumar, K. S. Rajan, and D. S., "Simultaneous enhancement of energy and power density of reduced graphene oxide by the effect of dispersed metal oxide nanoparticles in the electrolyte," *Journal of The Electrochemical Society*, vol. 167, no. 14, p. 140524, 2020, doi: https://doi.org/10.1149/1945-7111/abc434.

[233] W. Luo, X. Li, and J. Y. Chen, "All-fabric flexible supercapacitor for energy storage," *Journal of Industrial Textiles*, vol. 49, no. 8, pp. 1061–1077, 2020, doi: https://doi.org/10.1177/1528083718804208.

[234] R. Guo, J. Li, Y. Jia, F. Xin, J. Sun, L. Dang, Z. Liu, and Z. Lei, "Nitrogen-doped carbon sheets coated on conio2@textile carbon as bifunctional electrodes for asymmetric supercapacitors," *J. Mater. Chem. A*, vol. 7, pp. 4165–4174, 2019, doi: https://doi.org/10.1039/C9TA00014C.

[235] J. Zhao, L. Cao, F. Lai, X. Wang, S. Huang, X. Du, W. Li, Z. Lin, and P. Zhang, "Double-cross-linked polyaniline hydrogel and its application in supercapacitors," *Ionics*, vol. 28, no. 1, pp. 423–432, 2022, doi: https://doi.org/10.1007/s11581-021-04251-2.

[236] L. Guo, W.-B. Ma, Y. Wang, X.-Z. Song, J. Ma, X.-D. Han, X.-Y. Tao, L.-T. Guo, H.-L. Fan, Z.-S. Liu, Y.-B. Zhu, and X.-Y. Wei, "A chemically crosslinked hydrogel electrolyte based all-in-one flexible supercapacitor with superior performance," *Journal of Alloys and Compounds*, vol. 843, p. 155895, 2020, doi: https://doi.org/10.1016/j.jallcom.2020.155895.

[237] R. Na, X. Wang, N. Lu, G. Huo, H. Lin, and G. Wang, "Novel egg white gel polymer electrolyte and a green solid-state supercapacitor derived from the egg and rice waste," *Electrochimica Acta*, vol. 274, pp. 316–325, 2018, doi: https://doi.org/10.1016/j.electacta.2018.04.127.

[238] X. Wang, W. Xu, P. Chatterjee, C. Lv, J. Popovich, Z. Song, L. Dai, M. Y. S. Kalani, S. E. Haydel, and H. Jiang, "Food-materials-based edible supercapacitors," *Advanced Materials Technologies*, vol. 1, no. 3, p. 1600059, 2016, doi: https://doi.org/10.1002/admt.201600059.

[239] W. G. Moon, G.-P. Kim, M. Lee, H. D. Song, and J. Yi, "A biodegradable gel electrolyte for use in high-performance flexible supercapacitors," *ACS Applied Materials & Interfaces*, vol. 7, no. 6, pp. 3503–3511, 2015, doi: https://doi.org/10.1021/am5070987.

[240] Y. Huang, J. Liu, J. Zhang, S. Jin, Y. Jiang, S. Zhang, Z. Li, C. Zhi, G. Du, and H. Zhou, "Flexible quasi-solid-state zinc ion batteries enabled by highly conductive carrageenan bio-polymer electrolyte," *RSC Adv.*, vol. 9, pp. 16 313–16 319, 2019, doi: http://dx.doi.org/10.1039/C9RA01120J.

[241] S. Alipoori, S. Mazinani, S. H. Aboutalebi, and F. Sharif, "Review of pva-based gel polymer electrolytes in flexible solid-state supercapacitors: Opportunities and challenges," *Journal of Energy Storage*, vol. 27, p. 101072, 2020, doi: https://doi.org/10.1016/j.est.2019.101072.

[242] S. Hosseini, A. Abbasi, L.-O. Uginet, N. Haustraete, S. Praserthdam, T. Yonezawa, and S. Kheawhom, "The influence of dimethyl sulfoxide as electrolyte additive on anodic dissolution of alkaline zinc-air flow battery," *Scientific reports*, vol. 9, no. 1, pp. 1–12, 2019, doi: https://doi.org/10.1038/s41598-019-51412-5.

[243] C. Decaux, C. Matei Ghimbeu, M. Dahbi, M. Anouti, D. Lemordant, F. Béguin, C. Vix-Guterl, and E. Raymundo-Piñero, "Influence of electrolyte ion–solvent interactions on the performances of supercapacitors porous carbon electrodes," *Journal of Power Sources*, vol. 263, pp. 130–140, 2014, doi: https://doi.org/10.1016/j.jpowsour.2014.04.024.

[244] M. Ue, "Mobility and ionic association of lithium and quaternary ammonium salts in propylene carbonate and gamma-butyrolactone," *Journal of The Electrochemical Society*, vol. 141, no. 12, pp. 3336–3342, dec 1994, doi: https://doi.org/10.1149/1.2059336.

[245] G. Feng, J. Huang, B. G. Sumpter, V. Meunier, and R. Qiao, "Structure and dynamics of electrical double layers in organic electrolytes," *Phys. Chem. Chem. Phys.*, vol. 12, pp. 5468–5479, 2010, doi: http://dx.doi.org/10.1039/C000451K.

[246] H. Gao, J. Li, and K. Lian, "Alkaline quaternary ammonium hydroxides and their polymer electrolytes for electrochemical capacitors," *RSC Adv.*, vol. 4, pp. 21 332–21 339, 2014, doi: DOIhttps://doi.org/10.1039/C4RA01014K.

[247] P. Sun, M. Qiu, M. Li, W. Mai, G. Cui, and Y. Tong, "Stretchable ni@nicop textile for wearable energy storage clothes," *Nano Energy*, vol. 55, pp. 506–515, 2019, doi: https://doi.org/10.1016/j.nanoen.2018.10.067.

[248] Y. Huang, M. Zhong, F. Shi, X. Liu, Z. Tang, Y. Wang, Y. Huang, H. Hou, X. Xie, and C. Zhi, "An intrinsically stretchable and compressible supercapacitor containing a polyacrylamide hydrogel electrolyte," *Angewandte Chemie International Edition*, vol. 56, no. 31, pp. 9141–9145, 2017, doi: https://doi.org/10.1002/anie.201705212.

[249] M. J. Tan, B. Li, P. Chee, X. Ge, Z. Liu, Y. Zong, and X. J. Loh, "Acrylamide-derived freestanding polymer gel electrolyte for flexible metal-air batteries," *Journal of Power Sources*, vol. 400, pp. 566–571, 2018, doi: https://doi.org/10.1016/j.jpowsour.2018.08.066.

[250] Q. Huang, D. Wang, H. Hu, J. Shang, J. Chang, C. Xie, Y. Yang, X. Lepró, R. H. Baughman, and Z. Zheng, "Additive functionalization and embroidery for manufacturing wearable and washable textile supercapacitors," *Advanced Functional Materials*, vol. 30, no. 27, p. 1910541, 2020, doi: https://doi.org/10.1002/adfm.201910541.

[251] F. Cheng, X. Yang, S. Zhang, and W. Lu, "Boosting the supercapacitor performances of activated carbon with carbon nanomaterials," *Journal of Power Sources*, vol. 450, p. 227678, 2020, doi: https://doi.org/10.1016/j.jpowsour.2019.227678.

[252] P. Ruschhaupt, S. Pohlmann, A. Varzi, and S. Passerini, "Determining realistic electrochemical stability windows of electrolytes for electrical double-layer capacitors," *Batteries & Supercaps*, vol. 3, no. 8, pp. 698–707, 2020, doi: https://doi.org/10.1002/batt.202000009.

[253] D. Weingarth, A. Foelske-Schmitz, and R. Kötz, "Cycle versus voltage hold – which is the better stability test for electrochemical double layer capacitors?" *Journal of Power Sources*, vol. 225, pp. 84–88, 2013, doi: https://doi.org/10.1016/j.jpowsour.2012.10.019.

[254] J. Shang, Q. Huang, L. Wang, Y. Yang, P. Li, and Z. Zheng, "Soft hybrid scaffold (shs) strategy for realization of ultrahigh energy density of wearable aqueous supercapacitors," *Advanced Materials*, vol. 32, no. 4, p. 1907088, 2020, doi: https://doi.org/10.1002/adma.201907088.

[255] S. Tan and K. D. Li-Oakey, "Effect of structural orientation on the performance of supercapacitor electrodes from electrospun coal-derived carbon nanofibers (CCNFs)," *Journal of The Electrochemical Society*, vol. 166, no. 14, pp. A3294–A3304, 2019, doi: https://doi.org/10.1149/2.0651914jes.

[256] X. Li, L. Yuan, R. Liu, H. He, J. Hao, Y. Lu, Y. Wang, G. Liang, G. Yuan, and Z. Guo, "Engineering textile electrode and bacterial cellulose nanofiber reinforced hydrogel electrolyte to enable high-performance flexible all-solid-state supercapacitors," *Advanced Energy Materials*, vol. 11, no. 12, p. 2003010, 2021, doi: https://doi.org/10.1002/aenm.202003010.

[257] H. Xu, X. Hu, H. Yang, Y. Sun, C. Hu, and Y. Huang, "Flexible asymmetric micro-supercapacitors based on bi2o3 and mno2 nanoflowers: Larger areal mass promises higher energy density," *Advanced Energy Materials*, vol. 5, no. 6, p. 1401882, 2015, doi: https://doi.org/10.1002/aenm.201401882.

[258] M. Wagih, A. Komolafe, and N. Hillier, "Screen-printable flexible textile-based ultra-broadband millimeter-wave dc-blocking transmission lines based on microstrip-embedded printed capacitors," *IEEE Journal of Microwaves*, vol. 2, no. 1, pp. 162–173, 2022, doi: https://doi.org/10.1109/JMW.2021.3126927.

[259] G. Chen, X. Xiao, X. Zhao, T. Tat, M. Bick, and J. Chen, "Electronic textiles for wearable point-of-care systems," *Chemical Reviews*, vol. 122, no. 3, pp. 3259–3291, 2022, doi: https://doi.org/10.1021/acs.chemrev.1c00502.

[260] M. Wagih, N. Hillier, A. S. Weddell, and S. Beeby, "E-textile rf energy harvesting and storage using organic-electrolyte carbon-based supercapacitors," in *2021 IEEE MTT-S International Microwave Workshop Series on Advanced Materials and Processes for RF and THz Applications (IMWS-AMP)*, 2021, pp. 391–393, doi: https://doi.org/10.1109/IMWS-AMP53428.2021.9643994.

[261] ——, "Textile-based radio frequency energy harvesting and storage using ultra-compact rectennas with high effective-to-physical area ratio," in *2021 IEEE 20th International Conference on Micro and Nanotechnology for Power Generation and Energy Conversion Applications (PowerMEMS)*, 2021, pp. 32–35, doi: https://doi.org/10.1109/PowerMEMS54003.2021.9658367.

[262] W. Sun, Y. Zhang, and F. Yang, "A high-performance symmetric supercapacitor from porous activated carbon under compression," *Energy Technology*, vol. 9, no. 5, p. 2100068, 2021, doi: https://doi.org/10.1002/ente.202100068.

[263] Y. Wang, Z. Pei, M. Zhu, Z. Liu, Y. Huang, Z. Ruan, Y. Huang, Y. Zhao, S. Du, and C. Zhi, "A wearable supercapacitor engaged with gold leaf gilding cloth toward enhanced practicability," *ACS Applied Materials & Interfaces*, vol. 10, no. 25, pp. 21 297–21 305, 2018, doi: https://doi.org/10.1021/acsami.8b03780.

[264] A. Singh, M. A. Akhtar, and A. Chandra, "Trade-off between capacitance and cycling at elevated temperatures in redox additive aqueous electrolyte based high performance asymmetric supercapacitors," *Electrochimica Acta*, vol. 229, pp. 291–298, 2017, doi: https://doi.org/10.1016/j.electacta.2017.01.167.

[265] Q. Zhang, J. Rong, D. Ma, and B. Wei, "The governing self-discharge processes in activated carbon fabric-based supercapacitors with different organic electrolytes," *Energy Environ. Sci.*, vol. 4, pp. 2152–2159, 2011, doi: http://dx.doi.org/10.1039/C0EE00773K.

[266] D. L. Paul, H. Giddens, M. G. Paterson, G. S. Hilton, and J. P. McGeehan, "Impact of body and clothing on a wearable textile dual band antenna at digital television and wireless communications bands," *IEEE Transactions on Antennas and Propagation*, vol. 61, no. 4, pp. 2188–2194, 2013, doi: https://doi.org/10.1109/TAP.2012.2232632.

[267] M. Wagih, A. S. Weddell, and S. Beeby, "Rectennas for radio-frequency energy harvesting and wireless power transfer: A review of antenna design [antenna applications corner]," *IEEE Antennas and Propagation Magazine*, vol. 62, no. 5, pp. 95–107, 2020, doi: https://doi.org/10.1109/MAP.2020.3012872.

[268] A. Okba, D. Henry, A. Takacs, and H. Aubert, "Autonomous rfid sensor node using a single ism band for both wireless power transfer and data communication," *Sensors*, vol. 19, no. 15, 2019, doi: https://doi.org/10.3390/s19153330.

[269] P. Li, Z. Long, and Z. Yang, "Rf energy harvesting for batteryless and maintenance-free condition monitoring of railway tracks," *IEEE Internet of Things Journal*, vol. 8, no. 5, pp. 3512–3523, 2021, doi: https://doi.org/10.1109/JIOT.2020.3023475.

[270] A. Okba, A. Takacs, and H. Aubert, "Compact rectennas for ultra-low-power wireless transmission applications," *IEEE Transactions on Microwave Theory and Techniques*, vol. 67, no. 5, pp. 1697–1707, 2019, doi: https://doi.org/10.1109/TMTT.2019.2902552.

[271] S. D. Assimonis, S.-N. Daskalakis, and A. Bletsas, "Sensitive and efficient rf harvesting supply for batteryless backscatter sensor networks," *IEEE Transactions on Microwave Theory and Techniques*, vol. 64, no. 4, pp. 1327–1338, 2016, doi: https://doi.org/10.1109/TMTT.2016.2533619.

[272] W. Zhao, K. Choi, S. Bauman, Z. Dilli, T. Salter, and M. Peckerar, "A radio-frequency energy harvesting scheme for use in low-power ad hoc distributed networks," *IEEE Transactions on Circuits and Systems II: Express Briefs*, vol. 59, no. 9, pp. 573–577, 2012, doi: https://doi.org/10.1109/TCSII.2012.2206935.

[273] S.-E. Adami, P. Proynov, G. S. Hilton, G. Yang, C. Zhang, D. Zhu, Y. Li, S. P. Beeby, I. J. Craddock, and B. H. Stark, "A flexible 2.45 ghz power harvesting wristband with net system output from 24.3 dbm of rf power," *IEEE Transactions on Microwave Theory and Techniques*, vol. 66, no. 1, pp. 380–395, 2018, doi: https://doi.org/10.1109/TMTT.2017.2700299.

[274] R. Jurdak, A. G. Ruzzelli, and G. M. O'Hare, "Radio sleep mode optimization in wireless sensor networks," *IEEE Transactions on Mobile Computing*, vol. 9, no. 7, pp. 955–968, 2010, doi: https://doi.org/10.1109/TMC.2010.35.

[275] Z. Chen, C. Song, J. Zhang, X. Zheng, V. Volskiy, P. Chu, and G. A. E. Vandenbosch, "Wearable rectenna with integrated miniaturized feeding slot and rectifier structure," *IEEE Transactions on Antennas and Propagation*, pp. 1–1, 2023, doi: https://doi.org/10.1109/TAP.2023.3249827.

[276] J.-M. Lopez-Garde, R. Del-Rio-Ruiz, J. Legarda, and H. Rogier, "2 × 2 textile rectenna array with electromagnetically coupled microstrip patch antennas in the 2.4 ghz wifi band," *Electronics*, vol. 10, no. 12, 2021, doi: https://doi.org/10.3390/electronics10121447. [Online]. Available: https://www.mdpi.com/2079-9292/10/12/1447

[277] A. S. Rao, A. Aziz, K. Aljaloud, M. A. Qureshi, A. Muhammad, A. Rafique, and R. Hussain, "Concomitance of radio frequency energy harvesting and wearable devices: A review of rectenna designs," *International Journal of RF and Microwave Computer-Aided Engineering*, vol. 32, no. 12, p. e23536, 2022, doi: https://doi.org/10.1002/mmce.23536.

[278] O. O. Umeonwuka, B. S. Adejumobi, and T. Shongwe, "Rectenna designs for energy harvesting iot devices: Overview of current trends and future directions," in *2021 International Conference on Electrical, Computer and Energy Technologies (ICECET)*, 2021, pp. 1–6, doi: https://doi.org/10.1109/ICECET52533.2021.9698604.

[279] L. Guo, X. Li, W. Sun, W. Yang, Y. Zhao, and K. Wu, "Designing and modeling of a dual-band rectenna with compact dielectric resonator antenna," *IEEE Antennas and Wireless Propagation Letters*, vol. 21, no. 5, pp. 1046–1050, 2022, doi: https:/doi.org/10.1109/LAWP.2022.3157322.

[280] M. Wagih, A. S. Weddell, and S. Beeby, "Rectennas for radio-frequency energy harvesting and wireless power transfer: A review of antenna design [antenna applications corner]," *IEEE Antennas and Propagation Magazine*, vol. 62, no. 5, pp. 95–107, 2020, doi: https:/doi.org/10.1109/MAP.2020.3012872.

[281] J. Bito, R. Bahr, J. G. Hester, S. A. Nauroze, A. Georgiadis, and M. M. Tentzeris, "A novel solar and electromagnetic energy harvesting system with a 3-d printed

package for energy efficient internet-of-things wireless sensors," *IEEE Transactions on Microwave Theory and Techniques*, vol. 65, no. 5, pp. 1831–1842, 2017, doi: https://doi.org/10.1109/TMTT.2017.2660487.

[282] M. Wagih, Y. Wei, and S. Beeby, "Flexible 2.4 ghz node for body area networks with a compact high-gain planar antenna," *IEEE Antennas and Wireless Propagation Letters*, vol. 18, no. 1, pp. 49–53, 2019, doi: https://doi.org/10.1109/LAWP.2018.2880490.

[283] G. Mattana, T. Kinkeldei, D. Leuenberger, C. Ataman, J. J. Ruan, F. Molina-Lopez, A. V. Quintero, G. Nisato, G. Tröster, D. Briand, and N. F. de Rooij, "Woven temperature and humidity sensors on flexible plastic substrates for e-textile applications," *IEEE Sensors Journal*, vol. 13, no. 10, pp. 3901–3909, 2013, doi: https:/doi.org/10.1109/JSEN.2013.2257167.

[284] T. Yamashita, T. Hayashi, H. Iwasaki, M. Awatsu, and H. Yokoyama, "Ultra-low-power energy harvester for microbial fuel cells and its application to environmental sensing and long-range wireless data transmission," *Journal of Power Sources*, vol. 430, pp. 1–11, 2019, doi: https://doi.org/10.1016/j.jpowsour.2019.04.120.

[285] L. Xu, H. Zhai, X. Chen, Y. Liu, M. Wang, Z. Liu, M. Umar, C. Ji, Z. Chen, L. Jin, Z. Liu, Q. Song, P. Yue, Y. Li, and T. T. Ye, "Coolmax/graphene-oxide functionalized textile humidity sensor with ultrafast response for human activities monitoring," *Chemical Engineering Journal*, vol. 412, p. 128639, 2021, doi: https://doi.org/10.1016/j.cej.2021.128639.

[286] L. Wang, C. Zhang, X. Jiao, and Z. Yuan, "Polypyrrole-based hybrid nanostructures grown on textile for wearable supercapacitors," *Nano Research*, vol. 12, pp. 1129–1137, 2019, doi: https://doi.org/10.1007/s12274-019-2360-5.

[287] H. Sun, S. Xie, Y. Li, Y. Jiang, X. Sun, B. Wang, and H. Peng, "Large-area supercapacitor textiles with novel hierarchical conducting structures," *Advanced Materials*, vol. 28, no. 38, pp. 8431–8438, 2016, doi: https://doi.org/10.1002/adma.201602987.

.